CIVIL ENGINEERING JOURNAL

číslo 1/2024

Obsah:

CIVIL ENGINEERING JOURNAL

Article no. 1

THE CIVIL ENGINEERING JOURNAL 1-2024

THE EVOLUTION OF CINEMAS IN THE SECOND HALF OF THE TWENTIETH CENTURY IN PRAGUE IN A CONTEMPORARY PERSPECTIVE

Tereza Čivrná

CzechTechnical University in Prague, Faculty of Civil Engineering, Department of Architecture, Prague, Thákurova 2077/7, Czech Republic; tereza.civrna@fsv.cvut.cz

ABSTRACT

The article approaches the situation of Prague cinemas in the second half of the 20th century from the end of the Second World War to the Velvet Revolution within the socio-historical background from the point of view of an architect and a cinephile. The entire text is arranged chronologically in four paragraphs reflecting the contemporary political and social situation. It approximates the post-war period full of ideological ideals, when the construction of a dense network of cinemas became a key element of national renewal, not only in large cities but also in the regions. The following decade brought a paradigmatic shift, when local single-screen cinemas gave way to large cultural houses with multifunctional use (film, theatre, gallery, restaurant, sports facilities, etc.). It deals with the socially relaxed sixties, reflecting the synergy of various artistic disciplines, thanks to which Czechoslovakia presented to the world new artistic disciplines based precisely on film projection – "polyekran" (polyscreen) and "laterna magika" (a combination of projection and performance with live actors). The imaginary culmination of the new wave period was the opening of the luxury cinema 64 U Hradeb, which is given more attention in the text below. Furthermore, the text outlines the situation of cinemas in large Prague housing estates and deals with Czech brutalism in the context of foreign architecture and with the only brutalist cinema still operating today – the Dlabačov cinema. The final part of this article gives a brief overview of the total number of cinemas established in this period in the territory of Prague and a comparison with other European metropolises with a similar socio-cultural background. The research has the ambition to understand and approach how to integrate valuable cinema buildings on the territory of Prague into the daily life of contemporary Prague residents through the investigation of the cinema phenomenon, and the development of cinematography and cinema architecture as such, from its inception to the present day. The general logical processing methods are historical and socio-cultural analysis, architectural and urban research including architectural drawings, photographic documentation and a study of the urban development of the appearance of individual cinemas, comparison and deduction.

KEYWORDS

Prague cinemas, 20th-century film culture, Movie theatre evolution, Post-war movie theatres, Polyekran, Laterna magika, Cinema 64 U Hradeb, Czech brutalism, Dlabačov cinema, Prague housing estate cinemas, European cinema comparison, Cinematography and architectural development

INTRODUCTION

The post-war period meant significant social and cultural changes for Czechoslovakia, mainly related to the nationalization of not only film production and distribution, but also the power of projection, which was also reflected in the architecture of movie theatres. In the first post-war

decade, film infrastructure became an integral part of national recovery. More than 500 cinemas were built, which served not only to show films, but became places of meeting and cultural interaction, reflecting post-war hopes and visionaries. The second half of the fifties brought a cultural turn, when the architecture of screening spaces began to slide towards new paradigms. Local single-screen cinemas have been replaced by large cultural houses with multifunctional use, combining theatre, film, restaurant, gallery etc. This transformation reflected an effort to strengthen the collective way of life, corresponding to the social ideals of the time and the idea of collective connection. The sixties bring a certain relief in all branches of culture and above all the connection of individual branches. On the basis of this cooperation, the Czechoslovak representatives presented a new style of projection on multiple screens – the „polyekran“ and the associated connection with the theater and dance arts – „laterna magika“. In this spirit, the long-awaited cinema 64 U Hradeb was created, which will be discussed in more detail in the following text. Furthermore, it will approach the scene of Prague brutalism with the only Dlabačov cinema still operating. In the final part, attention is paid to the cinemas of the Prague housing estates, followed by an analysis of the number of cinemas in Prague during the twentieth century in comparison with metropolises influenced by a similar socio-cultural environment, Berlin, Vienna and Warsaw. The article deals with history and typology, examines cinema as a phenomenon of the twentieth century, its influence on social and cultural discourse, of which architecture is a part, and brings new facts about the specific uses of buildings primarily intended for watching films, their impact on society and their spillover into public urban space. Individual chapters are arranged chronologically.

METHODS

It is a theoretical-empirical scientific work in the form of qualitative research. The methodology of the work is the collection of information from literature and visual sources, visiting objects and examining their current operations, studying and visiting converged projects in the Czech Republic and abroad. Obtaining feedback from the affected community. The general logical processing methods are historical and socio-cultural analysis, architectural and urban research including architectural drawings, photographic documentation and a study of the urban development of the appearance of individual cinemas, comparison and deduction.

THE MAIN FEATURES OF POST-WAR CULTURE IN RELATION TO CINEMA BUILDINGS

The silent era of cinemas definitively ended with the arrival of the Second World War, bringing significant changes to the film industry. After the signing of the Munich Agreement in 1938, Czechoslovakia lost a considerable portion of its border territory, resulting in a reduction in the number of cinemas from 1850 to 1279. With the demise of the republic, the total number of cinemas decreased further, including Slovak and Subcarpathian cinemas. At the beginning of the Protectorate, there were 1115 cinemas in our territory. Despite the long-term stagnation between 1933-1938, there was an increase of almost 12% in the period 1939-1944, reaching 1244 cinemas. It's worth mentioning that cinemas were not exclusive to large cities. In 1944, out of 7775 municipalities, in 930 of them were cinemas (565 in Bohemia and 365 in Moravia). However, most of them fell under German administration. New regulations were issued under the new order, significantly affecting cinema operations. Anti-Jewish laws had a profound impact on the content of cinema programs and the exclusion of Jews from the film industry. Screening of British, American, French, and Soviet films was prohibited, leading to the dominance of Czech, German, and Italian productions. A distinctive feature of the Protectorate's cinematography was the establishment of permanent cinemas for narrow films. From 1941, 77 cinemas were established in our territory. The number of mobile cinemas also increased, which had a declining trend in the 1930s. However, these cinemas did not have a significant impact on the economic situation or cultural significance.

Substantial changes have occurred in the operating conditions of cinemas. The existing licensing system from 1913 was abolished on July 31, 1941, replaced first by membership in the Czech-Moravian Film Institute (ČMFÚ) and later by the introduction of film concessions in 1943, conditional on professional qualifications. Changes also occurred in the structures of cinema operators. The most important operator, Sokol, was stopped in the spring of 1941. In the following year, the Czech cinematographic company was established under German administration, which took over cinemas not only from Sokol, but also from legionnaires. Cinema attendance during the Protectorate sharply increased, rising by 132% compared to 1939 - 1944. This phenomenon was not unique to our territory and was observed in other European countries. Society viewed film as an autonomous phenomenon, an escape from the ubiquitous war reality. The enjoyment of cinema was amplified by the suppression of other forms of entertainment, especially with the closure of theaters in the summer of 1944. After the war, significant changes occurred in the film industry. One key event was the nationalization of cinematography following President Edvard Beneš's decree No. 50 on August 11, 1945. This meant a reorganization of the film industry, later replaced by government regulation No. 72/1948, establishing the state enterprise Czechoslovak State Film. This marked a new era in cinema construction, with the number of cinemas in Czechoslovakia increasing to 1650. In Prague, there were 111 cinemas shortly after the war [1], [2].

The main features of post-war culture were evident even during the Second World War, showcasing Czechoslovakia's political shift from west to east. The idea of social equality and national unity, absent during the national oppression, gained prominence, and the popularity of leftist ideology grew across social strata. The first three years after the war were filled with hope, extravagance, expectations, and visions of the future. In July 1945, the Block of architectural progressive associations (BAPS) was reestablished, led by Oldřich Starý, advocating for the new state's construction with a manifest program of socialist architecture. Architectural society gradually moved away from functionalism, still a predominant architectural style, due to its inadequacy in portraying monumentality and emphasizing the importance of public buildings in the post-war reestablished state. Emphasis was placed on the standardization and typification of residential construction, metallurgy, engineering industry, and infrastructure buildings. The ubiquitous effort to standardize all architecture also led to a competition for exemplary cinema projects at the turn of 1946-1947. Proposals were divided into three categories: “A” for small halls with a capacity of up to 250 seats for 16 mm film projection in smaller communities, and categories “B” and “C” included halls with 550-800 seats and quality acoustic design, reflected in prominent interior elements. In all categories, functionality was emphasized. Therefore, the designs abandoned boxes and balconies, focusing on a unified auditorium space with an arched profile. The winning project, due to a formal exclusion, was the design by František Stalmach and Josef Svoboda (who are also the authors of the Karlín cinema Atlas) [3], [4].

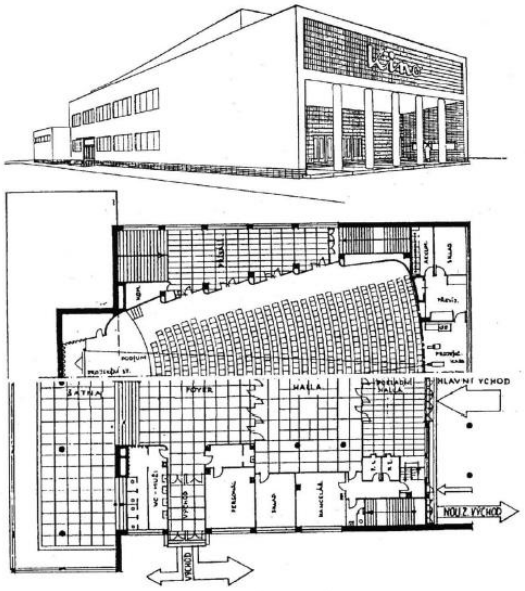

Fig. 1 - Competition design for exemplary cinemas by Edmund Holub and Jiří Michálek, 1946 [26]

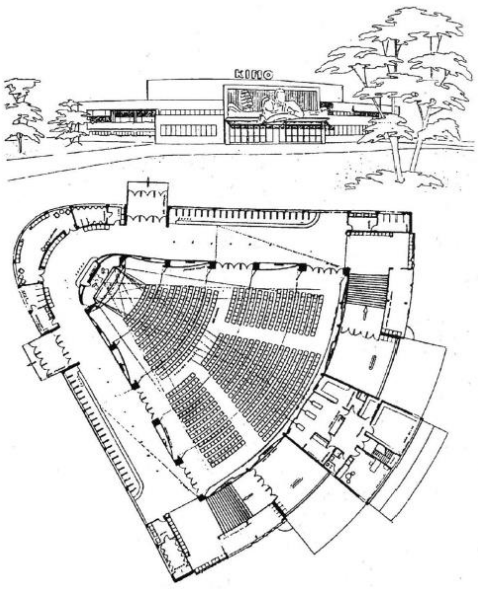

Fig. 2 - The winning competition design (category C) for exemplary cinemas by František Stalmach and Josef Svoboda, 1946 [26]

In the film sphere, the suppression of individualistic art and its replacement with socialist art, more understandable to the working class, emerged in the early 1920s. Czech cinema, with an annual production of 25 films, ranked fourth in Europe, just behind Germany, France, and England. This was accompanied by a growing trend of establishing new cinemas. During the war, attendance increased as people sought to escape everyday worries, letting themselves be carried away in darkened halls into different realities. By 1944, Prague already had 111 cinemas, including 8 premier cinemas **(Adria, Juliš, Kapitol, Lucerna, Passage, Phönix, Alfa, Viktoria)** and 8 second-class cinemas **(Apollo, Atlas, Astra, Kammerlichtspiele, Letka, Mars, Metro, Praga).** The nationalization of cinematography was discussed during the war by filmmakers themselves, believing in the independence of creation from commercial entities. Thus, in August 1945, Czechoslovak State Film was established [5].

Not only film production but also film exhibition was nationalized. All cinemas came under state administration, making the film industry one of the main cultural sectors at the forefront of state interests. People could attend film premieres sitting in the same auditorium with government members or President Edvard Beneš. As part of the two-year plan, a cinema was to be established in every municipality in our territory. Once again, meeting the predetermined quantity took precedence over architectural quality. Consequently, there were over 500 cinemas in our territory in 1948. Cinemas throughout the country were classified according to a 1945 classification based on the number of seats, technical equipment, and the provision of quality films. The act regulating the work of cinemas required the continuous operation of cinemas in municipalities. Exceptions were made only for those cinemas that, due to circumstances, could not operate in normal working hours, such as those without the necessary equipment for screening or where the audience had dropped to a level that could not cover the necessary expenses. Throughout the country, cinemas were mostly constructed in the style of revised functionalism, emphasizing the elevation of individual functional parts and facade articulation. In contrast to pre-war functionalism, these structures were massive and somewhat cumbersome, characterized by natural, earthy colors, as opposed to the white color prevalent in the First Republic, in an effort to create coziness in line with the theory of folk buildings. Brick often appeared as cladding material, leading to a loss of formal diversity and uniformity with recurring patterns. In the pursuit of monumentality, elements of traditionalism and neoclassicism were employed, including symmetry, facades with columns, and sculptural

decoration. Generally, discussions on monumentality revealed that functionalism struggled to meet such demands, as evident in some proposals for the completion of the Old Town Hall or the parliamentary building on Letná. These conclusions contributed to the acceptance of Socialist Realism as the main architectural program. In response to the events of 1948, Czechoslovak architects created the Central Action Committee, which led to the nationalization of individual studios, leading to the creation of Stavoprojekt, the world's largest state organization with 1,200 employees. The idea of own adaptations of socialist realism within the national studios faded away in 1950, when sorela became the only permitted style. As a result, architecture also became another tool for the promotion of communist ideology, similar to what happened with the film industry [6], [7].

In spite of numerous competitive standardized cinema projects, only one cinema was newly built in Prague during this period – **Part** in Libeň (1951). This intimate cinema with a minimalist interior, located at Zenklova Street 24 in the basement, had a capacity of 70 seats and primarily served for screening 16 mm newsreels. Two additional screening rooms were opened in the outskirts of Prague. A falconry in Jinonice, originally used for film screenings before World War II, was inadequate, leading to the conversion of a hall on the first floor of the inn at Butovická 10 for screenings (1951). In December of the same year, Kino **Pionýr** with 240 seats was established in a former factory hall in Záběhlice. In the late fifties, there was a certain revival in the cultural environment, characterized by a shift away from historicizing forms and a close connection between architecture, painting, sculpture, and applied arts. Cinemas' construction receded in cities, giving way to large cultural centers that integrated functions of theater, cinema, restaurant, dance and concert hall, educational spaces (club rooms, libraries), and, if needed, accommodation facilities. These aimed to strengthen collective living (Cultural House in Ostrov nad Ohří, 1955 – Jaroslav Krauz, Cultural House in Ostrava, 1958 – Jaroslav Fragner, Cultural House in Příbram – Březové hory, 1959 – Bohuslav Fuchs, Václav Hilský, etc.). These structures tended to be conservative, with simplified symbolism, applying column orders with an inclination towards monumentality in line with pre-war national traditions. The buildings featured excessively spacious halls and entrance areas with cladding from valuable building materials, were non-variable, single-purpose, functioning only as a container for occasional crowds. In response to these megalomaniacal structures, small cultural houses emerged in the sixties [8], [4].

THE NEW WAVE OF CZECHOSLOVAK ARCHITECTURE AND FILM

As in the whole of Europe, in the sixties, the young generation got the main say in the creation, bringing with them a collective and spiritual awakening, optimism and the belief that the course of things can be changed for the better. Political liberalization allowed the growth of self-confident individuals. The rise took place in the whole culture, especially in the field of film, the young generation is making a significant impact on European and world cinema [9]. A similarly optimistic situation prevails in architecture. Czech architecture reaps success with the ironic theme "One day in Czechoslovakia" at the Expo 58 international exhibition in Brussels with a program linking architecture, art and scenography promoted by the socialist regime [8] - Laterna magika, a performance by director Alfred Radok and set designer Josef Svoboda, is presented to the world for the first time. This name, after the success in Brussels, carries the whole style, which the ensemble of the National Theater devotes itself to. The reconstructed Adria cinema on Národní třída became the home stage of this ensemble, and now it operates on the New Stage of the National Theatre [10]. Another Czechoslovak innovation by Emil Radok and Josef Svoboda presented in Brussels was the polyekran projection system. As the name itself suggests, it was a projection of several jointly controlled projectors onto multiple screens at the same time, accompanied by a sound recording. The first polyekran production was the performance of Prague Spring, where the authors tried to capture the atmosphere of the music festival and at the same time bring closer the history of Prague. After the end of the exhibition, it was possible to see the production in Prague. The success of the polyekran in Brussels was followed up by the Czech representation at EXPO 67 in Montreal (diapolyekran) and EXPO 90 in Osaka (spherical polyekran).

The technology was also used at many important events abroad, e.g. in Australia, Egypt, India, Iran, Japan, Canada, Germany, the USSR, Tunisia, the USA or Venezuela. Both principles – the polyekran, and the laterna magika emerging from it, became the basis for contemporary stage projection [11], [12].

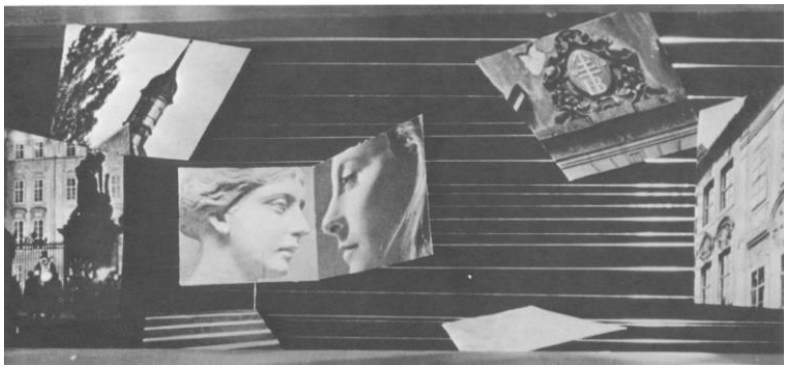

Fig. 3 - Polyekran at EXPO 58 in Brussels. The individual screens shot at different angles were static and placed almost in one plane [23]

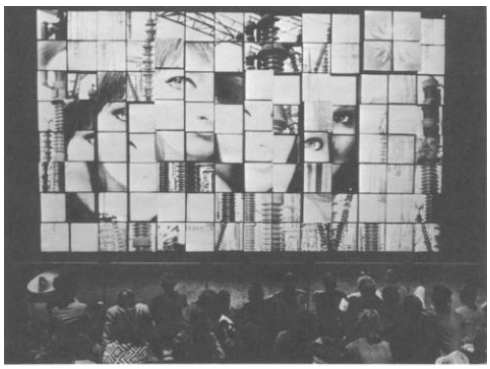

Fig. 4 - Diapolyekran at EXPO 67 in Montreal. The photo shows how it is possible to create rather complex collages using a system of several diapoly screens [24]

Another innovative element was presented in the Czechoslovak pavilion at the world exhibition EXPO 67 in Montreal. In addition to the already mentioned diapolyekran, visitors could see Kinoautomat directed by Radúz Činčera for the first time. The innovative device represented a breakthrough in the interactive movie experience and left a lasting mark on the history of the film industry. The film „Člověk a jeho dům“ (One Man and His House) was projected on two conventional 35 mm projectors. At crucial moments, the film was stopped and the audience, led by the emcee, voted for one of the two options, thereby determining which direction the following story would take. The projection thus enables decisions to be made only at points where both variants must be refined. Činčera's visionary idea of moving the audience from the static role of observers to active participation opened up new possibilities for interactive film experiences. This event showed that the boundaries between the creator and the viewer can be blurred, which influenced the further development of the film industry and its formats. The same principle was used in Činčera's next film „Bláznivá cesta“(Crazy Journey), screened at EXPO 81 in Kobe, Japan [11]. The first presentation of the Kinoautomat became not only an important chapter in the history of cinematography, but also a precursor to current trends in the interactive art of film and virtual reality. International recognition also affected the situation at home. The previously forced combination of architecture with other spheres of art has turned into a real Gesamkunstwerk with a lot of unexpected quality connections. Czechoslovak architecture once again follows Western patterns, new technologies and new architectural forms are used [7]. We are talking about the peak of the era of prefabrication. In this sector, we could turn our attention to the west again, to France, which was a model for the whole of Europe, although the Soviet Union was still officially adored. In the area of architecture intended for film consumption, large cultural houses still appear as a residue of the fifties (Cultural house of the revolutionary trade union movement in Jihlava, 1962 – V. Machoninová, V. Machonin.; Cultural house of Joint-stock company for the automotive industry in Mladá Boleslav, 1972 – F. Řezáč). Due to the current culture of mass consumption of new media, culture houses are an almost extinct building type, moreover affected by rising energy prices, the "paraphrase" of which is the shopping center in the architecture of Western capitalism [8]. In addition to the Expo 58 exhibition pavilion and restaurant, the culmination of the Brussels style was also Prague's long-awaited premiere **cinema 64 U Hradeb.**

Preparatory work for the construction of the cinema in Mostecká street began already at the end of the thirties, but the continuation of the construction was interrupted by the complications of the foundation work of the rear section of the building with the cinema space, as well as the war

[2]. The new architectural solution from 1954 preserved the character of the original two Gothic houses with gables and thus the architecture was subordinated to the character and scale of the whole street. Inside, a courtyard with Prague paving was created as a typical element of the Lesser Town's courtyard interiors. The layout was adjusted to 32 apartments, a dairy buffet, a cinema, a wine bar and a library. As it was the first post-war new building in Prague with a focus on the socialist cinematographic scene, the most modern materials and techniques were used. The interior was modern, in the Brussels style according to František Trmač's design, the projection technology and stereophonic sound were also state-of-the-art [13]. The building was completed in 1964, and in September of the same year, the audience could watch the opening film „Starci na chmelu" (Green Gold) from 540 soft-upholstered chairs. Cinema 64–U Hradeb was successful in every way and became a building model for other newly established cinemas such as Ruzyně (1970), Kosmos on the housing estate Novodvorská (1973) and Vltava (1980) in Prague 15.

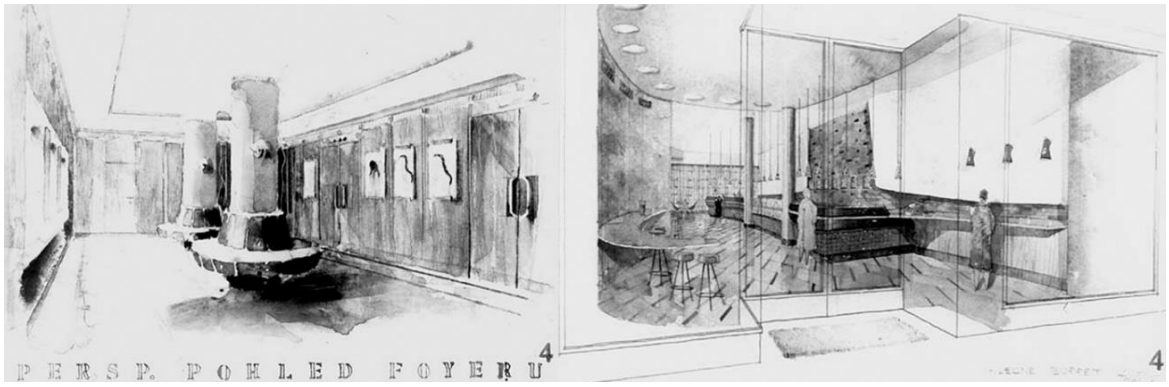

Fig. 5 - Sketches of the interior of the U Hradeb cinema (private archive of architect František Trmač)

Within a few years after privatization, when the cinema was owned by the Barrandov film studio, several Czech films premiered here. The end of the famous era came in the second half of the nineties with the arrival of the first multiplexes, and the final point was the year 2002. The show stopped in May, the screening was replaced by a black theater, an exhibition of spiders and torture objects, and after the floods in August, only concrete pillars and foundations remained in the damaged cinema hall. The object continued to remain unused. The cinema itself has an area of around 3,000 square meters, and part of its foundations is a preserved part of the Lesser Town fortification walls from the 13th century [2].

Fig. 6 - Production of The Trial (Maxim Didenko) [24]

Fig. 7 - Auditorium of the cultural space 64 U Hradeb during reconstruction [25]

Concurrently with the construction of Cinema 64 U Hradeb, a cultural center named 17. listopadu (November 17th) was also being developed in Ruzyně with a cinema hall

in the basement of the building. Since the initial design phase in 1957, the plan included widescreen projection. The hall of cinema **Ruzyně**, measuring 16.6 x 12 m and accommodating 227 seats with a significant elevation, opened in 1968 due to the challenging construction. During this period, several cinema reconstructions took place, such as **Maceška**, **Aero**, **Letná**, and **Adria**, involved significant alterations to the seating area elevation and the removal of balconies to accommodate performances of laterna magika. Another public competition in 1960-1961 introduced new trends in cinema design. The competition, divided into two categories, focused on model projects for cinemas with capacities of 380 and 550 viewers. The winning architects in both categories were V. Bořuta and A. Daříček. Conceptually, both projects were very similar, featuring a hall in the shape of a spherical triangle with other cinema spaces arranged orthogonally. The two structures had distinct roofing and facade treatments. New approaches to cinema design were predominantly reflected in the reconstruction of existing cinema halls. The focus was generally on modifying the sightline curve, involving increased elevation of the auditorium, the removal of boxes and balconies, and technical innovations related to widescreen projection. Cinemas like **Alfa** (1967) and **Světozor** (1968) were reconstructed in this spirit. Kinoautomat, allowing audience participation by voting on key plot decisions, was installed in Světozor – viewers could choose between two options at crucial moments in the film. Simultaneously, the projection booth was expanded to the entire width of the hall. Similar modifications were made to the **Kyjev** cinema in Dejvice. Acoustic panels adorned the side walls and ceiling of the cinema hall, while the foyer was transformed into an occasional gallery space [4].

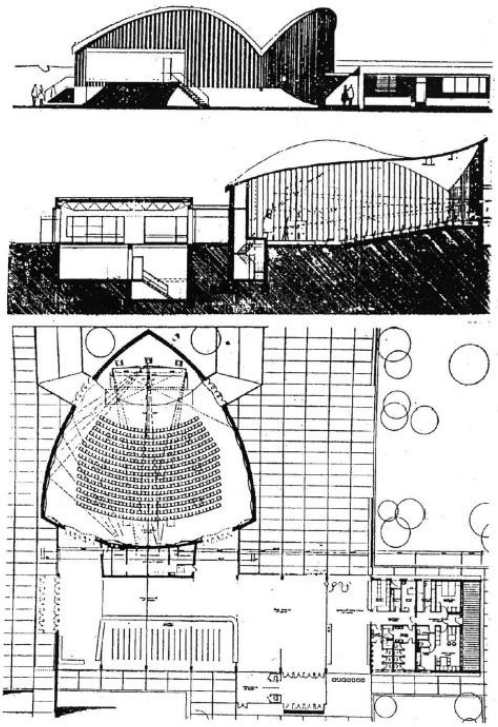

Fig. 08 - The winning project of the competition for model cinema designs (1960-61) by V. Bořuta and A. Daříček [26]

Fig. 09 - Kyjev Cinema – – interior of the hall after reconstruction in 1969 [26]

The 1960s are considered a watershed. The last echoes of late modernity are appearing, and following the solution to the ecological crisis, a new phenomenon is emerging - alternative and ecological architecture. At the same time, two new directions appear in opposition to it: high-tech and soft-tech. So it became a decade of trying new ideas and directions. A palette of many looks and styles. The symbiosis of several generations of architects - interwar functionalists (František Cubr, František Maria Černý, Václav Hilský, Josef Hrubý, Richard F. Podzemný, Jiří Šturza etc.),

the generation of budding architects after the Second World War (Karel Filsak, Emil Hlaváček, Karel Hubáček, Zdeněk Kuna, Věra Machoninová, Vladimír Machonin, Karel Prager, Alena Šrámková, Jan Šrámek et al.), "disciples" of functionalists (Jan Bočan, Miroslav Masák, Zdenka Nováková-Smitková, Dagmara Šestáková, Stanislav Švec et al.) and the generation of architects born around 1945 (Tomáš Brix, Jan Línek, Vlado Milunić etc.) [8].

BRUTALIST CINEMAS AND CINEMAS OF PRAGUE HOUSING ESTATES

The "Golden Era" of Brussels optimism came to an end in August 1968 with the invasion of occupying forces, significantly impacting the situation in the 1970s. The cultural scene experienced a notable weakening due to the emigration of influential personalities from all cultural sectors. The challenging societal climate of that era under harsh totalitarianism is reflected in the negative assessment of the architecture from these years, often leading to the oversight of exceptionally high-quality structures. The prevailing style of the 1970s was brutalism, already widespread in Western Europe. With the mass adoption of televisions in Czechoslovak households in the 1980s, interest in cinema attendance gradually declined. State financial support enabled screenings for a small audience, and new cinemas emerged, including **Ruzyně** (1968), **Kosmos** in the Novodvorská housing estate (1973), **Moskva** (1977) in the Ďáblice housing estate, **Vltava** (1980) in Prague 15, and the **Dlabačov** cinema in the ROH Recreation House (1988) [8], [14], [15].

Kosmos cinema of Lhotka housing estate was opened in 1973 with the film „Tajemství zlatého Buddhy“ (The Secret of the Golden Buddha) as the third most important enterprise, out of the ninety cinemas operating in Prague at the time, since the end of the war, right after the U Hradeb and Ruzyně cinemas. The cinema, designed as a part of a two-story modern cultural building designed by Aleš Bořkovec, was the first in Prague to be part of the urban planning for the entire Lhotka housing estate from 1964. The cultural center included, in addition to the cinema, a large social hall for 580 people, a puppet theater with a capacity of 120 seats, a library, club rooms, and facilities. The sloping auditorium of the trapezoidal-shaped cinema, with rounded walls at the screen and behind the last row of seats, had 485 seats. It featured modern audio-visual technology projecting onto a widescreen, which was already a standard at that time. The side walls of the hall were covered with cork panels, serving both aesthetic and acoustic purposes. The rear wall was clad in smaller-sized sandstone blocks. The length of the hall, as well as its maximum width, was 22.3 meters. The structure had a skeletal framework with massive columns. The main volume of the building was on the second floor – on a column base, giving it an airy appearance. The visual lightness was further enhanced by ribbon windows extending to the edge of the facade. The entrance on the first floor level was fully glazed and recessed. Prefabricated elements primarily constituted the non-load-bearing structures. The cinema's popularity declined in the mid-nineties, and from 2001, Kosmos remained unused and deteriorated. The future of the cinema was sealed with the publication in late June 2005 of the tragic incident where an employee fatally fell onto the cinema seats. In a subsequent survey conducted by Prague 4 City Hall, the prevailing opinion was to close the cinema, also considering the opening of the Cinema City multiplex in the Novodvorská Plaza shopping center across the street. Since 1999, the cultural house has been undergoing continuous renovation and functions as a cultural center with a social hall and five classrooms for rent, mainly for the residents of the Lhotka housing estate [2]. In 2013, the cinema premises were renovated at the expense of the city district and reapproved as a relaxation center with a swimming pool, whirlpools and massage parlors on the first floor and a warm pool for babies and a salt cave on the second floor. On the ground floor, there were also two surgeries connected to the neighboring Medical House Jílovská. Even this operation did not last long here. In 2021, a public tender was launched for the reconstruction of the building with use for medical purposes. The new medical center will bear the name Kosmos cinema, but nothing will remain of the original interiors. The order is conceived as "shell and core".

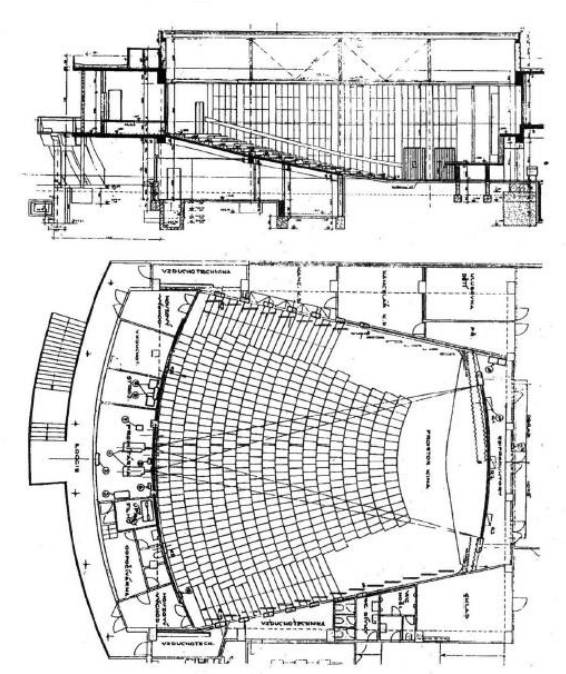

Fig. 10 Kosmos Cinema – Floor plan and cross-section [26]

Fig. 11 –Kosmos Cinema, former interior [27]

Fig. 12 –Kosmos Cinema – exterior [26]

Prior to the opening of the Kosmos cinema, construction began on the **Moskva** cinema in the Ďáblice housing estate on the opposite side of Prague, based on Jiří Kulišťák's 1971 design. František Trmač designed the interior. The distinctive feature is the amphitheater-style hall, with side walls exhibiting triple expansions resembling rectangular notches, corresponding to the segmental floor plan and the arrangement of rows of audience seats. The stage in front of the screen has a lens-shaped design, similar to the Kosmos cinema, and acoustic wall cladding is similarly addressed. The 23-meter-long hall accommodates 494 seats. During construction, an additional smaller hall with a capacity of 54 seats was decided for the originally planned clubhouse. The two-story facade features prominent glass areas set between tall pillars. The grand opening of the Moskva cinema took place on November 3, 1977, coinciding with the celebrations of the 60th anniversary of the Russian Revolution [4].

Vltava - the only cinema in the territory of Prague 15 with seats for 170 spectators on the grounds of the national enterprise Waterworks in Hostivař was opened in 1980 with great hopes due to its equipment with state-of-the-art Meopton X-5 projectors. After the revolution, the joint-stock company Lucernafilm rented and renovated the cinema, but even that did not attract viewers to the cinema. Within two years, the Vltava cinema disappeared. The Černý Most housing estate opened its cinema named **Sparta in** 1984, according to the design by Miroslav Vajzr from the studio of Vladimír Machonin, Institute of Urban Development of the City of Prague. The floor plan in the trapezoid shape has a capacity of 226 seats arranged in eleven distinct ascending rows. The entire hall is clad in dark wood – with planks of a sawtooth arrangement on the side walls and narrow vertically oriented slats on the back. The foyer and buffet are also designed in a similar style. Twelve non-profit years later was replaced by a multiplex in the Černý Most Center. The premiere cinema of the **Eden** Cultural House, designed by architects Hana and Dalibor Pešek, on what was then SNB Street (today Vršovická Street) screened from 1987 until 2005. In addition to the cinema hall, there was also a multi-purpose hall for 1,500 people and a restaurant. Today, the building is closed due to its poor condition and continues to deteriorate despite the fact that there is no similar building in Prague 10 [2]. The construction of the building consists of a reinforced concrete skeleton with a suspended glass shell. Rolled I-beams are placed on the columns and steel beams perpendicular to them at an axial distance of 1.6 m, which support the corrugated sheet

covered with concrete. Above the auditorium space is a distinctive acoustic ceiling in the shape of a white wave, which has been preserved to the present day without significant damage. The back wall of the cinema hall, separating the auditorium from the projection room, is lined with white and ocher acoustic panels of smaller dimensions. The overall color scheme of the hall is complemented by a blue carpet on the floor, blue side walls of the hall and wooden seats with red upholstery. The backs of the seats were equipped with ocher folding tables at the back, which could be used by the spectators sitting one row away. The side lighting of the hall from several white light bulbs arranged in irregular rows at several height levels is very specific.

Fig. 13 – Eden Culture House, exterior [28]

Fig. 14 – Cinema Eden, interior (Vladimír Lacena) [29]

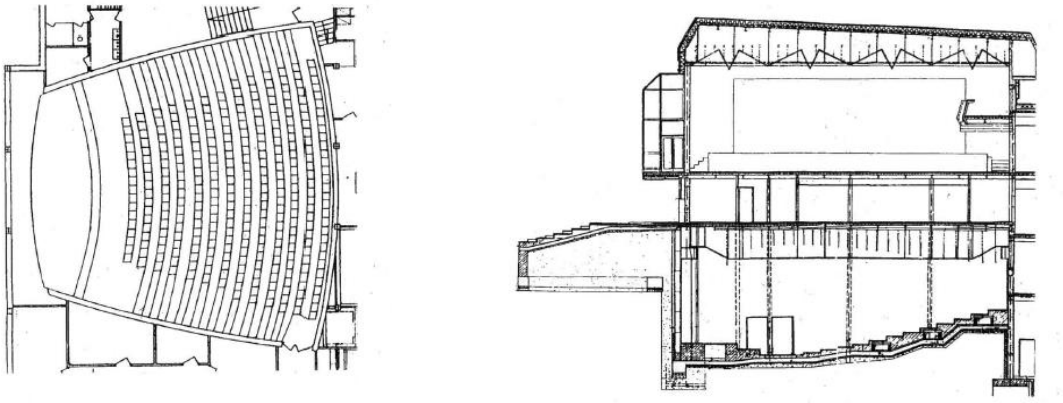

Fig. 15 - Eden Cinema – Floor plan and cross-section, 1987, architects Hana Pešková and Dalibor Pešek [26]

In 1989, the **Sigma** cinema opened on the Spořilov housing estate. Architect Václav Oupor designed a premiere cinema for 273 visitors in sloping rows with boxes with barrier-free access. Although the assumptions of the cinema predicted a bright future, after November 89 attendance was around 24% and the cinema had to be closed in 2001. The effort to restore the cinema under the new name Grand Bio Edison also did not lead to successful tomorrows, and since 2008 it has not been shown definitively in Sigma. The municipality, together with a private investor, occasionally uses the former cinema as a multi-purpose cultural hall. Sigma cinema is an independent one-story building with a reinforced concrete skeleton system. In the interior, noble materials were used - stone paving on the floor of the foyer, tiles on its walls in combination with solid wood. The floor of the hall with an elevation is covered with a beige carpet, including the podium. The orthogonally positioned seats are fully upholstered in an ocher shade and provide high seating comfort. The walls of the hall are tuned to ocher red in combination with mirrors and carry significant side lighting solved by vertical strips. The soffit is flat, undivided, bright. The new cultural center on the border of Ruzyně and Liboc - **Delta**, designed by Jiří Rauch, was opened in 1987. It featured a multipurpose hall

located on the third and fourth floor. The auditorium spans an area of 30 x 15 meters with a total of 200 seats on tiered seating, which can be retracted into the block at the rear of the hall. The cinema operated until 2008. In the nineties, the foyer functioned as an exhibition space, and people from the Pražská pětka exhibited there, for example. In 2017, the association Kino otevřeno succeeded in reopening a music club with regular screening times. The premises of the original cinema are now offices. Not a single one of the original cinema theaters of the panel housing estates from the 1970s and 1980s remains in operation [2].

Fig. 16 –Sigma Cinema, exterior [30]

Fig. 17 –Sigma Cinema, interior (Vladimír Lacena) [31]

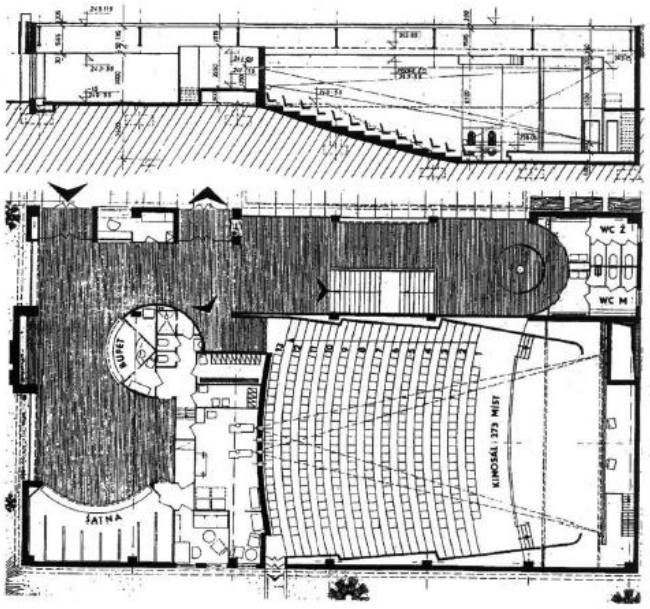

Fig. 18 - Sigma Cinema – Floor plan and section, 1989, architect Václav Oupor [26]

A distinctly dominant style emerging from the urban structure, but fully corresponding to its function, it deliberately appears unambiguous and firmly anchored in space, which is why the architecture of brutalism was often criticized by experts and the lay public. "Paradoxically, brutalist buildings are victims of their own success. The architects managed to perfectly fulfill the stylistic and architectural maxims of the time. However, it is precisely in these criteria that the double pitfalls that brutalism runs into are hidden [16]. When shaping their own architectural statement, Czechoslovak architects based their knowledge of foreign architecture, primarily on the brutalist works of the late works of Le Corbusier, Oscar Niemeyer, Louis Kahn, Alvar Aalto or the practices of the Japanese metabolists with a focus on material and structural innovations.

The light structures of metal shells were combined with raw reinforced concrete with an emphasis on connecting the interior with the exterior. Czech brutalism, characterized by its expressive creativity and connection with other elements of art, high-quality aesthetic and functional rendering, is mainly represented by the work of Věra and Vladimír Machonin (Kotva department store, 1975, Hotel Thermal, Karlovy Vary, 1976 or the building of the Czechoslovak Embassy in Berlin, 1978, House of Residential Culture , 1981 – independent project of Věra Machoninová), Karel Filsak (Hotel Intercontinental, 1974, K. Filsak, K. Bubeníček) and Jan Šrámek (Czechoslovak Embassy in London, 1970, J. Bočan, J. Šrámek, K. Štěpánský) [7]. Brutalism was a whiff of western influence, and the communist regime did not take much pride in it. Unlike the functionalism referred to, it is not possible to mechanically apply a system of rules to it. Brutalist buildings are always highly original, iconic, exclusive and unique. Today, many of these buildings are at risk of demolition, mainly related to long-term neglect of care or possible partial reconstructions.

The Pyramida Hotel (originally the Revolutionary Trade Union Movement (ROH) Recreation House, 1979-1987, Neda and Miloslav Cajthaml) in Břevnov, at Bělohorská street 125/24, is also among the important buildings of Prague brutalism. The Dlabačov cinema was reopened to the public after a thirteen-year hiatus in October 2016. The building from the 1980s, built in the triangular concept of brutalism, hides quality architecture. Already at the time of its creation, the hotel was supposed to become a cultural and social center, which it remains to this day. The cinema hall opened to the public in May 1988, and 387 viewers could see the film here at once. At the turn of the 1980s and 1990s, cinema focused mainly on the "performance art".It is a reinforced concrete skeletal system consisting of 48 columns arranged in an orthogonal grid. The ceiling is supported by beams (the longest spanning 19.7 m) and girders (the longest of which is 40 m). To improve the acoustic experience of the projection, additional acoustic structures in the floor plan shape of sharp triangles are added to the side walls of the auditorium, framing the angle of maximum visibility. Semi-cylindrical acoustic elements are inserted between individual beams at the ceiling level, serving as both a prominent design element and softening the otherwise prevalent sharp angles. The elevated seating area has 14 rows, gradually rising 1,8 m above the basic floor level. Seats are arranged parallel to the projection screen, with every other row shifted by half a seat. The hall also features a stage, allowing for theatrical performances. Backstage facilities are provided in two dressing rooms, each with its own sanitary amenities (one on each side of the stage). Despite being a single-story structure with a dedicated entrance from the exterior, the cinema hall is directly connected to the hotel building, sharing the structural system. Hotel guests can access the cinema directly through the foyer. After the revolution, the characteristic brutalist gray facade was replaced, for unknown reasons, with a beige color [2].

Currently, the reconstructed hall has 377 seats in a theater arrangement. The discreet architectural design of the interior of the hall acknowledges its most famous era in the normalization period with the strict shape of the stage, ceiling and wall panels, underlined by the amber color of the carpet. The retro shape of the wooden armchairs with purple upholstery fits perfectly into this clean composition and allows to maximize the viewer's experience In the vestibule, the original buffet was replaced by a cafe, and for reasons of sustainability and better use, the foyer now also functions as a small stage. Lectures, concerts, etc. take place here [17].

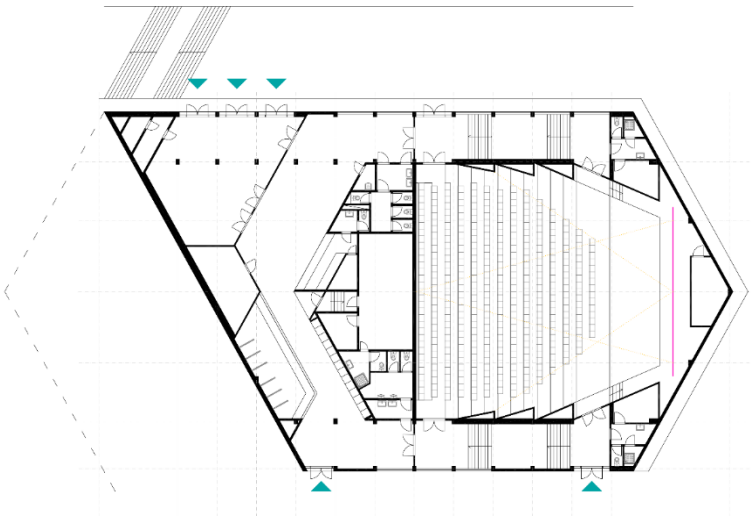

Fig. 19 – Pyramida Hotel, ground plan of the cinema hall, redrawn according to the documentation of the Prague 6 building office

Fig. 20 – The Pyramid Hotel, formerly the Revolutionary Trade Union Movement (ROH) House of Recreation, exterior (Cait Greeley) [32]

Fig. 21 – Dlabačov Cinema, interior after reconstruction [33]

The golden era of cinemas in Prague ends with the Velvet Revolution. With the opening of the borders, new influences of decomposition and deconstruction began to flow into our territory. Tschumi, Koolhaas, Hadid and others merely adopted a formal language for new intentions. Conflict, fragment, and even non-rational practices are emphasized instead of harmony, wholeness, and reason [18]. The "modern temple of capitalist consumption" - a shopping center and with it the trend of multiplexes - is coming to our territory.

COMPARISON OF THE SITUATION OF PRAGUE CINEMAS IN THE SECOND HALF OF THE TWENTIETH CENTURY WITH OTHER EUROPEAN METROPOLIS.

Between 1938 and 1983, not only Czechoslovakia, but also the whole Europe and European cinematography went through significant changes, conditioned on the one hand by war, social and political changes, and also by urban and architectural developments. Therefore, it is necessary to look at the situation of Prague and Prague cinemas in the context of other Central European cities. For example, the comparison with Berlin, where cinema culture has a very similar history to Prague, is interesting. Despite the fact that in the early days of the Czechoslovak state, the establishment of new cinemas was significantly hindered by a complicated system of granting

licenses to cinema operators, taken over from the legislation of Austria-Hungary (Vienna cinemas were in a similar situation), while Berlin cinemas were not subject to any licensing restrictions, the advent of sound film in Prague to such an increase in the number of new cinemas that, after recalculation with regard to the number of inhabitants, between the 1930s and 1950s it could be equal as the situation in Berlin. With significant support from the national exchequer, during the second half of the 20th century, Prague was even ahead of Berlin in terms of the number of inhabitants of both metropolises (Berlin had three times more inhabitants than Prague at the time) and the number of operating cinemas. In absolute numbers, regardless of population, Berlin had only 156 cinemas, Prague had 71 of them. It is clear from both graphs that the decline in the number of cinemas in both cities was striking [19].

The situation in Vienna mirrored that of Prague in relation to Berlin, as evident from the circular graphs below. The number of cinemas in Prague and Vienna between 1930-1950 was evenly matched. However, when considering the population of both metropolises in 1938, one cinema in Prague served 6,419 residents, while in Vienna, one cinema catered to 14,341 residents. Therefore, the density of the cinema network in Prague was more than double that of Vienna. In the second half of the twentieth century, with the widespread availability of televisions in households, the number of cinemas in both metropolises declined significantly and almost uniformly. In the 1960s, Prague had 101 officially registered and traceable cinemas, while Vienna had 120. By 1983, their numbers had nearly halved, with Vienna having 62 cinemas and Prague having 83. Despite a partial decrease in Vienna's population, in 1983, one cinema served 24,806 Viennese residents, while in Prague, one cinema accommodated 14,337 residents. Despite similar initial conditions imposed by the legislation controlling the number of licenses in the former Austrian Empire and a slight disadvantage for Prague, which received all cinema-related innovations and projections after Vienna, Prague managed to match and even surpass Vienna in the number of cinemas and cultural interest in film projection, considering the population size [20].

Even in Warsaw in the first half of the twentieth century it was similar to ours. The first permanent Bioskop cinema was opened in Warsaw in 1903, and in Prague only four years later. Despite the fact that Warsaw, which was significantly damaged during the First World War, faced several military attacks by Bolshevik Russia until the mid-twenties, the city experienced a very dynamic development during the years 1927-1929, during which many new cinemas were created. In 1938, Warsaw had 69 cinemas. At that time, Prague had 148 cinemas and Berlin, at that time with the more than four times bigger population of Prague, had 466 cinemas. However, the Second World War hit Warsaw hard. During September 1939, the city was bombed, then occupied by the Germans, and within a few days it found itself on the border of the demarcation line between Nazi Germany and the Soviet Union. A Jewish ghetto was created in the center of Warsaw, which became the center of the uprising against German rule. The second uprising involved the majority of Warsawites, to which the German army responded with massive bombing. More than 85% of the city was destroyed. Not a single cinema remained standing. In liberated Warsaw, its inhabitants immediately began to work on the repair of the city, and by the end of 1945 there were already 4 cinemas operating in Warsaw, with a total of 2573 seats. After the end of the war, Prague had 149 cinemas and Berlin 479 [21]. After the war, in the era of Soviet influence, Warsaw underwent a massive restoration with an emphasis on the restoration of historical parts and new socialist architecture. In the 1960s, the people of Warsaw could even see films in 72 cinemas, and in terms of the number of cinemas, the number of cinemas in Warsaw came significantly closer to that of Prague and Berlin. After the construction of new residential areas in the 1970s, the city's population grew considerably. Since 1975, Warsaw has also had a new central railway station, but the number of cinemas in the metropolis has decreased to less than half. A similar situation occurred in Berlin, where the number of cinemas decreased from 379 to 178. In Prague, the number of cinemas remained almost unchanged. In 1989, the communist government fell, and since then Warsaw has experienced an exceptional economic, cultural and architectural boom that has shaped the modern face of the city. This dynamic of architectural quality new buildings for collective film viewing and successful conversions can be an inspiration for Prague. Prague has the opportunity

not only to reflect on its own film history and architectural heritage, but also to open up to new creative directions and innovations in the field of cinematography and the spatial concept of cinemas. There are many possibilities for synergy between film culture and the urban environment [22].

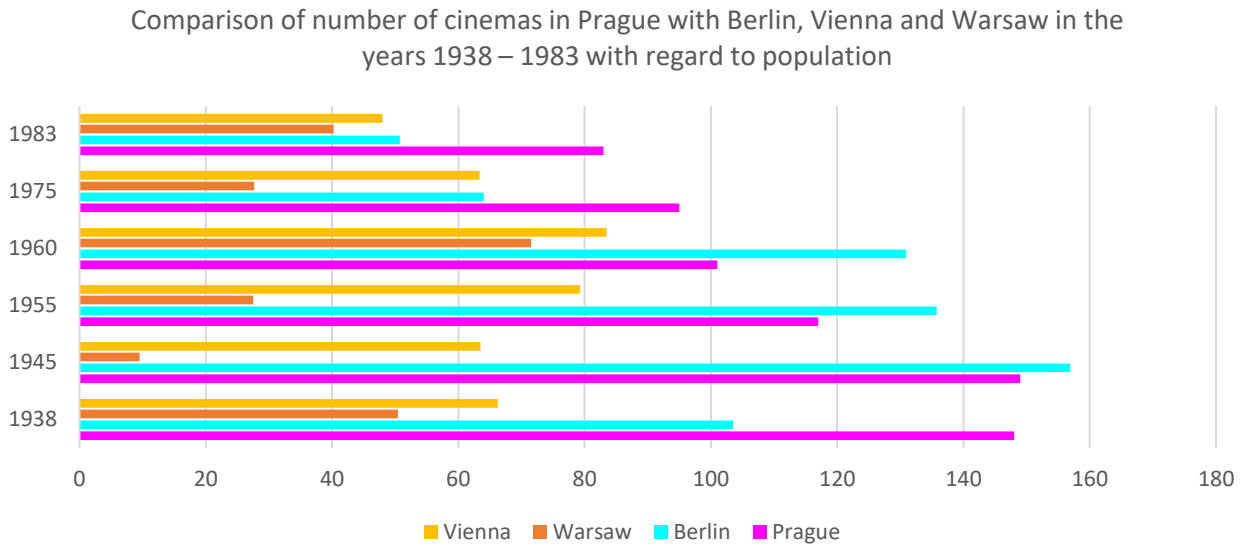

Fig. 22 – Graph comparing the number of cinemas in Prague with Berlin, Vienna and Warsaw in the years 1938 – 1983. The percentages of the outer circle are adjusted by a coefficient considering the number of inhabitants of individual metropolises.

In comparison to currently operated cinemas, Prague is doing relatively well. With a total of 32 cinemas, it ranks third out of four (Berlin – 92 cinemas, Warsaw – 34 cinemas, and Vienna – 24 cinemas). However, considering the population, it closely follows behind the first-ranked Berlin. This analysis clearly demonstrates the role that film has played for the Czech Republic over the years and highlights the numerous and significant group of structures dedicated to screening that has emerged in our territory.

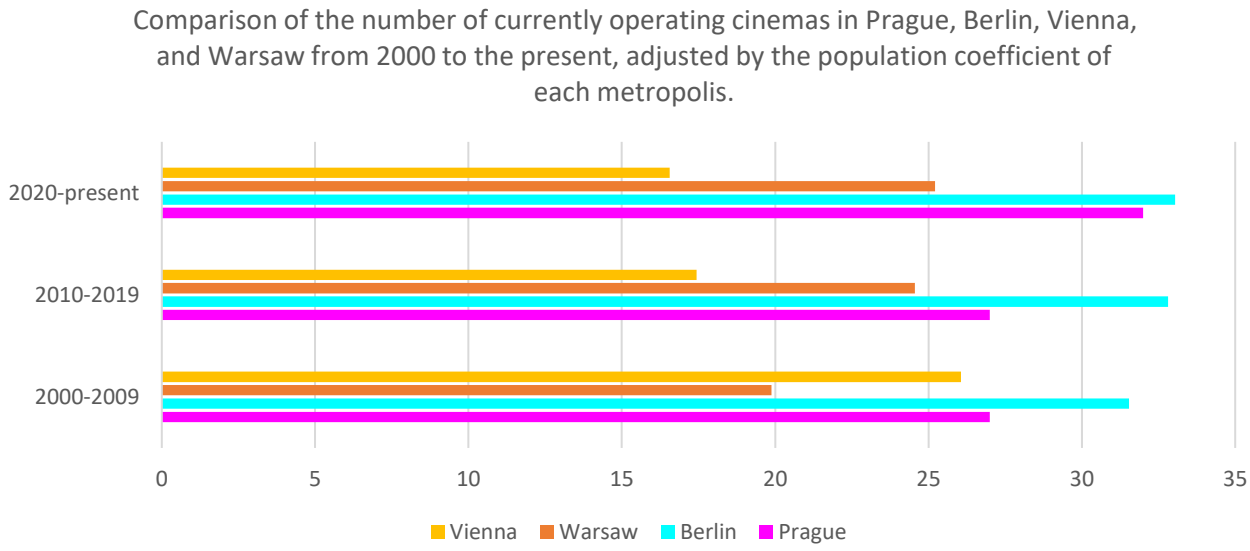

Fig. 23 – Graph comparing the number of cinemas in Prague with Berlin, Vienna and Warsaw in the years from 2000 to nowadays. The percentages of the outer circle are adjusted by a coefficient considering the number of inhabitants of individual metropolises.

CONCLUSION

In order to be able to understand the current situation of Prague cinemas and functionally integrate them into the everyday life of a 21st century Prague citizen, we must first deal with the history and development of the cinema phenomenon and film art in general. We can say that during the 20th century - the century of cinema, there was a solid connection between the art of cinema and the architecture. And through film and our attitude towards it as a communication medium today, we can observe how architecture is perceived by contemporary society. Overall, it can be concluded that the architectural and film scene of the post-war Czechoslovak Republic reflects the complex interrelationship of political ideologies, social aspirations and artistic expressions of that time.

The nationalization of cinematography in 1945 brought about not only changes in ownership but also in the operational conditions of cinemas. The establishment of the state enterprise Czechoslovak national film marked a new era in cinema construction. After the war, Prague experienced a significant increase in the number of cinemas, reaching 111. The pivotal moment came in 1948, when there was a political change and the establishment of a communist government. This influenced not only cinematography, but also architecture. The new ideological direction led to centralization and the introduction of a unified style - socialist realism. Functionalism was discarded in favor of more massive and monumental buildings emphasizing the social dimension. The new buildings were characterized by muted tones aimed at creating a cozy environment in accordance with the theory of folk buildings. Architectural trends in the cinema industry continued to evolve, with the 1950s witnessing a return to historicizing forms and a shift from standard cinemas to larger cultural centers. These comprehensive structures, incorporating theater halls, cinemas, restaurants, and other functions, aimed to strengthen collective life.

The 1960s brought a reaction to megalomaniacal constructions in the form of smaller cultural houses, where greater emphasis was placed on variability and multipurpose use. These structures served as a response to the previous pursuit of monumentality and demonstrated an effort to create spaces suitable for various cultural and social activities. In general, the sixties in Czechoslovakia represented a period of cultural and architectural transformation. In the field of cinema, a young generation of directors stood out, whose work reflected an optimistic atmosphere and experimented with new forms and styles. The architecture of the time reflected a similar spirit of innovation. In Brussels, a program combining architecture, art and scenography was a success. Laterna magika and the Polyekran projection system were introduced here, which was followed by the Kinoautomat interactive cinema and other new possibilities in the field of audiovisual art. One of the architectural highlights of the 1960s was the Prague cinema 64 U Hradeb, built in the Brussels style. Completed in 1964, it served as a multifunctional cultural center and was a model for other cinemas in Prague. The 1960s proved to be a period of experimentation and direction towards new ideas in both spheres - cinema and architecture. Both of these worlds reflected the spirit of the times, when art forms were intermingled and were looking for new ways to express themselves and interact with the audience.

In the 1970s and 1980s, Prague's housing estate cinemas - Kosmos, Vltava, Eden, Sigma and others - were not only an environment for cinema screenings, but also important social centers. These cultural points were not only used for showing films, but also as key meeting places and community life for the residents of the housing estates. At the time of their creation, they helped to create a community spirit and removed the anonymity of the residential environment. Despite grandiose urban plans that promoted modernist ideals, these efforts prove to have failed. Today's non-existence of these cinemas points to the dysfunctionality of these experimental urban theories in practice. None of these cinemas reflected the current economic situation of the market and the declining interest in collective viewing of films due to the mass spread of televisions into households. In addition, it was significantly oversized. Housing cinemas now exist only in memory, reminding us how complex and changeable life in the city can be. Some objects no longer even bear traces of the previous existence of a cinema hall. On the contrary to housing estate cinemas,

the only brutalist cinema in Prague – Dlabačov, is still in operation. Czech brutalist architecture in general represents a significant phenomenon. It became a popular style in Prague's urban structure through foreign influences, primarily Japanese Metabolists. Although this architectural direction was criticized, some of its works, such as the Dlabačov cinema in the Pyramida Hotel in Prague, represent today not only architecturally valuable objects, but also cultural centers for different generations.

In the context of the development of cinematography and urban planning between 1938 and 1983, it is necessary to observe the situation of Prague cinemas on a broader Central European scale. A comparison with Berlin, Vienna and Warsaw reveals similar fluctuations and changes in the number of cinemas during periods of war conflicts, political upheavals and subsequent urban renewal. The significant decline in the number of cinemas in Prague, Berlin and Warsaw in the second half of the 20th century reflects both the development of the film industry and complex changes in society and the architectural paradigm. While in post-war Warsaw and Berlin extensive reconstruction and construction of new cinema facilities took place, Prague with its cinematographic activities and urban plans, similarly to Vienna, remains in the shadow of past ambitions. The current state of Prague cinemas is thus not only a reflection of changes in film culture and technology, but also the inability to adapt to the dynamic development trends of contemporary urban life and the cultural scene. The presented historical comparisons show not only the decline of modernist cinemas in large housing estates, but also the need for new approaches in connecting film art with the contemporary urban environment.

As the examples of cinemas mentioned above show, in order to ensure the sustainability of cinema operations, it is not possible to isolate the film screening from other functions. The location of the cinema hall as a part of a multifunctional building with other commercial facilities is ideal. Even the hall as such should be used for other activities than just the projection of full-length films, for example theater and dance performances, laterna magika, broadcasts of important concerts or even as a digital gallery of visual and audiovisual art or a museum. In the future, thanks to virtual reality, we could also look forward to tours of very distant places in space. Despite all the conveniences of the digital age, we should not forget contact with living people. Spectators should not be left alone in dark halls with only technology. Even now, social interaction is needed to consume art. Maybe even more than in the past.

This partial research will be followed by a more complex treatment of the topic in the form of the author's dissertation thesis - Cinema architecture as an interface to the relationship to film. Another possible topic to follow up on this research is a more detailed treatment of cinemas in Prague housing estates, which were created or were only designed as part of large urban complexes and garden cities.

REFERENCES

[1] Klimeš I., 2016. Cinematography and the State in the Czech Lands 1895-1945, Prague: Charles University, Faculty of Arts.

[2] Čvančara J., Čvančara M., 2011. The Vanished World of Silver Screens: In the Footsteps of Prague Cinemas, Prague: Aca.

[3] Janů K., 1946. Socialistické budování. Publisher of Architecture of Czechoslovak Republic, Prague.

[4] Hilmera, J., Vočadlo K., 1998. "Architectural History of Prague Cinema Halls. Part IV – Post-war Half Century." Iluminace 10, no. 4: 75-101pp.

[5] Dvořák T., Rousek J., 2016. Prague Cinemas, The Fleeting Charm of Darkened Halls. Museum of the Capital City of Prague.

[6] Sedláková R., 1994. (ed.): Sorela: Czech Architecture of the 1950s: Exhibition Catalog: National Gallery in Prague. Architecture Collection: Kinsky Palace: April 14 - May 22, 1994. Prague: National Gallery.

[7] Biegel R.. Overview of the History of Czech Art. Architecture 1945-1989, lecture: Faculty of Arts, Charles University in Prague. [online]. [cited 05.07.2019]. Available at: http://duoppa.ff.cuni.cz/shared/files/prehled%20cz%20sylaby/51%20Ceska%20architektura%201945-1989.pdf

[8] Ševčík O., Beneš O., 2009. Architecture of the 1960s: "Golden Sixties" in Czech 20th Century Architecture. Prague: Grada.
[9] Březina V., 1996. Lexicon of Czech Cinema: 2000 Films 1930-1996. Prague: Cinema.
[10] National Theater, Laterna magika, History and Present [online]. [cited 16.06.2019]. Available at: https://www.narodni-divadlo.cz/cs/laterna-magika/historie
[11] Stýblo Z., 2014. Spaces for Film Projection: Cinema as a 20th Century Phenomenon, Česká technika, Prague.
[12] Burian, J. M., Svoboda J., 1970. Theatre Artist in an Age of Science in Educational Theatre Journal, Vol. 22, No. 2
[13] Hudec M., supplemented by Veselý J. 2004. Bulletin of the Club For Old Prague (New face of the U Hradeb building in Mostecká Street in Malá Strana) [online], [cited on 28.12.2017]. Available at: http://stary-web.zastarouprahu.cz/kauzy/mostecka/mostecka4.htm
[14] Lukeš Z., 2013. Invisible dog. (Architecture: Ambiguous legacy of the normalization era.) [online], [cited on 06.07.2019]. Available at: http://neviditelnypes.lidovky.cz/architektura-nejednoznacne-dedictvi-normalizacni-ery-pps-/p_architekt.aspx?c=A130217_234304_p_architekt_wag
[15] Michna J., 2016. Claim to Respect. Some Notes on Socialist Architecture. A2 cultural biweekly. Prague, 23. [online]. [cited on 07.07.2019]. Available at: https://www.advojka.cz/archiv/2016/23/narok-na-respekt
[16] Doudová H., 2017. Transgas or the pitfalls of one's own success – an architectural notebook. A2 cultural biweekly. Prague. [online]. [cited on 07.07.2019]. Available at: https://www.advojka.cz/archiv/2017/6/transgas-aneb-uskali-vlastniho-uspechu-architektonicky-zapisnik
[17] Dlabačov, technical equipment for projection, MC Dlabačov, cited: 05.07.2019, available online at: chrome-extension://efaidnbmnnnibpcajpcglclefindmkaj/https://www.mcdlabacov.cz/pdf/DLABACOV_technicke_vybaveni_PROJEKCE_ZVUK.pdf
[18] Ševčíková J., Ševčík J. 2010. Texts. Edited by Terezie Nekvindová. Praha: Tranzit.
[19] Bähr A., 1995. Alhambra-Lichtspiele. In: Sylvaine Hänsel, Angelika Schmitt (Hrsg.): Cinema Architecture in Berlin 1895–1995. Berlin.
[20] Official website portal of the city of Vienna, History of Vienna – Cinema section, [online]. December 9, 2022, [accessed on January 31, 2024]. Available at: https://www.geschichtewiki.wien.gv.at/Kino
[21] Bartoszewski W., Brzeziński B., Moczulski L., 1970. Chronicle of Events in Warsaw 1939–1949. Warsaw: Państwowe Wydawnictwo Naukowe, p. 122.
[22] Krzyżakowa K., 1987. Statistical Notes. in: Warsaw Calendar '88. Warsaw: Krajowa Agencja Wydawnicza, p. 140.
[23] https://www.jstor.org/stable/3205717?read-now=1&seq=1#page_scan_tab_contents
[24] https://www.facebook.com/pg/64UHradeb/photos/?tab=album&album_id=1250019801779272
[25] https://www.lidovky.cz/ln_lidovky/foto.aspx?r=ln_kultura&c=A170228_152010_ln_kultura_jto&foto=JTO698651_Kino64_interir_macha.jpg
[26] Hilmera, Jiří, and Vočadlo Karolina. "Building History of Prague Cinema Auditoriums. Part IV – Post-war Half Century." Iluminace 10, no. 4 (1998): 75-101.
[27] Dudek, M., 2014. Vzpomínka na kino Kosmos. Tučňák. Praha, vol. 01. [online]**.** [cit. 24.08.2022]. Available from: https://docplayer.cz/107767226-Vesele-vanoce-a-stastny-rok-2014-leden-2014-tema-mesice-co-nam-preji-cestni-obcane-do-roku-2014.html
[28] https://mapio.net/pic/p-82589608/
[29] https://www.a489.cz/kulturni-dum-eden
[30] https://commons.wikimedia.org/wiki/File:Spo%C5%99ilov,_Hlavn%C3%AD,_kulturn%C3%AD_centrum_a_kino_Sigma,_panel%C3%A1k_v_Choratick%C3% A9.jpg
[31] https://www.metro.cz/sporilovsti-uz-nebudou-odkazani-na-multiplexy-kino-sigma-se-po-letech-otvira-188- /praha.aspx?c=A141207_192910_co-se-deje_mpe
[32] https://www.builtheritagephotography.com/
[33] https://mapy.cz/zakladni?x=14.3802357&y=50.0858873&z=17&source=firm&id=13024517&gallery=1&sourcep=ffoto&idp=1964371

CIVIL ENGINEERING JOURNAL

Article no. 2

THE CIVIL ENGINEERING JOURNAL 1-2024

EFFECT OF SEGMENT DISLOCATION ON THE MECHANICAL PROPERTIES OF LINED TUNNELS IN A COMPLEX ENVIRONMENT

Fengchi Wang [1], Yingong Wang [1], Dong Li[2] and Yanfeng Li[1]

1. *School of Transportation and Geomatics Engineering, Shenyang Jianzhu University, Shenyang 110168, China; cefcwang@sjzu.edu.cn, wangyg@stu.sjzu.edu.cn, lyfneu@126.com.*
2. *School of Civil Engineering, Shenyang Jianzhu University, Shenyang 110168, China; 15054187223@163.com*

ABSTRACT

In complex environments, tunnels with a lined structure are more affected by the dislocation of a segment. This study uses finite element simulations to further investigate the relationship between environmental changes and segments in lined tunnels. Tunnels with and without a lining are simulated under varying strata resistance, buried depth, and water level conditions. The horizontal and vertical displacements and stress changes in the two tunnels are compared when segment dislocation occurs. The results show that the lateral displacement of the tunnel is relatively stable and less influenced by external loads. However, the longitudinal displacement change is the opposite, and it increases significantly when the displacement exceeds 10 mm. When the lined tunnel is subjected to a large external load and misalignment occurs, the performance of the tube sheet joint bolts deteriorates, resulting in a stress decrease. Furthermore, the lined tunnel exhibits an increased ability to resist deformation and does not exactly follow the law of small displacements from small misalignments. When a large misalignment occurs, the lined tunnel may be damaged by elliptical deformation along the 45° direction, and its internal forces would be much larger than those of the unlined tunnel.

KEYWORDS

Tunnel, Lining dislocation of the segment, Lined construction, Mechanical performance analysis

INTRODUCTION

With the rapid economic development, the utilization of urban underground space is gradually increasing. Lined tunnels include a secondary lining in their structure that can greatly increase the space for pipeline arrangement as well as improve the efficiency of power transmission. However, this unique lining structure also enhances the difficulty of daily operation and maintenance. Construction of a lined tunnel involves the application of the secondary lining, differentiating them from other tunnels. However, construction companies have failed to update the relevant operational experience; thus, the maintenance and overhaul of underground structures has become a primary challenge. The majority of quality problems in tunnels include dislocation of the segment of lining sheets due to shield machine turns, morphological changes, or jacking thrust changes, among others [1,2].

With the operation of lined tunnels, there has been a gradual increase in the occurrence of cracks or even breakage of the lining segment, as well as water seepage and leakage in the tunnel

due to dislocation of the segment [3,4]. Current research regarding lined tunnels has mainly focused on cast-in-place and prefabricated structures, with fewer studies on shield construction structures. Diemer [5] first investigated the mechanical and seismic performance of structurally similar water transfer tunnels using a model experimental approach. Sharghi [6] considers the effects of longitudinal offset, circumferential offset and incomplete contact of the support area on segment damage and obtains a numerical model that can accurately predict the performance of sectional tunnel lining. Botuan et al. [7] found that the joint position and axial pressure ratio predominantly affect the mechanical properties of the nodes of laminated slab-type corridors. Galli [8] studied the mechanical properties of the lining structure during tunnel excavation, and obtained a model that can be used to evaluate the lining–soil interaction and the stress distribution in both the lining and the reinforcing structural elements. Yang [9] highlighted two main external factors for structural stress changes in model tunnels under the influence of seismic forces: soil liquefaction in the tunnel and pore water pressure changes. A finite element (FE) model was developed for the formulation of a duct piece to simplify the calculation using the mean circular method [10], which considers the effect of the tube sheet joint on the deformation and bending moment. Morgan [11] assumed that forces on the tunnel lining would produce lateral deformation, causing the circular lining to become elliptical, and derived a closed solution after neglecting tangential stresses and strains. Chen and Majdi used finite elements to simulate the change in stress displacement of two adjacent lining rings when the joint function is considered in three-dimensional tunnel construction [12,13]. Regarding dislocation of the segment, Liu et al. [14] studied individual lining rings as a whole and showed that the maximum amount of dislocation of the segment occurred at the location of the capping block and adjacent blocks. Yuan et al. [15] analyzed the displacement phenomenon of a lining section caused by hydrostatic pressure during shield construction in water-rich strata. Wang [16] analyzed the phenomenon of lining segment displacement caused by grouting pressure and hydrostatic pressure during shield construction in hard rock areas. Zhou [17] examined the mechanism of lining dislocation of a segment and cracking under construction load in different construction stages of a tunnel through a river and proposed corresponding control measures. Arnau [18] analyzed the most influential parameters and their effects on the response of the lining structure when the lining of the segment tunnel is subjected to local loads or different deformations of adjacent rings.

The above results have focused on the effect of external environmental changes on the lining tube sheet itself and the tunnel structure. There is a lack of more detailed research on the stress–strain law for the internal structure of the tunnel due to the change in the misaligned volume. To further investigate the effect of misaligned volume changes on lined tunnels, this study evaluated the changes in mechanical characteristics of different types of tunnels under complex environmental conditions when misalignment occurs via numerical simulations. This work can provide a reference for the operation and maintenance of lined tunnels and their structural stability and durability in similar underground environmental conditions at a later stage.

Finite Element Method

Project Profile

An underground project was completed using the shield machine with a single circular section. The outer ring radius of the tunnel lining is 6 m, the inner ring radius is 5.4 m, and the tube section size is 300 mm × 1200 m. The single lining ring is assembled from six reinforced concrete precast blocks (three standard blocks, two adjoining blocks, and one capping block), and the longitudinal, circumferential, and lining pipe pieces are connected with M24 curved bolts. The soil parameters extracted from the ground investigation report involving this model interval are specified in Table 1.

Tab. 1 - Parameters of various layers spanning the tunnel section.5

Type of rock	Force density (γ) (kN/m3)	Cohesion (C) (kPa)	Angle of internal friction (∅) (°)	Lateral pressure at rest (K_0)
Silty clay	19.7	57.8	14.8	0.50
Silty fine sand	19.0	-	26.0	0.40
Gravelly sand	19.0	-	37.5	0.35
Rounded gravel	20.0	-	39.0	0.30

Model Parameters

For the lining segment, concrete material was used for the simulation. The constitutive relation is based on the intrinsic structure model proposed by the American scholar, Hongnestad. The model curve consists of a quadratic parabola and a section of the oblique straight line.

Upward phase:

$$\varepsilon \le \varepsilon_0, \sigma = f_c \left[2\frac{\varepsilon}{\varepsilon_0} - \left(\frac{\varepsilon}{\varepsilon_0} \right)^2 \right] \quad (1)$$

Declining phase:

$$\varepsilon_0 \le \varepsilon \le \varepsilon_u, \sigma = f_c \left[1 - 0.15 \left(\frac{\varepsilon - \varepsilon_0}{\varepsilon_u - \varepsilon_0} \right)^2 \right] \quad (2)$$

Here, f_c is the compressive strength. Hongnestad suggested using $\boldsymbol{\varepsilon_u}$ = 0.0038 for theoretical analysis. He also proposed that $\varepsilon_0 = 2\left(\frac{\sigma_0}{E_0} \right)$, where E_0 is the initial elastic modulus. The geometric size of the lining segment (Table 2) and the material properties (Table 3) are the parameters used in the numerical simulation.

Tab. 2 - Geometric dimensions of the segment in the design data

Segment outer diameter/mm	6000
Segment inner diameter /mm	5400
Segment width /mm	1200
Bolt length /mm	464

Tab. 3 - Material parameter

Name of the material	Density (kg/m³)	Elastic modulus (Mpa)	Poisson ratio	Element type
Lining segment	2500	3×10^4	0.17	C3D8R
Bolt	7850	2.1×10^5	0.3	B31

To reduce the complexity of the calculation, the original bolts were replaced with straight bolts according to the conversion formula for curved and straight bolts proposed by Guo [19]. In addition, in practical engineering, the bolts do not interact with the lining segment when deformed by external

forces. Therefore, contact between the bolt and bolt hole was not considered in the simulation, and the bolt was simplified using a curved instead of a straight approach. There is no external action in the middle of the bolt, and the end of the bolt is connected to the lining segment cell using the same node. In this paper, the change in segment dislocation is simulated by setting the displacement values in all directions in the boundary conditions.

To reduce simulation tolerances, the modeling scheme of two adjacent rings was abandoned in favour of a monolithic tunnel model with a multi-ring lining segment. The bolts are embedded to connect two adjacent lining rings so that they form a single unit and are jointly stressed. During the numerical simulation, the two contact surfaces of the lined lining segment will approach each other, and additional normal external forces need to be applied to the intrusion area to control the amount of intrusion within the convergence range [20]. The intrusion distances are as follows:

$$p_n = min\alpha l_{AB} \ , \ \alpha = \begin{cases} 1, (X_B - X_A) \cdot n^A \leq 0 \\ 1, (X_B - X_A) \cdot n^A \geq 0 \end{cases} \quad (3)$$

where n is the unit normal vector of A; X_B and X_A are the spatial coordinate vectors of points A and B, respectively.

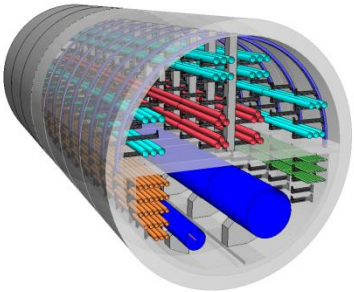

Fig. 1 - Lined tunnel 3D model

The lined tunnel is shown in Figure 1. The lining structure is highlighted using a block in Figure 2(b). It was poured after completion of the main body of the original tunnel, when the overall tunnel structure had not yet reached stability. The newly poured lining structure will share the forces with the tunnel and limit the overall displacement of the tunnel, offsetting some of the internal forces in the lining segment. Most current lining structures have similar mechanical parameters to the initial support. To simplify the calculations, the Hognestad approach was employed for the tunnel constitutive relation. The grid division of the lined tunnel is depicted in Figure 2, with a grid density of 0.4 m.

(a) (b)

Fig. 2 - Mesh division of (a) unlined and (b) lined tunnel

Load Application

To investigate the effect of segment dislocation, incremental dislocations of the segment were set for each scenario as 0, 5, 10, 15, 20, 25, and 30 mm. Variables were separated according to the different environments, with a burial depth of 12 m; a water table height of H = 4, 8, and 12 m; and a ground reaction coefficient $K=i\times10^4$ kN/m^3, i=[1,5]∈N+.

Taking the tunnel and lining segment as the main object of study, the load-structure method was considered for load application, considering factors such as strata resistance, burial depth, and water level.

Arch back soil pressure:

$$G = 2\left(1 - \frac{\pi}{4}\right) R_H^2 \gamma = 0.43 R_H^2 \gamma \quad (4)$$

where γ is the soil heaviness (kN/m^3), and R_H is the radius of the lining (m).

Lateral uniform active soil pressure:

$$p_1 = q tan^2\left(45° - \frac{\varphi}{2}\right) - 2c tan\left(45° - \frac{\varphi}{2}\right) \quad (5)$$

where q is the vertical soil pressure.

Lateral triangular distribution of active soil pressure:

$$p_2 = 2R_H \gamma tan^2\left(45° - \frac{\varphi}{2}\right) \quad (6)$$

Water pressure: hydrostatic pressure mode of action.

Longitudinal restraints were set on both sides of the tunnel and vertical restraints at the bottom, which limited the overall movement of the lined pipe sheet. The earth pressure generated by the strata was simulated using spring units and restrained at the end of the spring cells.

The horizontal and vertical soil and water pressures in an actual project are considered as surface loads combined with gradient orders acting on the solid unit, and the lining segment is restrained, as in Figure 3.

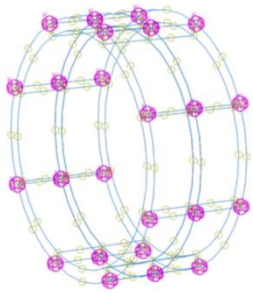

Fig. 3 - Lining segment constraint diagram

Simulation of the Effect of Dislocation of the Segment on Lined Tunnels under Changes in Strata Resistance

Tunnel Without Lining

Gunding springs were used to simulate the strata resistance, the values were formulated through the type of interval overburden in the ground survey report and set in linear increments. To ensure the uniqueness of the formation resistance variables and the accuracy of the results, the groundwater level was maintained at 8 m. When the tunnel as a whole is not misplaced and K = 1 × 10^4 kN/m^3, it can be seen from Figure 4 that the tunnel arch waist and arch foot positions produce a larger displacement. This phenomenon is due to the deformation of the concrete in the middle of the tunnel by the bending moment generated from the earth pressure. The ground resistance coefficient is controlled at a constant value, and the overall tunnel is subjected to the upper active earth pressure, which is displaced downward by the equivalent load generated by the upper soil layer of the tunnel. The additional stress of the soil on the tube pieces is large at the top and small at the bottom; the upper area of the tunnel is subjected to larger vertical pressure, and the lower part is

subjected to passive earth pressure, resulting in a larger displacement of the arch waist and arch foot. The location where the maximum displacement of the structure occurs coincides with the pipe piece connection, and the inspection of the displacement area and nearby areas should be increased during operation to avoid accidents caused by connection failure.

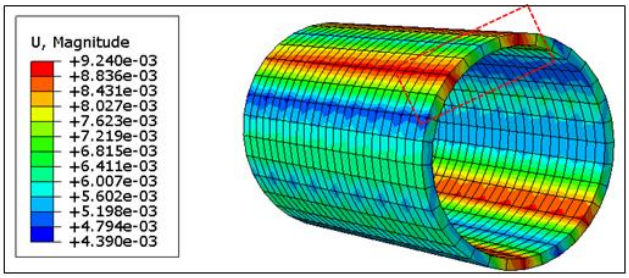

Fig. 4 - Displacement of unlined tunnel without misplacement of platform

When dislocation of the segment occurs, the lining segment responds more sensitively to the load, producing an oblique downward deflection of approximately 45° along the direction of the dislocation of the segment at the arch waist and arch shoulder. As the force increases in the red area marked in Figure 3, the lining ring is cut into multiple parts and its integrity is destroyed: irregular deformation occurs, as depicted in Figure 5(a). If no dislocation of the segment occurs, the lining ring is an intact part, the overall force is uniform, and its displacement is in the form of flat movement, as presented in Figure 5(b).

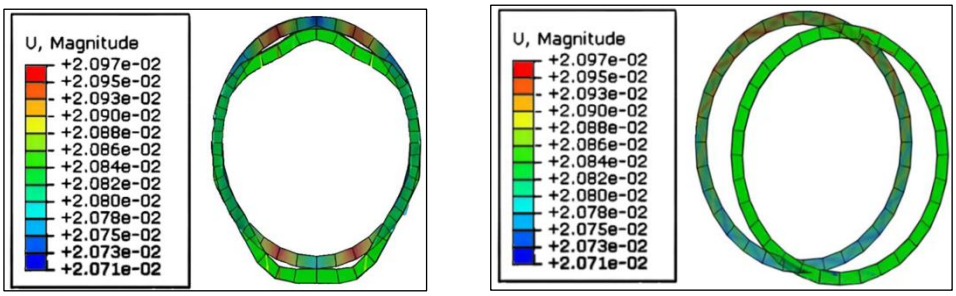

(a) (b)

Fig. 5 - Displacement comparison between misplaced and non-misplaced segments under external load: (a) during and (b) without segment dislocation

(1) Variation in tunnel lining segment displacement

The comparative results of the overall maximum horizontal displacement of the tunnel, varying the amount of dislocation of the segment and the strata resistance factor conditions, are displayed in Figure 6. At the segment dislocation of 30 mm, the maximum lateral deflection of the tunnel occurs at the shoulder and foot of the arch near the dislocation of the segment ring, exhibiting positive correlation with the amount of dislocation of the segment and a distribution that decreases toward the shoulder of the arch, centered on the dislocation of the segment ring. When the dislocation of the segment is less than 10 mm, the horizontal displacement increases at a slower rate and the overall height of K_1 is above K_2, indicating a limiting effect of the strata resistance on the horizontal displacement of the structure. When the dislocation of the segment is greater than 10 mm, the difference between the working conditions increases, indicating a faster rate of increase in horizontal displacement. A comparison of the height difference between K_1 and K_5 shows that the strata resistance can act as a more significant restraint on the lining segment. When the ground resistance is raised to 5×10^4 kN/m^3, the increase in horizontal displacement of the lining is reduced by approximately one-fifth. This is similar to the phenomenon in actual engineering.

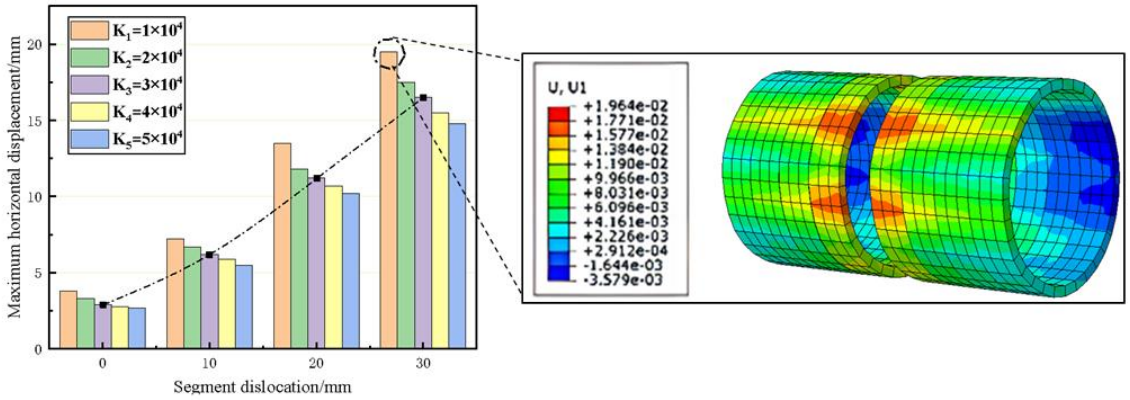

Fig. 6 - Strata resistances and horizontal displacements of unlined tunnel

Figure 7 presents the results of the comparison of the maximum vertical displacement of the tunnel as a whole under the change in strata resistance. At 30 mm dislocation of the segment, a large vertical displacement occurs at the position of the arch waist and foot of the tunnel, and the elliptical deformation of the tunnel section caused by the displacement increases the displacement at the top of the arch. The 2% and 3% decreases in K_5 compared with K_4 and K_2, respectively, indicate that the structure needs to provide higher internal forces than the general environmental conditions to generate displacement under the constraint of larger ground resistance. In summary, comparing the smaller variation in horizontal and vertical displacements with the amount of dislocation of the segment suggests that the strata resistance factor is a more significant constraint on vertical displacement.

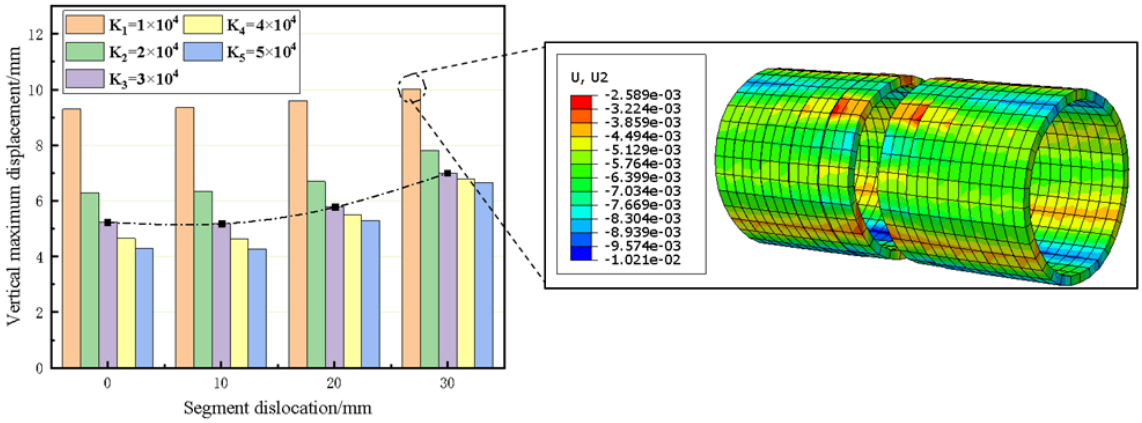

Fig. 7 - Vertical displacement of unlined tunnel with different lining segments

(2) Variation in main stress of tunnel lining segment

The maximum principal stress of the tunnel tube sheet under different stratigraphic resistance is divided into several zones: linear growth, smooth, and failure, as depicted in Figure 8. In the linear growth region, the amount of dislocation of the segment is small and the overall tunnel response to it is insignificant. The maximum principal stress increases linearly, and the lining segment deforms elastically; thus, the effect of strata resistance can be largely ignored. When the stress enters the smooth zone, the tunnel reaches a certain structural strength. For a small range, the increase in the amount of misalignment will not affect the change in stress; thus, the overall trend is gentler. At this time, the tube sheet can withstand stress close to the limit. When entering the failure zone, with increasing dislocation of the segment, the dislocation ring produces a larger deformation, and the tunnel loses the overall structure. At this time, the tunnel can be seen as two parts, both individually

stressed, resulting in a decline in overall resistance to external forces, and hence the K_4 and K_5 curves present downward trends. In this region, the change in strata resistance can influence the main stress changes, and the greater the resistance, the more pronounced the stress failure phenomenon. The stress cloud in the dashed box in the figure indicates that the misalignment disrupted the tunnel integrity, causing a discontinuity of sudden stress changes, and the stress is divided into several individual parts by the misalignment ring. The $K_1K_2K_3$ curve is a stable trend because the structure can maintain the equilibrium state due to the small external load.With the increase of strata resistance, the overall structure of the tunnel is completely destroyed, and the internal stress of the tunnel is released, so the curve decreases.

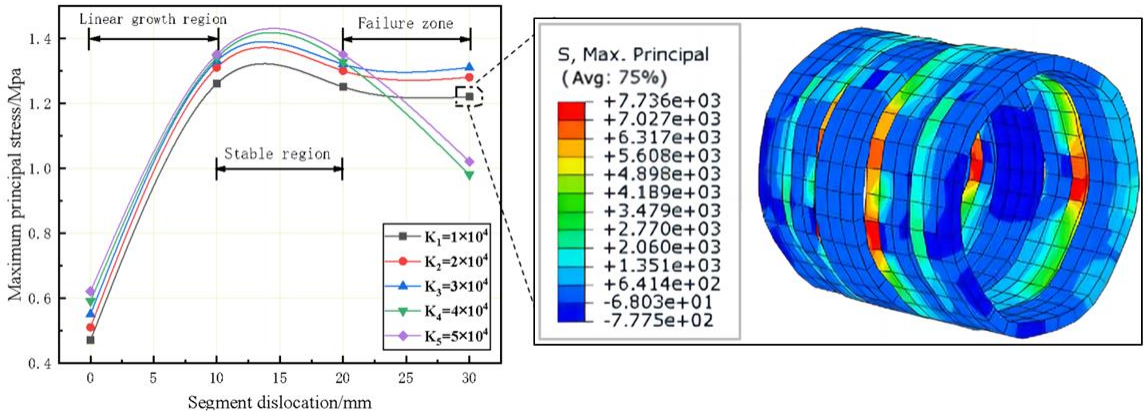

Fig. 8 - Maximum principal stresses in unlined tunnel under different strata resistances

Tunnel With Lining

The lined structure will increase the lateral stiffness of the tunnel and limit the development of dislocation of the segments, offsetting some of the displacements. However, its limiting effect can show differential results at different misbolts. When the misbolts are zero, the maximum displacement occurs at the position of the tunnel arch shoulder, and there is a large change in the position of the arch foot compared to the unlined tunnel, as shown in Figure 9(a). As the dislocation of the segment continues to increase, large displacements occur near the lined structure and the distribution changes dramatically, as shown in Figure 9(b). Cross section stiffness decreases with increasing dislocation. The stress field is redistributed when subjected to external loading, resulting in large deformation.

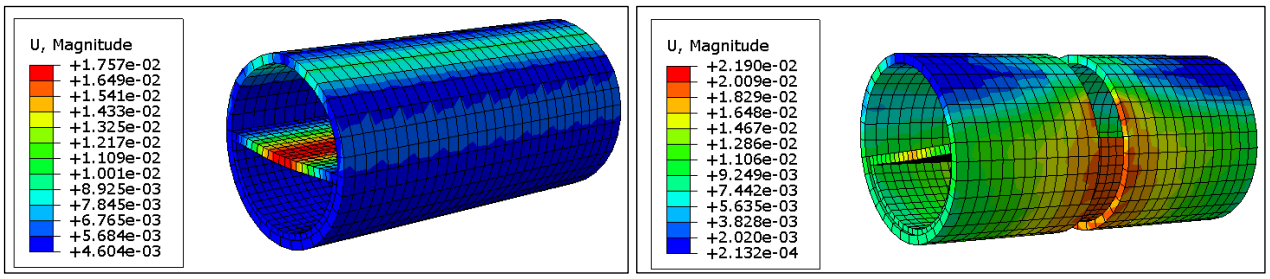

(a) (b)

Fig. 9 - Maximum displacement of pipe corridor under different fault levels: segment dislocations of (a) 0 and (b) 30 mm

(1) Variation in displacement of lined tunnel segment

The horizontal displacements of the tunnels do not vary significantly for different strata resistances and dislocations of the segment volumes, as shown in Figure 10. The reason for this is because the lined structure restricts the tunnel and produces oblique elliptical variations while

weakening the horizontal displacements, but the overall trend is the same as that for the unlined tunnel. With a dislocation of the segment of less than 10 mm, the trend of the horizontal displacement is slightly lower than in the next stage due to the balancing effect of the lined structure, which corroborates the conclusions drawn earlier. At this stage, the greater the horizontal resistance, the smaller the displacement in that direction. The resistance coefficient and displacement gradually increase when the zone dislocation exceeds 10 mm. This is mainly because the lining structure and the tunnel form a stressed whole, displacing the dislocation ring and increasing the uniformity of the adjacent ring. When the external load increases, displacement of the area near the dislocation ring occurs simultaneously; therefore, the maximum displacement increases.

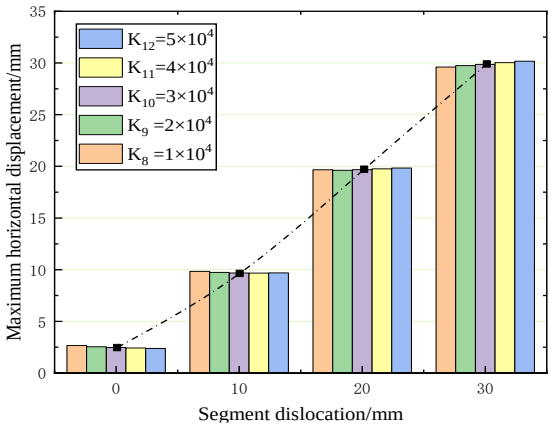

Fig. 10 - Horizontal displacement of lined tunnel with strata resistance

(2) Lined tunnel displacement variation and comparative analysis

As shown in Figure 11(a), the starting points of the curves are basically the same. Thus, the maximum horizontal displacement does not change significantly when the tunnel is subjected to varying resistance in the lining state, and the effect is relatively small. In addition, the maximum displacement of the lined tunnel varies in parallel with the amount of dislocation of the segment, as shown by the solid line in the diagram in 45° increments, indicating that the lined structure results in a more coordinated tunnel displacement. The different resistance conditions have less influence on the lined tunnel, and the lined structure improves the tunnel's adaptation to the ground. However, with the gradual increase in segmental misalignment, the overall maximum horizontal displacement curve for the lined tunnel is higher than that for the unlined tunnel. Thus, the lining structure promotes the influence of segmental misalignment on the tunnel, leading to the expansion of segmental misalignment on both sides and a decrease in the constraint.

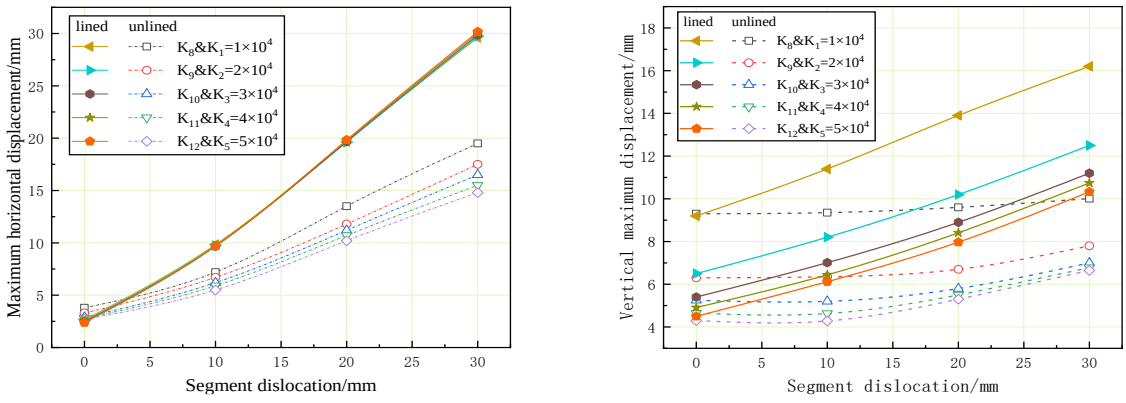

(a) (b)

Fig. 11 - Comparison of (a) horizontal and (b) vertical displacements in tunnels with different strata resistance

Figure 11(b) presents the vertical displacement with varying strata resistance. When no misalignment occurs, the lining structure has less influence on the tunnel structure under the same value of ground resistance, and the maximum vertical displacement of both is approximately equal. This is demonstrated by the coincidence of curves K_1 and K_8, K_2 and K_9, and the starting point. When the dislocation of the segment is less than 10 mm, a downward trend appears in the vertical displacement of unlined tunnels, while the opposite is true for lined tunnels. Comparing the horizontal and vertical displacements, it is clear that the lining improves the uniformity of tunnel displacements, but the overall displacement values and trends increase. Therefore, more attention should be paid to the occurrence of zone misalignments in the acceptance, operation, and maintenance of lined tunnels. Smaller section misalignments can also lead to larger lining section distress and structural damage.

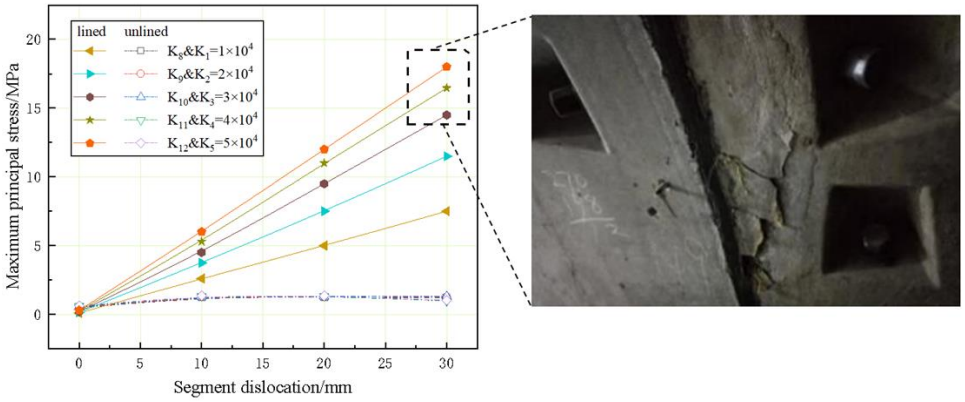

Fig. 12 - Comparison of maximum principal stresses in tunnel with different strata resistances

(3) Lined tunnel variation in main stress and comparative analysis

As shown in Figure 12, the lining structure significantly influences the trend and magnitude of the maximum principal stresses in the tunnel, with a positive correlation between the principal stresses in the structure and the amount of dislocation of the segment. The increased lateral stiffness of the lined structure improves the stability of the structure, and thus, a greater internal force is required to produce the same amount of displacement. However, this can also lead to irregular deformation of the lined tunnel, causing stress concentration in adjacent misaligned rings and pulling

down the lining section, which would create cracks and other stability hazards. In the area highlighted, the lining section is very susceptible to damage.

Simulation of the Effect of Lining Dislocation of the Segment on Lined Tunnels under Changing Groundwater Levels

Tunnel Without Lining

(1) Variation in tunnel lining segment displacement

The level of the groundwater table represents the amount of head around the tunnel soil and determines the strength of the erosion action. Groundwater can cause erosion of the lining segment and joint bolts, weakening the performance of the reinforcement inside the lining segment, and jeopardizing the durability and stability of the tunnel structure. The choice of groundwater level is based on the depth of 16 m, set to 4, 8, and 12 m above the top of the tunnel, and the strata resistance was taken as $K=2\times10^4$ kN/m^3.

Groundwater acts as a circumferential pressure on the lining segment with a linearly increasing distribution of the analytical field. The change in groundwater level is modelled by varying the load acting on the lining segment.

As can be seen from Figure 13(a), the rise in groundwater level can partially offset the soil load and reduce the force in the arch waist area, and the effect is significant with the rise in water level. More specifically, under the same misplaced amount, the change in water level hardly affects the change in horizontal displacement, the maximum water level difference in the figure is △H=12-4=8 m, but the horizontal displacement only differs by 2%.

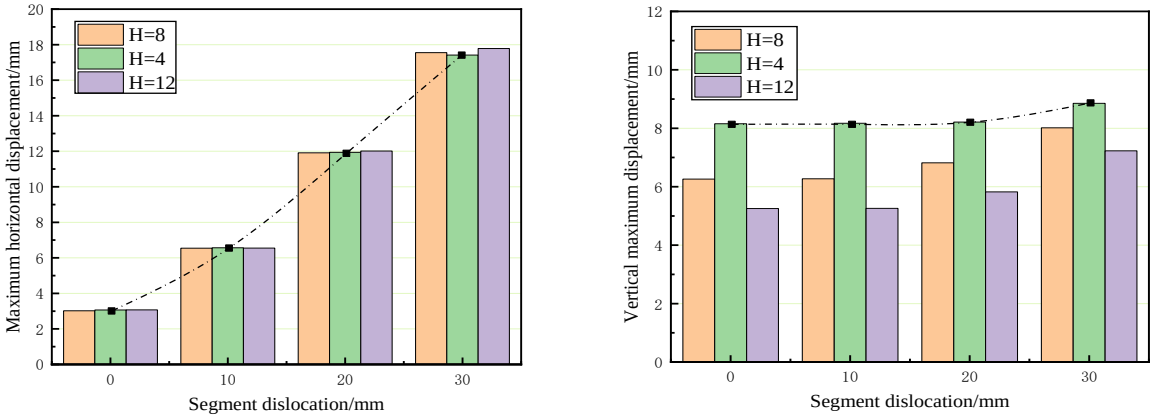

(a) (b)

Figure 13 - (a) Horizontal and (b) vertical tunnel displacement changes with water level.

The trends for the effects of water level and strata resistance on vertical displacement are similar, as demonstrated in Figure 13(b): the maximum vertical displacement at fixed water level is positively correlated with the amount of misplaced platform. When the amount of dislocation of the segment exceeds 20 mm, the vertical displacement of the tunnel under all water level conditions exhibits a large change and a significant increase. Under the influence of changing water level, the overall vertical displacement of the tunnel is not significant when the amount of dislocation of the segment is less than that required by the specification. However, if the amount of misplaced platform exceeds the limit, the tunnel immediately generates large vertical displacements that increase with the water level, seriously threatening the stability and durability of the structure.

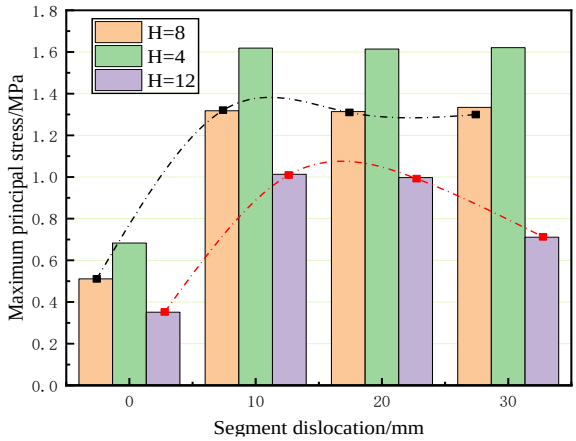

Figure 14 - Variation in maximum principal stress of unlined tunnel at different water levels.

(2) Stress change in tunnel lining segment

Figure 14 shows that the maximum principal stress in the misaligned ring varies significantly depending on the dislocation of the segment. In contrast to changes in stratigraphic resistance, changes in groundwater level present a greater range of numerical fluctuations and a more pronounced effect on the misaligned rings. When the amount of dislocation of the segment is zero, the maximum stress in the lining segment of H=4 m, compared with at H=12 m, increases by 85.1%. When the dislocation of the segment exceeds 10 mm, the δ–Δ curve of the dislocation of the segment ring tends to decrease and increases as the water level increases. This is because an increase in the water table leads to a decrease in the equivalent force and a reduction in the ground load.

Tunnel with Lining

(1) Lined tunnel displacement variation and comparative analysis

From Figure 15, the maximum horizontal displacement increases with the amount of dislocation of the segment in both tunnels under different water level conditions. When the dislocation of the segment is less than 10 mm, the maximum horizontal displacement increase is smaller. When the amount of misalignment of the segments exceeds 10 mm, the horizontal displacement increases, that is the slope increases. However, if the type of tunnel and the amount of segment misalignment are certain, the horizontal displacement value can remain constant in a small range. In addition, the higher horizontal displacement values for lined tunnels are because within the small dislocation of the segment, the lined structure improves the stability of the tunnel and the displacement is slightly lower than that in unlined tunnels. With a gradual increase in the amount of segment dislocation, the strength of the lined structure reaches its limit, can no longer guarantee its own stability, and begins to change; the horizontal displacement increases with the direction of the dislocation of the segment ring. If no action is taken at this point, there will be a high risk of damage to the arch shoulders, as shown in the figure.

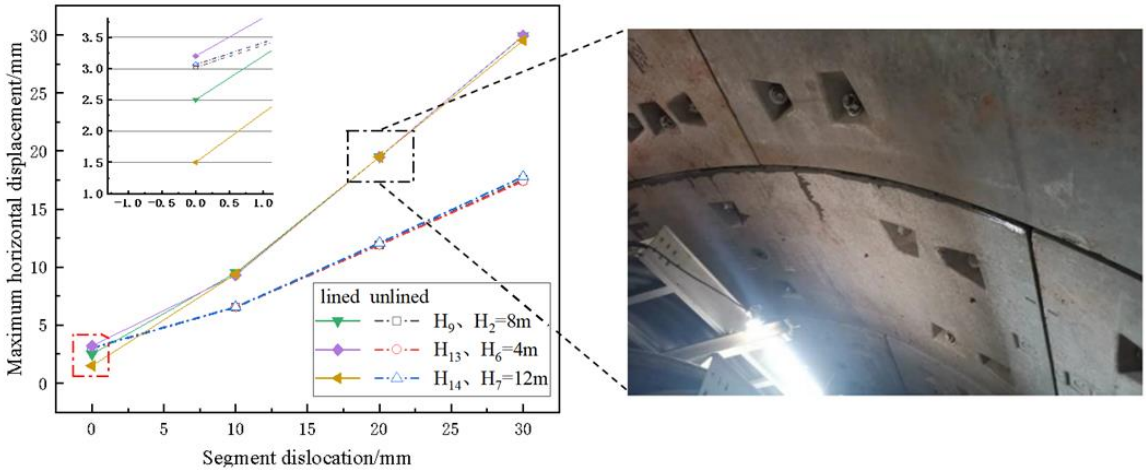

Fig. 15 - Comparison of maximum horizontal displacements in tunnel

As shown in Figure 16, the overall displacement of the lined tunnel tends to increase linearly with the amount of segmental misalignment. The unlined tunnel has a relatively flat change due to the oblique elliptical deformation of the tunnel caused by the lining structure. When no misalignment occurs, curve H_7 is above H_{14} indicating that the lined tunnel is structurally better under smaller external loads. When the amount of misalignment exceeds 20 mm, the vertical displacement of the lined tunnel in all cases exceeds that of the unlined tunnel. This phenomenon demonstrates that in practice, it is more important to increase the monitoring of lined tunnels near large misalignments to prevent displacement overruns.

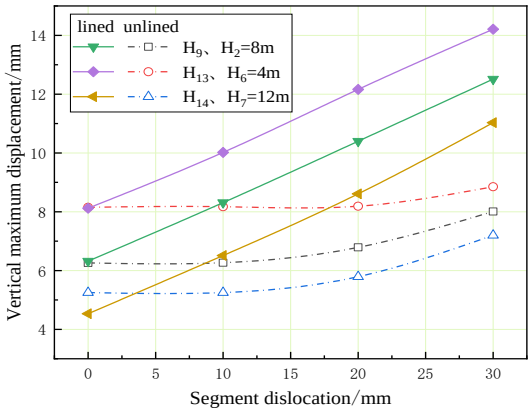

Fig. 16 - Comparison of maximum vertical displacement in tunnel

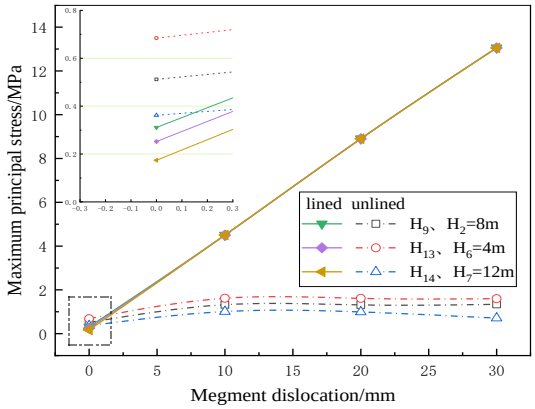

Fig. 17 - Comparison of maximum principal stress in tunnel

(2) Lined tunnel variation in main stress and comparative analysis

As indicated in Figure 17, the pouring of the lining structure did not have a significant effect on the main tunnel stresses under varying water table, but the range of change was more limited. As the amount of misbolts increases, the maximum principal stress in the misbolted ring of the lined tunnel changes more significantly, increasing rapidly with the amount of misbolts. The main stresses in the unlined tunnel are largely unaffected by changes in the amount of dislocation of the segment. When the dislocation of the segment is zero, the main stresses in the lined tunnel are low, as the lining structure shares some of the stresses. As the amount of segment dislocation increases, the lining structure reacts to increase its own principal stresses.

CONCLUSION

In this work, the mechanical properties of lined tunnels and the locations prone to damage when a tube sheet is misaligned were analyzed in the context of a completed lined tunnel. In addition, the effects of the change in misplaced volume on the structures of the two tunnels were compared and analyzed under different ground resistance and groundwater level conditions. The following conclusions were drawn:

(1) In the same environment, the displacement and stress of the lined tunnel are greater than those of the unlined tunnel, and the rate of change of both increases as the dislocation increases. However, for small displacements of the structure, the lining structure will increase the deformation resistance of the tunnel, as shown by the fact that part of the displacement curve is below the unlined tunnel. Therefore, when maintaining lined tunnels, the cracks and broken segments should be repaired and replaced in time to avoid the overall damage.

(2) The trends of the horizontal and vertical displacements of the lined tunnels in different environments were the same, wherein the amount of misalignment increased the displacement. The rate of change of the displacement of the tube sheet is bounded by 10 mm: the change is small when it is less than 10 mm and increases significantly when it is more than 10 mm. The horizontal displacement of the tunnel is less affected by external influences, while the vertical displacement exhibits the opposite trend. The main influencing factor causing the difference between the two is the load on the tunnel.

(3) The lined tunnel itself has a certain ability to balance the misalignment. This is mainly reflected in the significant increase of the main stress when a small misalignment (10 mm) occurs in the structure, and the peak value is reached in the adjacent lined pipe piece at the misalignment location. Under a large misalignment and external load, the mechanical properties of the tube sheet joint start to deteriorate, resulting in a stress drop with a slow growth rate.

ACKNOWLEDGEMENTS

Financial assistance from the Xingliao Talent Plan project of Liaoning Province, China (No. XLYC2005003), the Innovation team of universities in Liaoning Province, China (No. LT2019011) and the Central guidance on local science and technology development fund of Liaoning Province, China (No. 2023JH6/100100018) for conducting this experiment is gratefully acknowledged.

We would like to thank Editage (www.editage.cn) for English language editing.cknowledged.

REFERENCES

[1] Konda, Toru. "Shield tunneling method." Civil Engineering, Japan Society of Civil Engineers 39 (2001): 23-27.

[2] Koga D R, et al."Frame structure analysis model for the effect of typical tunnel diseases on lining structure." IOP Conference Series: Earth and Environmental Science 861.4(2021).

[3] Sharghi, M., et al. "Analysis of the possible cracking and damages of tunnel lining segments during installing stage." Soil Mechanics and Foundation Engineering 58 (2021): 287-294.

[4] Toll, D. G. "The framework of shield tunnel management system." Information Technology in Geo-Engineering: Proceedings of the 2nd International Conference (ICITG) Durham, UK. Vol. 3. IOS Press, 2014.

[5] Diemer D M , Miller M L , Pratt D L , et al. Seismic Evaluation and Improvement Program for a Major Water System[C] Lifeline Earthquake Engineering. ASCE, 2014.

[6] Sharghi, Mohammad, et al. "3D numerical study of the joint dislocation and spacing impacts on the damage of tunnel segmental linings." *Structures*. Vol. 56. Elsevier, 2023.

[7] Deng Botuan, et al."Rationality determination method and mechanical behavior of underground utility tunnels in a ground fissure environment." Bulletin of Engineering Geology and the Environment 81.1(2021).

[8] Galli, Gianfranco, Antonio Grimaldi, and A. Leonardi. "Three-dimensional modelling of tunnel excavation and lining." *Computers and Geotechnics* 31.3 (2004): 171-183.

[9] Yang J , Wang H . Seismic Response Analysis of Shallow Utility Tunnel in Liquefiable Soils[C]// CMI conference Beijing.
[10] Mao song Huang, et al."Upper bound solutions for face stability of circular tunnels in non-homogeneous and anisotropic clays."Computers and Geotechnics98.(2018).
[11] H. D. Morgan."A Contribution to the Analysis of Stress in a Circular Tunnel." Géotechnique 11.1(1961).
[12] Arnau, Oriol, and Climent Molins. "Three dimensional structural response of segmental tunnel linings." *Engineering structures* 44 (2012): 210-221.
[13] Majdi, Abbas, Hamed Ajamzadeh, and M. Kiani. "Numerical evaluation of the influence of bolted- and non-bolted joints on segmental tunnel lining behavior in line 4 Tehran subways." *ISRM International Symposium-Asian Rock Mechanics Symposium*. ISRM, 2010.
[14] Dejun Liu, et al."Structural responses and treatments of shield tunnel due to leakage: A case study." Tunnelling and Underground Space Technology incorporating Trenchless Technology Research 103.(2020).
[15] Mei Yuan, et al."Study on the Floating Law of Metro Segments in Water-Rich Sandy Silt and Silty Clay Strata." *KSCE Journal of Civil Engineering 26*.6(2022).
[16] Yun Wang. Study on the floating mechanism and prevention technology of subway tunnel segments in hard rock area [J].*Railway construction technology*, 2022 (12) : 170-173 + 206.
[17] M.B.Zhou.Research on mechanical response and construction control technology of segment structure of river-crossing shield tunnel [D].Hunan University of Science and Technology, 2017.
[18] Arnau, Oriol, and Climent Molins. "Theoretical and numerical analysis of the three-dimensional response of segmental tunnel linings subjected to localized loads." *Tunnelling and Underground Space Technology* 49 (2015): 384-399.
[19] R.Guo, et al." Research on the stability of shield tunnel tube sheet lining structure." China Journal of Highway and Transport 28.06(2015):74-81.
[20] Feng Kun, et al."Study on mechanical behaviors of large diameter shield tunnel during assembling." SMART STRUCTURES AND SYSTEMS 21.5(2018).

CIVIL ENGINEERING JOURNAL

Article no. 3

THE CIVIL ENGINEERING JOURNAL 1-2024

AN ELASTOPLASTIC CONSTITUTIVE MODEL OF LUNAR SOIL SIMULANT CONSIDERING SHEAR DILATANCY AND SOFTENING CHARACTERISTICS

Yunli Li[1], Luqi Wang[1], Jiawei Li[1], and Wenping Wu[2]

1. *School of Civil Engineering and Architecture, Wuhan Institute of Technology, Wuhan 430074, China; liyunli@wit.edu.cn*
2. *School of Civil Engineering, Wuhan University, Wuhan 430072, China*

ABSTRACT

The study of the constitutive relationship of lunar soil is the key to a deep understanding of the mechanical properties of lunar soil. Previous models mostly focused on the strengthening behavior, while rarely reflected the post-peak softening and residual deformation stages during shear deformation. A new elastoplastic constitutive relation is derived with combining kinematic hardening model and initial shear stress, which effectively compensates for the shortcomings of existing constitutive models, and the validity of the model is verified by comparing with existed laboratory test results. The developed constitutive model not only effectively captures the shear dilatancy and softening characteristics of lunar soil simulant, but also only requires fewer parameters to be easily determined by simple initial loading curves from direct shear tests, Furthermore, the influences of some key parameters on shear strength and softening behavior of lunar soil simulant can be easily obtained based on this constitutive model.

KEYWORDS

Lunar soil simulant, Constitutive model, Shear dilatancy, Softening, Residual deformation

INTRODUCTION

The lunar exploration project first requires studying the interaction between lunar probes and lunar soil, but there are very few real lunar soil samples, so only lunar soil simulant with similar properties (these similar properties include basic physical indicators, particle grading and distribution, as well as particle shape, etc.) can be used to replace real lunar soil [1-4]. The key challenges faced in this endeavor involve understanding the interaction mechanisms between the lunar drilling equipment and lunar soil under low-stress conditions, as well as the unique mechanical properties of lunar soil in low gravity environments [3-5]. To address these challenges effectively, a reasonable constitutive model is an essential approach to accurately describe the mechanical properties of lunar soil simulant, which will provide a significant reference value for lunar soil drilling and sampling, design of landers, rovers, and drilling equipment on the moon.

The success rate of lunar surface sampling primarily depends on the understanding the constitutive characteristics of lunar soil. In the past decade, some empirical constitutive models have been established based on data fitting from experimental tests and numerical simulations. For example,

Hasan and Alshibli [6] simulated the triaxial compression test of JSC-1A （the name of lunar soil simulant developed by Johnson Space Center）lunar soil simulant using a three-dimensional particle flow code (PFC3D). Based on the experimental data, they established an empirical constitutive model for the peak internal friction angle, residual friction angle, density, and average normal stress. Hicher and Chang [7] established a constitutive model considering the surface energy effects caused by static electric forces of lunar soil particles based on triaxial compression test data. They analyzed the influence of surface energy on the shear strength of lunar soil. Richard [8] used the Cambridge model to describe the constitutive behavior of lunar soil based on triaxial test data. By adjusting the friction angle, the fitted the modified Cambridge model's yield surface and critical state line suitable for lunar soil. Zou et al. [9] developed an internal stress model to investigate the bearing capacity and shear strength of lunar soil simulant. Hou et al. [10] and Jiang et al. [11] also proposed a novel contact model of lunar soil particles to investigate the main mechanical properties of lunar soil simulant, the results indicated that the lunar soil simulant under low gravity environment are different from those on the earth. Liu et al. [12] established a variable constitutive model based on discrete element simulations to study the shear strength and elastoplastic behavior of lunar soil simulant under loose and dense conditions. Furthermore, Liu et al. [13] further proposed an equivalent boundary method based on this constitutive model to effectively address the computational cost issue in discrete element simulations for lunar soil drilling and sampling. Schafer et al. [14] used an elastic-plastic constitutive model for dynamic behavior of lunar soil to study the sampling process under different surface gravity environments. Liang et al. [15] used ABAQUS finite element software based on Cap Drucker-Prager model to simulate the landing impact process of a lander. Mao and Liu [16] developed a smoothed particle hydrodynamics (SPH) model with the elastic-perfectly plastic constitutive equation and Drucker-Prager yield criterion to simulate the electrostatic transporting of multiple charged lunar dust particles. Li et al. [17] also developed a new wear mechanical model for lunar dust to investigate the mechanical properties of lunar dust (including adhesion, contact, and wear), and rationality of the model was verified through experiments. These models effectively reflect some special mechanical properties of lunar soil simulant from a certain perspective and obtain corresponding applications. However, there are few or almost no models consider strain softening characteristics caused by cementation failure in the lunar soil simulant, it is difficult to describe the shear dilatancy and softening characteristics of lunar soil simulant under low stress levels.

Focusing on this problem, many experimental and simulation works have shown that lunar soil simulant exhibits significant shear dilatancy and softening characteristics under low stress conditions [18-23]. A rational constitutive model should reflect the shear dilatancy and softening characteristics of lunar soil simulant under low stress levels. Though discrete element simulations can effectively capture microstructural deformation features and related mechanical properties, the small size of sample used in calculations cannot fully represent the macroscopic mechanical behavior of the entire material. Moreover, due to the lack of research on the shear dilatancy behavior of lunar soil simulant and strain softening caused by cementation failure at low stress levels, the understanding of the mechanisms of the shear dilatancy and softening remains unclear, resulting in lack of a clear understanding of mechanical properties of lunar soil in low gravity environment. Therefore, it is important to establish a

micromechanical constitutive model that considers the shear dilatancy and softening characteristics of lunar soil simulant. This would help reveal the constitutive properties of lunar soil in low gravity environment and accurately describe its mechanical behavior.

ELASTOPLASTIC CONSTITUTIVE THEORY

The schematic diagram of shear stress-shear strain curve is shown in Figure 1. This curve can be divided into three stages as the shear strain changes:

(1) Linear elastic stage: In this stage, the shear strain of the lunar soil simulant is relatively small, and the shear stress has not reached the yield threshold. The deformation of the lunar soil simulant sample can be considered as elastic.

(2) Elastoplastic stage: With increasing shear strain, the shear stress gradually reaches its peak value. Then, the sample enters the elastoplastic stage. At this time, the shear stress of the lunar soil simulant has reached the peak stress, the contact between particles begins to yield, and the shear stiffness decreases. In the process of shearing, there will also be relative deformation in the normal direction, and the sample will experience shear dilatancy.

(3) Softening stage: With the gradual increase of shear stress, the internal cementation of the lunar soil simulant is destroyed, and softening occurs, and the shear stress is greatly reduced. These three stages can be called elastic, elastoplastic, and softening stages, respectively (See Figure 1).

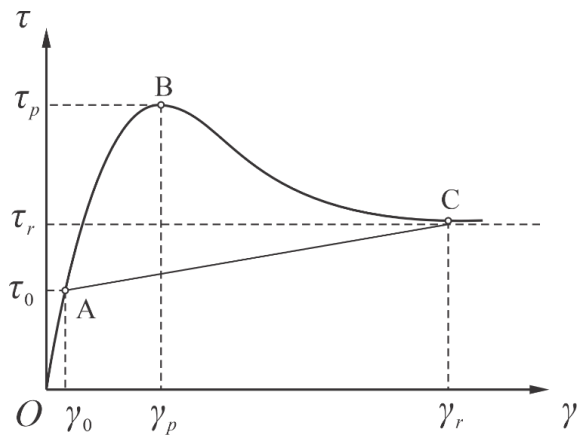

Fig.1 - Schematic diagram of shear stress-shear strain curve of lunar soil simulant

The current work will be based on the shear stress-shear strain curve OABC shown in Figure 1, which can be divided into two parts: the first part is the elastoplastic hardening stage OAC, and the second part is the shear dilatancy and softening stages ABC. Based on these two parts, corresponding constitutive equations will be proposed.

Development of the elastoplastic strain-hardening model

Based on the theory of elastoplasticity, during the process of shear deformation in the lunar

soil simulant specimen, the plastic potential function *Q*, the yield function *F*, the elastic scalar factor $d\lambda$, and the hardening modulus *H* are known. The strain increment of the lunar soil simulant under loading can be divided into two parts: elastic reversible and plastic irreversible strain increments:

$$d\varepsilon_i = d\varepsilon_i^e + d\varepsilon_i^p \quad (i = 1, 2)$$

(1)

In the equation, i =1, 2 correspond to the tangential direction and normal direction, respectively.

Furthermore, based on Hooke's Law, the relationship between the elastic deformation increment and the stress increment of the lunar soil simulant can be obtained:

$$d\sigma_i = K_{ij} d\varepsilon_j^e = K_{ij}(d\varepsilon_j - d\varepsilon_j^p)$$

(2)

where K_{ij} is the elastic stiffness matrix.

According to the plastic flow rule, the plastic strain increment of the lunar soil simulant can be obtained:

$$d\varepsilon_i^p = d\lambda \frac{\partial Q}{\partial \sigma_i} = \frac{1}{H}\left(\frac{\partial F}{\partial \sigma_j} d\sigma_j\right)\frac{\partial Q}{\partial \sigma_i} \tag{3}$$

Substituting (3) into (2) and multiplying both sides by $\frac{\partial F}{\partial \sigma_i}$, we obtain:

$$\frac{\partial F}{\partial \sigma_i} d\sigma_i = \frac{\frac{\partial F}{\partial \sigma_i} K_{ij} d\varepsilon_j}{1 + \frac{1}{H}\frac{\partial F}{\partial \sigma_k} K_{kl} \frac{\partial Q}{\partial \sigma_l}} \tag{4}$$

By substituting (4) into (3), the plastic strain increment can be obtained:

$$d\varepsilon_i^p = \frac{\frac{\partial F}{\partial \sigma_r} K_{rs} d\varepsilon_s \frac{\partial Q}{\partial \sigma_i}}{H + \frac{\partial F}{\partial \sigma_k} K_{kl} \frac{\partial F}{\partial \sigma_l}} \tag{5}$$

Finally, by substituting (5) into (2), the relationship between the stress increment and the strain increment can be obtained.

$$d\sigma_i = \left(K_{ij} - \frac{K_{ir}\frac{\partial Q}{\partial \sigma_r}\frac{\partial F}{\partial \sigma_s} K_{sj}}{H + \frac{\partial F}{\partial \sigma_r} K_{rs} \frac{\partial Q}{\partial \sigma_s}}\right) d\varepsilon_j = K_{ij}^{ep} d\varepsilon_j$$

(6)

Where K_{ij}^{ep} is the elastoplastic stiffness matrix. Equation (6) represents the general form of the elastoplastic constitutive equation under non-associated flow rule. The hardening modulus *H* has

different expressions for isotropic hardening, kinematic hardening, and other cases. Since the tangential stress and tangential displacement of the lunar soil simulant eventually approach a stable curve (residual stress tends to stabilize) under shear loading conditions, the strain-hardening model is used here to describe this deformation mechanism.

Under the kinematic hardening model assumption, the initial yield function is assumed to be the Mohr-Coulomb yield function [20-24]:

$$F(\sigma_i) = \tau - \sigma_n \tan(\varphi_b) - c \tag{7}$$

In the equation, c represents the cohesive strength of the cementation of the lunar soil simulant.
The subsequent yield surface of the kinematic hardening model in stress space is obtained by rigid translation. Therefore, the subsequent yield function can be assumed as:

$$f(\sigma_i, \varepsilon_i^p, k) = F(\sigma_i - \alpha_i) - k \tag{8}$$

In the equation, ε_i^p is the plastic strain, α_i is the back stress, which is a function of the coordinates of the loading surface center and the plastic strain. *k* is the hardening parameter.

In plastic deformation, the yield function satisfies the consistency condition:

$$df = \frac{\partial F}{\partial \sigma_i} d\sigma_i - \frac{\partial F}{\partial \sigma_i} \frac{\partial \alpha_i}{\partial \varepsilon_j^p} d\varepsilon_j^p = 0 \tag{9}$$

Based on the associative flow rule, by substituting (3) into (9), we obtain:

$$H = \frac{\partial F}{\partial \sigma_i} \frac{\partial \alpha_i}{\partial \varepsilon_j^p} \frac{\partial F}{\partial \sigma_j} \tag{10}$$

Assuming $d\alpha_i$ and $d\varepsilon_i^p$ are linearly relation, that is, following the Prager hardening rule:

$$d\alpha_i = c d\varepsilon_i^p \tag{11}$$

where *c* represents the work hardening function, which is expressed as follows:

$$c = \frac{\tau_r - \tau_0}{\gamma_r - \gamma_0} \frac{1}{\frac{\partial F}{\partial \sigma_i} \frac{\partial F}{\partial \sigma_j}} \tag{12}$$

In equation (12), τ_r represents the residual shear stress, and γ_r represents the residual shear strain.
Substituting (11) into (10), we obtain:

$$H = c \frac{\partial F}{\partial \sigma_i} \frac{\partial F}{\partial \sigma_j} \tag{13}$$

By combining (6), (12), and (13), the incremental stress-strain constitutive equation for the kinematic hardening model can be respectively obtained as follows:

$$d\tau = (K_{ss} - \frac{K_{ss} K_{ss}}{A}) d\gamma - \frac{\mu K_{nn} K_{ss}}{A} d\varepsilon, \quad d\sigma = -\frac{\mu K_{nn} K_{ss}}{A} d\gamma + (K_{nn} - \frac{\mu K_{nn} K_{nn} \mu}{A}) d\varepsilon \tag{14}$$

In the equation (14), $A = \mu K_{nn} \mu + K_{ss} + \frac{\tau_r - \tau_0}{\gamma_r - \gamma_0}$.

Usually, the normal stress is a constant value, and its stress increment $d\sigma = 0$. Therefore, we have:

$$d\tau = \frac{\tau_r - \tau_0}{\gamma_r - \gamma_0 + \frac{\tau_r - \tau_0}{K_{ss}}} d\gamma \tag{15}$$

Equation (15) reflects the deformation characteristics of the lunar soil simulant under shear loading. In Figure 1, the strengthening segment passes through the initial yield point A (γ_0, τ_0) and the residual strength point C (γ_r, τ_r). Thus, from equation (15), the following is obtained:

$$\tau_f = \frac{\tau_r - \tau_0}{\gamma_r - \gamma_0 + \frac{\gamma_r - \gamma_0}{K_{ss}}} (\gamma - \gamma_0) + \tau_0 \tag{16}$$

Since K_{ss} is much larger than $\tau_r - \tau_0$, the $\frac{\tau_r - \tau_0}{K_{ss}}$ in equation (16) can be neglected, that is:

$$\tau_f = \frac{\tau_r - \tau_0}{\gamma_r - \gamma_0} (\gamma - \gamma_0) + \tau_0 \tag{17}$$

In the initial elastic segment OA of Figure 1, $\tau_{OA} = K_{si} \gamma$ (18)

In the equation (18), K_{si} is the initial shear stiffness.

Development of the shear dilatancy and softening model

Due to the cementitious particles and their irregular geometrical shape in the real lunar soil [1], as shown in Figure 2, during the shear process, the cementitious particles in the lunar soil and their micro-asperities interlock with each other, leading to an enhanced stress concentration effect and the formation of shear planes that are prone to being sheared. This shearing action causes damage to the particles of lunar soil simulant. When the shearing of micro-asperities accumulates to a certain extent, the intact regions undergo instantaneous failure, resulting in a sudden drop in stress, known as the softening phenomenon. In most cases, as the particles undergo shear deformation, the shear stress first undergoes an increasing stage and then experiences a significant decrease, exhibiting both hardening and softening phenomena.

The shear dilatancy of lunar soil simulant primarily arises from the irregular surface morphology of its structural planes. It reflects the complex relationship between the tangential and normal deformations of the lunar soil simulant, and affects the variation of stress during tangential deformation. When subjected to shear, the interlocking action between micro-asperities inside the cementitious

particles significantly increases stress concentration. The appearance of sheared contact surfaces reduces the shear dilatancy angle. Therefore, the lunar soil simulant exhibits both shear dilatancy and softening during deformation. As deformation and damage of the cementitious material accumulate, it causes macroscopic structural failure of the cementitious material and significantly reduces stress, which is known as softening phenomenon. During the loading process, the shear stress of the lunar soil simulant first rises and then experiences a sharp drop, corresponding to the phenomena of shear dilatancy and softening, respectively.

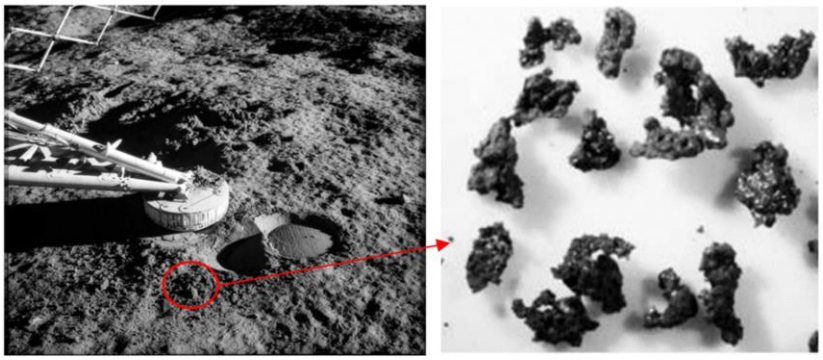

Fig.2 – Lunar soil and cementitious particles in the lunar soil [1].

The shear dilatancy and softening phenomena proposed in the present work are mechanical characteristic that lunar soil simulant during shear deformation process, and in our previous numerical simulations also focused on describing this deformation characteristic [21-23]. Based on this characteristic, we can assume an initial shear stress that represents the occurrence of both shear dilatancy and softening in the vertical direction when the lunar soil simulant undergoes shear deformation, with the softening phenomenon resulting from the failure of the cementitious materials. By isolating the strengthening mechanism, this part is considered the first component of the constitutive model for the lunar soil simulant. Combining the aforementioned the shear dilatancy-softening rules and previous studies [24-28], the following formula can be proposed to represent the shear dilatancy and softening characteristics of lunar soil simulant:

$$\tau(\gamma)=\frac{a(\gamma-\gamma_0)}{1+c(\gamma-\gamma_0)^{k_1}} \tag{19}$$

In the formula, *a*, *c* are parameters; k_1 is an amplitude parameter that can adjust the magnitude of the post-peak softening for different lunar soil simulants; γ_0 represents the initial yielding strain. The advantages of this formula mainly include three aspects: it has only one extremum within the specified region; the slope of the function tangent line at the peak is 0; as the strain approaches infinity, the function approaches 0. The function should also satisfy passing through point $P(\gamma_p, \tau p-\tau f(\gamma_p))$, which can be simplified as passing through point (γ_p, τ_0). $\tau f(\gamma_p)$ represents the shear strength of the follow-up strengthening model at γ_p. From this, we can obtain:

$$a = \frac{k_1(\tau_p - \tau_0)}{(k_1 - 1)(\gamma_p - \gamma_0)}, \quad c = \frac{1}{(k_1 - 1)(\gamma_p - \gamma_0)^{k_1}} \tag{20}$$

Substituting (20) into (19), we obtain:

$$\tau(\gamma) = \frac{k_1(\tau_p - \tau_0)(\frac{\gamma - \gamma_0}{\gamma_p - \gamma_0})}{k_1 - 1 + (\frac{\gamma - \gamma_0}{\gamma_p - \gamma_0})^{k_1}} \tag{21}$$

Furthermore, considering that the magnitude of shear stress in lunar soil simulant is also related to the normal stress, the compressive strength of cementitious material, and other factors, by modifying the above formula based on these two factors, a more comprehensive formula for the initial shear stress t_j can be obtained:

$$\tau_j = \frac{k_1(\tau_p - \tau_0)(\frac{\gamma - \gamma_0}{\gamma_p - \gamma_0})(1 - \frac{\sigma_n}{\sigma_t})}{k_1 - 1 + (\frac{\gamma - \gamma_0}{\gamma_p - \gamma_0})^{k_1}} \tag{22}$$

In the above formula, τ_{p} represents the peak shear stress, τ_0 represents the initial yield stress, σ_{t} represents the uniaxial compressive strength, which is approximately the compressive strength of the entire lunar soil simulant, and σ_{n} represents the normal stress on the lunar soil simulant during loading.

Establishment of the constitutive model and determination of model parameters

Based on the above analysis, the constitutive relationship for the lunar soil simulant in this study can be expressed as follows:

$$\tau = \begin{cases} \tau_{OA} & (\gamma \in (0 \quad \gamma_0)) \\ \tau_f + \tau_j & (\gamma \in (\gamma_0 \quad \gamma_r)) \end{cases} \tag{23}$$

After determining the constitutive model, the next step is to further determine the parameters in the constitutive model. The meanings and determination methods of the parameters are as follows:

(1) Peak shear strain ε_{p}, residual shear strain ε_{r}, basic friction angle φ_{b}, and residual friction angle φ_{r} can all be obtained from the monotonic shear loading tests.

(2) Peak shear stress τ_{p}: The peak shear stress of the lunar soil simulant can be obtained using the empirical equation proposed by Barton and Choubey [29], which is given by:

$$\tau_p = \sigma_n \tan\left[C \log\left(\frac{\sigma_{CS}}{\sigma_n}\right) + \varphi_b\right] \tag{24}$$

where *C* represents the strength of the cohesive force between the bonding particles, σ_{CS} represents the compressive strength of the cementitious material in lunar soil simulant.

(3) The residual shear stress τ_r is determined by Coulomb's criterion:

$$\tau_r = \sigma_n \tan \varphi_r \tag{25}$$

(4) Initial normal stiffness K_{ni}: Obtained from the normal monotonic loading test, its value is the initial slope of the normal stress-normal strain curve, as shown in Figure 3(a). The initial shear stiffness K_{si} is obtained from direct shear cyclic tests, and its value is related to the normal stress. Based on the shear stress-shear strain curve, the slope of the unloading portion after exceeding the initial yield point represents the initial shear stiffness, as shown in Figure 3(b). When it is challenging to determine through experiments, Bandis et al. [30] proposed an empirical formula for the initial shear stiffness K_{si} based on a large number of tests:

$$K_{si} = K_j(\sigma_n)^{n_j} \tag{26}$$

Where K_j is the stiffness coefficient, σ_n is the normal stress, and n_j is the initial stiffness exponent.

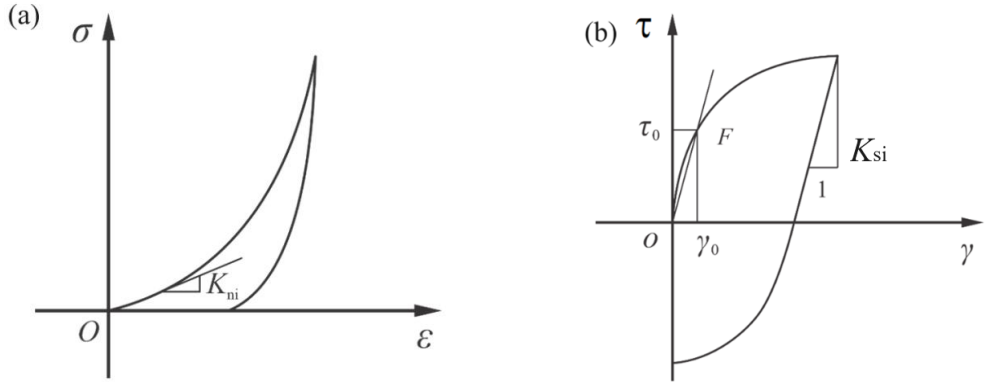

Fig.3 - Diagrams of (a) normal stress-normal strain curve and (b) shear stress-shear strain curve.

(5) The initial yield stress τ_o and the initial yield strain γ_0: Based on the method shown in Figure 3(b) for determining the initial shear stiffness, draw a line with a slope of K_{si} from the origin *o* which intersects the shear stress-shear strain curve at point *F*. This point *F* represents the initial yield point. When it is difficult to determine the initial yield point, according to Goodman's experimental tests [31], the initial yield point in the elastic phase is generally located at around 70% to 90% of the peak shear strength. Considering the yield characteristics of lunar soil simulant, we can estimate the initial yield point by taking 70% of the peak shear strength [20].

(6) The amplitude parameter k_1 reflects the shear dilatancy and softening characteristics of the material, which is related to the magnitude of the normal stress, and the adhesive force between cementing particles. Typically, for relatively rough particles of lunar soil simulant, the value of k_1 is taken as 4, which can be obtained from the first cycle of the shear loading test curve.

DIRECT SHEAR RESULTS AND VALIDATION OF THE MODEL

Based on the above derived constitutive model and the determined parameters, direct shear test and model validation will be conducted using this constitutive model. The parameters involved in the constitutive model are listed in Table 1.

Tab.1 - Key parameters of the model

γ_p (%)	φ_b /(°)	σ_{cs}/kPa	σ_τ/kPa	k_1
2.65	40	1000	700	4
γ_f (%)	φ_r /(°)	*C*/ kPa	γ_0 (%)	
8	30	4	1.35	

Figure 4(a) shows the shear stress-shear strain curves obtained by this theoretical constitutive model under different low normal stresses. From Figure 4(a), it can be observed that the shear stress first reaches its peak value, then rapidly decreases until it enters a relatively stable residual deformation stage, reflecting the shear dilatancy and softening characteristics of the lunar soil simulant. The peak shear stress and residual shear stress increase with the increase of the normal stress. Based on the shear stress-shear strain curves in Figure 4(a), the shear strength τ_p can be obtain under different normal stresses, as shown in Figure 4(b). By comparing with previous experimental results and theoretical results, there is a good agreement with experimental tests of Zhang et al. [18], indicating that the model not only captures the shear dilatancy and softening characteristics of the lunar soil simulant but also successfully simulates the direct shear test. Moreover, the values of cohesive force *C* and basic internal friction angle φ_b in the theoretical model are 4 kPa and 40^0, respectively. When the porosity e=1, the values *C* and φ_b in the experiment tests are 4 and 40.35^0 respectively. These two parameters used in constitutive model are almost consistent with those obtained in the experiment, and all belong to the range of variation of real lunar soil [1, 32], which further validates the rationality of the proposed model in the present work.

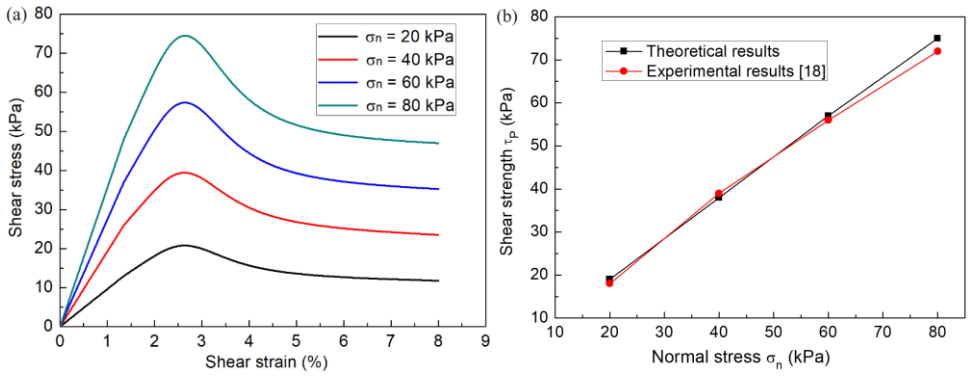

Fig.4 - Direct shear results at different normal stresses: (a) shear stress-shear strain curves, and (b) Comparison of shear strength obtained from experiments and theoretical model.

INFLUENCES ANALYSIS OF MODEL PARAMETERS

Since k_1 is an amplitude parameter that can adjust the magnitude of the post-peak softening of lunar soil simulant, the change in k_1 value will affect the residual shear stress after softening. Figure 5 shows the shear stress-shear strain curves at various amplitude parameters. It is found that the change in k_1 hardly affects the magnitude of peak shear stress, but it has a significant impact on the softening behavior and the magnitude of residual shear stress. When k_1=2 and 3, after the sample reaches their peak shear stress, although there is softening, the softening phenomenon is not obvious and there is no relatively stable residual deformation stage. The degree of softening increases as the value of k_1 increases, when k_1=4, there is a noticeable softening phenomenon, and relatively stable residual shear stress is observed, which is suitable for the shear deformation characteristics of lunar soil simulant. Therefore, k_1 = 4 is used in the present study.

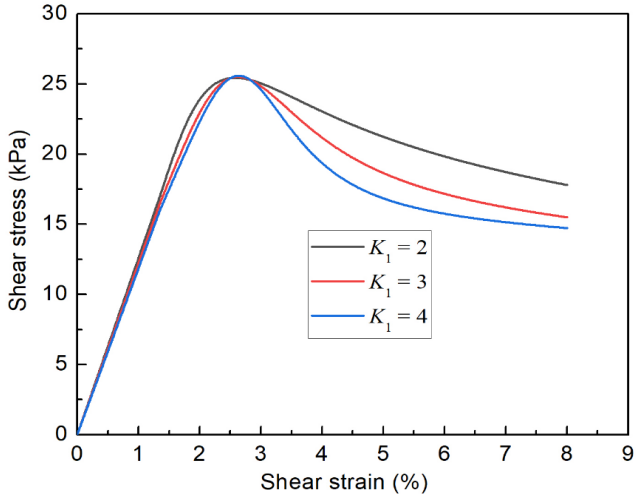

Fig.5 - Shear stress-shear strain curves at various amplitude parameters (K_1)

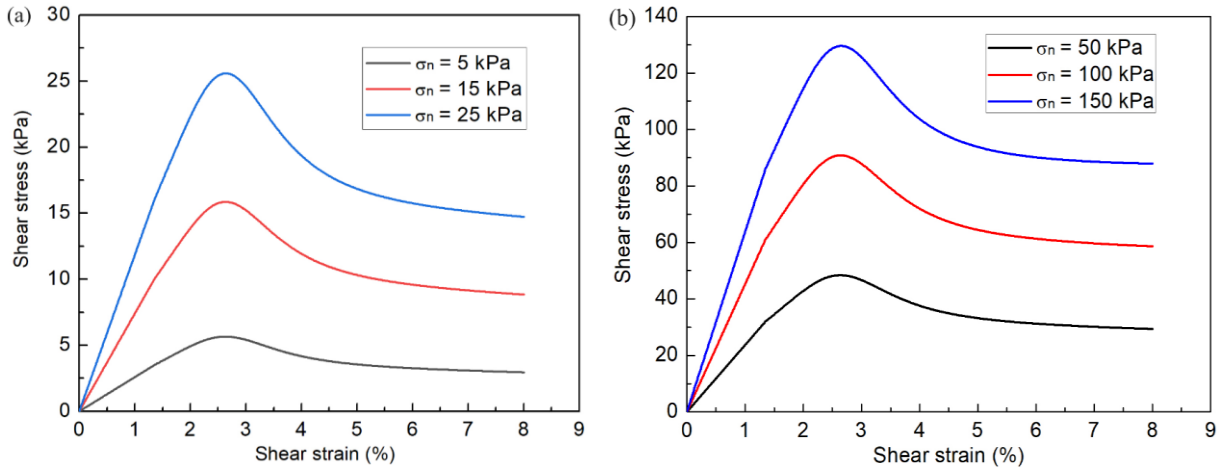

Fig.6 - Shear stress-shear strain curves of lunar soil simulant specimens under different normal stress conditions: (a) low normal stress, and (b) conventional normal stress.

Figure 6(a) and (b) show the shear stress-shear strain curves of the lunar soil simulant samples under low normal stress and conventional normal stress conditions, respectively. From Figure 6, it can be observed that the shear stress first increases to its maximum value and then softens, leading to a rapid decrease in shear stress and entering the residual shear stress stage. It indicates that lunar soil simulant exhibits significant shear dilatancy and softening characteristics both at low and conventional normal stress conditions. Moreover, at low normal stress, as the normal stress increases, the peak shear stress and residual stress increase. Similarly, at conventional normal stress, with an increase in the normal stress, the peak shear stress and residual stress also increase.

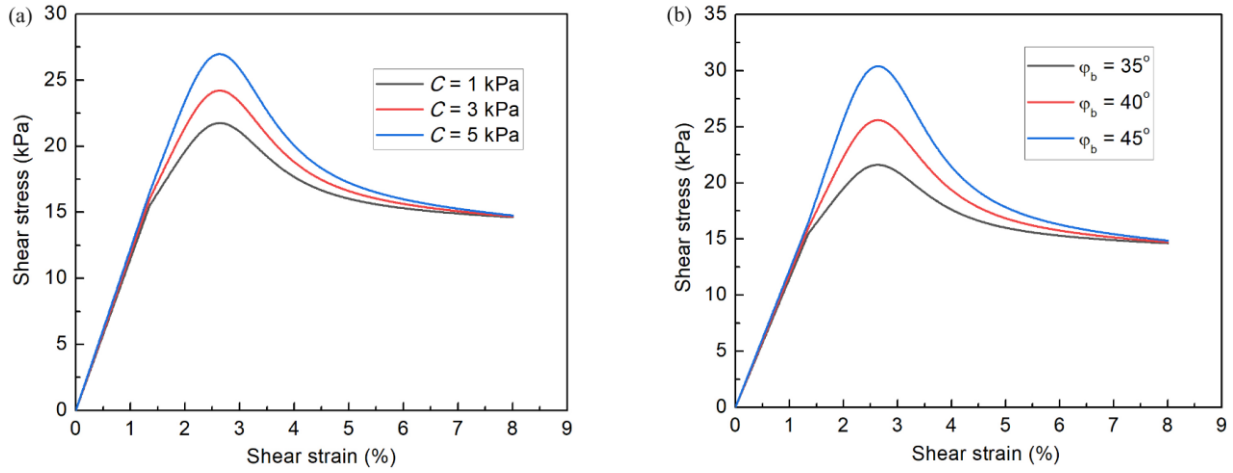

(a) *(b)*

Fig.7 - Influences of simulation parameters on the stress-shear strain curves of lunar soil simulant specimens.

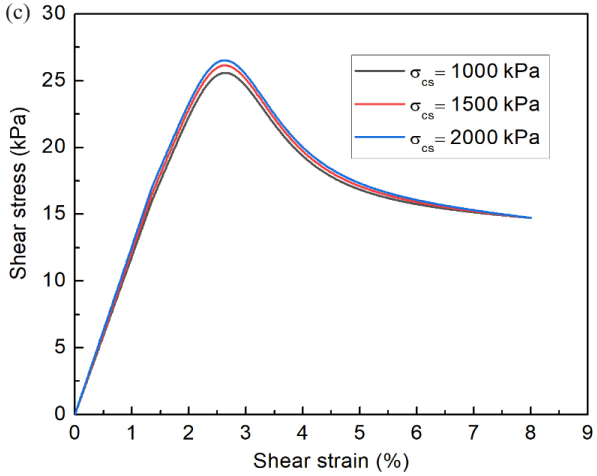

Fig.7 - Influences of simulation parameters on the stress-shear strain curves of lunar soil simulant specimens. (a) different particle cohesions, (b) different internal friction angles, and (c) different compressive strengths of cementitious particles.

To further reflect the influences of model parameters on the stress-strain curves and the shear

dilatancy and softening characteristics of lunar soil simulant specimens, Figure 7 presents the stress-shear strain curves under different values of particle cohesion, particle internal friction angle, and compressive strength of the cementitious material in lunar soil simulant. From Figure 7, it can be observed that regardless of how the model parameters are changed, the overall curve patterns remain unchanged, namely, the shear stress first increases to reach the peak stress, followed by softening and eventually reaching a stable residual stress stage. This trend also reflects the pronounced shear dilatancy and softening characteristics of the lunar soil simulant. In Figure 7(a), as the particle cohesion increases, the peak stress increases, and the residual stress after softening also increases. Finally, with increasing shear strain, the residual stress tends to stabilize. Similarly, for different variations in the particle internal friction angle (Figure 7(b)) and the compressive strength of the cementitious material in lunar soil simulant (Figure 7(c)), a similar trend is observed, with higher values resulting in increased peak stress and residual stress. Compared to the internal friction angle and particle cohesion, the influence of change in compressive strength of cementitious material on shear strength is very small.

CONCLUSIONS

(1) In this study, an elastoplastic constitutive model is developed to effectively captures the shear dilatancy and softening characteristics of lunar soil simulant. The model uses the kinematic hardening equations based on the classical elastoplastic theory to describe this strengthening phenomenon, and reflects the softening characteristics by introducing the concept of initial shear stress, which effectively compensates for the shortcomings of existing constitutive models in the literatures.

(2) The model only requires fewer parameters to be determined, and all of which can be obtained through simple initial loading curves from direct shear tests.

(3) The model allows for the analysis of the influences of parameters such as normal stress, particle cohesion, internal friction angle, amplitude parameter, and compressive strengths of cementitious material on the peak strength, residual strength, shear dilatancy and softening characteristics of lunar soil simulant. These results will provide some references for a deeper understanding of the mechanical behavior of lunar soil and the mechanical analysis involved in lunar soil mining and future lunar base construction.

The model proposed in this study mainly focuses on dry lunar soil simulant. For the icy lunar soil in the south pole region of the moon, its deformation characteristics are different due to the special properties such as water content and ice soil cement, and the corresponding constitutive model also needs further research.

ACKNOWLEDGEMENTS

The authors acknowledge the financial support provided by the National Natural Science Foundation of China (Grant No. 52009097), Education Department of Hubei Province of China (Grant No. B2021080), and Natural Science Foundation of Wuhan Institute of Technology (Grant No. K2021035).

REFERENCES

[1] Carrier W D, Olhoeft G R, Mendell W., 1991. Physical properties of the lunar surface: Lunar Source Book, (Cambridge University Press) 475–594.
[2] Sun X M, Zhang R, Li X J, Zou M, Wang C, ChenL., 2022. JLU-H: A novel lunar highland regolith simulant for use in large-scale engineering experiments. Planetary and Space Science, vol. 221: 105562. doi:10.1016/j.pss.2022.105562.
[3] Mills J N, Katzarova M, Wagner N J., 2022. Comparison of lunar and Martian regolith simulant-based geopolymer cements formed by alkali-activation for in-situ resource utilization. Advances in Space Research, vol. 69: 761–777. doi:10.1016/j.asr.2021.10.045.
[4] Dewoolkar M M, Edwards M, Walsh D., 2018. Shear strength and stiffness characterization of lunar simulant GRC-3. Journal of Aerospace Engineering, vol. 31: 04018024. doi:10.1061/(ASCE)AS.1943-5525.0000848.
[5] Yu H, Hu Z., 2013. Mechanical characteristics of a lunar regolith simulant at low confining pressure. Environmental Earth Sciences, vol. 71: 3697–3703. doi:10.1007/s12665-013-2763-7.
[6] Hasan A, Alshibli K A., 2010. Discrete element modeling of strength properties of Johnson Space Center (JSC-1 A) lunar regolith simulant. Journal of Aerospace Engineering, vol. 23: 157–165. doi:10.1061/(ASCE)AS.1943-5525.0000020.
[7] Hicher P Y, Chang C S., 2008. A constitutive model for lunar soil. 11th Biennial ASCE Aerospace Division International Conference on Engineering, Science, Construction, and Operations in Challenging Environments. doi:10.1061/40988(323)16.
[8] Richard A S., 2006. Cam cap models for lunar soil: a first look. Tenth Biennial ASCE Aerospace Division International Conference on Engineering, Construction, and Operations in Challenging Environments, Houston, Texas. doi:10.1061/40830(188)37.
[9] Zou M, Fan S C, Shi R Y, Yang Y J, Li J Q., 2015. Effect of gravity on the mechanical properties of lunar regolith tested using a low gravity simulation device. Journal of Terramechanics, vol. 60: 11–22. doi:10.1016/j.jterra.2015.04.003.
[10] Hou X Y, Ding T X, Chen T, Liu Y M, Li M, Deng Z Q., 2019. Constitutive properties of irregularly shaped lunar soil simulant particles. Powder Technology, vol. 346: 137–149. doi:10.1016/j.powtec.2019.02.012.
[11] Jiang M J, Shen Z F, Thornton C., 2013. Microscopic contant model of lunar regolith for high efficiency discrete element analysises. Computers and Geotechnics, vol. 54: 104–116. doi:10.1016/j.compgeo.2013.07.006.
[12] Liu T X, Liang L, Zhao Y, Cao D Q., 2020. An alterable constitutive law of high-accuracy DEM model of lunar soil. Advances in Space Research, vol. 66: 1286–1302. doi:10.1016/j.asr.2020.06.026.
[13] Liu T X, Liang L, Zhao Y, Cao D Q., 2020. Equivalent boundary model of lunar soil drilling simulation by DEM. Journal of Terramechanics, vol. 91: 85–95. doi:10.1016/j.jterra.2020.06.003.
[14] Schafer C M, Scherrer S, Buchwald R, Maindl T I, Speith R, Kley W., 2017. Numerical simulations of regolith sampling processes. Planetary and Space Science, vol. 141: 35-44. doi:10.1016/j.pss.2017.04.015.
[15] Liang D P, Chai H Y., 2012. Lunar soil constitutive model and finite element modeling for landing impact simulation. Spacecraft Engineering, vol. 21: 18–24. doi:10.1016/j.jrmge.2023.04.025.
[16] Mao Z R, Liu G R., 2018. A smoothed particle hydrodynamics model for electrostatic transport of charged lunar dust on the moon surface.Computational Particle Mechanics, vol. 5: 539-551. doi:10.1007/s40571-018-0189-4.
[17] Li R J, Cui Y H, Feng Y L, Wang J S, Huang W, Sui Y, Ren D P., 2023. New mechanical models to study the impact of contact, wear, and adhesion of lunar dust on space materials. International Journal of Applied Mechanics, vol. 15. doi:10.1142/S1758825123500254.
[18] Zhang Y, Chen S X, Yu F, Li J, Gao H., 2015. Experimental study of mechanical properties of lunar soil simulant CAS-1 under low stress. Chinese Journal of Rock Mechanics and Engineering, vol. 34: 174–181. doi:10.13722/j.cnki.jrme.2015.01.019.
[19] Jiang M J, Yin Z Y, Shen Z F., 2016. Shear band formation in lunar regolith by discrete element analyses. Journal of Granular Matter, vol. 18: 1–14. doi:10.1007/s10035-016-0635-z.
[20] Zou W L, Li Y L, Chen L, Zhang J F, Wang X Q., 2016. Mechanical properties of QH-E lunar soil simulant at low confining stresses. Journal of Aerospace Engineering, vol. 29: 04015036. doi:10.1061/(ASCE)AS.1943-5525.0000526.
[21] Li Y L, Zou W L, Wu W P, Chen L., 2018. Discrete element modeling of strength properties and failure modes of QH-E lunar soil simulant at low confining stresses. Stavební obzor-Civil Engineering Journal, vol. 2: 211–

226. doi:10.14311/CEJ.2018.02.0017.
[22] Li Y L, Zou W L, Wu W P, Chen L, Chu X H., 2018. Triaxial compression tests of QH-E lunar soil simulant under constant mean principal stress path using discrete element method simulations. Granular matter, vol. 20: 79. doi:10.1007/s10035-018-0855-5.
[23] Li Y L, Wu W P, Chu X H, Zou W L., 2020. Effects of stress paths on triaxial compression mechanical properties of QH-E lunar soil simulant by DEM simulation. Granular matter, vol. 22: 32. doi:10.1007/s10035-020-0999-y.
[24] Plesha M E., 1987. Constitutive models for rock discontinuities with dilatancy and surface degradation. International Journal of Numerical and Analytical Methods in Geomechanics, vol. 11: 345–362. doi:10.1002/nag.1610110404.
[25] Desai C S, Fishman K L., 1991. Plasticity-based constitutive model with associated testing for joints. International Journal of Rock Mechanics and Mining Sciences & Geomechnics Abstracts, vol. 28: 15–26. doi:10.1016/0148-9062(91)93229-Y.
[26] Wang J G, Ichikawa Y, Leung C F., 2003. A constitutive model for rock interfaces and joints. International Journal of Rock Mechanics and Mining Sciences, vol. 40: 41–53. doi:10.1016/S1365-1609(02)00113-2.
[27] Cai M, Horii H., 1992. A constitutive model of highly jointed rock masses. Mechanics of Materials, vol. 13: 217–246. doi:10.1016/0167-6636(92)90004-W.
[28] Xiao W G, Dui G S, Chen T L, Ren Q W., 2009. A study of constitutive model coupling dilatancy and degradation for jointed rock. Chinese Journal of Rock Mechanics and Engineering, vol. 28: 2535–2543. doi:10.1016/S1874-8651(10)60073-7.
[29] Barton N, Choubey V., 1977. The shear strength of rock joints in theory and practice. Rock Mechanics and Rock Engineering, vol. 10: 1–54. doi:10.1007/BF01261801.
[30] Bandis S C, Lumden A C, Barton N R., 1983. Fundamentals of rock joint deformation. International Journal of Rock Mechanics and Mining Sciences and Geomechanics Abstracts, vol. 20: 249–268. doi:10.1016/0148-9062(83)90595-8.
[31] Goodman R E., 1974. The mechanical property of joints. Proceedings of the 3rd Cong ISRM(Part A). 127–140. doi:10.1016/0148-9062(75)90743-3.
[32] Slyuta E N., 2014. Physical and mechanical properties of the lunar soil (a review). Solar System Research, vol. 48: 330-353. doi:10.1134/s0038094614050050.

CIVIL ENGINEERING JOURNAL

Article no. 4

THE CIVIL ENGINEERING JOURNAL 1-2024

GEOMONITORING OF THE OPEN-PIT MINE SLOPES DURING SUBSOIL DEVELOPMENT

Roman Shults[1], Marzhan Nurpeissova[2], Shugyla Burlibayeva[3], Aliya Umirbayeva[2] and Turar Turumbetov[3]

1. *King Fahd University of Petroleum and Minerals, Interdisciplinary Research Center for Aviation and Space Exploration, Dhahran, Academic Belt, Bld. 76, Saudi Arabia; roman.shults@kfupm.edu.sa*
2. *Satbayev University, Mining, and Metallurgical Institute named after O.A. Baikonurov, Department of Surveying and Geodesy, Almaty, Satbayev, 22a, Kazakhstan; m.nurpeissova@satbayev.university, a.umirbayevau@satbayev.university*
3. *Al-Farabi Kazakh National University, Faculty of Geography and Environmental Sciences, Department of Cartography and Geoinformatics, Almaty, Al-Farabi Ave, 71, Kazakhstan; burlibayeva.shugyla@gmail.com, turar.kz_star@mail.ru*

ABSTRACT

The concept of geomonitoring and its role in developing the mining industry as a case study of the development of copper and zinc deposits in central Kazakhstan ("East Saryoba" mine) has been considered. As a crucial element of the geomonitoring concept, the control of the open-pit mine's slope stability has been examined. Geomonitoring is being treated as a combination of geodetic monitoring data and geomechanical properties of the surrounding rocks to analyze the possible slopes' collapses. The refined approach of geomonitoring has been developed to provide appropriate reliability and accuracy. The technology is based on complex knowledge about the geological structure of the object of monitoring and applying state-of-the-art geodetic methods. Research on the geomechanical properties of the open-pit mine has been carried out. The results of these studies have been used to determine the collapse zones of the slopes of the open-pit mine. The limit values for the slopes' collapse zone and inclination angle for the prospective excavation regions in the open-pit mine have been calculated using the equilibrium state equation. Those values, namely, the size of the collapse zone and the slope's inclination angle, were used for the geodetic target setup. As a case study, the displacements of these targets were measured using robotic total stations placed on the control points over the geodetic network. For the installation of both geodetic equipment during the geomonitoring design and accomplishment, the authors developed the permanent measuring station construction, which provides fast and accurate centering. The first results showed that the problem of the geomonitoring design could be solved based on geomechanical rock properties accounting and their combination with the results of geodetic measurements.

KEYWORDS

Geomonitoring, Open-pit mine, Vertical displacements, Deformation target, Geomechanical properties, Slope stability

INTRODUCTION

The world industry of minerals mining affects both the global economy and the environment. The leading countries worldwide are conducting grave studies concerning reducing the impact of their mining activity on the environment. Among those countries by far is the Republic of Kazakhstan. The country occupies one of the prominent places in the balance of global minerals and raw materials. It is well-known that the country has a high potential for further developing mineral resources on the world market. Currently, in Kazakhstan, open pit mining technology is developing most of the mineral deposits. The deployment of robust geomonitoring systems is the solution to mitigate the unwanted impact of the mining industry on the environment. The state-of-the-art mining activity requires an essential improvement in monitoring the geomechanical processes occurring in the mining zones based on monitoring the open-pit slopes state. The question of slope stability in open-pit mines is a subject of numerous studies [1-5]. The present publications are focused on the application of equilibrium state methods. The work [6] indicates that approaches to estimate the stability of the open-pit mine slopes were developed years ago. However, the most widely used methods are still based on the equilibrium state condition. Those methods require detailed information obtained as a result of geological studies about the ground's inner structure. Furthermore, it is hardly possible to forecast the slope stability even with detailed information about the grounds' structure. Geological data alone are not capable of ensuring the precise slope movement model. This is the case when geodetic monitoring data come in handy and may complement a pure geological model [7-9]. A number of scholars have examined the application of geodetic technologies for slope monitoring using miscellaneous geodetic equipment. Among the terrestrial geodetic methods, the critical role plays total stations [10] and terrestrial laser scanners [11,12]. Among aerial surveying technologies, the primary contribution is UAVs equipped with cameras and LiDARs. Numerous studies have investigated the UAV photogrammetry application for geodetic monitoring [13-15]. Space technologies are another branch of geodetic technologies. Researchers have become increasingly interested in applying satellite and ground-based radar technologies for precision monitoring [16-26. The data collected by any mentioned methods, or their fusion are analyzed in different GIS platforms [27,28]. Besides monitoring the slopes of the open-pit mine, the problem of landslide monitoring is worth noting, which is similar to slope monitoring [29-32]. Even though the landslides are mostly natural objects, their monitoring is performed using the same LiDAR technologies, total stations, UAVs, and InSAR technology. This list is by no means exhaustive. However, it shows us the leading role of geodetic technologies in such a complicated task.

Therefore, combining geological knowledge and geodetic measurements leads to the more general concept of geomonitoring [33-35]. However, it raises the question of how to organize geodetic monitoring as a part of geomonitoring so its results are compatible with geological data. The answer is that it is necessary to find the slope stability parameters using geological data and, in what follows, control these parameters using geodetic methods. Of course, under such parameters, we mean just geometrical, as long as only these values are the subject of geodetic measurements. The stability factor characterizes the slope stability. The value of this factor shows the relative surplus of the rock mass strength compared to the shear stress [36-38]. Scientists account for the adjacent rock mass's geomechanical properties and hydrogeological conditions for the stability factor calculation. To date, no study has explicitly looked at the problem of geomonitoring using the key geometrical characteristics, namely, slope inclination angle and the size of the collapse zone. This study addresses the geomonitoring design issue and its part of geodetic monitoring. Given the centrality of this issue, as the first step, let us consider the general concept of geomonitoring and the features of the study area.

This paper is organized into five subsections. Section Material and Methods provides an overview of geomonitoring, a brief description of the study area, and a basic theoretical framework for open-pit

mine geomonitoring design and its practical application. The results section deals with analyzing the first onsite application of the developed geomonitoring concept and its discussion. The last subsection outlines the conclusions.

MATERIAL AND METHODS

General geomonitoring approach and study area

The traditional concept of geomonitoring boils down to the following steps: design, observations, simulation, and prediction [39-41]. The contemporary geomonitoring concept is presented below (Figure 1).

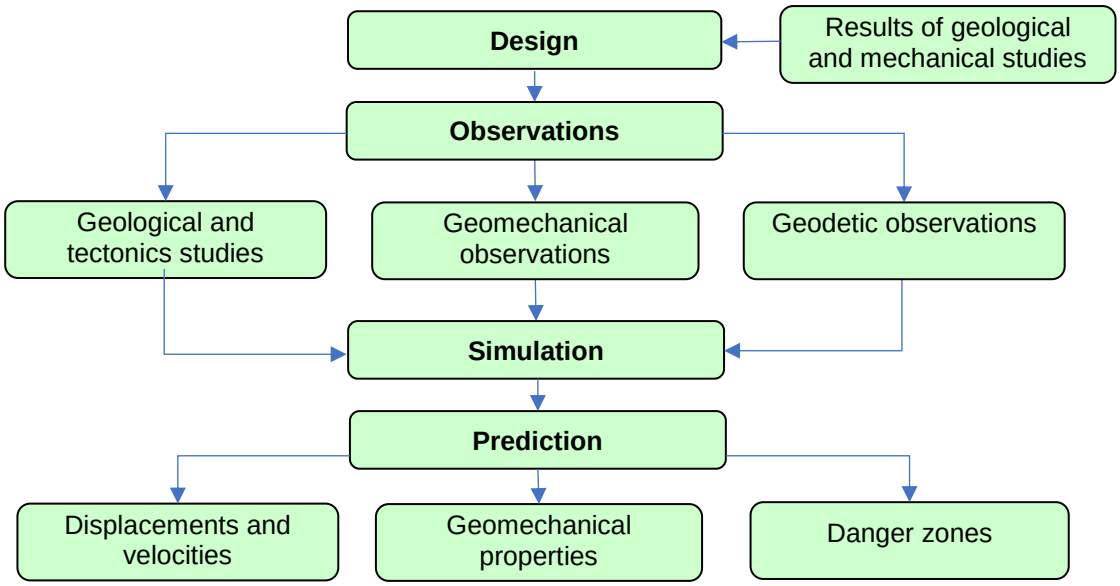

Fig. 1 – Scheme of the geomonitoring concept

Modern geomonitoring is an integrated process that uses different sensors for the observations. The results of these observations feed to the core of the monitoring system, the simulation block. The state-of-the-art concept of geomonitoring on the open-pit mine territories comprises three primary data sources. Geological, mechanical, and geodetic studies yield these data. For the case of open-pit mine geomonitoring, the primary goal is to determine the slopes' stability, which is described by spatial displacements of deformation targets. However, at the design step, those data are not being used. The crucial parameter for reliable geomonitoring is the width of the possible collapse zone B_0 (see Figure 2).

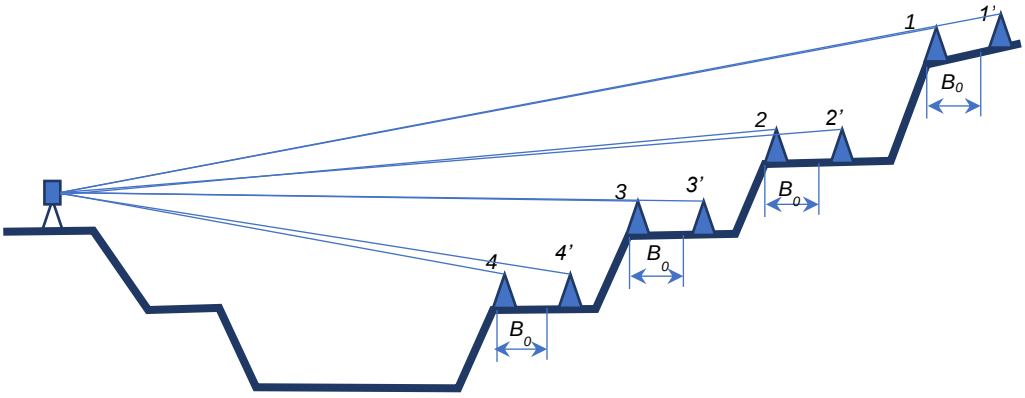

Fig. 2 – Station profile line and surveillance equipment

At each step of an open-pit mine, two targets must be placed—the first at the step rim and the second out of the possible collapse zone. Owing to the value B_0, the surveyor can correctly set up the monitoring targets. To calculate the value B_0 for the geomonitoring at the design stage, one needs to know the following ground properties: adhesion by crack, angle of friction, hardness of the rock, and density. These characteristics will be examined as a case study of the "East Saryoba" mine, located in Central Kazakhstan (Figure 3).

Fig. 3 – Study area, "East Saryoba" mine

The "East Saryoba" orefield is considered a large development mine. Since its discovery, 119 ore bodies have been explored. The largest deposits are in the northeast and have a length of up to 3200 m and a thickness of up to 17 m (Figure 4).

The output of the geomechanical properties research will be presented in the following subsection. These results have been used to determine the slopes' collapse zones and limit values for the slopes' inclination angle for the prospective excavation zones in the open-pit mine. Those values will be used for the emplacement of the deformation targets.

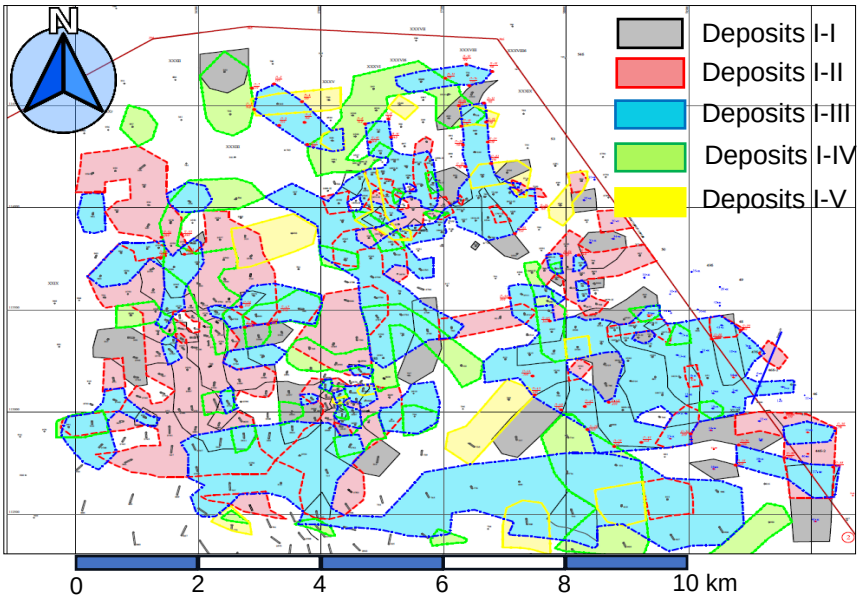

Fig. 4 – The combined contour of ore deposits in the depth range +340 m to 0 m "East Saryoba"

Geomechanical studies

Several geological studies have been conducted for the "East Saryoba" deposit. The present study has employed the results of geological surveys analyzed in the laboratory and field testing. Satbayev University conducted different research and obtained indicators of rock strength properties. Table 1 shows the physical and mechanical properties of the deposit rocks based on the laboratory test results.

Tab. 1 - Geomechanical properties of rocks in the sample data of Satbayev University for 2002-2008

Sampling depth, m	Name of the rock	Uniaxial compression strength σ_{com}, MPa	Uniaxial Strength σ_p, МПа	Density γ, 10^3 kg/m^3	Adhesion in block *k*, MPa	Angle of friction, degrees	Hardness of rock, *f*
50.1-51.8	Cement rock	110	13.0	2.66	25	32	8.0
83.5-84.0		125	14.0	2.67	28	32	8.3
112.0-113.0		126	14.3	2.68	32	31	8.6
152.6-153.0		139	14.5	2.71	34	31	9.2
170.0-170.8		140	14.8	2.72	34	29	9.5
218.1-218.6		140	14.8	2.73	35	31	9.6
53.6-54.0	Greenstone	138	16.0	2.62	36	30	7.6
115.0-115.6		160	16.8	2.65	42	30	8.2
155.0-156.0		170	16.0	2.67	46	30	8.8
200.0-201.5		171	16.2	2.69	48	30	9.0

The study of rock geomechanical properties was repeated in 2018. The results are presented in Table 2.

Tab. 2.- Geomechanical properties of rocks in the sample data of Satbayev University for 2018

Sampling depth, m	Name of the rock	Uniaxial compression strength σ_{com}, MPa	Uniaxial Strength σ_p, МПа	Density γ, 10^3 kg/m^3	Adhesion in block *k*, MPa	Angle of friction, degrees	Hardness of rock, *f*
260	Cement rock	170.1	16.5	2.71	37	28	8.2
265		173.1	17.2	2.72	49	30	8.8
545		170.0	16.0	2.73	45	30	9.0
545		172.0	16.9	2.71	48	35	8.2
505		170.0	16.2	2.72	48	30	8.8
505		170.0	16.8	2.73	50	38	9.5

Using data from Tables 1 and 2, we obtained the analytical dependencies that describe the relationship between the slopes' parameters and the rock properties (Figure 5 and Table 4).

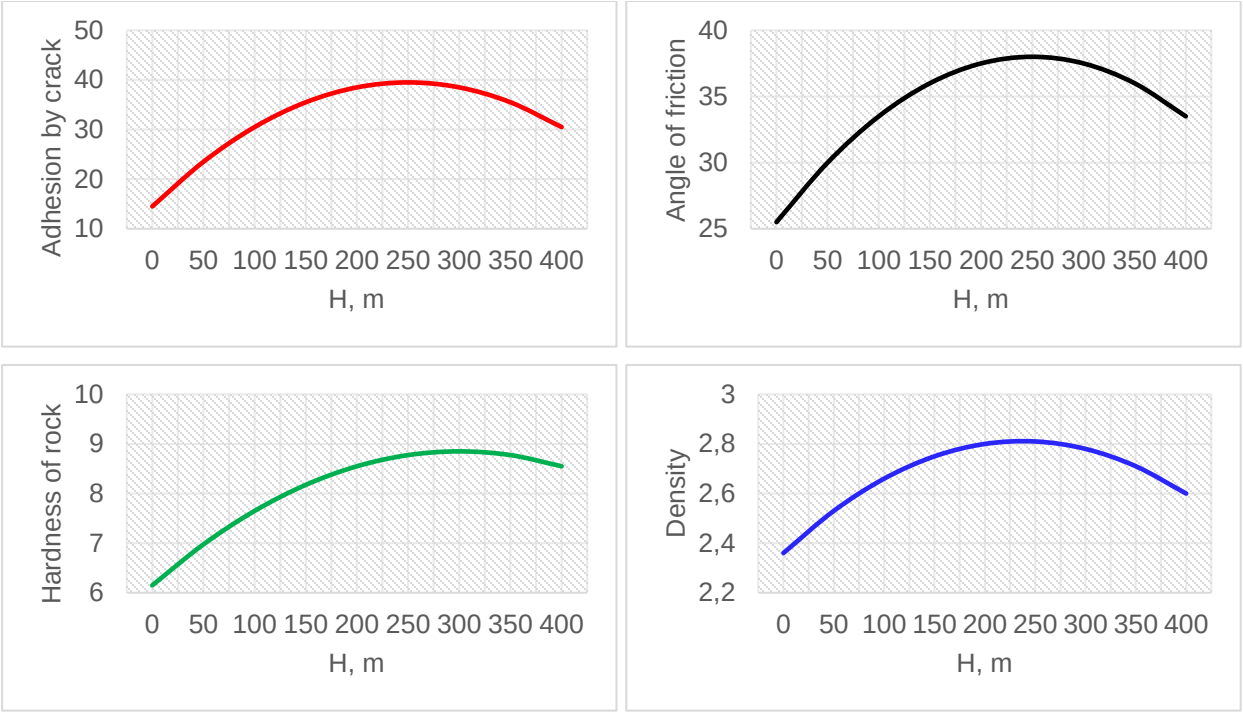

Fig. 5 – Analytical dependencies for rock geomechanical properties at the "East Saryoba" mine.

The analysis shows that rocks' strength properties change significantly with the depth of their occurrence.

The next step is the calculation of the slopes' stability. Having this parameter, one may calculate the possible collapse zone B_0 and critical slope inclination δ, the parameters that are crucial for geomonitoring. The equilibrium condition has been used to accomplish this task:

$$M_y = Rtg\varphi_S \sum_{i=1}^{i=k} P_i cos\theta_i + RC_S \sum_{i=1}^{i=k} L_i, \quad (1)$$

where R – radius of the cylindrical sliding surface; $P_i = h_i b_i \gamma_S$ (h_i – block's height; b_i – block's width, γ_S – simulated density); θ_i – inclination angle of the sliding surface; φ_S – a simulated value of the inner

friction angle; C_S – a simulated value of the adhesion; L_i – length of the sliding surface. The meaning of these values can be clarified in Figure 6.

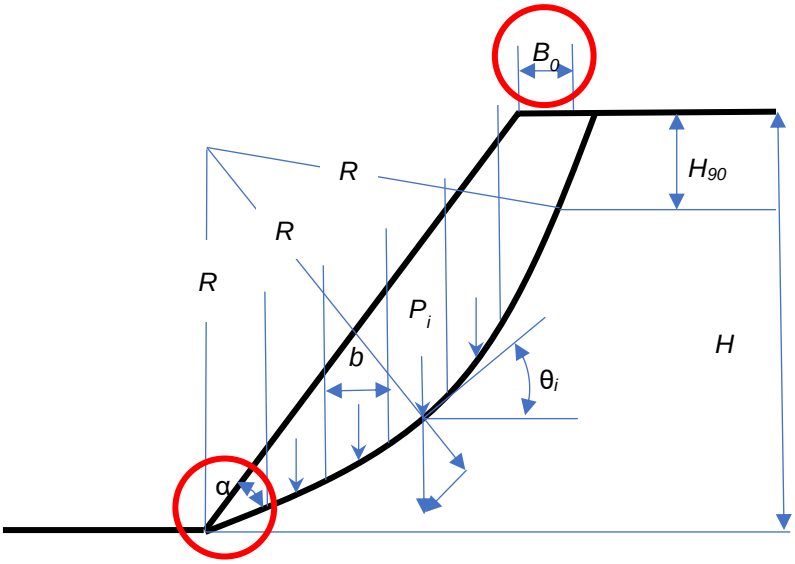

Fig. 6 – Diagram of slope stability calculation

The two indispensable parameters for geomonitoring have been calculated. The width of the possible collapse zone equals:

$$B_0 = {2H\left[1 - ctg\alpha tg\left((\alpha + \varphi_S)/2\right)\right] - 2H_{90}}\Big/{ctg(45° - \varphi_S/2) + tg\left((\alpha + \varphi_S)/2\right)}, \quad (2)$$

the value H_{90} can be calculated as:

$$H_{90} = 2C_S ctg(\alpha - \varphi_S/2)/\gamma_S. \quad (3)$$

The values B_0 for each slope were used for target emplacement along the east side of the W-E profile (Figure 7). The vertical displacements for the targets along this profile were determined and will be analyzed in the results section.

The second parameter—the allowable slope's inclination angle—has been found through simulation. The most suitable method for fractured rocks is the one that simulates stable slope parameters, considering rocks' sliding surface and strength properties. The simulation was carried out for each block of pit mine cross-section W-E (Figure 7). The results are given in Table 5.

Along with calculating the allowable slope's inclination angle, pit slopes were partitioned into zones accounting for stability factors. The complex analysis of data in Table 5 and the stability factor showed that the eastern and western sides of the mine have the slope's stability at angles of 65-70^0. In fact, the actual slope's angles do not exceed 50°. Therefore, from the geomechanical point of view, the slopes are treated as stable.

Fig. 7 – Orientation of the profile W-E on the "East Saryoba" mine

Tab. 5 - Allowable slope's inclination angles for cross-section W-E.

Relative height H/H_{90}	Angle of friction, deg			
	25	30	35	40
1	90.0	90.0	90.0	90.0
1.5	84.0	84.5	85.0	85.5
2	77.3	78.1	79.6	80.6
2.5	71.0	72.5	74.4	76.0
3	65.2	68.0	70.2	72.8
3.5	60.2	64.0	66.5	69.9
4	56.0	60.1	63.6	67.5
4.5	52.5	56.9	60.9	65.2

The cross-section of the pit mine and the targets is given in Figure 8.

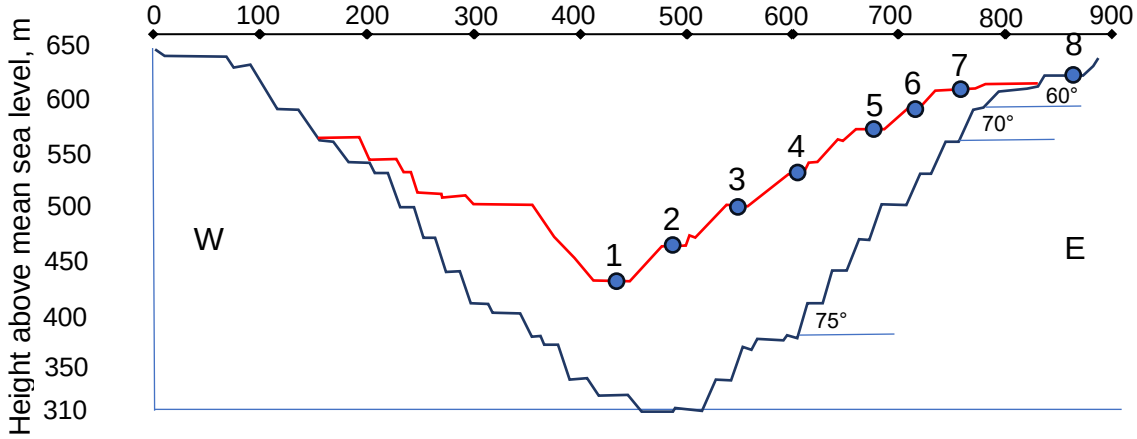

Fig. 8 – Current and prospective profiles of deposit development for "East Saryoba" mine.

Totally 16 deformation targets were placed along the east profile W-E, two for each slope. The distances between them were equal to B_0. Under such a premise, the first target is treated as deformed, and the second is treated as stable for control. The targets were attached to the slope surface and marked by retroreflective targets. The total station was used (Figure 9, c) to measure the displacements of these targets. For reliable observations, we have developed a permanent measuring station installed at the reference points for monitoring (Figure 9, a). This station aims to facilitate observation procedures, increase measurement accuracy, and speed up monitoring procedures.

(a) *(b)* *(c)*

Fig. 9 – Measuring station: (a) Design of the permanent measuring station: 1- concrete or steel pillar; 2- metal plate 3- mark center; 4-steel set; 5- frame hole; 6,7- attachment screws; 8 - butt; 9- cover; (b) Cover setup; (c) Total station setup and measurements.

RESULTS

Monitoring results

After setting the targets along the profile W-E, the measurements were accomplished. Total station Leica carried out observations of the vertical displacements of rock mass from the permanent measuring station placed outside the pit mine. For 2015-2019, seven epochs of geodetic observations were performed. The first epoch was considered a "zero" epoch with no displacements. According to the observations' results, the vertical displacements were fixed for deformed targets (Figure 10) and stable targets (Figure 11). The analysis of the results shows that the displacements of the deformed targets (Figure 10) tend to increase with height. The targets placed at the top rims of the pit mine have significant displacements. During the first observation years, the displacements did not exceed 25 mm. However, further observations have shown an evident trend. This trend is clear from the mean vertical displacement for each target that is calculated by

$$S_{mean} = \frac{\sum S_i}{q}, \quad (4)$$

where q is the number of observation epochs; $\sum S_i$ - total vertical displacement for all epochs. The graph of mean displacement is attached to Figure 10.

Unlike the deformed targets in Figure 10, stable targets have considerably smaller displacements. The maximum displacement reached 11 mm for the upper rim of the pit mine. The displacements of the stable targets mainly change randomly. There is only an insignificant trend for upper targets for the last observation year (points 7‘ and 8‘).

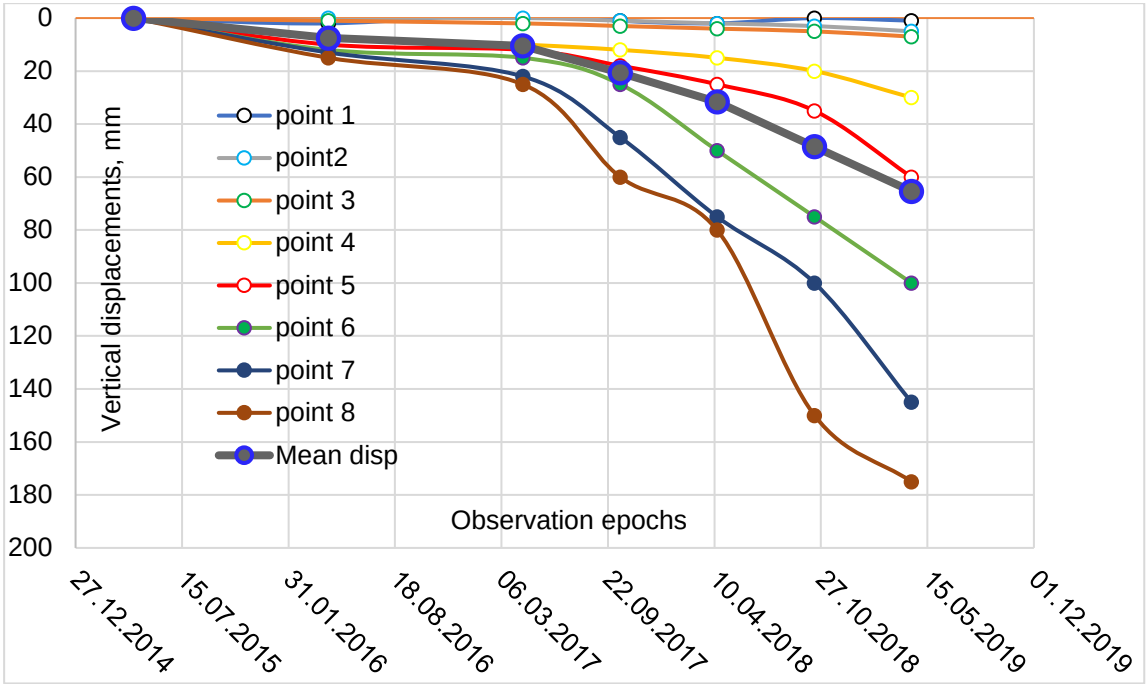

Fig. 10 – Displacements of deformed targets

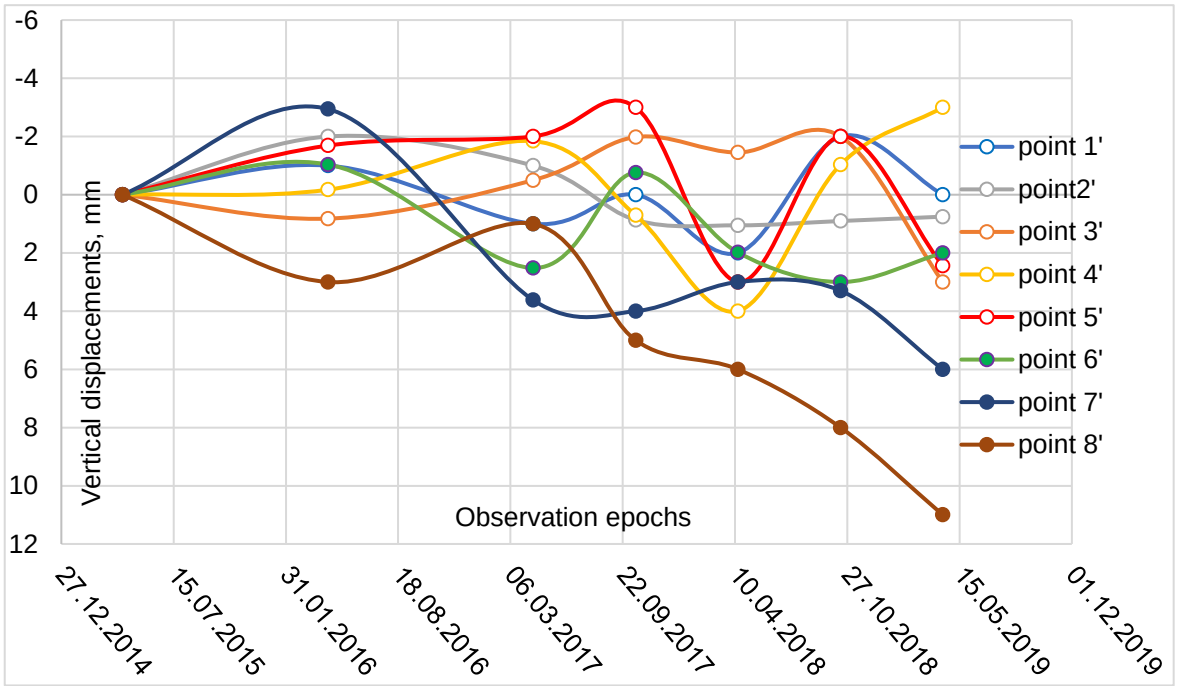

Fig. 11 – Displacements of stable targets

For the deformed targets, we may calculate the mean displacement velocity

$$v_{meansQ} = \frac{\sum_i^q v_Q}{q}, \quad (5)$$

where $\sum_i^q v_Q$ - the total velocity of the vertical displacement.

The velocity graphs are presented in Figure 12. This figure includes the graph of the mean displacement velocity.

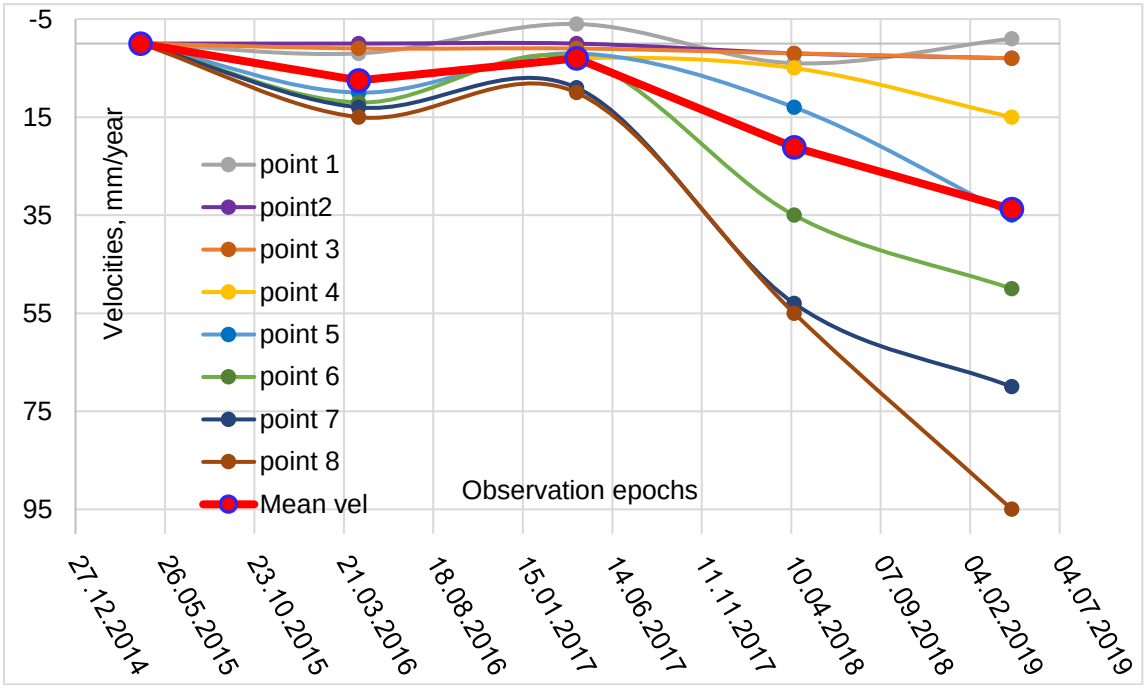

Fig. 12 – Graphs of target velocities

Since the number of epochs is limited, developing a prediction model based on statistical premises will provide unreliable results. The correct solution is the application of the interpolation model. However, the determined values of displacements are contaminated by random measurement errors. Therefore, applying the interpolation model that will simulate the deformation process and smooth the effect of random errors is recommended. One such model is the spline function (parabolic or cubic). The approximation is carried out using the least squares approach to reduce the impact of the random errors. Parabolic and cubic spline models describe the deformation process for all deformed targets with accuracy, as shown in Table 6. The model based on cubic spline provides more smoothed results with smaller values of root mean square errors (RMS) and absolute residuals.

The results of the least squares cubic spline approximation are presented in Figure 13.

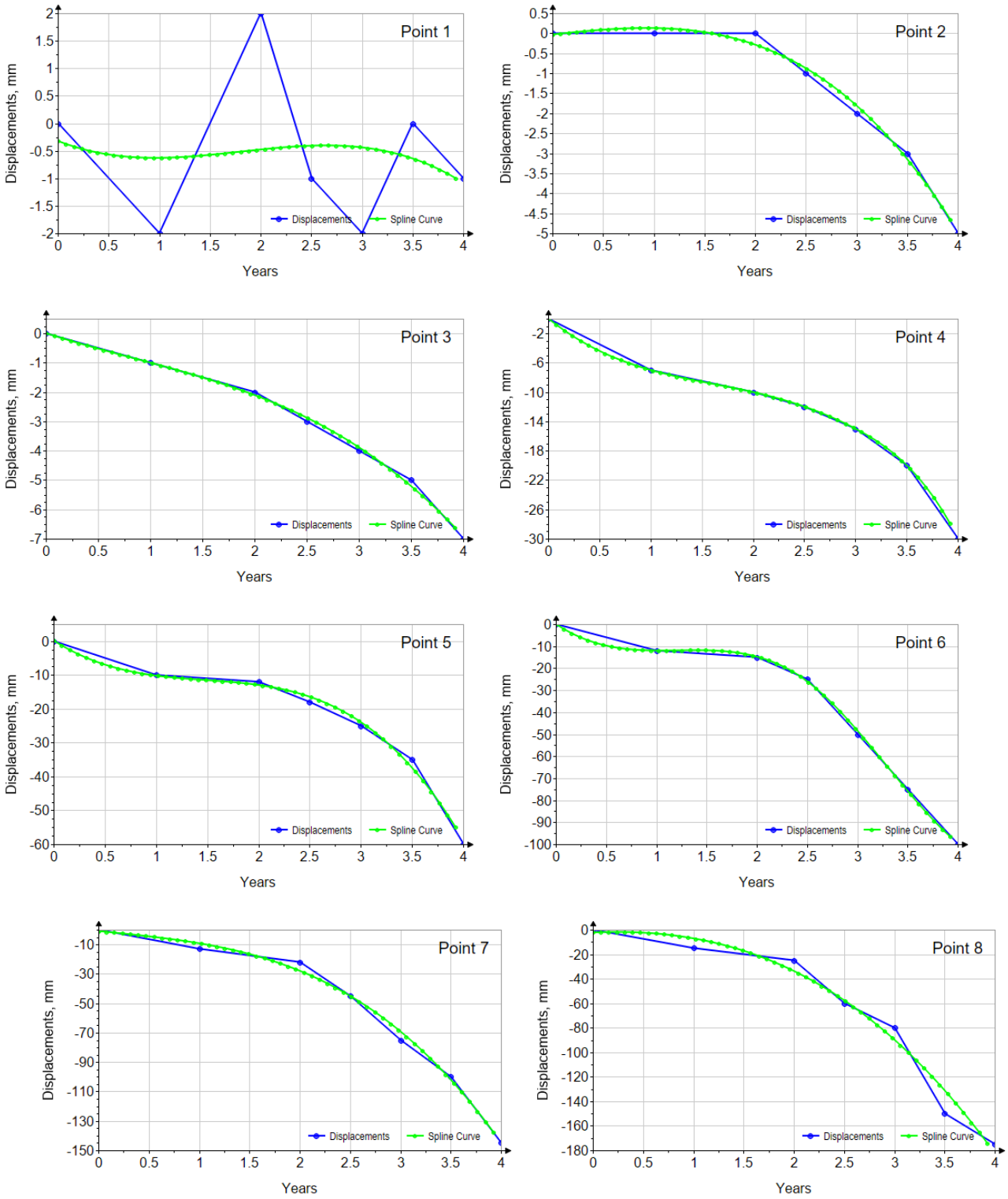

Fig. 13 – Graphs of cubic spline approximation for deformed targets

Tab. 6 - Approximation accuracy.

Target	Parabolic spline		Cubic spline	
	RMS, mm	Abs max, mm	RMS, mm	Abs max, mm
1	1.3	2.4	1.2	2.5
2	0.2	0.4	0.2	0.3
3	0.3	0.2	0.1	0.2
4	0.6	0.4	0.0	0.0
5	6.9	4.4	1.3	2.5
6	9.8	4.9	0.8	1.5
7	9.2	4.8	3.6	6.0
8	17.4	9.9	9.7	18.7

The obtained results presented in Figure 13 and Table 6 provide a clear explanation of the deformation process. The suggested observation scheme with two deformation targets on each slope ensured the correct interpretation of the whole pit mine displacement. It was determined that the targets emplaced in the possible collapse zone had undergone vertical displacements. The largest displacements were detected for the deformation targets placed on the upper levels of the pit mine (points 5-8). The calculated velocities show the increasing speed of the deformation process. Therefore, it is recommended that the time between observation epochs be decreased by up to three months.

CONCLUSION

The paper presents the results of geomonitoring and considers its role in the mining industry. The monitoring of the open-pit mine's slope stability has been examined. The critical point of the geomonitoring is a combination of geodetic monitoring data and rock geomechanical properties. Geomechanical studies of rock mass strength properties and structural features have been conducted. The results of geomechanical studies were leveraged to calculate the width of the possible collapse zone and the allowable slope's inclination angle for the "East Saryoba" mine. With these two parameters, geodetic monitoring technology has been improved.

The geodetic monitoring has been accomplished for the slopes of the "East Saryoba" mine. Total station observations have been leveraged for vertical displacement measurements. The preliminary results have shown the high efficiency of geomonitoring in the suggested approach. The results have demonstrated the growth of the vertical displacements from the pit mine bottom (7 mm) to the rim (175 mm). The vertical displacements are free of total displacements of the whole pit mine and present each slope's pure vertical displacement. Prospective research will have to address the geomonitoring problem in more detail. Future studies will have to concentrate on integrating additional measuring equipment, e.g., inclinometers, extensometers, etc., into geomonitoring schemes and address the issue of the complex processing and analysis of different data and measurements.

REFERENCES

[1] Yang Z., Gao Q., Li M.-H., Zhang G. 2014. Stability Analysis and Design of Open-Pit Mine Slope in China: A review. Electronic Journal of Geotechnical Engineering, Vol. 19: 10247-10266.

[2] Ortega J. H., Rapiman M, Lecaros R., Medel F., Padilla F., Garcia A. Predictive index for slope instabilities in open pit mining. Available online: https://arxiv.org/abs/1607.05085 (accessed on 04 August 2023) https://doi.org/10.48550/arXiv.1607.05085

[3] Harries N., Noon D., Rowley K. 2006. Case studies of slope stability radar used in open-cut mines. In: Proceedings of the International Symposium on Stability of Rock Slopes 335-342.
[4] Sjoberg, J. Large scale slope stability in open pit mining – a review. Technical report 1996:10T, Lulea university of technology, 1996, 229 p.
[5] Karam K.S., He M.C., Sousa L.R. 2015. Slope stability risk management in open pit mines. In: Proceedings of the 7th GiT4NDM and 5th EOGL International Conference, UAE, Al-Ain, 19p
[6] Stacey T.R., Xianbin Y., Armstrong R., Keyter G.J. 2003. New slope stability considerations for deep open-pit mines. Journal of the South African Institute of Mining and Metallurgy, 103(6): 373–389.
[7] Little, M.J. 2006. Slope monitoring strategy at prust open pit operation. In: Proceedings of the International Symposium on Stability of Rock Slopes in Open Pit Mining and Civil Engineering, 211-230.
[8] Vinoth S., Kumar L.A., Kumar E. 2015. Slope Stability Monitoring by Quantification and Behavior of Microseismic Events in an Opencast Coal Mine. Jour. Geol. Soc. India, Vol.85: 450-456.
[9] Narendranathan S., Nikraz H. 2011. Optimal System Design for Instrumented Slope Monitoring in Open Pit Mines. In: Proceedings of the International Conference on Advances in Geotechnical Engineering, Perth, Australia, 311-317.
[10] Rákay Š., Zuzik J., Weiss G., Labant S. 2013. Surveying of inaccessible rock faces and volume calculation of the irregular solids using robotic total station. Acta Montanistica Slovaca, 18(3): 164-171.
[11] Bazarnik M. 2018. Slope stability monitoring in open pit mines using 3D terrestrial laser scanning. In: Proceedings AG 2018 – 4th International Conference on Applied Geophysics, E3S Web of Conferences, 66. https://doi.org/10.1051/e3sconf/20186601020
[12] Long N.Q., Buczek M.M., Hien L.P., Szlapin'ska S.A., Nam B.X., Nghia N.V., Cuong C.X. 2018. Accuracy assessment of mine walls' surface models derived from terrestrial laser scanning. Int J Coal Sci Technol, 5(3): 328–338. https://doi.org/10.1007/s40789-018-0218-1
[13] Pagano M., Palma B., Ruocco A., Parise M. 2020. Discontinuity Characterization of Rock Masses through Terrestrial Laser Scanner and Unmanned Aerial Vehicle Techniques Aimed at Slope Stability Assessment. Appl. Sci, 10(8): 2960. https://doi.org/10.3390/app10082960
[14] Török Á., Bögöly G., Somogyi Á., Lovas T. 2020. Application of UAV in Topographic Modelling and Structural Geological Mapping of Quarries and Their Surroundings—Delineation of Fault-Bordered Raw Material Reserves. Sensors, 20(2): 489. https://doi.org/10.3390/s20020489
[15] Tong X., Liu X., Chen P., Liu S., Luan K., Li L., Liu S., Liu X., Xie H., Jin Y., Hong Z. 2015. Integration of UAV-Based Photogrammetry and Terrestrial Laser Scanning for the Three-Dimensional Mapping and Monitoring of Open-Pit Mine Areas. Remote Sens, 7(6): 6635-6662. https://doi.org/10.3390/rs70606635
[16] Gee D., Bateson L., Sowter, A., Grebby S., Novellino A., Cigna F., Marsh S., Banton C., Wyatt L. 2017. Ground Motion in Areas of Abandoned Mining: Application of the Intermittent SBAS (ISBAS) to the Northumberland and Durham Coalfield, U.K. Geosciences, 7(3): 85. https://doi.org/10.3390/geosciences7030085
[17] Czikhardt R., Papco J., Bakon M., Liscak P., Ondrejka P., Zlocha M. 2017. Ground Stability Monitoring of Undermined and Landslide Prone Areas by Means of Sentinel-1 Multi-Temporal InSAR, Case Study from Slovakia. Geosciences, 7(3): 87. https://doi.org/10.3390/geosciences7030087
[18] Pavelka,K., Šedina,J., Matoušková, E., Hlaváčová, I., Korth, W. 2019. Examples of different techniques for glaciers motion monitoring using InSAR and RPAS, European Journal of Remote Sensing, 52:sup1, 219-232, DOI: 10.1080/22797254.2018.1559001
[19] Hlaváčová, I.; Halounová, L.; Stanislav, P. 2016. SENTINEL-1 InSAR Processing of Corner Reflector Information in the Northern-Bohemian Coal Basin. The International Archives of the Photogrammetry, Remote Sensing and Spatial Information Sciences, 2016 XXIII ISPRS Congress, Prague. Göttingen: Copernicus GmbH (Copernicus Publications, 2016. p. 763-767. ISSN 2194-9034. DOI: 10.5194/isprs-archives-XLI-B7-763-2016
[20] Kumar A., Villuri V.G.K. 2015. Role of mining radar in mine slope stability monitoring in open cast mines. Procedia Earth and Planetary Science, 11: 76 – 83.
[21] Solari L., Montalti R., Barra A., Monserrat O., Bianchini S., Crosetto M. 2020. Multi-Temporal Satellite Interferometry for Fast-Motion Detection: An Application to Salt Solution Mining. Remote Sens, 12(23): 3919. https://doi.org/10.3390/rs12233919

[22] Brown C., Daniels A., Boyd D.S., Sowter A., Foody G., Kara S. 2020. Investigating the Potential of Radar Interferometry for Monitoring Rural Artisanal Cobalt Mines in the Democratic Republic of the Congo. Sustainability, 12(23): 9834. https://doi.org/10.3390/su12239834
[23] Wei L., Feng Q., Liu F., Mao Y., Liu S., Yang T., Tolomei C., Bignami C., Wu L. 2020. Precise Topographic Model Assisted Slope Displacement Retrieval from Small Baseline Subsets Results: Case Study over a High and Steep Mining Slope. Sensors, 20(22): 6674. https://doi.org/10.3390/s20226674
[24] Chen D., Chen H., Zhang W., Cao C., Zhu K., Yuan X., Du Y. 2020. Characteristics of the Residual Surface Deformation of Multiple Abandoned Mined-Out Areas Based on a Field Investigation and SBAS-InSAR: A Case Study in Jilin, China. Remote Sens, 12(22): 3752. https://doi.org/10.3390/rs12223752
[25] Liang H., Li X., Zhang L., Chen R.-F., Ding X., Chen K.-L., Wang C.-S., Chang C.-S., Chi C.-Y. 2020. Investigation of Slow-Moving Artificial Slope Failure with Multi-Temporal InSAR by Combining Persistent and Distributed Scatterers: A Case Study in Northern Taiwan. Remote Sens, 12(15): 2403. https://doi.org/10.3390/rs12152403
[26] Zheng L., Zhu L., Wang W., Guo L., Chen B. 2020. Land Subsidence Related to Coal Mining in China Revealed by L-Band InSAR Analysis. Int. J. Environ. Res. Public Health, 17(4): 1170. https://doi.org/10.3390/ijerph17041170
[27] Theilen-Willige B., Ait Malek H., Charif A., El Bchari F., Chaïbi M. 2014. Remote Sensing and GIS Contribution to the Investigation of Karst Landscapes in NW-Morocco. Geosciences, 4(2): 50-72. https://doi.org/10.3390/geosciences4020050
[28] Chalkias C., Ferentinou M., Polykretis C. 2014. GIS-Based Landslide Susceptibility Mapping on the Peloponnese Peninsula, Greece. Geosciences, 4(3): 176-190. https://doi.org/10.3390/geosciences4030176
[29] Bláha P. 2009. Landslide and its complex investigation. Acta Montanistica Slovaca, 14(3): 221-231.
[30] Dalyot S. 2015. Landform Monitoring and Warning Framework Based on Time Series Modeling of Topographic Databases. Geosciences, 5(2): 177-202. https://doi.org/10.3390/geosciences5020177
[31] Desrues M., Lacroix P., Brenguier O. 2019. Satellite Pre-Failure Detection and In Situ Monitoring of the Landslide of the Tunnel du Chambon, French Alps. Geosciences, 9(7): 313. https://doi.org/10.3390/geosciences9070313
[32] Bossi G., Mantovani M., Frigerio S., Schenato L., Marcato G., Pasuto A. 2016. A Monitoring Network to Map and Assess Landslide Activity in a Highly Anthropized Area. Geosciences, 6(3): 40. https://doi.org/10.3390/geosciences6030040
[33] Bonetto S., Umili G., Ferrero A.M., Carosi R., Simonetti M., Biasi A., Migliazza M.R., Bianchini S. 2020. Geostructural and Geomechanical Study of the Piastrone Quarry (Seravezza, Italy) Supported by Photogrammetry to Assess Failure Mode. Geosciences, 10(2): 64. https://doi.org/10.3390/geosciences10020064
[34] Tao Z., Zhu C., Zheng X., He M. 2018. Slope stability evaluation and monitoring of Tonglushan ancient copper mine relics. Advances in Mechanical Engineering, Vol. 10(8): 1–16. https://doi.org/10.1177/1687814018791707
[35] Wessels S.D.N. Monitoring and management of a large open pit failure. Master of Science in Engineering, University of Witwatersrand, Johannesburg, November 2009.
[36] Gilani S.-O., Sattarvand J. 2015. A new heuristic non-linear approach for modeling the variable slope angles in open pit mine planning algorithms. Acta Montanistica Slovaca, 20(4): 251-259.
[37] Pandit B., Tiwari G., Latha G.M., Babu G.L.S. 2018. Stability Analysis of a Large Gold Mine Open-Pit Slope Using Advanced Probabilistic Method. Rock Mechanics and Rock Engineering, 51: 2153–2174. https://doi.org/10.1007/s00603-018-1465-6
[38] Fleurisson J.-A. 2012. Slope Design and Implementation in Open Pit Mines: Geological and Geomechanical Approach. Procedia Engineering, 46: 27 – 38.
[39] Mphathiwa N., Cawood F.T. 2014. Design principles for optimizing an established survey slope monitoring system. The Journal of The Southern African Institute of Mining and Metallurgy, 114: 463-470.
[40] Osasan K.S., Afeni T.B. 2010. Review of surface mine slope monitoring techniques. Journal of Mining Science, 46(2): 177-186.
[41] Ammirati L., Mondillo N., Rodas R.A., Sellers C., Di Martire D. 2020. Monitoring Land Surface Deformation Associated with Gold Artisanal Mining in the Zaruma City (Ecuador). Remote Sens, 12(13): 2135. https://doi.org/10.3390/rs12132135

CIVIL ENGINEERING JOURNAL

Article no. 5

THE CIVIL ENGINEERING JOURNAL 1-2024

STUDY ON CONSTRUCTION MONITORING AND CONTROL OF MULTI-SPAN PRESTRESSED CONCRETE CONTINUOUS BEAM BRIDGE

Xilong Zheng and Di Guan

School of Civil and Architectural Engineering, Harbin University, No.109 Zhongxing Road, Harbin, Heilongjiang Province, China; sampson88@126.com

ABSTRACT

This article focuses on the construction monitoring and control of a pre-stressed concrete continuous beam bridge, consisting of 13 spans. The goal is to ensure that the bridge structure meets the design requirements throughout the entire construction process. By comparing the theoretical and measured values of the bridge's alignment and stress during the cantilever construction, closure, and completion phases, it can be observed that the deflection deformation of the bridge is generally in agreement with the theoretical calculations. After the completion of the entire bridge, the measured elevations of each section have an error range of -18mm to 20mm compared to the design elevations, which satisfies the specifications. A comparison analysis of the measured and theoretical stress values at the root and mid-span of the cantilever indicates that the stress difference at the root is within the range of -0.2MPa to 0.2MPa, and the stress differences at the mid-span after completion are 0.03MPa (upper) and 0.09MPa (lower), all of which meet the structural design and code requirements. By establishing a gray GM (1,1) model and using gray system theory, the deflection error during the construction process is predicted and controlled. The prediction accuracy of different methods is compared to determine a reasonable prediction method suitable for long-span pre-stressed continuous beam bridges, providing reference for similar engineering projects.

KEYWORDS

Long-span bridge, Continuous beam bridge, Grey system theory, Construction control

INTRODUCTION

A continuous beam bridge refers to a beam bridge with two or more continuous spans, belonging to a statically indeterminate system. Under the effect of constant and live loads on a continuous beam bridge, the negative bending moment at the supports can relieve the positive bending moment at the mid-span, resulting in a more uniform and rational internal force distribution. Therefore, continuous beam bridges have advantages such as reduced height, material savings, high stiffness, good overall performance, high overload capacity, high safety, and low cost. Pre-stressed concrete continuous beam bridges are a type of pre-stressed bridge that offers advantages such as good overall performance, high structural stiffness, minimal deformation, and good seismic performance. In particular, the deflection curve of the main beam is smooth, with small deformation and comfortable driving conditions [1-3]. Furthermore, the design and construction of this type of bridge are relatively mature, ensuring control over construction quality and duration, and requiring less maintenance after completion. These factors have led to the widespread application of such bridges in highway, urban, and railway bridge projects [4-6].

The development of continuous beam bridges saw significant progress in the 1950s when pre-stressed concrete surpassed spans of 100 meters. By the 1980s, spans even exceeded 440

meters. Conventional reinforced concrete structures had several drawbacks, such as premature cracking, inability to effectively utilize high-strength materials, high structural weight, and poor load-carrying capacity, resulting in low material efficiency. To address these issues, pre-stressed concrete structures emerged. Since the mid-20th century, with the construction of the Rhein River cantilever casting bridge in Germany, cantilever casting and cantilever assembly construction methods have been improved, refined, and widely adopted worldwide for pre-stressed concrete continuous beam bridges [7-10]. However, the diversification of bridge structures and the continuous increase in span lengths have presented greater challenges in bridge design, construction, and management. While promoting the development of related industries, ensuring the structural safety of bridges has become a crucial concern for construction managers [11-13]. Ensuring structural safety has become an indispensable part of the bridge construction process. Consequently, bridge construction control technology has become a popular research topic. It involves identifying influential parameters, determining key factors, and providing reasonable guidance for bridge construction through error analysis and adjustment [14-16].

Ye Zaijun [17] used the grey system theory and established a GM(1,1) prediction model to predict the elevation errors of the beam segment box beams during the cantilever pouring process of the Danjiangkou Bridge in the South-to-North Water Diversion Project. This allowed for adjustments to be made to the subsequent construction process based on the predicted errors. The application of the grey system theory in this predictive model is a common and effective method in engineering construction. Qu Guangzhen [18] conducted a study on the effects of system transformation and shrinkage on the elevation and stress of the bridge, using the Wuhan-Jingmen High-speed Railway Hanjiang Extra-large Bridge as the background. Additionally, this study analyzed the impact of other parameter errors and the closure sequence on the structure, aiming to reduce construction errors. Zhou Langfeng [19] conducted a simulation analysis of the entire construction process of the Hanjiang Extra-large Bridge in the Wuhan-Jingmen High-speed Railway project. This study analyzed the effects of concrete shrinkage and creep on the bridge's alignment and investigated the impact of temperature on structural deformation and stress. These analyses ensured the control of elevation and stress during the closure process.

This paper takes a prestressed concrete continuous beam bridge as the engineering background, with a specific main bridge as a 13-span continuous system. The study focuses on monitoring the alignment and stress during the bridge construction process. The grey system theory is applied to predict and control the deflection error during construction, ensuring that the structure meets the design requirements throughout the entire construction process.

BACKGROUND

This paper takes a dual-purpose road-rail bridge in Fujian province, with a total length of 3713.475m, as the engineering background. The main bridge is a 13-span continuous variable-section box girder, with span arrangements of 40m + 11×64m + 40m, and a total length of 784m, as shown in Figure 1. The superstructure adopts a single-box single-cell variable-section prestressed continuous box girder. The beam body has a single-box single-cell, variable-section, and variable-height structure. The top width of the box girder is 17.5m. The inclined diaphragm and the height of each control section beam are as follows: 2.8m at the end support and mid-span, and 4m at the mid-support, with a varying height in accordance with a circular curve. The bridge deck is set as a dual carriageway with a total width of 35.5m. The width of the left and right carriageways is both 17.5m, with a 0.5m gap in the middle. The transverse layout includes: 1.25m (guardrail and water pipe) + 0.5m (anti-collision wall) + 3.0m (hard shoulder) + 11.25m (driving lane) + 0.75m (road shoulder) + 2.0m (central separator) + 0.75m (road shoulder) + 11.25m (driving lane) + 3.0m (hard shoulder) + 0.5m (anti-collision wall) + 1.25m (guardrail and water pipe), totalling 35.5m. The elevation view of the main bridge is shown in Figure 2.

Fig. 1 – The main bridge of a dual-purpose road-rail bridge in Fujian province

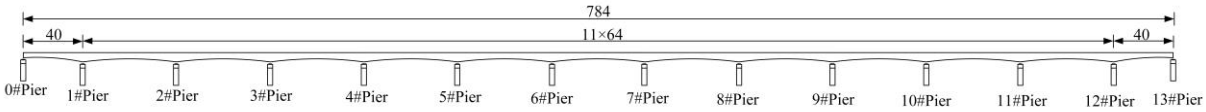

Fig. 2 – Elevation view of the main bridge (unit: m)

The box girder adopts C55 high-performance concrete, the pier and abutment body adopt C50 concrete, the fill concrete for pier and abutment adopts C20 concrete, and the foundation adopts C40 concrete. The prestressing of the box girder is done using low relaxation high-strength prestressing steel strands with a nominal area of 140mm2, a nominal diameter of 15.2mm, an elastic modulus of 1.95×105MPa, and a standard tensile strength of 1860MPa. The anchoring system uses wedge anchorage, and the drilling is done using metal corrugated pipes.

The vertical prestressing bars use prestressed threaded steel reinforcement, with the model JL785. The standard tensile strength of the prestressing steel reinforcement for prestressed concrete is 785MPa, and the controlled stress under anchorage is 650MPa. The prefabricated holes are φ35 with iron skin. During construction, a two-stage tensioning process is used, and the anchorage device should not have a retraction greater than 1mm. The ordinary reinforcement uses smooth round steel bars HPB300 and ribbed steel bars HRB400.

ESTABLISHMENT OF FINITE ELEMENT MODEL

The main bridge is primarily modelled and analyzed using the Midas/Civil finite element software. The finite element model of the entire bridge is shown in Figure 3. Since the longitudinal and transverse arrangements of the two spans of the bridge are completely identical, calculations are only performed on a single span bridge model. The upper structure of the entire bridge is divided into 262 nodes and 261 elements. Considering the construction sequence and the effects of shrinkage and creep, the structural analysis is conducted using the positive-loading method.

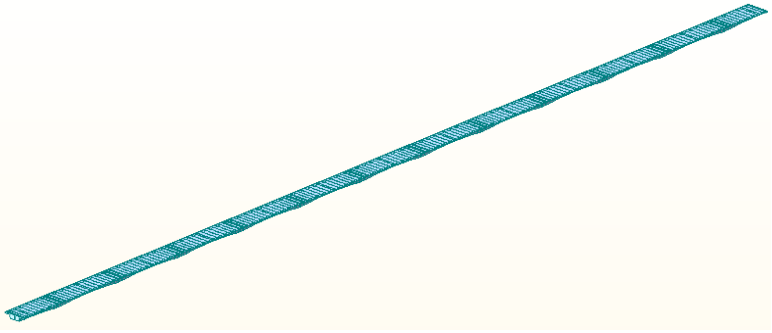

Fig. 3 – Midas/Civil finite element model diagram

The entire bridge consists of 13 spans, and during the cantilever casting construction process, it is divided into 12 T-segments. Each T-segment has a maximum cantilever state divided into 8 casting segments for cantilever casting. The casting segments for smaller distances are represented as 0'#~7'#, while the casting segments for longer distances are represented as 0#~7#. The division of T-segment beams is shown in Figure 4.

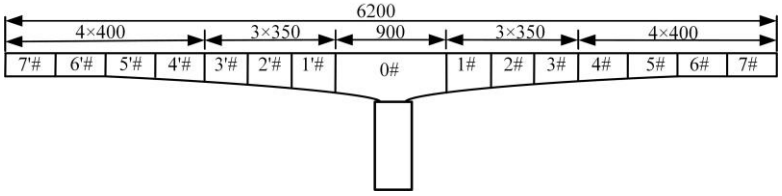

Fig. 4 – Cantilever construction beam segment division diagram (cm)

ARRANGEMENT OF CONSTRUCTION MONITORING POINTS

The main monitoring contents during the construction process include the following points:

(1) Deflection observation: Perform periodic levelling measurements on the top observation points of the box girder according to the construction process (before and after pouring, before and after prestressing, before and after basket hanging).

(2) Stress observation: Perform stress measurements on the embedded components installed inside the box girder.

Deflection observation

The main content of deflection observation is to measure the elevation of each cast-in-place segment of the box girder to determine if the bridge alignment and elevation match the design. Three symmetrical elevation observation points are set up at each construction stage to measure the deflection of the box girder and observe if any torsion occurs. The specific process involves measurements by the construction unit, verification by the supervision unit, and then compilation and processing by the monitoring unit. The measurement points are shown in Figure 5.

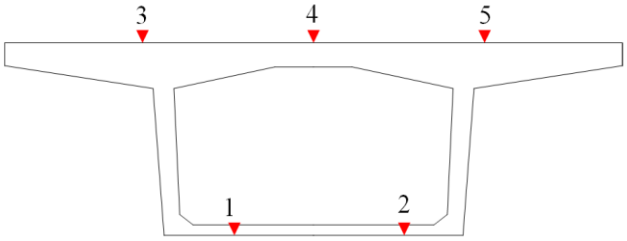

Fig. 5 – Elevation measurement point layout diagram for formwork

Stress observation

According to the characteristics and requirements of this project, different stress monitoring positions are selected. Four measurement points are arranged on each main beam stress testing section. One measurement point is arranged on each temporary fixed support on the top of each pier. Three sling measurement points are arranged on each hanging basket. The layout of main beam measurement points is shown in Figure 6 and Figure 7, using embedded concrete strain gauges with temperature sensors. The strain sensors should be fixed on the steel reinforcement frame before concrete pouring, and the test wires should be led into the box and properly marked and protected. According to the actual construction process, a total of four measurements are conducted for each segment during construction: before and after concrete pouring, before and after pre-stressing, and stress-strain monitoring should also be carried out after main beam closure and completion of phase two permanent loading construction.

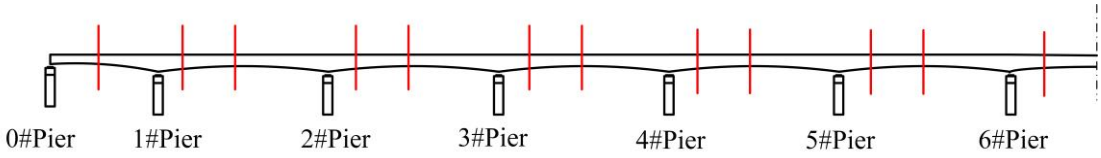

Fig. 6 – Layout diagram of stress testing sections for Continuous Beam 1/2

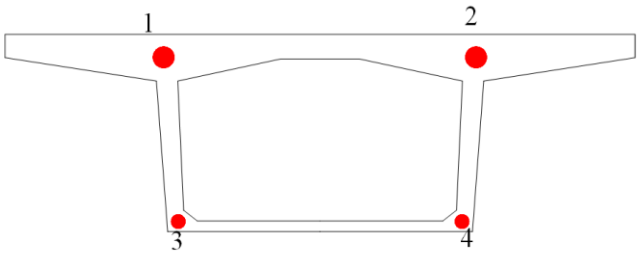

Fig. 7 – Layout diagram of stress measurement points

CONSTRUCTION MONITORING AND CONTROL

Linear monitoring

The main task of linear control is to collect real-time measurement data during the actual construction process, compare the measured deflection variations with the finite element model, analyze, identify, and adjust the discrepancies between the two, and provide feedback to the model. By adjusting the model, it predicts the future state of the structure reasonably, ensuring a smooth alignment. Bridge alignment monitoring primarily includes three main stages: cantilever construction stage, final closure stage for each span, and the ultimate bridge completion stage.

Alignment control results during the cantilever casting stage

Due to the large number of spans in this project and the similarity of each structure during the cantilever construction stage, we only analyze the cantilever casting process of Pier 2. We compare the measured deflection changes of each beam section with the theoretical calculation deflection during the concrete casting, prestressing, and basket movement processes. Sections 0'# to 7'# represent short-distance beam sections, while sections 0# to 7# represent long-distance beam sections. The difference is calculated as the measured value minus the theoretical value. The deflection variations at each construction stage of Pier 2 during the entire construction process are shown in Figure 8 to Figure 10.

From the above analysis, it can be observed that during the cantilever construction process of Pier 2#, the deflection errors caused by concrete casting range from -1.29mm to 0.56mm, the errors due to prestressing range from -0.74mm to 1.32mm, and the errors caused by basket movement range from -0.49mm to 0.13mm. The deflection variations of each beam section are comparable to the theoretical deflection variations, meeting the accuracy requirements of alignment monitoring. The monitoring during the cantilever stage has achieved good results.

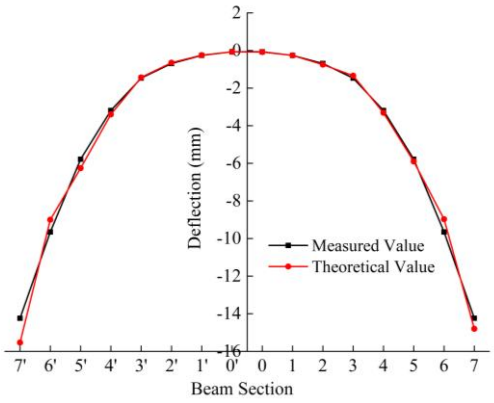

Fig. 8 – The diagram showing the variation of deflection in concrete pouring

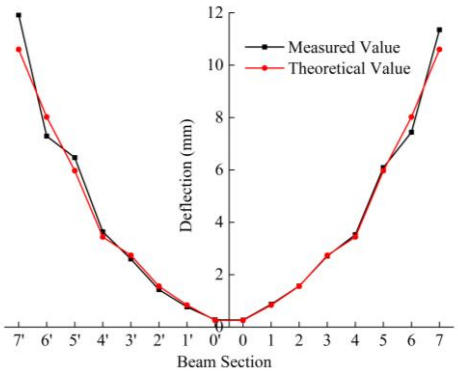

Fig. 9 – The diagram showing the variation of deflection in prestressed concrete

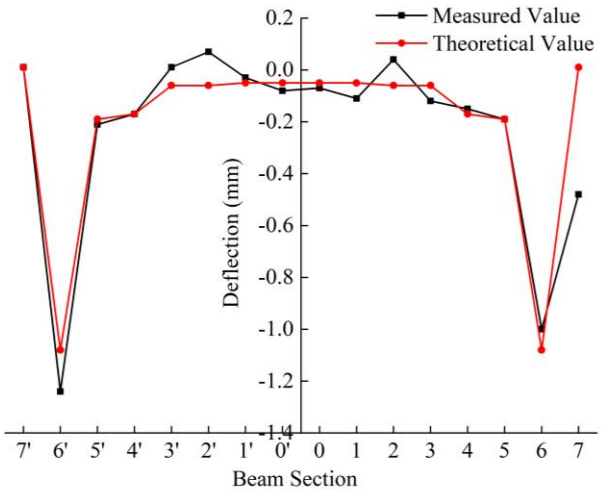

Fig. 10 – The diagram showing the variation of deflection in suspended scaffolding movement

The control results during the bridge closure stage

Due to the complexity of the bridge closure process and the involvement of multiple system conversion processes, this study focuses on the case of the closure of span 3# between pier 2# and pier 3# to analyze the monitoring results and the influence of closure on the deflection of span 3 at various points. Through analysis, the deflection effects of the closure of span 3 are shown in Figure 11 to Figure 13. It can be observed that during the closure of span 3, the deflection errors caused by concrete pouring range from -0.14mm to 0.1mm, the errors caused by prestressing range from -1.77mm to 2.56mm, and the errors caused by the removal of suspended scaffolding range from -0.69mm to 0.52mm. The deflection changes in each beam segment are similar to the theoretical deflection changes, meeting the accuracy requirements of linearity monitoring. The monitoring during the cantilever stage has achieved good results.

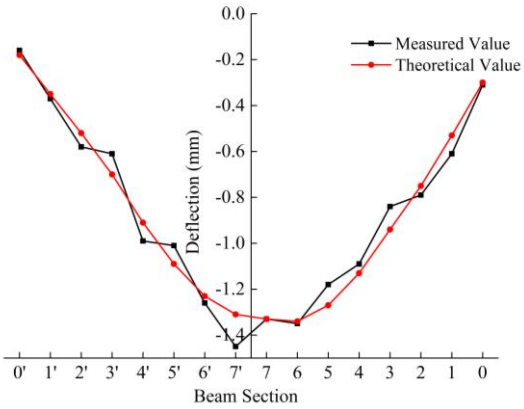

Fig. 11 – The deflection variation of the main beam during the concrete pouring in the bridge closure section

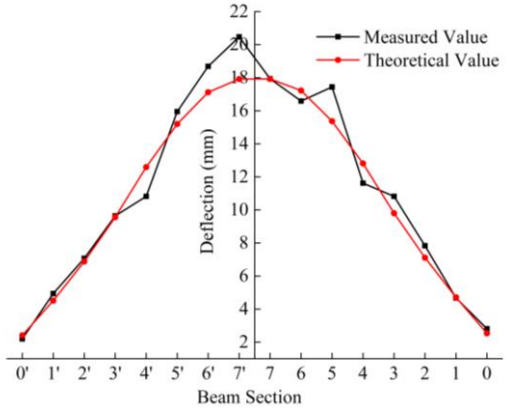

Fig. 12 –The deflection variation of the main beam during the prestressing in the bridge closure section

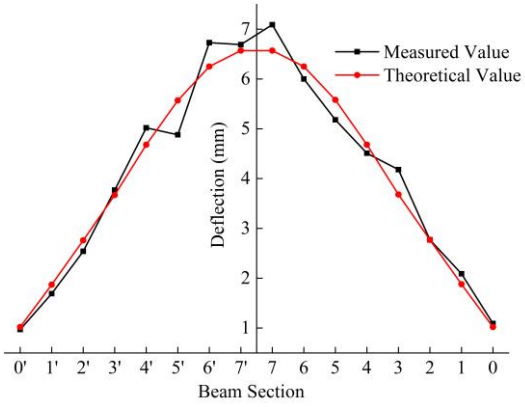

Fig. 13 – The deflection variation of the main beam during the removal of suspended scaffolding in the bridge closure section

The overall bridge closure line condition

The evaluation of whether the bridge alignment meets the design requirements after the completion of bridge closure in each span is an important criterion for judging the effectiveness of construction monitoring. Due to the long total span of the bridge, we can evaluate the monitoring results by comparing the measured elevations with the theoretical elevations, taking the span 3# between pier 2# and pier 3# as an example. The comparison between the measured elevations and the theoretical elevations at the control section of span 3# is shown in Table 1. From Table 1, it can be seen that the measured elevation values of each beam segment are in good agreement with the design elevation values, with errors ranging from -18mm to 20mm, which are within the specified requirements. The construction control of the project has achieved good results in terms of alignment.

Tab.1 - Alignment control effectiveness of Span 3 (m)

Beam segment	Theoretical elevation	Measured elevation	Difference
0'	48.123	48.125	0.002
1'	48.081	48.098	0.017
2'	48.039	48.045	0.006
3'	47.998	47.995	-0.003
4'	47.951	47.965	0.014
5'	47.906	47.903	-0.003
6'	47.862	47.843	-0.019
7'	47.819	47.825	0.006
7	47.808	47.815	0.007
6	47.797	47.783	-0.014
5	47.756	47.740	-0.016
4	47.715	47.725	0.010
3	47.676	47.696	0.020
2	47.638	47.640	0.002
1	47.605	47.587	-0.018
0	47.573	47.587	0.014

Cantilever construction process deflection prediction analysis

Comparison of different prediction methods

According to the characteristics of continuous beam bridge construction with long-term prestressing, the grey system theory is chosen to predict the deflection error. The cantilever pouring process of this project is regarded as a grey system, and the prediction of the adjustment value of pre-camber during the structural construction process is conducted. In order to demonstrate the reliability of the grey system prediction method, a comparative analysis is carried out between the grey system, BP neural network, and least squares method for predicting the elevation of the pouring process for the 5# to 7# beam segments at the 2# pier. The prediction errors are calculated using the three methods, and the results are shown in Table 2. The comparative analysis is illustrated in Figure 14.

Tab.2 - Comparison table of results from different prediction methods (mm)

Beam segment	Measured error value	Grey prediction value	BP prediction value	Least squares prediction value
5#	10.7	9.97	9.8	13.4
6#	8.5	8.71	8.7	7.8
7#	6.3	5.67	6.44	5

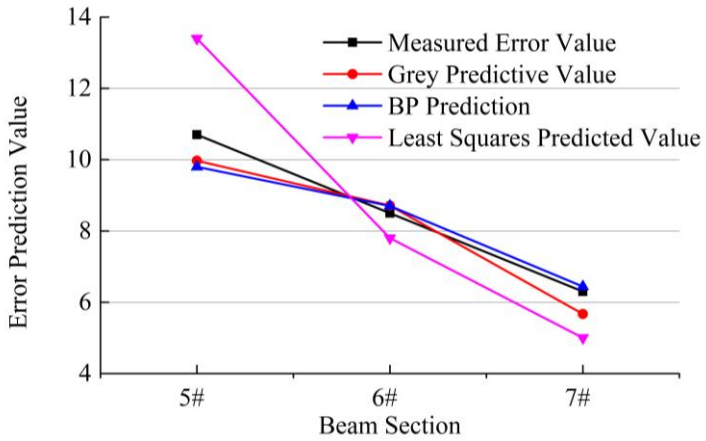

Fig. 14 – Comparison chart of three prediction values

According to Table 3 and Figure 14, it can be observed that the three prediction methods exhibit similar trends in predicting errors as the actual error development. All of them can effectively adjust the influence of construction errors in the project. Among the three prediction methods, the maximum error of grey prediction is 10.0%, the maximum error of BP neural network prediction is 9.03%, and the maximum error of least squares method is 27.55%. Both grey system theory and BP neural network prediction accuracy meet the requirements, and they can be regarded as effective methods for predicting the elevation of continuous beam bridges.

Stress monitoring results

Due to being a 13-span prestressed concrete continuous beam bridge, there are a total of 24 stress monitoring sections, and 4 monitoring points are required for each construction process in each segment, resulting in a large amount of data. Therefore, this study only compares the root of the cantilever at the far end of Pier 2# and the mid-span section of Span 2# at different construction stages. These two parts are divided into different construction stages for monitoring, as shown in Table 3.

Tab.3 - Construction stage division

Root of cantilever at Pier 2#				Mid-span of Span 2#	
Numbering	Construction phase	Numbering	Construction phase	Numbering	Construction phase
1	Pouring of Block 0#	16	Post-tensioning of Block 7#	1	Closure of Span 2# and Span 4#
2	Post-tensioning of Block 0#	17	Closure of Span 2# and Span 4#	2	Pouring of Segment 8# in Span 1#
3	Pouring of Block 1#	18	Pouring of Segment 8# in Span 1#	3	Closure of Span 3#
4	Post-tensioning of Block 1#	19	Closure of Span 3#	4	Closure of Span 6#
5	Pouring of Block 2#	20	Closure of Span 6#	5	Closure of Span 8#
6	Post-tensioning of Block 2#	21	Closure of Span 8#	6	Closure of Span 7#
7	Pouring of Block 3#	22	Closure of Span 7#	7	Closure of Span 5#
8	Post-tensioning of Block 3#	23	Closure of Span 5#	8	Closure of Span 10# and Span 12#
9	Pouring of Block 4#	24	Closure of Span 10# and Span 12#	9	Pouring of Segment 8# in Span 13#
10	Post-tensioning of Block 4#	25	Pouring of Segment 8# in Span 13#	10	Closure of Span 11#
11	Pouring of Block 5#	26	Closure of Span 11#	11	Closure of Span 9#
12	Post-tensioning of Block 5#	27	Closure of Span 9#	12	Closure of the side span
13	Pouring of Block 6#	28	Closure of the side span	13	Phase 2 pavement
14	Post-tensioning of Block 6#	29	Phase 2 pavement		
15	Pouring of Block 7#				

Monitoring results of stress at the root of the cantilever

The comparative analysis of Figure 15 and Figure 16 shows that during the entire cantilever pouring process, no tensile stress was observed at the root of the cantilever. The stress values continuously increased as the construction stages progressed, and the stress trend matched the actual conditions. The theoretical calculated values were generally consistent with the measured values, with a margin of error ranging from -0.2MPa to 0.2MPa, meeting the specifications requirements. The structural calculation model was reasonable, and the calculated results were accurate, providing guidance for the project. After the pouring was completed, the maximum stress at the upper edge of the cantilever root was 7.82MPa, and the maximum stress at the lower edge was 7.92MPa. After the completion of the bridge, the stress values at the upper edge were 7.35MPa, and at the lower edge were 7.93MPa. The results complied with the specification requirements, indicating that the structure was in a safe condition.

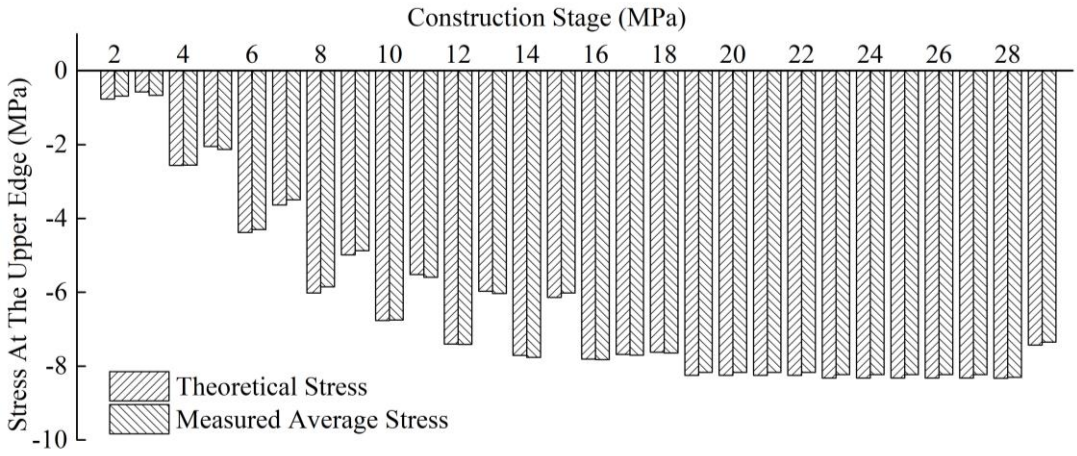

Fig. 15 – Comparison chart of upper edge stress

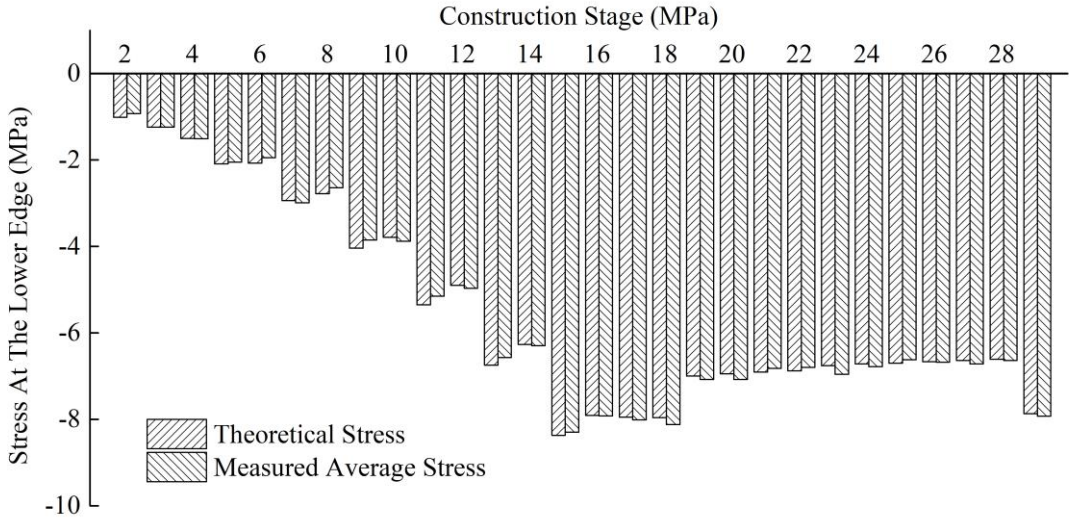

Fig. 16 – Comparison chart of lower edge stress

Monitoring results of stress at midspan

Taking the midspan section of 2# span as an example, as shown in Figure 17 and Figure 18. During the structural system transformation, the measured stress variation trend is consistent with the theoretical trend, with an error range of -0.2MPa to 0.17MPa, meeting the specifications requirements. During the pouring of segment A8 of 1# span, a tensile stress of 0.56MPa appeared at the upper edge of the midspan of 2# span. This tensile stress is a temporary stress effect during the construction stage, which will disappear in later stages and its magnitude meets the specification requirements, not affecting the safety performance of the entire construction process. After the completion of the second phase of bridge paving, the stress at the upper edge of the midspan of 2# span is -1.66MPa, with an error of 0.03MPa, and the stress at the lower edge is -10.39MPa, with an error of 0.09MPa, indicating that the structure meets design and specification requirements.

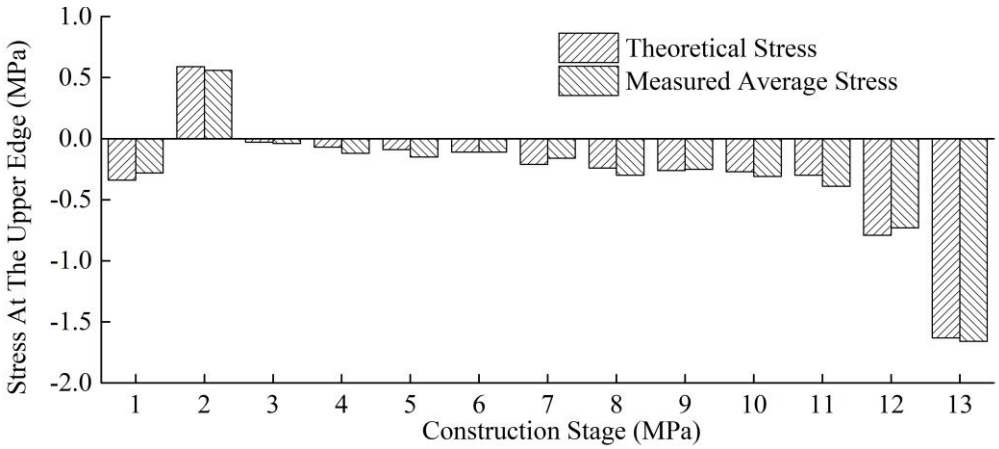

Fig. 17 –Comparison chart of upper edge stress

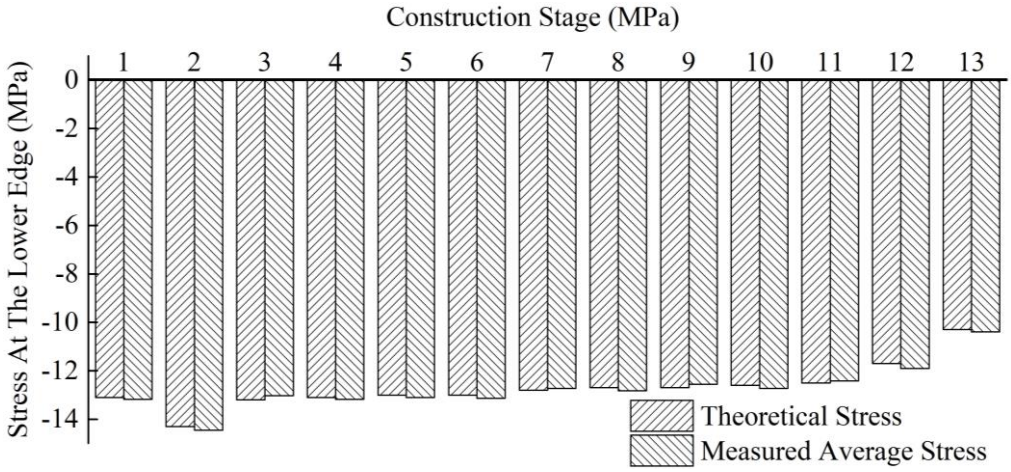

Fig. 18–Comparison chart of lower edge stress

CONCLUSION

This paper takes the prestressed concrete continuous beam bridge of the 13th span as the background and conducts monitoring and analysis in conjunction with the actual construction process. The main work conducted and the conclusions drawn are as follows:

(1) Taking the overhang pouring process of Pier 2# as an example for engineering alignment control, the results show that the deflection deformation of the bridge during various construction stages is essentially consistent with the theoretical calculations. In the final bridge completion stage, the alignment conforms to the design requirements. The construction monitoring work has achieved good results in terms of alignment.

(2) Using grey system theory to predict errors and adjust the deflection of beam segments during cantilever construction, a comparison and analysis of different prediction methods were conducted. The results show that both BP neural network and grey system theory have achieved good results in predicting the deflection of long-span prestressed concrete continuous beam bridges in the maximum cantilever state.

(3) Taking the root and mid-span sections of a certain cantilever as an example for stress monitoring, a comparison was made between the theoretical stress and actual stress throughout the construction process. The results show that the root of the cantilever experienced compressive

stress during the entire construction process, with the measured values closely matching the theoretical values. At the mid-span upper section, a temporary tensile stress of 0.56MPa occurred during the construction process, while other stages exhibited compressive stress, with the measured values closely approximating the theoretical values. The entire monitoring process achieved good results in terms of stress monitoring.

REFERENCES

[1] ZHANG, Chunyu, et al. Seismic reliability research of continuous girder bridge considering fault-tolerant semi-active control [J]. Structural Safety, 2023, 102: 102322.
[2] WU, Bitao, et al. Damage identification method for continuous girder bridges based on spatially-distributed long-gauge strain sensing under moving loads [J]. Mechanical Systems and Signal Processing, 2018, 104: 415-435.
[3] CHENG, Xiao-Xiang. Model updating for a continuous concrete girder bridge using data from construction monitoring [J]. Applied Sciences, 2023, 13.6: 3422.
[4] ZHENG, Shangmin, et al. Semi-active control of seismic response on prestressed concrete continuous girder bridges with corrugated steel webs [J]. Applied Sciences, 2022, 12.24: 12881.
[5] Yang Z , Ping Z , Zhu Y , et al. NC-UHPC Composite Structure for Long-Term Creep-Induced Deflection Control in Continuous Box-Girder Bridges[J]. Journal of Bridge Engineering, 2018, 23(6).
[6] Lounis Z , Cohn M Z . Optimization of Precast Prestressed Concrete Bridge Girder Systems[J]. Pci Journal, 1993, 38(4):60-78.
[7] Wang J . Constructing linear control of continual beam bridge cantilever pouring in railway passenger traffic special line[J]. Shanxi Architecture, 2008.
[8] XU, Changjie; XU, Lige; ZHOU, Jian. Integral lifting of a three-span continuous beam bridge [J]. Journal of Performance of Constructed Facilities, 2015, 29.4: 04014117.
[9] HUANG, Fu Wei, et al. Analysis on attenuation-amplification effect and vibration monitoring of pier-beam of continuous beam bridge under near blasting [J]. Applied Mechanics and Materials, 2013, 353: 1919-1922.
[10] LUO, Lanxin, et al. Finite element model updating method for continuous girder bridges using monitoring responses and traffic videos [J]. Structural Control and Health Monitoring, 2022, 29.11: e3062.
[11] LIANG, Ruijun, et al. Multiple tuned inerter-based dampers for seismic response mitigation of continuous girder bridges [J]. Soil Dynamics and Earthquake Engineering, 2021, 151: 106954.
[12] Chen S . The Test Research of Stress Monitoring in Construction Stage of WuZhong Yellow River Bridge[J]. Proceedings of the National Academy of Sciences, 2005, 80(15):4842-6.
[13] Zhang H , Yang B , Huang S . Dynamic geometry monitoring system and its application in Sutong Bridge construction[J]. Geo-spatial Information Science, 2010, 13(002):137-143.
[14] Krontal, Ludolf, Tamms, et al. Monitoring of bridge structures as a tool of construction supervision[J]. Bautechnik, 2015, 92(2):123-133.
[15] Sthler S C , Sens-Schnfelder C , Niederleithinger E . Monitoring stress changes in a concrete bridge with coda wave interferometry[J]. The Journal of the Acoustical Society of America, 2011, 129(4):1945-1952.
[16] Saman, Farhangdoust, Armin, et al. Health Monitoring of Closure Joints in Accelerated Bridge Construction: A Review of Non-Destructive Testing Application[J]. Journal of Advanced Concrete Technology, 2019, 17(7):381-404.
[17] LIANG, Ruijun, et al. Multiple tuned inerter-based dampers for seismic response mitigation of continuous girder bridges [J]. Soil Dynamics and Earthquake Engineering, 2021, 151: 106954.
[18] ZHANG, Lu, et al. Reference-free damage identification method for highway continuous girder bridges based on long-gauge fibre Bragg grating strain sensors [J]. Measurement, 2022, 195: 111064.
[19] ZHANG, X. Y., et al. Endowing BIM Model with Mechanical Properties--Finite Element Simulation Analysis of Long-Span Corrugated Steel Web Continuous Beam Bridge [J]. In: Journal of Physics: Conference Series. IOP Publishing, 2022: 012006.

CIVIL ENGINEERING JOURNAL

Article no. 6

THE CIVIL ENGINEERING JOURNAL 1-2024

RESEARCH ON THE DEVELOPMENT OF LOW-TEMPERATURE-RESISTANT FAST-CURING STRUCTURAL ADHESIVE AND STEEL PLATE STRENGTHENING CONCRETE BEAM FLEXURAL TEST

Guanhua Zhang[1], Chengzhe Song[1,2], Xihang Han[3] and Bo Lu[4]

1. *Liaoning Provincial Transportation Planning and Design Institute Co., Ltd, 110166, Shenyang, China; (E-mail: lnzgh123@163.com)*
2. *Liaoning Datong Highway Engineering Co., Ltd, 110111, Shenyang, China; (E-mail: songzhe0323@163.com)*
3. *Shenyang Jianzhu University, School of Transportation and Geomatics Engineering, Shenyang, 110168, China; (E-mail: hxihang@163.com)*
4. *Shenyang University of Chemical Technology, School of Material Science and Engineering, Shenyang, 110142, China; (E-mail: lubo608@sina.com)*

ABSTRACT

Steel plate strengthening method is a common, efficient, and mature reinforcement method that utilizes structural adhesive to bond steel plates with concrete components to work together. It takes advantage of the excellent tensile strength of steel plates to improve the mechanical properties of the original structure. However, epoxy-based structural adhesives are highly sensitive to the environment, and curing effect at low temperatures is a key issue. This study developed a low-temperature-resistant fast-curing structural adhesive (LTR-FCA) that can achieve rapid curing at low temperatures of -5 °C. The flexural performance of reinforced concrete beams strengthened with steel plates using LTR-FCA was compared with that using Normal Structural Adhesive (NSA). Experimental results indicated that LTR-FCA could rapidly cure at a low temperature of -5°C. Compared to NSA, which cures at room temperature, the use of LTR-FCA effectively delayed the debonding of the steel plates.

KEYWORDS

Epoxy resin structural adhesive, Low temperature rapid curing, Debonding failure, Steel plate strengthening method, Concrete structure

INTRODUCTION

The safety and durability of in-service concrete structures have always been hot topics in civil engineering. The main methods for repairing and strengthening concrete structures include enlarging the cross-section [1-4], bonding plates [5-8], or applying prestress [9-12].

The steel plate bonding method is widely studied and used due to its mature technology and effective reinforcement. R Thamrin et al. [13,14] investigated how different reinforcement methods and the lengths of steel plates affect the flexural strength of RC beams. The test results revealed that the length of steel plate application influenced the failure mode of the reinforced beams. Additionally, beams that failed due to debonding bore loads similar to the control beams. Yan et al.

[15] conducted a study to analyze the effects of steel plate thickness and U-shaped steel plate hoops on the failure mechanism and dynamic response of the structure. The result of the research indicates that as the bonded the steel plate thickness increased, the peak displacement and residual displacement in the mid-span decreased by 6.55% and 29.53%, respectively, and the residual flexural capacity increased by 25.02%. When U-shaped steel plate hoops were implemented, the residual flexural capacity of the reinforced beam was significantly improved, and both the peak displacement and residual displacement in the mid-span decreased. Thamrin et al. [16] studied the mechanical properties of reinforced concrete beams with steel plates bonded to the webs. The test variables included the ratio of longitudinal reinforcement and the position of the steel plates. The study emphasized the importance of avoiding steel plates debonding.

Structural adhesives play a crucial role in steel plate reinforcement technology, ensuring that the steel plates are tightly bonded to the structures to be reinforced, thereby enhancing the synergistic effect between them. Epoxy resin and curing agents are the main materials for bridge-strengthening adhesives [17-19]. Consequently, extensive research has been conducted on developing structural adhesives.

Wu et al. [20] evaluated the mechanical properties of two types of hydroxyl-terminated polyurethanes (HTPU1 and HTPU2) modified bisphenol A (DGEBA)/diethyl toluene diamine (DETDA) systems, specifically assessing the influence of phase structure on the overall performances of the resin at room temperature (RT) and cryogenic temperature (77 K). Mohammad et al. [21] studied the effects of carbon-based and silicon-based nanomaterials on the physical-chemical properties of a structural epoxy adhesive. The results showed that the addition of nanomaterials altered the chemical composition of the NE. In addition, impregnating the nanoparticles into NE affected its physical structure, resulting in an increase in porosity and a decrease in crystallinity with increasing wt.%. S Ranji et al. [22] conducted research on the synthesis of new urethane epoxy adhesives and their adhesive properties on different substrates. The findings revealed that compared to common DGEBA-based epoxy adhesives, the novel urethane-epoxy adhesive exhibited superior mechanical properties, specifically in terms of shear strength and elongation. Leena Karthikeyan et al. [23] developed a new type of room-temperature-cured epoxy resin and mixed it with different amounts of hydroxyl-terminated poly(etheretherketone)s (PEEKTOH), a thermoplastic toughening agent. The mixed resin was then cured using triethylenetetramine (TETA). Their research showed that the viscosity of the resin increased with the proportion of PEEKTOH in the epoxy matrix, which subsequently reduced the wetting characteristics. Moreover, the introduction of PEEKTOH phases into the mixture reduced the gel time from 175 minutes to 30 minutes.

However, epoxy resin adhesives are highly susceptible to environmental conditions, with the curing temperature being primarily determined by the reactivity of both the curing agent and the resin itself. In situations where the ambient temperature is below 0 °C, the adhesive may experience crystallization hardening and other related issues. Many current adhesives either cannot be fully cured at low temperatures or require extended curing times, which directly impact progress and quality of the project. Therefore, the development of low-temperature-resistant fast-curing structural adhesives (LTR-FCA) has always been a crucial topic within the field of engineering reinforcement.

Moussa et al. [24,25] discovered that the tensile properties of a commercial structural epoxy adhesive are greatly influenced by the curing temperature. At lower temperatures, the curing process slows down significantly, resulting in a corresponding reduction in the development rate of mechanical properties. At 0 °C, the curing process is either completely inhibited or fails to initiate altogether. Younes Jahani et al. [26] conducted a comprehensive experimental study to investigate the influence of temperature on the mechanical properties and glass transition temperature (T_g) of a structural epoxy adhesive. The results showed that the curing process (curing and post-curing) temperature had a positive impact when it was below the T_g, but had a negative impact when it exceeded the T_g. Ricardo Cruz et al. [27] studied the effects of the preparation, curing, and hygrothermal conditions on the viscoelastic response of a structural epoxy adhesive. The results showed that the preparation method had a significant impact on the tensile properties of the adhesive,

particularly on its viscoelastic response. Specimens that were degassed and cured at 20 °C exhibited lower creep deformations. However, specimens that were exposed to 98% relative humidity experienced tertiary creep before ultimately rupturing.

This study aims to prepare a low-temperature-resistant fast-curing structural adhesive (LTR-FCA) by adjusting the ratio of epoxy resin to low-temperature curing agents, and introducing toughening agents, promoters, and inorganic fillers as modifiers. Subsequently, flexural tests on reinforced concrete beams were conducted under different temperature conditions (-25°C, -5°C and 20°C), to investigate the bonding performance of LTR-FCA in low-temperature environments, and compare its adhesive effects with that of normal structural adhesives used under room temperature conditions.

DEVELOPMENT OF STRUCTURAL ADHESIVE FOR STEEL BONDING

Material composition

Epoxy resin curing agents commonly used include dicyandiamide, imidazole derivatives, anhydrides, and aromatic amines [28-31], among these curing agents typically require high or relatively high temperatures to effectively cure epoxy resin. At room temperature and low temperatures, mercaptan-based curing agents and thiourea-modified amine curing agents can achieve a rapid cure. There are numerous types of mercaptan-based curing agents [32-34], with common examples being liquid oligomers or multi-thiol compounds. The selection of accelerators varies depending on the structure of the mercaptan curing agent, resulting in differences in curing temperature and time.

Polythiol curing agent [35-37] is a type of multi-thiol that can be prepared by reacting β-mercaptopropionic acid with pentaerythritol to generate a multi-thiol ester. This ester is then heated and extended using a small amount of E-51 epoxy resin. The polythiol curing agent acts as a fast-curing agent at room temperature or low temperature, with low toxicity. When combined with an amine promoter, the epoxy resin can be cured within 1-5 minutes. Even under low temperatures (-20-0°C) and humid environments, the addition of promoter DMP-30 can also cure the epoxy resin. The curing time is 2-10 minutes, and the strength for use can be reached after 10-30 minutes. Full cure takes 7 days.

The main research and development ideas are: (a) By adjusting the ratio of epoxy resin E-51 and epoxy resin JD919, an epoxy resin that does not crystallize in a low temperature environment of -5 °C is formulated; (b) Fillers such as silica, white carbon black, and microbeads make the adhesive paste-like, with thixotropic and non-slippery properties during application, and reduce the linear expansion coefficient of the adhesive. (c) Toughgeners can improve the toughness and low-temperature resistance of the adhesive, and reduce the cure shrinkage. (d) Low-temperature curing agents (thiourea-modified aliphatic polyamines and polythiols) can promote the curing of the adhesive in a low-temperature environment of -5 °C or above, with good resistance to acids, bases, and water.

After multiple experiments, the optimal ratio of low-temperature-resistant fast-curing structural adhesive was obtained. Refer to Table 1 for details.

Tab. 1 - Recipe of structural adhesive for steel bonding (unit: g)

Type of glue	Materials	Component
A	Epoxy resin E-51	80.0
	Epoxy resin JD919	10.0
	polysulfide rubber	15.0
	coupling agent	2.0
	silica micro powder	98.0
	white carbon black	2.0
	microbeads	1.5
B	thiourea fatty polyamine	20.0
	polymeric mercaptan	10.0
	accelerator; promoter	3.0
	silica micro powder	31.0
	white carbon black	2.0
Proportion: A / B	100 / 32.5	

Material Properties

The material tests of low-temperature-resistant fast-curing structural adhesive (LTR-FCA) were carried out, and the average values of 5 specimens in each group were taken, as shown in Figure 1.

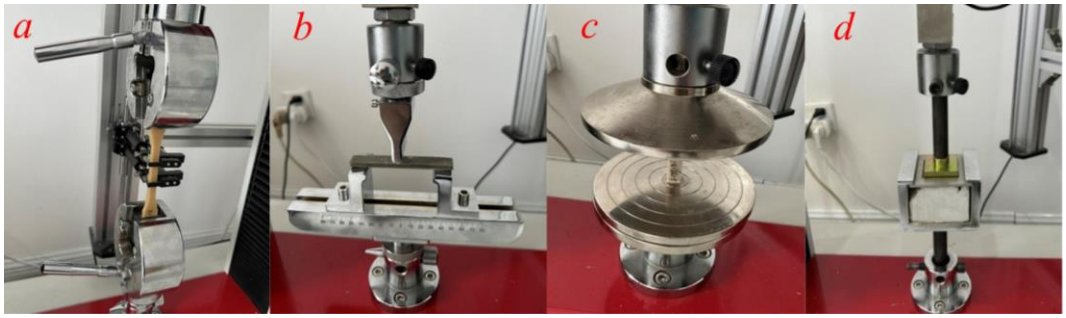

(a) Tensile test, (b) Flexural test, (c) Compressive test, (d) Test of normal tensile bond strength with concrete.

Fig.1 - Material Test

There are 2 types of test curing stages:

Curing stage I: At -5 °C, the curing period is 7 days, marked as 7d (-5 °C); According to the specifications [38], during this curing stage, the strength of the glue should reach 90% of the technical indicators.

Curing stage II: After curing for 7 days at -5 °C, it shall be cured for another 3 days at 23±2 °C, marked as 7d (-5 °C) + 3d (23±2 °C). At the same time, the specifications stipulate that after the curing stage, the strength of the rubber should meet the requirements of technical indicators.

Table 2 shows the test results of the material properties of LTR-FCA under the two conditions mentioned above.

Tab. 2 - Material properties of LTR-FCA

Material index	7d(-5 °C)		7d(-5 °C) + 3d(23±2 °C)	
	Indicator	Test value	Indicator	Test value
Tensile strength (MPa)	≥ 27.0	39.3	≥ 30	43.2
Tension elastic modulus (MPa)	≥ 2.9(×10^3)	5.2	≥ 3.2(×10^3)	5.5
Elongation (%)	≥ 1.1	1.4	≥ 1.2	1.4
Flexural strength (MPa)	≥ 40.5	65.2	≥ 45.0	95.7
Compressive strength (MPa)	≥ 58.5	63.7	≥ 65.0	74.8
Tensile shear strength of steel-steel (MPa)	≥ 13.5	13.5	≥ 15.0	15.3
Steel-steel T impact stripping length (mm)	≤ 27.8	0.0	≤ 25.0	0.0
Tensile strength of steel-steel butt bond (MPa)	≥ 29.7	30.3	≥ 33.0	34.1
The tensile bond strength with concrete (MPa)	≥ 2.2	2.6	≥ 2.5	3.0
Non-volatile matter content (%)	≥ 89.1	99.6	≥ 99.0	99.6

From Table 2, it can be seen that all material performance tests meet the requirements of the technical specifications, especially with regards to tensile strength and flexural strength, which reached 43.2MPa and 95.7MPa respectively, demonstrating excellent material performance.

TEST OF STRENGTHENING CONCRETE BEAMS WITH STRUCTURAL ADHESIVES

This study has developed a low-temperature-resistant fast-curing structural adhesive (LTR-FCA) for steel bonding in concrete reinforcement, aiming to improve the construction convenience and reliability of the structural adhesive in low-temperature environments. In addition, to verify the superiority of its materials and mechanical properties, the strengthening beam was conducted flexural test to compare and analyze it with normal structural adhesives (NSA).

A total of 3 groups of test beams were designed, with dimensions of 2900mm in length, 280mm in width, and 340mm in height. The three groups of specimens were tested at 20 °C, -5 °C, and -25 °C. Each group consists of 3 test beams, one of which is a normal reinforced concrete beam without steel plate bonding, while the other two beams are strengthened with NSA and LTR-FCA, respectively. Strengthening beams with 1600 mm×200 mm×3 mm Q235 steel plates at the bottom, and the thickness of the adhesive layer is controlled at 2mm. The main parameters of the test beams are shown in Table 3.

Tab. 3 - Main parameters of the test beams

Group	Label	Type of structural adhesives	Steel plate thickness (mm)	Cultivation method	Testing temperature (°C)
I	CB+20	/	/	/	20
	NTB+20	NSA	3	7d (23±2 °C)	
	LTB+20	LTR-FCA	3	7d (-5 °C) + 3d (23±2 °C)	
II	CB-5	/	/	/	-5
	NTB-5	NSA	3	7d (23±2 °C)	
	LTB-5	LTR-FCA	3	7d (-5 °C) + 3d (23±2 °C)	
III	CB-25	/	/	/	-25
	NTB-25	NSA	3	7d (23±2 °C)	
	LTB-25	LTR-FCA	3	7d (-5 °C) + 3d (23±2 °C)	

The test beams were crafted from C40 commercial concrete, and the concrete cube strength (f_{cu}) was determined through experiments conducted at 20 °C, -5 °C, and -25 °C, resulting in values of 48.7MPa, 44.0MPa, and 52.3MPa, respectively. The longitudinal tensile steel bars incorporate four HRB400 steel bars with a diameter of 28mm (f_y = 420MPa). The stirrups and bracket steel bars

feature HRB400 steel bars with a diameter of 10mm (f_y = 448MPa). The steel plate is fashioned from Q235 steel with a yield strength of 235 MPa. Both the steel bars and steel plates are assumed to have an elastic modulus of 200 GPa. The configuration of reinforcement in the test beams is presented in Figure 2.

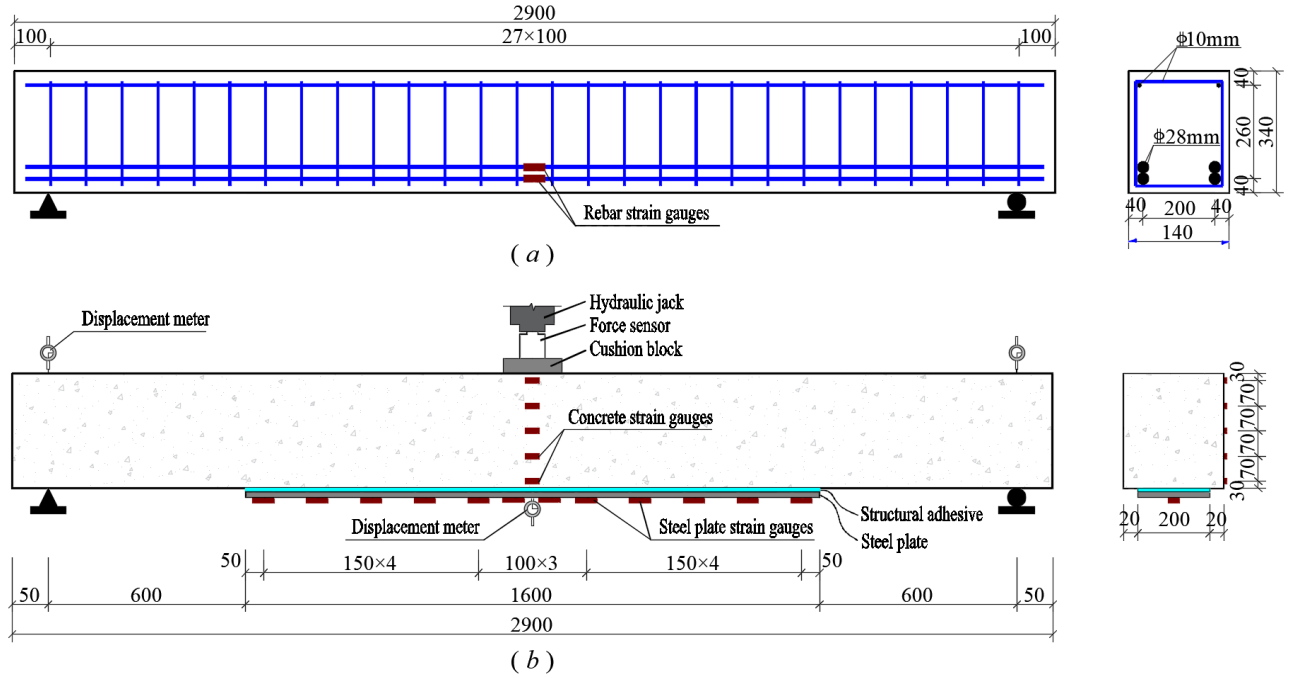

Fig. 2 - Design of test beam (unit: mm)

Displacement meters were arranged at the support and mid-span positions of the test beam, and concrete strain gauges were installed along the height of the beam at the mid-span position. Rebar Strain gauges were adhered to the longitudinal reinforcement at the mid-span position. Steel plate strain gauges were affixed to the steel plate at the bottom of the beam to monitor the strain values in real-time during the loading process and determine whether the steel plate has peeled off.

After the test beams were poured and cured for 90 days, the steel plate was pasted. The specific pasting method and curing process are as follows:

(1) NTB+20, NTB-5, NTB-25: Paste and cure for 7 days at (23±2) °C.

(2) LTB+20, LTB-5, LTB-25: Paste and cure for 7 days at -5 °C, then cure for 3 days at (23±2) °C.

After the completion of the curing process, the test beams were placed in an environmental simulation chamber, and after 4 hours at the predetermined temperature, a uniaxial three-point load was applied. The load was applied in a displacement gradient manner through a jack.

FAILURE PHENOMENON AND RESULT ANALYSIS OF TEST BEAMS

Load – displacement curve and failure process

A total of 9 beams were tested, respectively at 20 °C, -5 °C and -25 °C. The main variables in the experiment were the type of adhesive and the test temperature.

The main experimental results are shown in Table 4. By bonding steel plates to the bottom surface of the concrete beam with structural adhesive, the steel plates and the test beam were integrated, effectively bearing the stress at the bottom of the beam, enhancing the stiffness of the beam, and increasing the cracking load of the beam. The cracking load of the reinforced test beams increased by 10~20 kN, and the propagation of bottom cracks in the concrete beams was effectively delayed before the steel plates peeled off.

Tab - 4 Main experimental results

Label	Cracking load (kN)	Peeling load of steel plate (kN)	Ultimate load of beam (kN)
CB+20	49.7	/	429.7
NTB+20	61.2	261.9	418.1
LTB+20	69.6	309.7	422.1
CB-5	48.3	/	424.8
NTB-5	62.0	287.1	412.4
LTB-5	70.5	311.4	419.3
CB-25	47.5	/	424.3
NTB-25	59.5	290.2	442.9
LTB-25	69.4	321.7	425.0

The strengthened beams in the test all experienced steel plate peeling before the beam failure, with NTB-5, LTB+20 and LTB-25 as examples, which is illustrated in Figure 3. Ultimately, both the control beams and the reinforced beams experienced flexural failure, with CB-25, NTB-25 and LTB-25 as examples, which is illustrated in Figure 4.

(a) NTB-5

(b) LTB+20

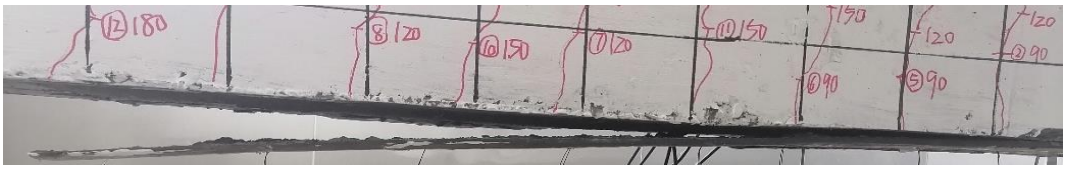

(c) LTB-25

Fig. 3 - Peeling of steel plate

(a) CB-25

(b) NTB-25

Fig. 4 - The crack distribution of test beams

(c) LTB-25

Fig. 4 - The crack distribution of test beams

Figure 5 shows the load-displacement relationship of the test beams at different temperatures. When the test temperature was reduced from 20°C to -5°C and -25°C, the peel loads of both types of structural adhesives increased. For the test beams NTB-5 and NTB-25 using NSA, their peel loads increased by 9.6% and 10.8% respectively compared to NTB+20; while for the test beams LTB-5 and LTB-25 using LTR-FCA, the increase was 0.5% and 3.9% respectively compared to LTB+20. Compared to NSA, LTR-FCA has a lower sensitivity to temperature changes, demonstrating better curing stability.

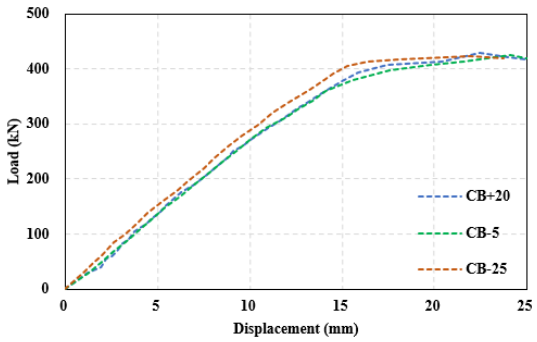

(a) CB

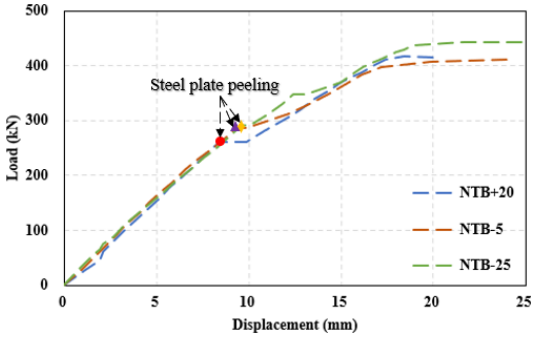

(b) NSA

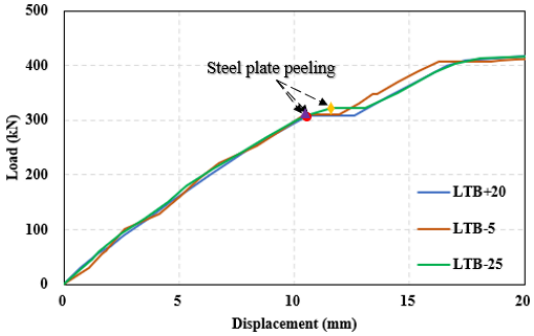

(c) LTR-FCA

Fig. 5 - Load – displacement curve

As shown in Figure 6, at different test temperatures, the peeling load of the test beams reinforced with LTR-FCA was generally higher than that of the beams reinforced with NSA. Specifically, at -25°C, the peeling load of LTR-FCA increased by 10.78% compared to NSA; it increased by 8.50% at -5°C; and at +20°C, it increased by 18.21%. This indicates that the LTR-FCA can effectively cure even in low-temperature environments and demonstrates superior bonding performance.

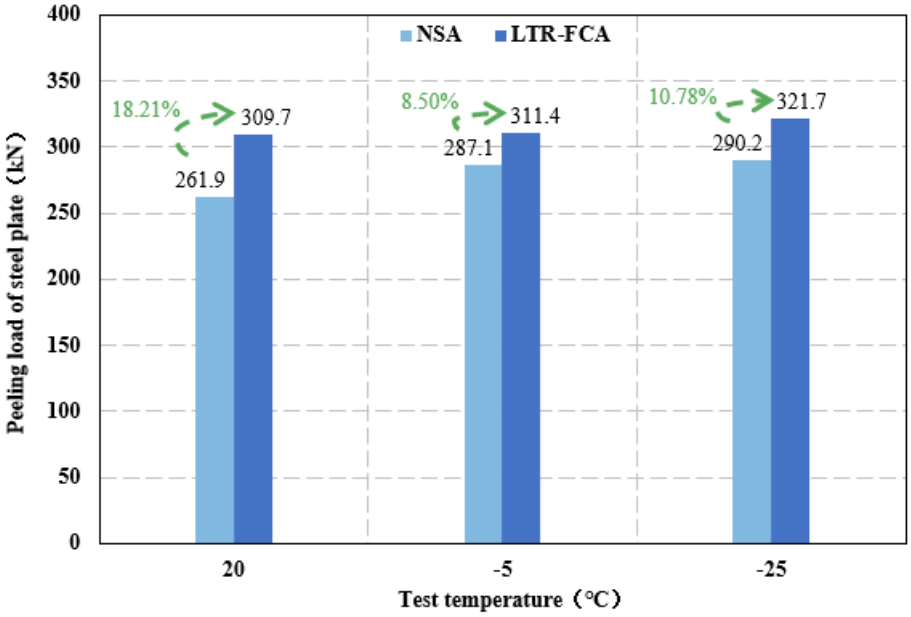

Fig. 6 - Peeling load of steel plate (kN)

In the later stages of the test beams after the steel plate was peeled off, the flexural capacity of the strengthened beams was not significantly different from the control beams. This is because the flexural load-bearing capacity of the beam is mainly determined by the dimensions of the beam, the number of longitudinal reinforcements, and the strength of the concrete. In addition, the test beams exhibited typical flexural failure.

Strain

The curves of strain versus load for test beams are shown in Figure 7. It can be seen from Figure 7 that during the initial loading period, the neutral axis remained stable near the mid-span of the beam, and the cross-section approximately met the plane section assumption. As the load increased, the cross-section cracked, and the neutral axis gradually shifted towards the compressive zone. Overall, however, the strain condition remained largely consistent with the plane section assumption.

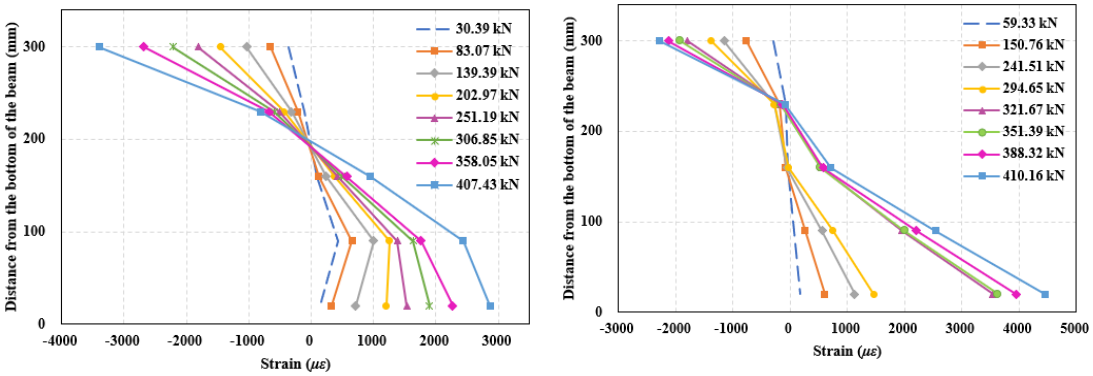

(a) CB+20 *(b) LTB-25*

Fig. 7 - Load-strain curve in the mid-span section of the test beam

Figure 8 shows the strain response curves of longitudinal reinforcement under different loads. It is observed that the trend of strain variation in the longitudinal reinforcement of the test beams with increasing load is consistent with their load-displacement curves. When the steel plate peeling occurs, the strain in the longitudinal reinforcement of the strengthened beams increases sharply,

ranging from 476 με (NTB-5) to 746 με (NTB+20). This indicates that once the steel plate peeling, it loses its load-bearing capacity, leading to a greater load on the longitudinal reinforcement and thus a significant increase in strain. All test beams ultimately experienced the yielding of longitudinal reinforcement and the crushing of concrete in the compression zone, demonstrating good ductility and exhibiting a typical flexural failure mode.

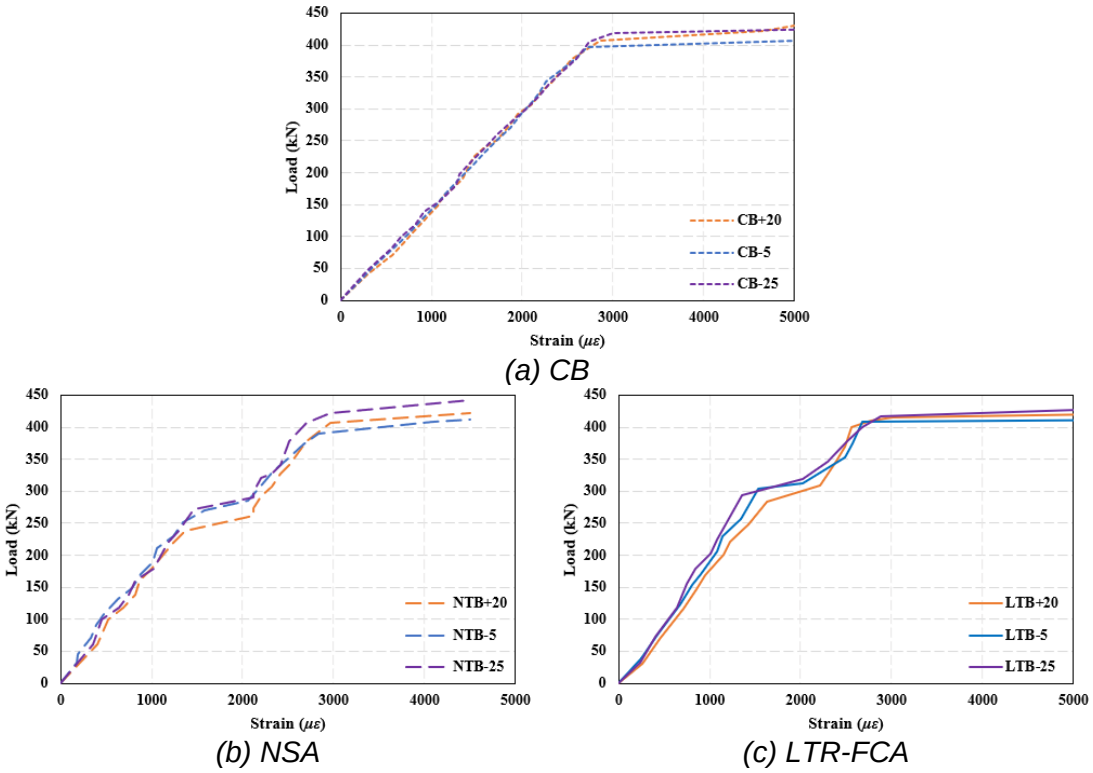

(a) CB

(b) NSA

(c) LTR-FCA

Fig. 8 - Load-strain response curves of the longitudinal reinforcements

Figure 9 shows the relationship curve between the steel plate strain and load for some of the test beams. It can be observed that as the load gradually increases, the strain in the steel plate correspondingly rises. This is particularly noticeable at the mid-span position of the steel plate, where the strain increment is significantly higher than at the ends, while the stress at the ends remains almost unchanged; when the end steel plates become detached, the stress at the mid-span position drops rapidly. This indicates that during the loading process, the steel plate mainly bears shear forces at the mid-span, while it primarily withstands normal stress at the ends. It is recommended that in practical engineering applications, bolting at the ends of steel plates should be used for anchoring to delay the peeling phenomenon.

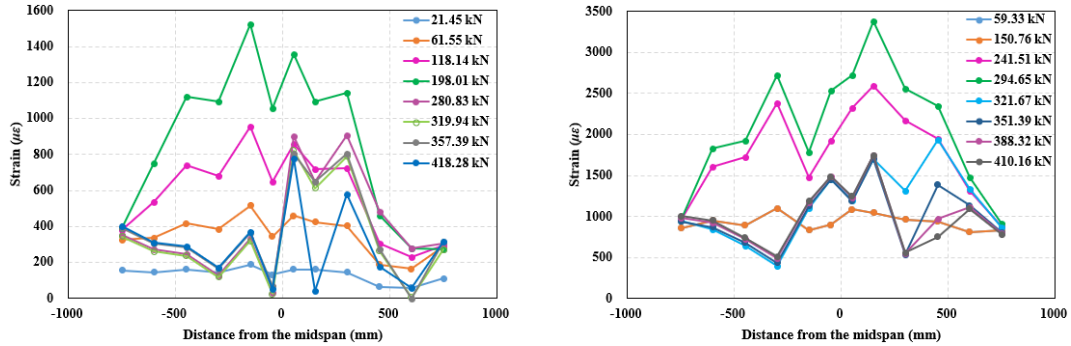

(a) NTB+20

(b) LTB-25

Fig. 9 - Load-strain curve in steel plates of the test beam

As shown in Figure 10, when the test temperature was reduced from 20°C to -25°C, the loads corresponding to the maximum steel plate strain for beams using NSA were 261.9kN, 287.1kN, and 290.2kN, respectively, while for beams using LTR-FCA, the loads were 309.7kN, 311.4kN, and 321.7kN, respectively. These results indicate that as the test temperature decreases, the maximum strain of the steel plate increases, consistent with the relationship between peel load and temperature. This phenomenon can be explained by the principle of thermal expansion and contraction: the reduction in temperature causes the inter-particle spacing between the substrate and the adhesive to decrease, enhancing their bonding strength. And at the same test temperature, the maximum strain of steel plate LTR-FCA (1753 με~2723 με) is greater than that of NSA (1347 με~1893 με), which is consistent with the relationship between the peeling load of the two adhesives, exhibits better bond strength of LTR-FCA.

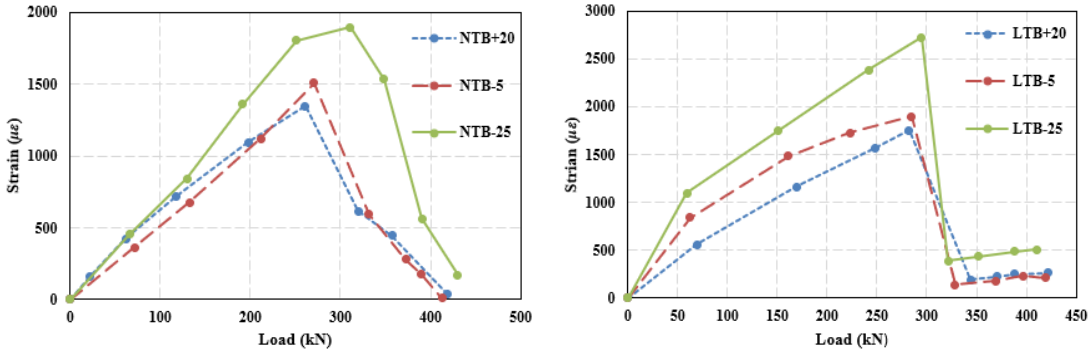

(a) Load strain at midspan of the NSA steel plate

(b) Load strain at midspan of the LTR-FCA steel plate

Fig. 10 - Load-strain curve in steel plates of the test beam

CONCLUSION

This study developed a low-temperature-resistant fast-curing structural adhesive for winter construction and tested its mechanical properties. Additionally, experimental research on the application of structural adhesives to reinforce concrete was conducted. The main conclusions are as follows:

(1) By bonding steel plates to the bottom surface of concrete beams with structural adhesive, the steel plates and the test beams are integrated to effectively bear the stress at the bottom of the beam. This method enhances the stiffness of the beam and increases its cracking load. It also effectively delays the expansion of cracks at the bottom of the concrete beam before the steel plates peel off.

(2) For the NTB-5 and NTB-25 beams using NSA, the peeling load increased by 9.6% and 10.8% compared to NTB+20. While for LTB-5 and LTB-25 beams using LTR-FCA, the peeling load increased by 0.5% and 3.9% compared to LTB+20. Whether it is NSA or LTR-FCA, their peel load shows a certain trend of increasing with the decrease of the test temperature.

(3) At 20 °C, -5 °C, and -25 °C, the peeling load of LTR-FCA is 18.21%, 8.50%, and 10.57% higher than that of NSA, respectively. That is, at the same test temperature, the peeling load of LTR-FCA is always higher than that of NSA. This reflects the good effect of LTR-FCA on the reinforcement of concrete structures.

(4) The developed LTR-FCA can effectively cure in low-temperature environments and possesses excellent material properties and adhesive strength. Considering that the ends of steel plates primarily bear normal stress, it is recommended to use bolt anchoring at the ends of steel plates in engineering applications to mitigate the peeling phenomenon.

ACKNOWLEDGEMENTS

This research was funded by the Transportation Science and Technology Project of Liaoning Provincial (202129).

REFERENCES

[1] X. Gao, K. Wu, Y. Guo, Y. Zhao, J. Guo, Experimental and numerical study on flexural behaviors of damaged RC beams strengthened with UHPC layer using the bonding technology of post-installed reinforcing bar, Construction and Building Materials. 391 (2023) 131835, doi: 10.1016/j.conbuildmat.2023.131835.

[2] M.M.A. Kadhim, A. Jawdhari, W. Nadir, A. Majdi, Experimental study on RC beams strengthened in flexure with CFRP-Reinforced UHPC overlays, Engineering Structures. 285 (2023) 116066, doi: 10.1016/j.engstruct.2023.116066.

[3] W. Nadir, M.M.A. Kadhim, A. Jawdhari, A. Fam, A. Majdi, RC beams strengthened in shear with FRP-Reinforced UHPC overlay: An experimental and numerical study, Structures. 53 (2023) 693-715, doi: 10.1016/j.istruc.2023.04.117.

[4] D. Mirdan, A.R. Saleh, Flexural performance of reinforced concrete (RC) beam strengthened by UHPC layer, Case Studies in Construction Materials. 17 (2022) e1655, doi: 10.1016/j.cscm.2022.e01655.

[5] X. He, C. Zhou, M. Lv, Y. Wang, Y. Liu, Interfacial stresses of beams hybrid strengthened by steel plate with outside taper and FRP pocket, Journal of Building Engineering. 75 (2023) 107034, doi: 10.1016/j.jobe.2023.107034.

[6] S. Hadi, E. Kazeminezhad, S. Safakhah, Full-scale experimental evaluation of flexural strength and ductility of reinforced concrete beams strengthened with various FRP mechanisms, Structures. 43 (2022) 1160-1176, doi: 10.1016/j.istruc.2022.07.011.

[7] M.J. Jedrzejko, J. Tian, S.S. Zhang, Y. Ke, X.F. Nie, Y.M. Yang, Strengthening of RC beams in shear with novel near-surface mounted (NSM) U-shaped fiber-reinforced polymer (FRP) composites, Engineering Structures. 292 (2023) 116479, doi: 10.1016/j.engstruct.2023.116479.

[8] D. Guo, H. Zhou, H. Wang, J. Dai, Effect of temperature variation on the plate-end debonding of FRP-strengthened steel beams: Coupled mixed-mode cohesive zone modeling, Engineering Fracture Mechanics. 270 (2022) 108583, doi: 10.1016/j.engfracmech.2022.108583.

[9] Z. Wang, J. Xie, J. Li, P. Liu, C. Shi, Z. Lu, Flexural behaviour of seawater–sea sand concrete beams reinforced with GFRP bars: Effects of the reinforcement ratio, stirrup ratio, shear span ratio and prestress level, Journal of Building Engineering. 54 (2022) 104566, doi: 10.1016/j.jobe.2022.104566.

[10] H. Wang, Z. Bian, M. Chen, L. Hu, Q. Wu, Flexural strengthening of damaged steel beams with prestressed CFRP plates using a novel prestressing system, Engineering Structures. 284 (2023) 115953, doi: 10.1016/j.engstruct.2023.115953.

[11] W. Du, C. Yang, Y. Pan, Y. Chen, H. Zhang, Study on the flexural behaviours of precracked hollow core beams strengthened with core filling and unbonded prestressing steel strands, Engineering Structures. 274 (2023) 115075, doi: 10.1016/j.engstruct.2022.115075.

[12] J. Deng, K. Rashid, X. Li, Y. Xie, S. Chen, Comparative study on prestress loss and flexural performance of rectangular and T beam strengthened by prestressing CFRP plate, Composite Structures. 262 (2021) 113340, doi: 10.1016/j.compstruct.2020.113340.

[13] R. Thamrin, Effect of strengthening method and development length on flexural strength of rc beams with steel plates, Journal of Engineering Science and Technology. 13 (11) (2018) 3781-3794.

[14] R. Thamrin, R.P. Sari, Flexural Capacity of Strengthened Reinforced Concrete Beams with Web Bonded Steel Plates, Procedia Engineering. 171 (2017) 1129-1136, doi: 10.1016/j.proeng.2017.01.474.

[15] X. Yan, T. Zheng, C. Lin, G. Lan, H. Mao, Experimental Research on the Impact Resistance of Partially Precast Concrete Beams Strengthened with Bonded Steel Plates, in: Applied Sciences, 2023, p.

[16] R. Thamrin, Zaidir, A. Wahyuni, Shear capacity of reinforced concrete beams strengthened with web bonded steel bars or steel plates, Results in Engineering. 17 (2023) 100953, doi: 10.1016/j.rineng.2023.100953.

[17] C. Liu, Y. He, M. Sun, X. Zhang, B. Zhang, X. Bai, Influence of epoxy resin species on the curing behavior and adhesive properties of cyanate Ester/Poly(aryl ether nitrile) blends, Polymer. 288 (2023) 126450, doi: 10.1016/j.polymer.2023.126450.
[18] F. Zhu, Q. Fu, M. Yu, J. Zhou, N. Li, F. Wang, Synthesis and curing properties of multifunctional castor oil-based epoxy resin, Polymer Testing. 122 (2023) 108017, doi: 10.1016/j.polymertesting.2023.108017.
[19] J. Wei, Y. Duan, H. Wang, W. Zhang, Study on copolymerization modification and properties of bio-based trifunctional diphenolic acid epoxy resin by CE and DPR, Polymer. 284 (2023) 126308, doi: 10.1016/j.polymer.2023.126308.
[20] T.Y.N.G. Wu, Cryogenic mechanical properties of epoxy resin toughened by hydroxyl-terminated polyurethane, Polymer Testing. 74 (2019).
[21] M. Al-Zu'Bi, L. Anguilano, M. Fan, Effect of incorporating carbon- and silicon-based nanomaterials on the physico-chemical properties of a structural epoxy adhesive, Polymer Testing. 128 (2023) 108221, doi: 10.1016/j.polymertesting.2023.108221.
[22] S. Ranji, M.C. Lee, Study on synthesizing new urethane epoxy adhesives and their adhesive properties on different substrates, International Journal of Adhesion & Adhesives (2022) 117A.
[23] L. Karthikeyan, T.M. Robert, D. Mathew, D.D. Suma, D. Thomas, Novel epoxy resin adhesives toughened by functionalized poly (ether ether ketone) s, International Journal of Adhesion and Adhesives. 106 (2021).
[24] O. Moussa, A.P. Vassilopoulos, J. de Castro, T. Keller, Early-age tensile properties of structural epoxy adhesives subjected to low-temperature curing, International Journal of Adhesion and Adhesives. 35 (2012) 9-16, doi: 10.1016/j.ijadhadh.2012.01.023.
[25] O. Moussa, A.P. Vassilopoulos, T. Keller, Effects of low-temperature curing on physical behavior of cold-curing epoxy adhesives in bridge construction, International Journal of Adhesion and Adhesives. 32 (2012) 15-22, doi: 10.1016/j.ijadhadh.2011.09.001.
[26] R. Cruz, L. Correia, S. Cabral-Fonseca, J. Sena-Cruz, Effects of the preparation, curing and hygrothermal conditions on the viscoelastic response of a structural epoxy adhesive, International Journal of Adhesion and Adhesives. 110 (2021) 102961, doi: 10.1016/j.ijadhadh.2021.102961.
[27] Y. Jahani, M. Baena, C. Barris, R. Perera, L. Torres, Influence of curing, post-curing and testing temperatures on mechanical properties of a structural adhesive, Construction and Building Materials. 324 (2022) 126698, doi: 10.1016/j.conbuildmat.2022.126698.
[28] J. Kamalipour, M.H. Beheshty, M.J. Zohuriaan-Mehr, Novel phosphonated hardeners derived from diamino diphenyl sulfone for epoxy resins: Synthesis and one-pack flame-retardant formulation alongside dicyandiamide, Polymer Degradation and Stability. 199 (2022) 109917, doi: 10.1016/j.polymdegradstab.2022.109917.
[29] S. Lin, G. Lai, M. Chen, L. Su, J. Lan, W. Zhong, H. Zhang, Boosting both flame retardancy and mechanical properties of carbon fiber/epoxy composites via polycyclic phosphorus-nitrogen imidazole derivative, Chemical Physics Letters. 805 (2022) 139946, doi: 10.1016/j.cplett.2022.139946.
[30] X. Liu, J. Zhou, M. Wu, S. Liu, J. Zhao, Design and synthesis of anhydride-terminated imide oligomer containing phosphorus and fluorine for high-performance flame-retarded epoxy resins, Chemical Engineering Journal. 461 (2023) 142063, doi: 10.1016/j.cej.2023.142063.
[31] J. Li, Z. Weng, Q. Cao, Y. Qi, B. Lu, S. Zhang, J. Wang, X. Jian, Synthesis of an aromatic amine derived from biomass and its use as a feedstock for versatile epoxy thermoset, Chemical Engineering Journal. 433 (2022) 134512, doi: 10.1016/j.cej.2022.134512.
[32] H. Zhang, J. Gao, Z. Guo, X. Wang, Q. Li, Z. Miao, The influence of the helical twisting power on the bistable electro-optical performance of the liquid crystalline epoxide/mercaptan /negative-dielectric-anisotropy cholesteric liquid crystal composite films, Optical Materials. 142 (2023) 114091, doi: 10.1016/j.optmat.2023.114091.
[33] F. Ahangaran, M. Hayaty, A.H. Navarchian, Y. Pei, F. Picchioni, Development of self-healing epoxy composites via incorporation of microencapsulated epoxy and mercaptan in poly(methyl methacrylate) shell, Polymer Testing. 73 (2019) 395-403, doi: 10.1016/j.polymertesting.2018.11.041.

[34] W. Shen, L. Wang, T. Zhong, G. Chen, C. Li, M. Chen, C. Zhang, L. Zhang, K. Li, Z. Yang, H. Yang, Electrically switchable light transmittance of epoxy-mercaptan polymer/nematic liquid crystal composites with controllable microstructures, Polymer. 160 (2019) 53-64, doi: 10.1016/j.polymer.2018.11.022.
[35] Z. Zhang, F. Gao, L. Li, L. Wei, Z. Su, H. Li, Y. Liu, H. Liu, Y. Liu, Performance study of an epoxy–polythiol curing system for local insulating spraying based on the imbalance stoichiometric ratio, Materials Letters. 351 (2023) 135123, doi: 10.1016/j.matlet.2023.135123.
[36] Z. Belbakra, Z.M. Cherkaoui, X. Allonas, Photocurable polythiol based (meth)acrylate resins stabilization: New powerful stabilizers and stabilization systems, Polymer Degradation and Stability. 110 (2014) 298-307, doi: 10.1016/j.polymdegradstab.2014.09.012.
[37] Y.C. Yuan, M.Z. Rong, M.Q. Zhang, Preparation and characterization of microencapsulated polythiol, Polymer. 49 (10) (2008) 2531-2541, doi: 10.1016/j.polymer.2008.03.044.
[38] MOHURD, Technical code for safety appraisal of engineering structural strengthening materials, in: GB 50728 - 2011, China Architecture & Building Press.

CIVIL ENGINEERING JOURNAL

Article no. 7

THE CIVIL ENGINEERING JOURNAL 1-2024

DAMAGE DETECTION ON COOLING TOWER SHELL BASED ON MODEL TEXTURES

David Zahradník and Filip Roučka

Czech Technical University in Prague, Faculty of Civil Engineering, Department of Geomatics, Thákurova 7, Praha 6, Czech Republic; david.zahradnik@fsv.cvut.cz

ABSTRACT

Ensuring the structural integrity of cooling towers is paramount for safety and efficient operation. This paper presents a novel approach for detecting damage on cooling tower shells, utilising textures derived from laser scanning and close-range photogrammetry. The proposed method delves beyond the limitations of solely relying on colour information by harnessing the rich details embedded in various textures, including diffuse, normal, displacement, and occlusion. The study demonstrates the efficacy of this approach for identifying significant concrete damage. A Convolutional Neural Network (CNN) trained on diffuse textures successfully detects high damage instances with minimal misdetection. However, accurately pinpointing low damage, often manifesting as subtle cracks, and mimicking other patterns like air pores, ribbing, and colour variations, presents a formidable challenge. To tackle this challenge, the authors introduce a novel "composed raster layer" that merges information from multiple textures. This pre-processed layer amplifies the visual cues associated with low damage, facilitating its differentiation from similar patterns. While the current implementation employing multi-resolution segmentation and rule-based classification exhibits promising results, further optimization is acknowledged to refine the accuracy of low damage detection. The successful application of textures commonly used in rendering techniques underscores their remarkable potential for enhancing damage detection in civil engineering applications. While acknowledging limitations such as the analysis of a single cooling tower and the reliance on specific software for damage detection, the study proposes future research directions. This research holds significant implications for the field of civil engineering by offering a promising approach for automated and efficient damage detection on cooling tower shells.

KEYWORDS

Cooling tower, Texture, Diffuse, Normal, Displacement, Concrete damage, CNN, UAV

INTRODUCTION

Over the past decade, interest in UAV-sourced data and Structure from Motion (SfM) photogrammetry has surged, transforming aerial remote sensing and mapping. Unmanned Aerial Vehicles (UAVs) represent one of the fastest-growing sectors across various industries including construction, industry, forestry, and ecology, with their applications continually expanding [1]. UAVs play a crucial role in documenting cultural heritage sites, offering a unique perspective and detailed imaging capabilities that aid in preservation efforts [2-4]. The increased availability of UAVs with onboard GNSS RTK offers a promising alternative to georeferencing using ground control points (GCPs), although systematic elevation errors persist [5-6]. Their ability to capture high-resolution imagery provides valuable insights into vegetation health, growth patterns, and environmental changes over time. This versatility underscores the wide-ranging utility of UAVs in ecological research and management practices.

Cooling towers are heat rejection devices used to transfer waste heat from the production process in power, chemical or nuclear plants. The hot water is transferred to air spray and sprayed

on inlet filling where it is cooled and collected in a cold-water basin. Multiple types of cooling towers exist, including the smaller force draft cooling tower, which is box-shaped and uses a propeller within the tower to provide an airflow for the cooling process. The second type of cooling tower is designed in the shape of a hyperboloid and utilises a natural air draft for cooling [7-8].

The design of the hyperbolic cooling tower includes the primary parameters of the tower: height, outlet radius, inlet radius, and throat radius. The throat radius should be smaller than the outlet radius to ensure an uninterrupted flow of steam in the cooling tower. The throat radius's height is around two-thirds of the cooling tower's height. The tower outlet is indicated by red and white aircraft markings. Every construction that exceeds a certain height threshold must display aircraft markings to ensure the preservation of safe airspace [9]. The most vulnerable part of the cooling tower is the tower shell. The thickness of the shell is lower than 30cm, which makes the structure vulnerable to gusts of wind and seismic events [10-11]. The tower should periodically undergo a geometry control to prevent a collapse of the structure. Basic geometric control uses the total station to estimate the imperfection of tower geometry. Points are measured in vertical lines from a minimum of three positions. The limitation of the methods is the count of measured points. For detailed measurements, laser scanning is a suitable method, whose precision is similar to total station. Laser scanning is faster and gives more data on tower conditions for further analysis [12-16]. High humidity is not a suitable environment for reinforced concrete. Cooling tower shells degrade during years of operation. Humidity from the cooling process precipitates on the inner tower shell and it is looking for the easiest way out. When a crack in the tower shell appears, humidity flows through the material and reinforcement steel bars to corrode. Over time, corrosion begins to spread along the iron, leading to the expansion of the crack. More humidity starts to flow into the crack and stays there. In the last step, the size of a crack causes detachment of the concrete’s part and the cavity creation. The structural integrity of the tower shell is compromised, posing a threat to the vicinity of the cooling tower and its operational stability [17].

Detection of damage caused by humidity is important to stop spreading of the corrosion along reinforced steel. Companies which provide cooling tower maintenance use visual control of damage from the ground by binoculars. This method does not provide accurate results. There are several solutions for damage detection and the first is the localisation of damage by laser scanning. Damage with concrete detachment is detectable by local curvature estimation [18]. Another approach involves employing thermography to identify alterations in concrete materials, such as structural damage [19]. An alternative for detecting damage by laser scanning is photogrammetry [20-21]. UAVs increase data availability from the above. It is not possible to take sufficient resolution from images by terrestrial photogrammetry. The UAV is used to record the entire tower shell even at height [22].

It is essential to provide a summary of cooling tower shell damage for the effective management of building ageing, particularly in terms of financing requirements. Damage is classified into several types: low damage/crack, high damage without reinforcement steel and high damage with reinforcement steel. High damage can be detected on Terrestrial laser scanning (TLS) data, low damage is hard to detect by TLS and close-range photogrammetry is needed. Crack detection algorithms can detect low damage, but tower shells contain several patterns, resembling cracks, including air pores, ribbing and formwork [23]. Mostly used are edge detectors like Sobel or Canny for crack detection, but when dealing with noisy image, which shares similar patterns, the task becomes more challenging. To improve the accuracy of detection cracks, the input images must be pre-processed by filters or change the colour space to HSI [24]. Another approach used RANdom SAmple Consensus (RANSAC) to detect lines on images and classified lines by Random Forest algorithm to crack and other patterns [25].

Currently, machine learning is predominantly used for detection tasks. Mandatory to use are convolution neural networks (CNN) or fully convolutional networks (FCN) with pre-trained models like VGG16 or ResNet [26]. To improve segmentation, U-NET design models CrackUnet [27-28].

The solution for low damage detection should be using multiple textures from processing images and laser scans in photogrammetric software. Textures like diffuse, normal, displacement and occlusion used in renderings technique contain important information on tower shell geometry.

Combining colour and geometric information in the same data format eliminates data preparation. The focus of this article revolves around utilising textures for detection in the field of civil engineering.

METHODS

Testing data

This article utilised data from a conference paper - Cooling tower measurement by laser scanner and close-range photogrammetry [17]. The following information pertains to the ITTERSON 100m cooling tower, which is the type designed by the Czech company ARMABETON Praha. The tower's height is 100 metres, and its shell is shaped like a rotating hyperbola. The tower shell starts at 5 metres and extends to 100 metres, with an inlet radius of 28.5 metres and an outlet radius of 18.17 metres. The analysis relied on a high-resolution mesh model of the cooling tower, obtained through laser scanning and photogrammetry. This detailed model captured textural information with a resolution of 3 mm per pixel, enabling precise damage detection.

$$\frac{x^2}{a^2}+\frac{y^2}{a^2}-\frac{z^2}{c^2}=1 \quad (1)$$

The cooling tower was measured by laser scanning and photogrammetry for the calculation of a detailed mesh model with texture. The interface of aerial markings and columns of the cooling tower is located at the interfaces between the laser scans and the RGB images. Input for this article was a detailed mesh model of the cooling tower with 3mm/px texture resolution.

Projection

The textures of the mesh model were united into a map projection. A similar approach was used for laser scanning data to estimate the difference between mathematical model and measured model of cooling tower [29-30]. Cooling towers can be divided according to meridians and parallels, parallel are horizontal lines of circuit and meridians are vertical lines of height.

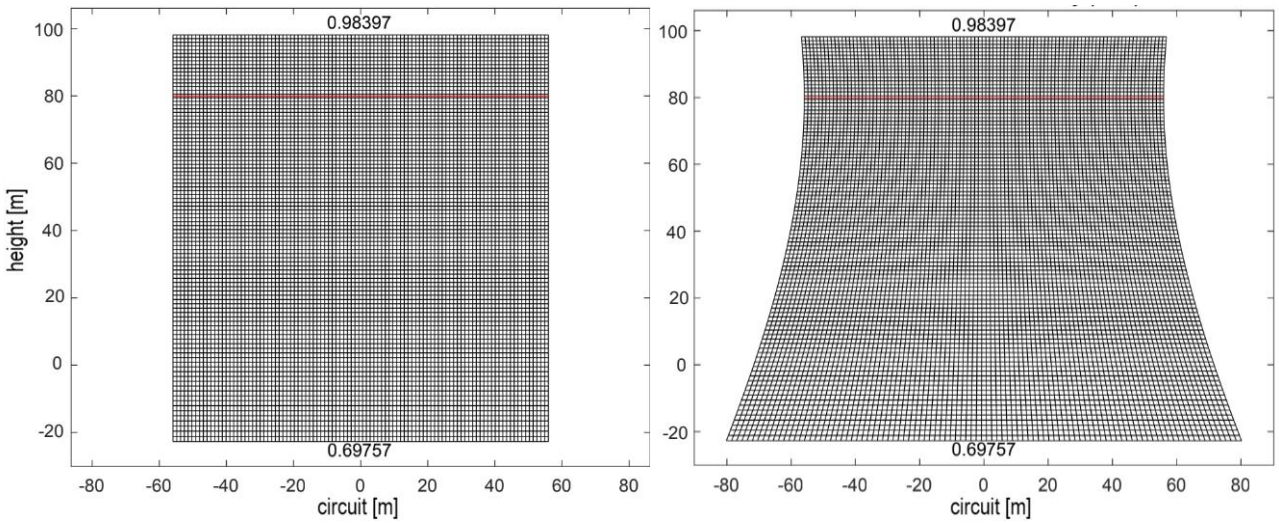

Fig. 1 – Textures (diffuse, normal, displacement, occlusion)

A cylindrical projection with one undistorted parallel was used for projecting hyperboloid onto a plane. For the projection, these are goniometric functions, where α is an angle which has the same meaning as the latitude. In this case, it is an angular distance between the undistorted parallel and any chosen parallel.

$$x = cosh(\alpha) \quad (2)$$

$$y = sinh(\alpha) \tag{3}$$

Mathematical model of the cooling tower was modelled in Blender Software [31] with edited UV maps of texture with descriptive projection. Texture projection was produced by Agisoft Metashape [32] from high detail model to mathematical model.

Textures

The sub-goal of this article is to utilise textures commonly used in rendering techniques to enhance detection in the field of civil engineering. Diffuse texture is used to define the base colour of an object. It is also known as the albedo map. The diffuse map is responsible for the colour of the object when it is not affected by any lighting conditions. Lighting conditions during the capture of input images impact the diffuse texture in photogrammetry if de-lighter software is not used. Normal texture is used to provide the perception of depth on a flat surface. It is used to add small details to the surface of an object without changing the geometry of the object. The normal map is created by using a high-resolution model and then transferring the surface details to a low-resolution model. The purpose of displacement texture is to enhance the three-dimensional appearance of an object's surface. It is used to create the illusion of geometry that is not present in the model. The displacement map is created by using a high-resolution model and then transferring the surface details to a low-resolution model. In the field of photogrammetry, a displacement texture is analogous to a Digital Elevation Model (DEM), except it is derived from a distinct foundational model rather than a flat plane. An occlusion texture is employed to replicate the phenomenon of shadowing that arises when two objects are close to one another. It is employed to enhance the three-dimensional appearance of the shadows and indentations on an item. [33] These textures are visible on Figure 2.

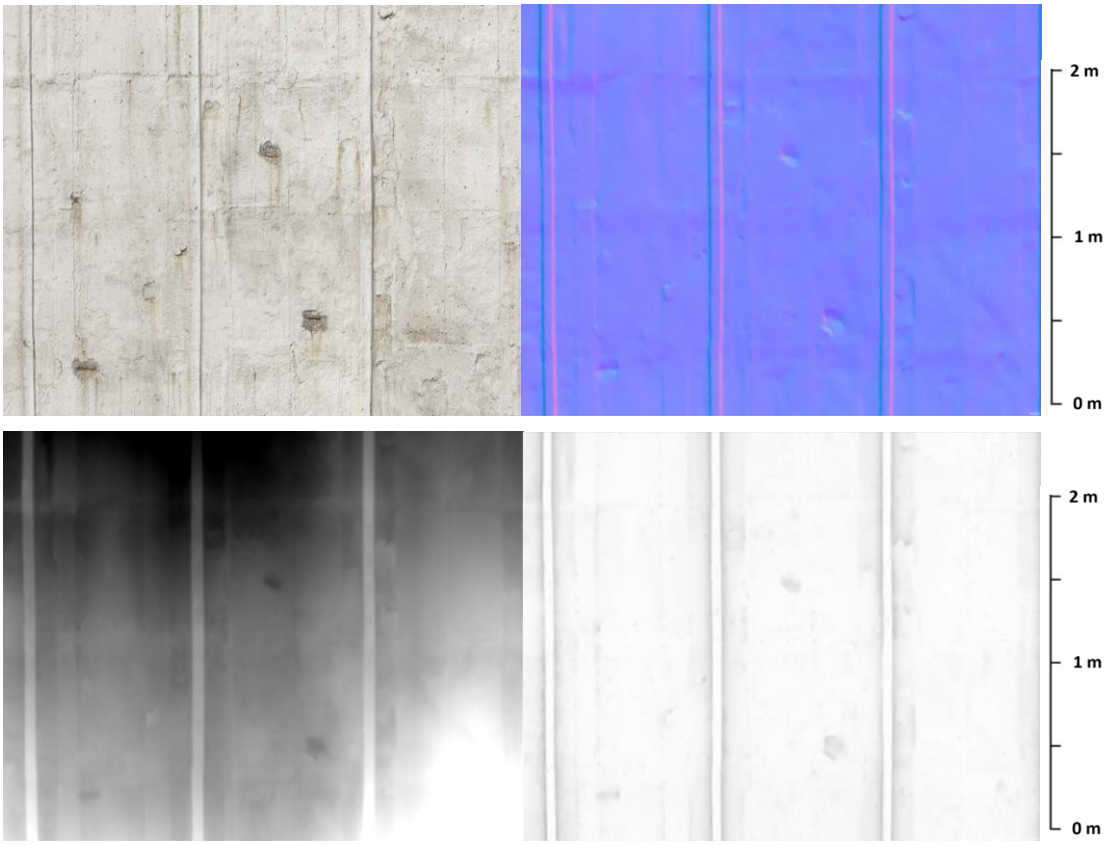

Fig. 2 – Textures (diffuse, normal, displacement, occlusion)

The intriguing texture is the normal texture. The texture consists of three bands that carry X, Y, and Z values of the normal vector visible on Figure 3. The normal vector values from the high-resolution model are recorded as pixel values in a normal texture. In the figure below, it is visible that the Y band eliminates the ribbing on concrete. This effect is achieved by aligned ribbing with a coordinate system of normals, which is helpful for the detection of ribbing.

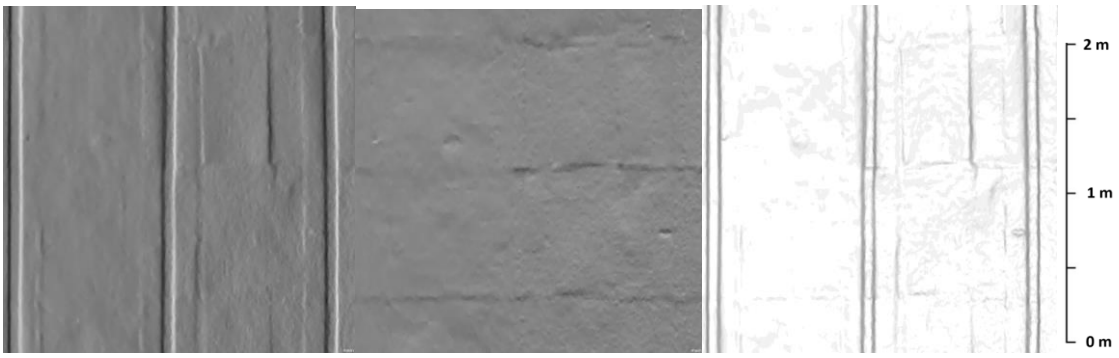

Fig. 3 – Normal texture - x (left), y (middle) and z (right)

RESULTS

The goal of the research was the automatic detection of damaged concrete on the tower shell. Damage is categorised into 4 categories visible in Figure 4: fine concrete, low damage, high damage without reinforcement and high damage with reinforcement. The key characteristics defining damage in the sustainability lifecycle of a cooling tower include the area, depth, volume, and length of visible reinforcement.

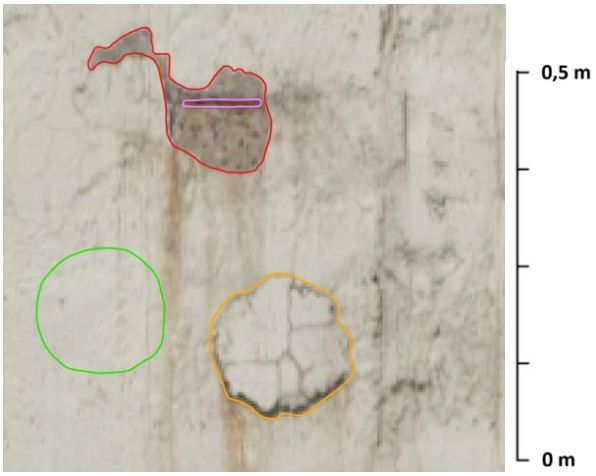

Fig. 4 – Red - high damage, pink - steel reinforcement, yellow - low damage, green - concrete

Detect high damage

Identifying extensive damage poses the least challenging aspect of the detection process. High damage is characterised by disturbed concrete with a different colour than fine concrete. For detection, diffuse texture (RGB) was used as the input layer for CNN in eCognition software version 10.3. Samples were created in QGIS as polygon objects with type attributes: concrete, low and high. Table1.

Tab. 1 - Summarization of samples

Type	Sum of samples
Concrete	40
Low damage	30
High damage	50

Across polygons, samples were created with augmentation multiplying samples 10 times. It was used for rotation, horizontal and vertical flip and zoom, this created many samples in Table 2. Size of the polygon concrete type was larger than other categories. The size of the samples was 32px.

Tab. 2 - Summarization of samples

Type	Sum of samples
Concrete	46150
Low damage	1420
High damage	2430

The Convolutional Neural Network contained 2 hidden layers. The kernel of the first layer was set at 7 and the number of distinct feature maps was 12. The kernel of the second layer was set to 5. CNN was trained by a 0.0006 learning rate, with 5000 training steps and 50 samples were used in each training step. Applying CNN heat maps with probabilities of occurrence of wanted objects were created. The raster layer was multi-resolution segmentation by Object-based image analysis (OBIA) with each layer (RGB texture and heatmaps). Generated objects were classified by heatmap values. Objects with the same classification were merged visible on Figure 5.

Fig. 5 – Detected High damage

Extract ribbing

Ribbing on tower shells is a disruptive element for low damage detection. Vertical edges of ribbing are similar to cracks of low damage. Meanwhile, testing detection of low damage with CNN was found to require the elimination of ribbing, for detection of ribbing CNN was used with the same design as in High damage detection. It was compared to the input layer to CNN: diffuse and normal texture visible on Figure 6. Polygons for sample creation were identical. For sample augmentation: horizontal flip and zoom. Rotation and vertical flip are unwanted due to ribbing orientation.

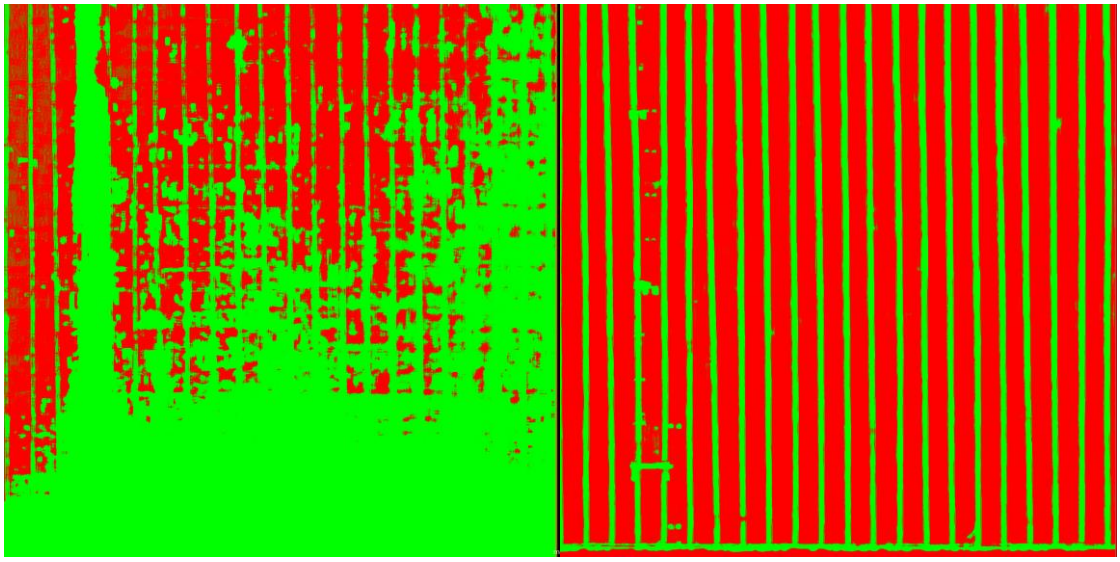

Fig. 6 – Classified concrete ribbing from diffuse (left), from normal (right)

Detect low damage

Low damage detection is the most challenging part. There are a lot of patterns on tower shells similar to cracks of low damage like air pores, edges of concrete formwork, ribbing and colour changes. Separating these patterns on diffuse texture (RGB) from crack is a hard task. In Figure 7 below is visible CNN detection of low damage on diffuse texture and composed raster layer. Detecting low damage based on diffuse texture is insufficient, to improve detection and eliminate unwanted patterns, a composed raster layer was created.

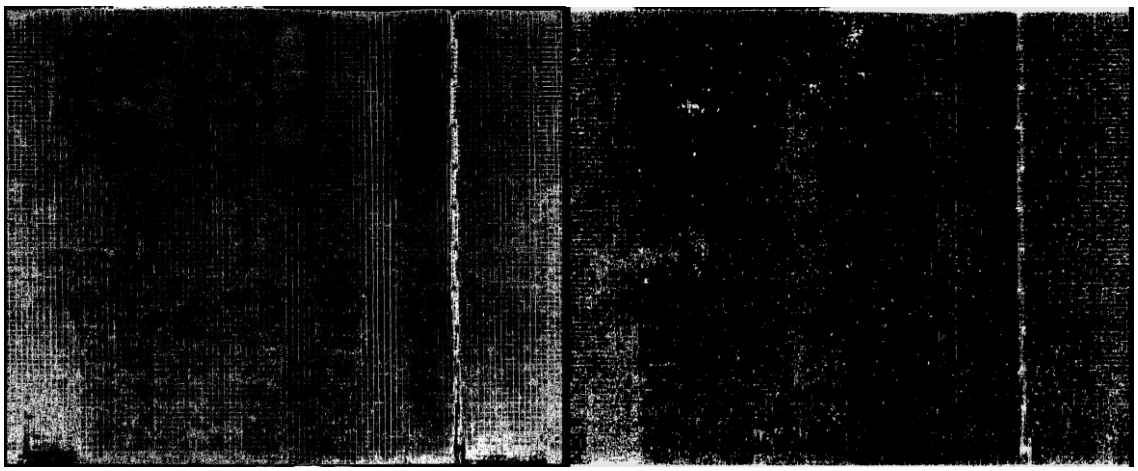

Fig. 7 – Heatmap of classified Low damage (from diffuse texture - left, from composed raster layer - right)

The composed raster layer is based on diffuse texture, normal texture, and displacement texture. The diffuse texture was converted from RGB to HSI colour space. An intensity band from HSI was used for further processing. From normal texture were used only bands with y values - normal Y. Displacement texture containing values from -20cm to 20cm, which is not suitable for slope estimation, so displacement texture was multiplied 1000x times to increase values to prevent numerical errors. Each raster is visible on Figure 8.

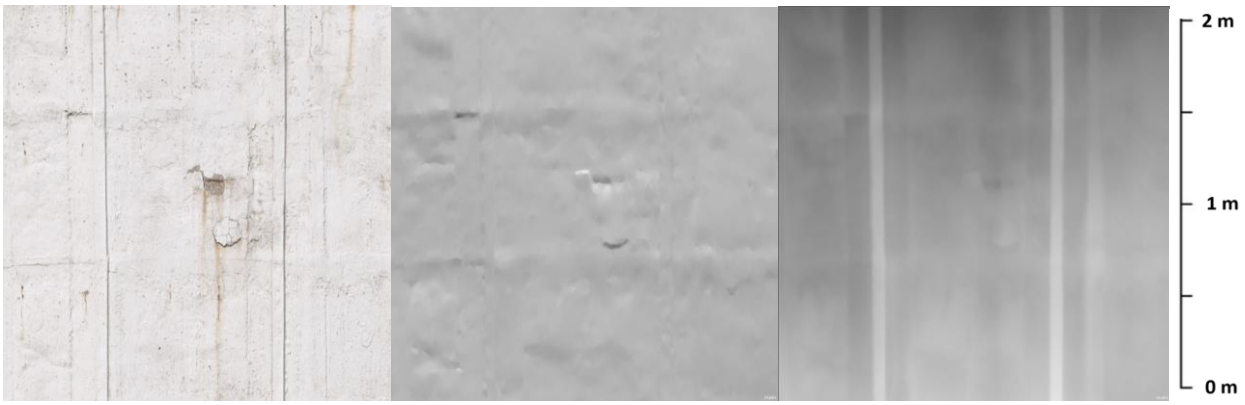

Fig. 8 – (input - diffuse, normal y, displacement)

The intensity layer and normal Y were processed by the Ridge filter to highlight raster edges. The kernel of the Ridge filter was set to size 3. The slope raster is calculated from multiplied displacement texture visible on Figure 9.

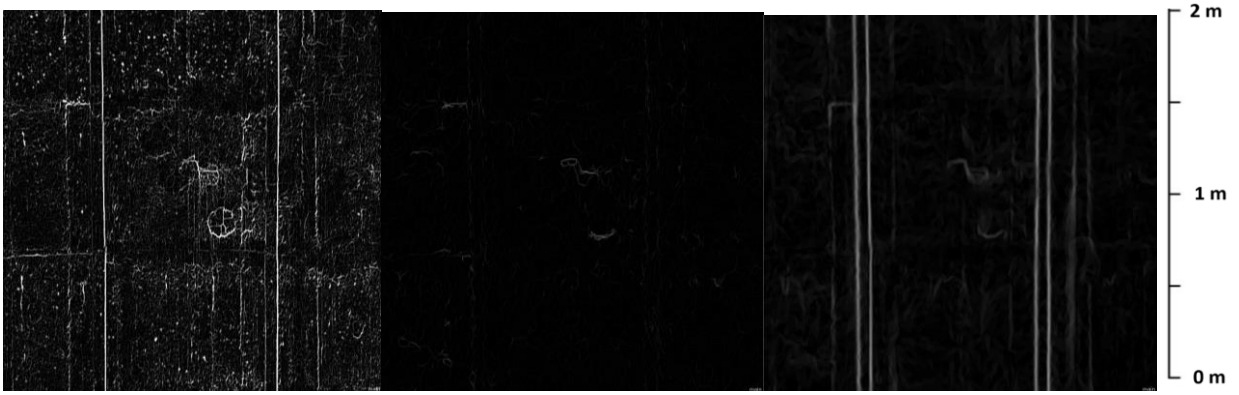

Fig. 9 – (Intensity ridge filter, normal Y ridge filter, slope)

Layers with highlighted edges were joined together with the same weight and blurred by a median filter to remove air pores. The final raster layer is composed of the Intensity band and the blurred band visible on Figure 10.

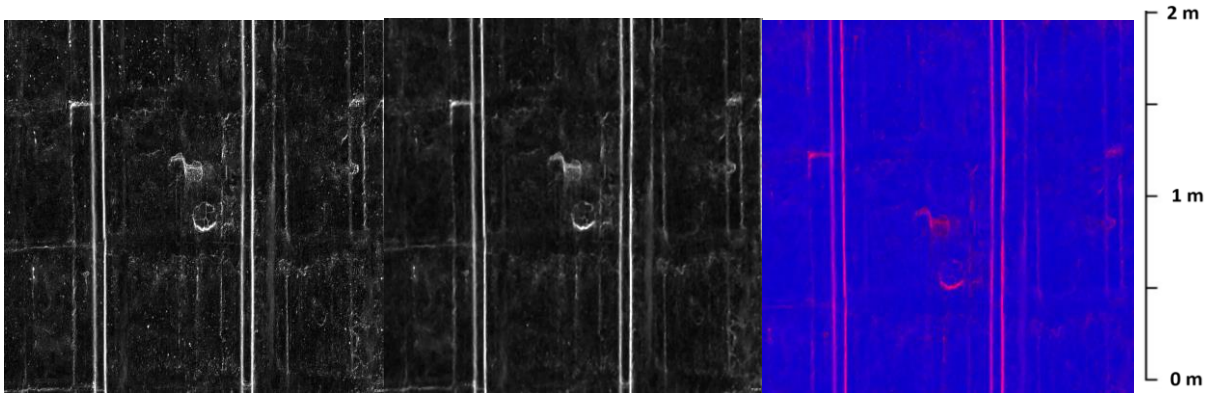

Fig. 10 – (summarization of highlight edges raster, median blur filter, composed raster layer)

The composed raster layer is used for multi-resolution segmentation by OBIA in eCognition software. The scale parameter was set to default on value 42. The shape parameter was set to 0.2 and compactness 0.7. Created objects were classified by rules in Table 3 below into 4 categories: fine concrete, ribbing, low and high damage visible on Figure 11.

Tab. 3 - Classification rules

	Fine concrete	Ribbing	High Damage	Low damage
CNN Heatmap ribbing	<0.9	>0.9	<0.9	<0.9
CNN Heatmap high damage	<0.9	-	>0.9	<0.9
Blurred band	<median(blur)	-	>median(blur)	>median(blur)

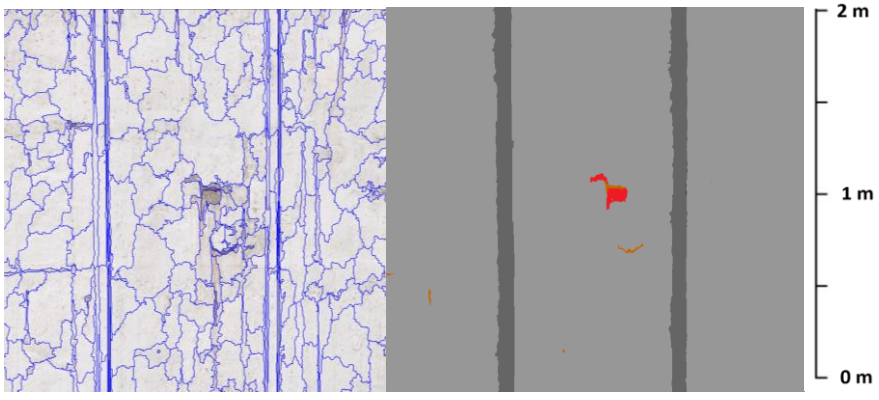

Fig. 11 – (segmented objects - left, classified object - right)

The volume of high damage

Estimation of missing concrete volume is processed by pixel summarization like on DEM. On the contrary, DEM utilises displacement texture, assigning values based on the disparity between the actual geometry and the design geometry. Volume is estimated by summarization of pixel values on high-damage objects reduced by mass given by a boundary-like fitting plane on the boundary. Example of estimation of missing concrete is visible on Figure 12, 13.

$$V = (\Sigma(pixel\ value\ inside \times pixel\ resolution^2) - \frac{\Sigma(pixel\ value\ boundary)}{n} \times S) \times m_p \quad (4)$$

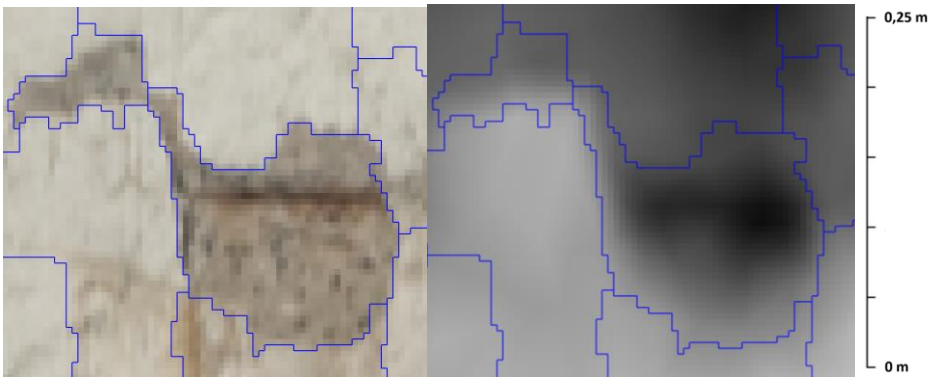

Fig. 12 – high damage on diffuse (left) and displacement texture (right)

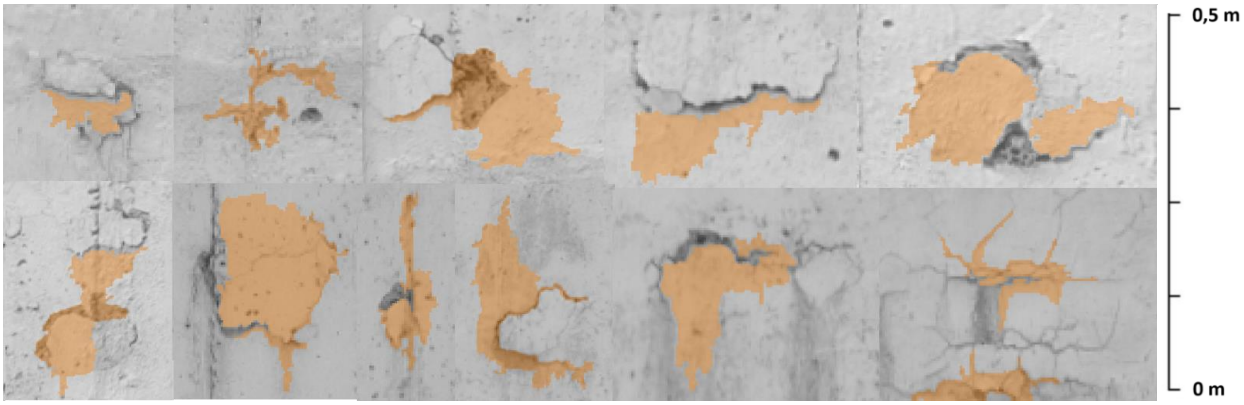

Fig. 13 – (examples of detected low damage)

CONCLUSION

Damage classification and summarization on cooling tower shells is an integral part of controlling the ageing of buildings and structures. During the lifecycle of the cooling tower, the shell is damaged and needs repairs. Damages are classified into low damage/ cracks, high damage without visible reinforcement steel and high damage with reinforcement steel The proposed method of detecting damage is based on data from laser scanning and close-range photogrammetry by UAV. A mesh model with several types of textures (diffuse, normal, displacement and occlusion) is created by measured point clouds and images.

Textures are modified to map projection to view the entire tower shell in one raster. The mathematical model of the hyperbolic cooling tower was modelled in Blender software which defines UV maps for projection. It used cylindrical projection with one not distorted axis. Based on the mathematical model diffuse, normal, displacement and occlusion textures were generated. Each texture was used in damage detection except for the occlusion texture. Occlusion texture provides information about the visualisation of shadow, similar information is also on normal and displacement texture.

Detecting high damage was done by CNN in eCognition software. Training samples were created by manual vectorization on part of the tower shell. All high damages were detected with misdetection on the ladder and shadows area. Misdetection was caused by a low number of samples

and labels of samples. eCognition uses labels in the form of labels for one sample, in some cases this leads to an inaccurate CNN model. High damages are not aligned with image coordinates, which leads to label samples which contain damage and fine concrete.

The tower shell is full of patterns similar to low damages/cracks like air pores, ribbing, formwork and change colour. Detecting low damage only on diffuse texture by CNN was insufficient. For detection of low damage, a pre-processed composed raster layer based on diffuse, normal and displacement texture. The composed raster layer increases low damage based on colour and geometry, which helps to separate low damage from other patterns. The Tower shell was segmented by multiresolution segmentation and classified by composed raster layer and additional rules. This method leads to low accuracy detection of low damage. The position of low damage is precise, but the damage is typically not inaccurately marked.

The successful usefulness of textures from rendering techniques has been demonstrated for damage detection and cooling tower shells. The study was limited by only one measured cooling tower and selection of eCognitions software for damage detection. Easy usage of CNN inside commercial software minimises options for optimization of detection methods. Future work will focus on different machine learning models like U-NET for low damage detection. Also adding thermography during right weather conditions may help improve detection of low damage. Low damage is a piece of concrete which is detached from the tower shell and its temperature capacity will be different.

The demonstrated method for evaluating damage on cooling towers offers practical benefits in localising and summarising damage, aiding operators in repair planning and decision-making processes. Utilising drone-based visual inspection proves to be a cost-effective alternative to employing professional climbers, significantly reducing inspection time. While measurements by drones are completed within 6 hours, the conventional approach with climbers can take several days to inspect all tower shells. The collected data from drone inspections not only facilitate immediate repair planning but also serve as valuable input for future predictive maintenance through periodic measurements. By leveraging this data, operators can anticipate potential damage trends and prioritise maintenance efforts, accordingly, ultimately optimising the lifespan and performance of cooling tower structures. The method can also be used on other concrete structures (bridges, silos, dams).

ACKNOWLEDGEMENTS

This work was supported by the Grant Agency of the Czech Technical University in Prague, grants SGS24/050/OHK1/1T/11.

REFERENCES

[1] Berra, E. F. & Peppa, M. V. 2020. Advances and challenges of UAV SFM MVS photogrammetry and remote sensing: Short review. (2020) IEEE Latin American GRSS & ISPRS remote sensing conference (lagirs) (pp. 533-538). IEEE.

[2] Pavelka, K., Hůlková, M., Šedina & J., Pavelka, K. 2019. RPAS for documentation of Nazca aqueducts European Journal of Remote Sensing. (2019), 52(1), 174-181. ISSN 2279-7254. https://doi.org/10.1080/22797254.2018.1490321

[3] Bouček, T., Stará, L., Pavelka, K. & Pavelka, K., Jr. 2023. Monitoring of the Rehabilitation of the Historic World War II US Air Force Base in Greenland. Remote Sens. 2023, 15, 4323. https://doi.org/10.3390/rs15174323

[4] Marčiš, M.; Fraštia, M.; Kovanič, Ľ.; Blišťan, P. 2023. Deformations of Image Blocks in Photogrammetric Documentation of Cultural Heritage—Case Study: Saint James's Chapel in Bratislava, Slovakia. Appl. Sci. 2023, 13, 261. https://doi.org/10.3390/app13010261

[5] Štroner, M., Urban, R., Seidl, J., Reindl, T. & Brouček, J. 2021. Photogrammetry using UAV-mounted GNSS RTK: Georeferencing strategies without GCPs. Remote Sensing (2021), 13(7), 1336. https://doi.org/10.3390/rs13071336

[6] Štroner, M., Urban, R., Reindl, T., Seidl, J. & Brouček, J. 2020. Evaluation of the georeferencing accuracy of a photogrammetric model using a quadrocopter with onboard GNSS RTK. Sensors (2020), 20(8), 2318. https://doi.org/10.3390/s20082318
[7] Asadzadeh E. & Alam M. 2014. A survey on hyperbolic cooling towers., International Journal of Civil, Environmental, Structural, Construction and Architectural Engineering 8, 1079-1091 (2014).
[8] Gupta, A. K., & Maestrini, S. 1986. Investigation on hyperbolic cooling tower ultimate behaviour. Engineering Structures, 8(2), 87-92. https://doi.org/10.1016/0013-7944(86)90012-1
[9] Kraetzig W. B., et al. 2009. From large natural draft cooling tower shells to chimneys of solar upwind power plants., Symposium of the International Association for Shell and Spatial Structures (2009).
[10] Hara, T. & Gould, P. L. 2003. Local–global analysis of cooling tower with cutouts, Computers & structures 80.27-30, 2157-2166. https://doi.org/10.1016/S0045-7949(02)00250-X
[11] Kulkarni S. & Kulkarni A. V., 2014. Case study of seismic effect on hyperbolic cooling towers. Civil Environ. Res 6.11, 85-94 (2014).
[12] Głowacki, T., Muszyński, Z. 2018. Analysis of cooling tower's geometry by means of geodetic and thermovision method IOP Conf. Ser.: Mater. Sci. Eng. 365 042075, https://doi.org/10.1088/1757-899X/365/4/042075
[13] Głowacki T., Grzempowski P., Sudoł E., Wajs J. & Zając M., 2016, The assessment of the application of terrestrial laser scanning for measuring the geometrics of cooling towers, Geomatics, Landmanagement and Landscape, 4, 49–57 (2016).
[14] Bajtala M., et al. 2011. Exploitation of Terrestrial Laser Scanning in Determining of Geometry of a Factory Chimney., Proceedings of the 5th International Conference on Engineering Surveying (INGEO 2011). Brijuni, Croatia, September. (2011).
[15] Pandžić J., et al. 2016, TLS in determining geometry of a tall structure. Engineering geodesy for construction works, industry and research, proceedings of the international symposium on engineering geodesy. (2016).
[16] Kocierz R., Rębisz M. & Ortyl L., 2018. Measurement points density and measurement methods in determining the geometric imperfections of shell surfaces., Reports on Geodesy and Geoinformatics 105 (2018).
[17] Zahradník, D. 2023. Cooling tower measurement by laser scanner and close-range photogrammetry. AIP Conference Proceedings (Vol. 2928, No. 1). AIP Publishing https://doi.org/10.1063/5.0079223
[18] Makuch M. & Gawronek P. 2020. 3D point cloud analysis for damage detection on hyperboloid cooling tower shells, Remote Sensing 12.10 1542 (2020). https://doi.org/10.3390/rs12101542
[19] Głowacki T. & Muszyński Z. 2018 Analysis of cooling tower's geometry by means of geodetic and thermovision method, IOP Conference Series: Materials Science and Engineering. Vol. 365. No. 4. IOP Publishing (2018).
[20] Chisholm N. W. T. 1997. Photogrammetry for cooling tower shape surveys. The Photogrammetric Record 9.50 173-191 (1977).
[21] Ioannidis, C., Valani, A., Soile, S., Tsiligiris, E. & Georgopoulos, A. 2007. Alternative techniques for the creation of 3D models for finite element analysis—Application on a cooling tower. Proc. Opt. https://doi.org/10.13140/2.1.5124.2887
[22] Castiglioni, C. A., Rabuffetti, A. S., Chiarelli, G. P., Brambilla, G., & Georgi, J. 2017. Unmanned aerial vehicle (UAV) application to the structural health assessment of large civil engineering structures. In Fifth International Conference on Remote Sensing and Geoinformation of the Environment (RSCy2017) (Vol. 10444, pp. 355-370). SPIE.
[23] Fujita, Y., Mitani, Y., & Hamamoto, Y. 2006. A method for crack detection on a concrete structure. In 18th International Conference on Pattern Recognition (ICPR'06) (Vol. 3, pp. 901-904). IEEE.
[24] Nnolim, U. A. 2020. Automated crack segmentation via saturation channel thresholding, area classification and fusion of modified level set segmentation with Canny edge detection. Heliyon, 6(12). https://doi.org/10.1016/j.heliyon.2020.e05748
[25] Prasanna, P., Dana, K. J., Gucunski, N., Basily, B. B., La, H. M., Lim, R. S. & Parvardeh, H. 2014. Automated crack detection on concrete bridges. IEEE Transactions on automation science and engineering, 13(2), 591-599.
[26] Dung, C. V. 2019. Autonomous concrete crack detection using deep fully convolutional neural network. Automation in Construction, 99, 52-58.
[27] Zhang, L., Shen, J. & Zhu, B. 2021. A research on an improved Unet-based concrete crack detection algorithm. Structural Health Monitoring, 20(4), 1864-1879.
[28] Liu, Z., Cao, Y., Wang, Y. & Wang, W. 2019. Computer vision-based concrete crack detection using U-net fully convolutional networks. Automation in Construction, 104, 129-139.

[29] Kwinta A. and Bac-Bronowicz J., 2021. Analysis of hyperboloid cooling tower projection on 2D shape, Geomatics, Landmanagement and Landscape (2021).
[30] Beshr, A. A., Basha, A. M., El-Madany, S. A. & El-Azeem, F. A. 2023, Deformation of High-Rise Cooling Tower through Projection of Coordinates Resulted from Terrestrial Laser Scanner Observations onto a Vertical Plane. ISPRS International Journal of Geo-Information, 12(10), 417. https://doi.org/10.3390/ijgi12100417
[31] blender.org - Home of the Blender project - Free and Open 3D Creation Software. (n.d.). blender.org. https://www.blender.org/ (cited 30-3-2024)
[32] Agisoft Metashape: https://www.agisoft.com/ (cited 30-3-2024)
[33] Texture Maps Explained | Poliigon Help Center. (n.d.). https://help.poliigon.com/en/articles/1712652-texture-maps-explained (cited 30-3-2024)

CIVIL ENGINEERING JOURNAL

Article no. 8

THE CIVIL ENGINEERING JOURNAL 1-2024

FINITE ELEMENT SIMULATION ANALYSIS OF CURVILINEAR CONTINUOUS BEAM BRIDGE JACKING AND TRANSLATION CONSTRUCTION

Xilong Zheng[1], Wei Li[1], Honglei Zhang[2] and Qiong Wang [1]

1. *School of Civil and Architectural Engineering, Harbin University, No.109 Zhongxing Road, Harbin, Heilongjiang Province, China; sampson88@126.com*
2. *Beijing xinqiao technology, No.8 Xitucheng Road, Haidian District, Beijing, China*

ABSTRACT

This paper investigates the issue of beam misalignment in curved continuous beam bridges. Taking the D0 to D6 spans of the Gongbin Road viaduct as the basis, the main influencing factors causing misalignment in curved beam bridges are analyzed and the causes of transverse and longitudinal misalignment in curved beam bridges are calculated and analyzed using Midas/Civil finite element simulation software. The results indicate that the main influencing factor causing misalignment in the operation of curved continuous beam bridges is the system temperature, with the displacement caused by it being larger than the cumulative displacement caused by self-weight, construction phase, gradient load, vehicle load, and bearing settlement. During operation, the failure of expansion joints changes the boundary conditions of the beam, preventing the bridge from freely expanding and contracting longitudinally under temperature load. As a result, the transverse displacement increases to 2-3 times the normal working state of the expansion joint, leading to beam misalignment.

KEYWORDS

Continuous beam bridge, Jacking simulation, Translation simulation, Misalignment, Simulation analysis

INTRODUCTION

Small and medium-span bridges account for approximately 88% of the total number of highway bridges in our country, and due to their large quantity, they deserve more attention in terms of daily maintenance and repair work [1-3]. Due to the fact that many of these bridges were built in the previous century, they were limited by the technology available at that time. As a result, their design load standards and capacity are inadequate to meet current requirements [4-7]. Currently, in China, the majority of funds allocated for highway bridge construction are focused on major bridge projects. As a result, there is limited funding available for small and medium-span bridges. For those smaller bridges that cannot meet current traffic demands, it is nearly impossible to demolish and reconstruct them on a large scale. Instead, it is necessary to modify these existing bridges, making them compliant with current traffic requirements [8-11].

To better renovate small and medium-span bridges and ensure their efficient service to the

people, it is crucial to address the common structural defects. However, there is still insufficient attention given to these issues. One such concern is the significant problem of lateral displacement in the superstructure, which severely affects the normal functioning of the bridges. In particular, small and medium-span curved continuous beam bridges are more prone to such displacements due to their complex structure and load characteristics under long-term effects [12]. Analyzing the causes of bridge lateral displacement is of great significance for improving the efficiency of treating this issue, reducing structural defects in small and medium-span bridges in China, and ensuring the safety of bridges during their operational phase [13-15]. This article will establish bridge models using finite element software to identify the influencing factors contributing to beam displacement. The objective is to analyze the extent to which these factors impact the lateral and longitudinal displacements of the bridge.

INTRODUCTION TO ENGINEERING BACKGROUND

The design load level for the elevated bridge is Class A. The main span of the Gongbin Road elevated bridge consists of 119 segments. This study mainly focuses on the displacement analysis of spans D0 to D6. The upper structure of spans D0 to D6 is a continuous curved box girder made of ordinary reinforced concrete, with a span combination of 20+4×25+20=140 m. The box girder is a twin-box six-cell structure with a height of 1.4 m. The total width of spans D0 to D6 is 28 m, and the width distribution is as follows: 0.5 m crash barrier + 12.0 m roadway + 2.0 m median strip + 12.0 m roadway + 0.5 m crash barrier. The lower structure consists of pier D1 to D5#, which are column-type bridge piers, and pier D6 is a prestressed concrete inverted T-shaped cap beam pier. The substructure also includes reinforced concrete rectangular abutments. The aerial view of the elevated structure is shown in Figure 1, and the elevation, plan, and cross-sectional views of the bridge are shown in Figure 2 - Figure 4.

Fig. 1 – Aerial view of the elevated bridge

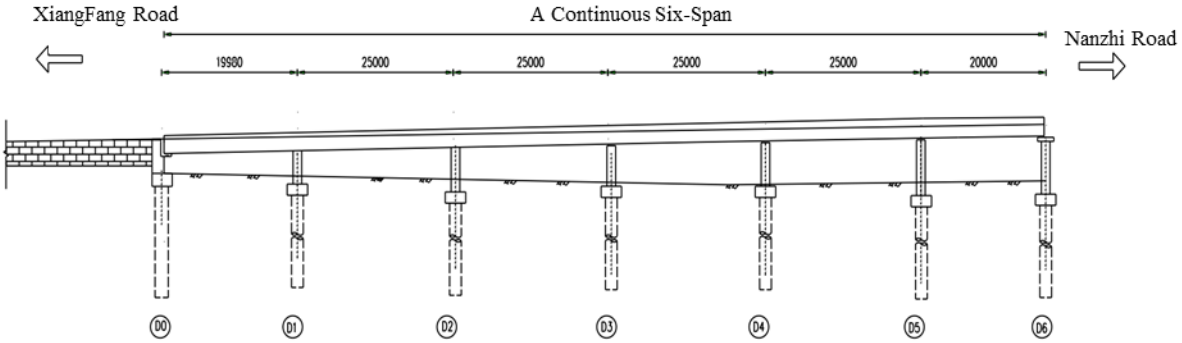

Fig. 2 – Bridge elevation layout diagram (unite: mm)

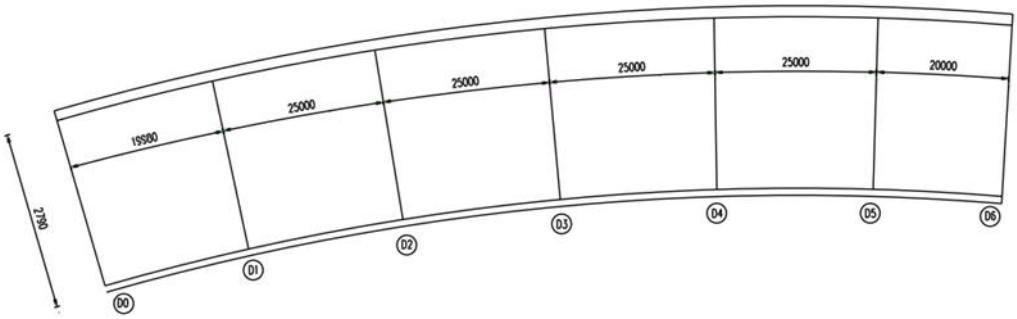

Fig. 3 – Plan layout diagram (unite: mm)

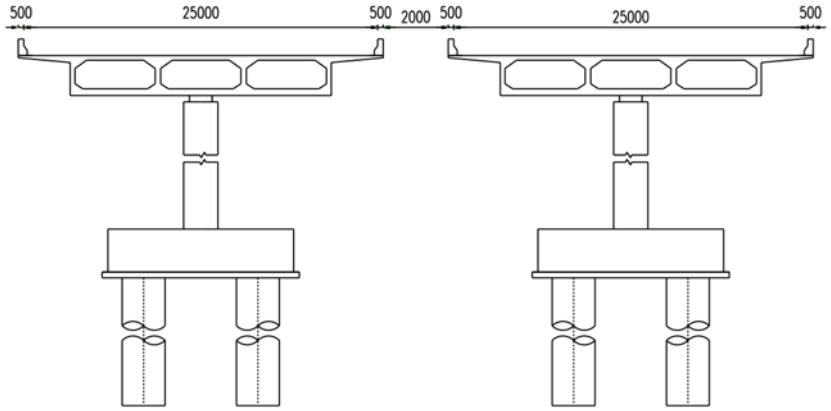

Fig. 4 – Cross-section layout diagram (unite: mm)

OFFSETTING DEFECT

(1) During the inspection of a curved continuous beam bridge, significant lateral displacement of the main beam towards the outside of the curve was observed. The D6# pier box beam exhibited the most noticeable lateral displacement, with a measured lateral displacement at the end of the continuous box beam of at least 90 mm at the outer side of the curve abutment. Due to this lateral displacement, the continuous box beam has caused severe structural damage to its lower bearings, the bridge piers, and even the adjacent ramp bridge. At the end of the 6# pier cap beam (outer side of the curved beam), the retaining block has fractured under the lateral pressure exerted by the main beam, posing a risk of falling as shown in Figure 5.

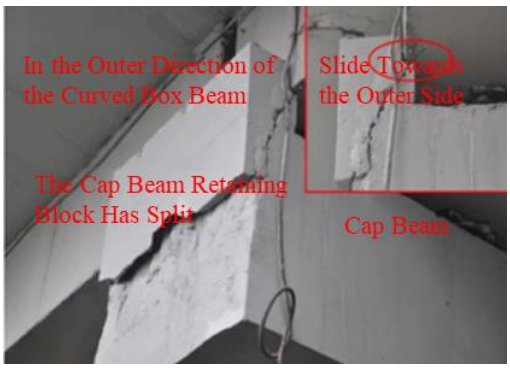

Fig. 5 – Diagonal splitting of bridge abutment cap beam block

(2) The lateral displacement of the curved girder bridge will cause the steel plate on the bearing to move along with it. Inspection revealed that there is a common phenomenon of outward sliding movement of the upper steel plate in the bidirectional movable bearings, and in some severe cases, there is a 40 mm displacement between the upper steel plate and the steel basin, as shown in Figure 6 and Figure 7.

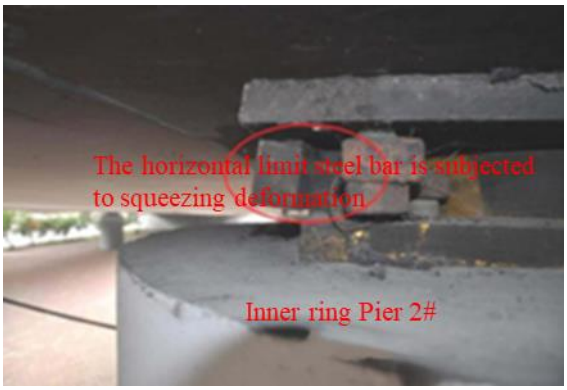

Fig. 6 – Compression deformation of lateral restraining steel bar

Fig. 7 – Sliding of upper steel plate out of steel basin by 40 mm

(3) The lower outer surface of the bridge pier column has several semi-circular cracks, as shown in Figure 8. The maximum width of the cracks is 0.26 mm. The crack distribution schematic is shown in Figure 9. The analysis indicates that this is due to the presence of fixed basin-type bearings above the bridge pier. The lateral displacement tendency of the main beam is constrained by the fixed bearings. According to the principle of force interaction, the main beam exerts radial forces on the bearings in the crawling direction, causing a transition of the bridge pier column from an axially compressed state to an eccentrically compressed state and even resulting in tensile stress in the outer concrete.

Fig. 8 – Bottom half-ring crack in bridge pier concrete

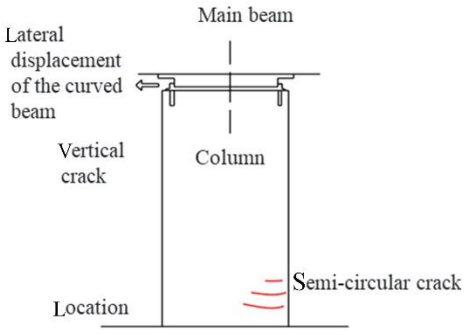

Fig. 9 – Schematic diagram of crack in bridge pier column

MODEL ESTABLISHMENT

The process of bridge jacking and translation may appear simple, but the selection of construction schemes and the control standards during construction are extremely complex. The main challenge lies in how to control the displacement and stress of the beam within a reasonable range during the construction process, without causing damage to the beam. To address this issue,

a focused analysis is conducted on the causes of beam deformation and stress during construction, in order to identify corresponding avoidance measures.

Simulation of the Boundary for Curve Continuous Beam Jacking

(1) Selection of jacking method. Bridge jacking techniques can be divided into two categories: integral jacking and partial jacking. Due to the fact that the D0~D6 spans of the Gongbin Elevated Bridge consist of a six-span continuous beam structure, and considering the relatively large jacking height required for this project, the integral jacking method is adopted to minimize damage to the beam. The jacking process mainly includes installing temporary supports, jacking the beams, replacing bearings, and releasing the oil from the jacks, totally four phases. The specific operational steps are illustrated in Figure 10.

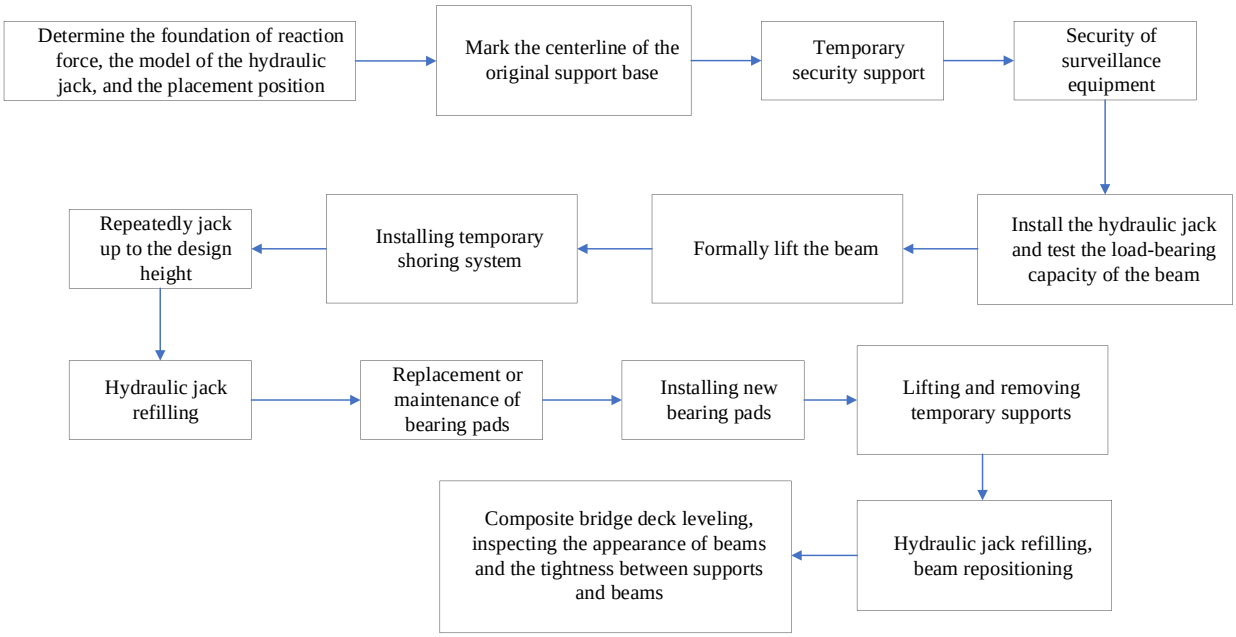

Fig. 10 – Jacking construction steps

(2) In the process of synchronously jacking a bridge, the main control is the variation of the beam stress values generated by the height difference during the start of synchronous jacking and the final placement of the beam. Therefore, the simulation of the supports is controlled by node displacement to achieve the desired effect.

(3) The main beam supports of the original bridge design adopt the form of GPZ8000 pot rubber bearings. Therefore, this paper simulates the bridge supports using compressed springs.

(4) Bridge uplift force and lifting height design.

Based on the size of the beam and considering the effects of various adverse loads, the rated lifting force of the jack is increased by 200% as a safety margin. When lifting the bridge, a 650t hydraulic jack with mechanical locks is used, and the lifting height is 80 mm. The method of staged synchronous lifting is adopted.

Simulation of The Translation Boundary of a Curved Continuous Beam Bridge.

(1) The bridge displacement construction method adopts the whole top pushing and resetting construction method.

(2) During the vertical boundary simulation of bridge displacement and resetting construction, the bowl-shaped rubber bearings have been removed. Horizontal sliding devices are used as vertical supports for the beam structure during the displacement construction. Polyethylene PTFE sheets are applied with silicone oil to reduce friction during construction. Therefore, during the simulated process of top pushing and displacement, compressed rigid supports are used to replace the vertical boundary conditions of the main beam.

(3) During the lateral boundary simulation of bridge displacement and resetting, the lateral boundary conditions of the beam are released. Under the thrust of the jacks, the beam overcomes the frictional resistance of the slide and moves towards the inner side of the arc. During the displacement process, the beam mainly undergoes rigid body motion; at the same time, the beam may experience small recoverable deformations. When the beam is translated to the contact with the stopper at the end of the beam and the bridge abutment, the stopper acts as a lateral rigid constraint. The beam will cease rigid body rotation and accompanied by significant recoverable deformations.

(4) The design of lateral top pushing force and displacement for the bridge. When the main beam is laterally pushed, considering the adverse factors such as temperature stress and the shear deformation of the bearings themselves, the principle of adding a 200% safety margin to the rated lifting force of the jacks is followed. For the displacement process, a 150 T jack is selected for controlled top pushing with graded control. The top pushing speed of the jacks during horizontal displacement should not exceed 1mm/min to ensure that the entire beam moves towards the inner side of the curve as per design requirements.

Control of The Uplift and Translation Reaction Forces.

During the uplift and translation resetting operation of the bridge under traffic closure, it is crucial to ensure that there is no void under the bearings. This means that the bridge, in its displaced state, must have a minimum reaction force of the jacks that is not less than 0 under the most unfavorable load combinations, controlled by hydraulic pressure. This is necessary to prevent the risk of beam overturning and to perform stress verification.

The finite element model is established by using the finite element software Midas/Civil. The main beam is simulated by the beam element and the support is generally supported. During the lifting process, forced displacement is applied to the position of the support. One fixed support is on the D3 pier, and the rest are movable supports.

In the condition of traffic closure, the minimum reaction forces of each bearing of the bridge under the load combination of 1.2 dead load + 1.4 live load are shown in Figure 11.

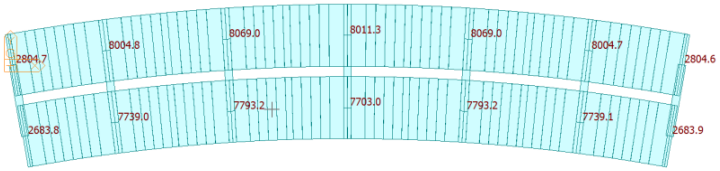

Fig. 11 – Bearing reaction forces

When the bridge reaches its maximum displacement of 90 mm under traffic closure, the minimum value of the inner-side bearing reaction force for a curved girder bridge is 2683.9 kN, and

the support force of the jacks is greater than 0. Therefore, it can be concluded that when the beam displacement reaches 90 mm under traffic closure, the bridge support is in a safe condition.

In the condition where traffic is not controlled and vehicles travel along the original lanes, the reaction forces at each support position are shown in Figure 12. In this state, the minimum bearing reaction force is 2432.5 kN. Hence, it can be concluded that when the bridge is in a displaced condition without traffic control, the support forces decrease under the action of eccentric loads. If the bridge is not properly maintained and continues to operate in the displaced state, the displacement will continue to increase, and there is a risk of overturning under the action of eccentric loads.

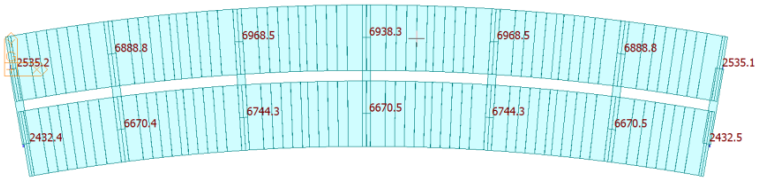

Fig. 12 – Bearing reaction forces

Hydraulic Lifting Stress Control

Traffic control is required during the construction of hydraulic lifting and translation to ensure construction safety and normal travel for the public. The stress increment generated at the most critical section during the construction process should be less than the stress increment generated by live loads at the same section.

Under the action of the most unfavourable eccentric load, tensile stress is generated at the upper edge of the main beam section as Pt, and compressive stress is generated in the main beam section as Pc. To ensure the safety and sufficient safety factor of the main beam during the hydraulic lifting and translation construction process, the stress variation at the most critical section is controlled to not exceed 80% of the stress increment under the action of live loads at the same section. Specifically, the incremental tensile stress at the most critical section of the main beam should not exceed 0.8 Pt, and the incremental compressive stress at the most critical section of the main beam should not exceed 0.8 Pc, which ensures the safety of the construction. The calculation results are shown in Figure 13.

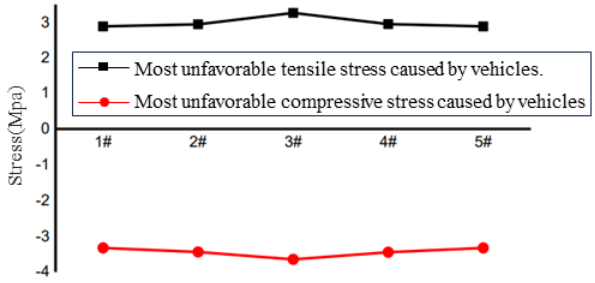

Fig. 13 – The stress limits during the bridge translocation and repositioning process

Using this stress control method is safer and more accurate compared to directly using the design value of concrete tensile strength as the construction stress control criteria.

SIMULATION ANALYSIS OF CURVED CONTINUOUS BEAM BRIDGE.

Simulation of the Jacking Process

In the jacking process of the bridge, a step-by-step jacking method is adopted, with a jacking increment of 5-10 mm per step. This study takes a step increment of 10 mm as an example to analyze the stress increment of each section under different jacking conditions. The specific conditions are listed in Table 1.

Tab. 1 - Simulation of Jacking Conditions

Operating condition	The jacking height
Operating condition one	10 mm single-point jacking for Pier 0 and Pier 3
Operating condition two	Pier 0 jacked up by 10 mm, Pier 1 jacked up by 5 mm, Pier 3 jacked up by 10 mm, Pier 2 and Pier 4 jacked up by 5 mm
Operating condition three	Pier 0 jacked up by 10 mm, Pier 1 jacked up by 8 mm.Pier 3 jacked up by 10 mm, Pier 2 and Pier 4 jacked up by 8 mm
Operating condition four	Synchronized jacking up by 10 mm

(1) Condition 1: The single-point jacking of Piers 0 and 3 by 10 mm. The increment of stress and deformation of the main beam is shown in Figure 14 – Figure 17.

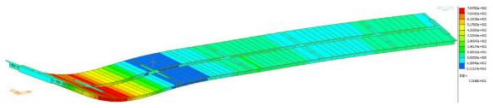

Fig. 14 – Stress distribution diagram of main beam (0# Abutment raised by 10 mm)

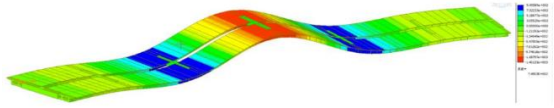

Fig. 15 – Stress distribution diagram of main beam (3# Pier cap raised by 10 mm)

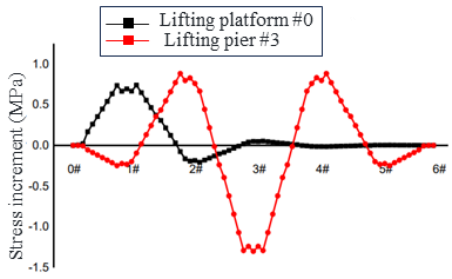

Fig. 16 – Increment of stress on the lower edge of the main beam during single point jacking

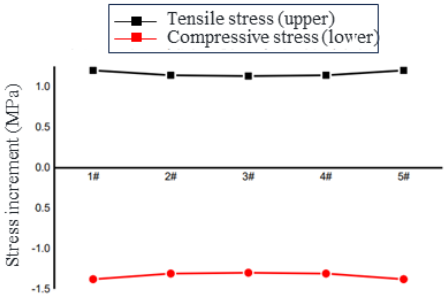

Fig. 17 – Increment of stress on main beam cross-sections for each pier during single point jacking

From the above figure, when the single point is raised to 10 mm, the main beam section at the 0# abutment is in an unconstrained state, resulting in no increase in the bottom stress increment. However, the adjacent main beam section at the 1# pier has a positive increase in bottom stress, indicating tensile stress, and the maximum stress value. When the single point is raised to 10 mm at the 3# pier, the bottom stress increment at the 3# pier is negative, indicating compressive stress and the maximum stress value, while the bottom stress increment at the adjacent piers 2# and 4# is positive, indicating tensile stress with relatively large stress values.

(2) Condition 2: The lifting height at the 0# abutment and the 3# pier is 10 mm, while the adjacent piers on the left and right have a lifting height of 5 mm. The stress increments and deformations of the main beam section are shown in Figure 18 - Figure 21.

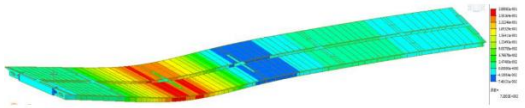

Fig. 18 – Stress distribution diagram of main beam (0# Abutment raised)

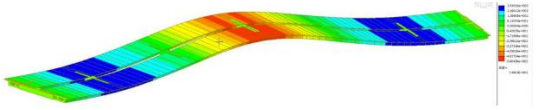

Fig. 19 – Overall bridge stress distribution diagram (3# Pier raised)

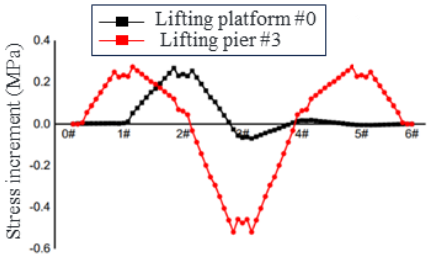

Fig. 20 – Increment of stress on the lower edge of the main beam (0# Abutment, 3# Pier raised)

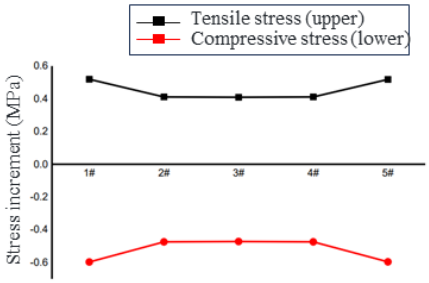

Fig. 21 – Maximum increment of stress on the main beam (1#~5# Pier raised)

From the above figures, it can be observed that when the 0# abutment is lifted to 10 mm and the 1# pier is lifted to 5 mm, the main beam section at the 0# abutment experiences no increase in bottom stress increment due to its unconstrained state. However, the bottom stress increment at the adjacent 1# and 2# piers undergo significant changes. When the 3# pier is lifted to 10 mm and both the 2# and 4# piers are simultaneously lifted to 5 mm, the stress increment across the entire bridge remains large.

(3) Condition 3: The lifting height at the 0# abutment and the 3# pier is 10 mm, while the adjacent piers on the left and right have a lifting height of 8 mm. The stress increments and deformations of the main beam section are shown in Figure 22 - Figure 25.

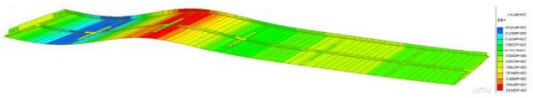

Fig. 22 – Stress distribution diagram of the main beam (0# Abutment raised)

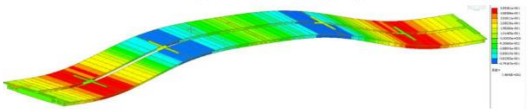

Fig. 23 – Stress distribution diagram of the main beam (3# Pier raised)

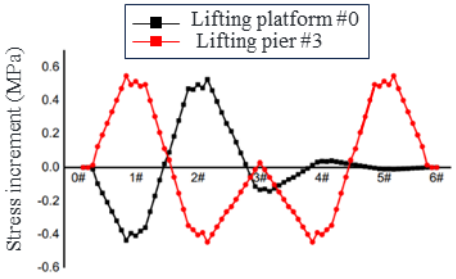

Fig. 24 – Increment of stress on the lower edge of the main beam (0# Abutment, 3# Pier raised)

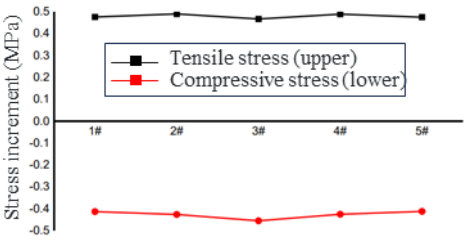

Fig. 25 – Maximum increment of stress on the main beam (1#~5# Pier raised)

From the above figures, it can be seen that when the 0# abutment is lifted to 10 mm and the 1# pier is lifted to 8 mm, the stress increments across the entire bridge are not significant. However, when the 3# pier is lifted to 10 mm and both the 2# and 4# piers are simultaneously lifted to 8 mm, the stress increment at the 3# pier is relatively large and compressive, while the stress increments at the other piers and abutments are relatively small.

(4) Condition 4: Synchronized lifting of the entire bridge by 10 mm, the stress increments of the main beam section are shown in Figure 26.

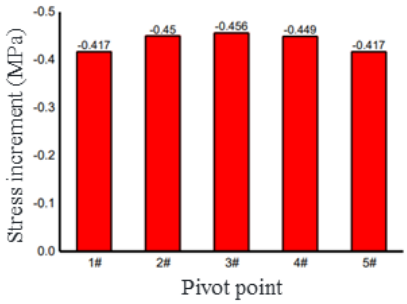

Fig. 26 – Increment of stress on the lower edge of the main beam during synchronized lifting

From the above figure, it can be observed that when the entire bridge is synchronously lifted by 10 mm, the stress increments at the 1# to 5# piers are relatively uniform and the magnitude of the stress increments is also similar.

By utilizing finite element software, a simulation analysis was conducted to analyze the stress increments of the entire bridge under four different loading conditions when the incremental lifting height reached 10 mm. Due to the significantly large total weight and a lifting height of 80 mm for the Gongbin Road viaduct, considering its structural system as a continuous beam bridge, the synchronized lifting scheme is deemed more reasonable, resulting in relatively minimal structural damage.

SIMULATION ANALYSIS OF THE TRANSLATIONAL PROCESS

The translational process simulation is carried out by simulating the top pushing force through the application of concentrated forces. Multiple loading conditions are simulated based on different directions and magnitudes of the top pushing force. The details are as follows.

(1) Condition 1: During the translational process, the jacks exert equal pushing forces in a direction perpendicular to the beam end, pushing towards the inside of the curve. The angle between the pushing force direction and the tangent line of the curve is shown in Table. 2. When simulating the pushing force direction of the bridge using finite element software, the angle between the pushing force direction and the Y-axis is shown in Table 3. The displacement in the transverse, longitudinal, and vertical directions of the main beam is shown in Figure 27 - Figure 29. The maximum stress increments on the upper and lower edges, as well as the inner and outer sides of the main beam, are shown in Figure 30 - Figure 33.

Tab. 2 - Angle between the top-down direction at various support point locations and the normal of the curve

Pivot point	Platform#0	Pier #1	Pier #2	Pier #3	Pier #4	Pier #5	Pier #6
Angle (°)	-9.96	-7.16	-3.58	0	3.58	7.16	9.96

Table. 3 - Angle between the top-down direction and the Y-axis at various support point locations

Pivot point	Platform#0	Pier #1	Pier #2	Pier #3		Pier #4	Pier #5	Pier #6
Angle (°)	0	0	0	0		0	0	0

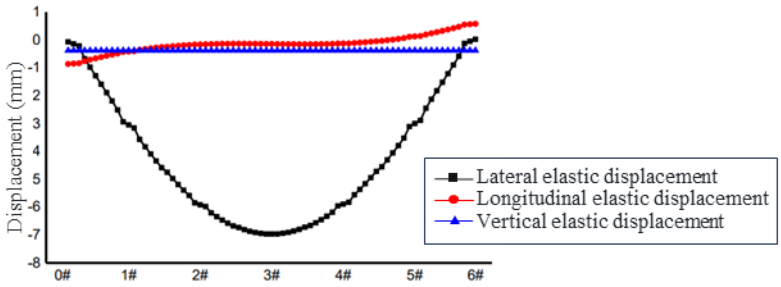

Fig. 27 – Three-dimensional elastic displacement of the main beam during translation process

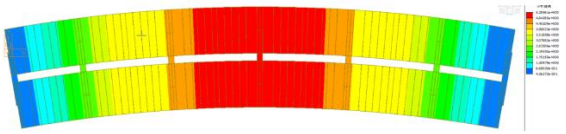

Fig. 28 – Deformation diagram of the main beam during translation process

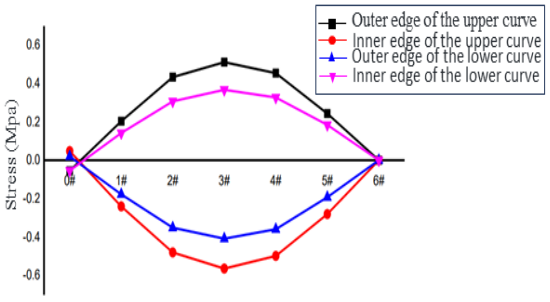

Fig. 29 – Stresses on upper and lower flanges, inner and outer sides of the main beam during translation process

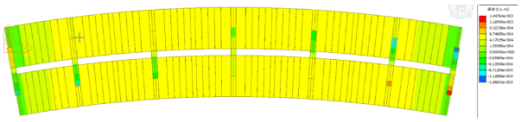

Fig. 30 – Stress distribution on the upper outer surface of the main beam section during translation process

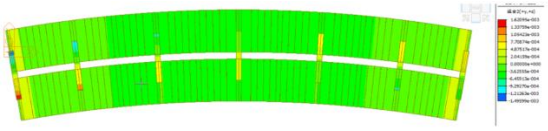

Fig. 31 – Stress distribution on the upper inner surface of the main beam section during translation process

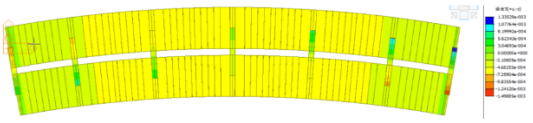

Fig. 32 – Stress distribution on the lower outer surface of the main beam section during translation process

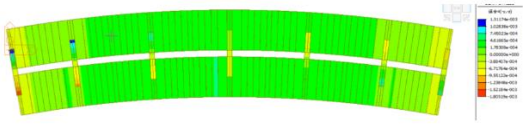

Fig. 33 – Stress distribution on the lower inner surface of the main beam section during translation process

(2) Condition 2: The pushing force is applied in the direction perpendicular to the main beam's line form, pushing towards the inside of the curve. The pushing force magnitude is the same for each pier section. The angle between the pushing force direction and the curve's normal vector is shown in Table 4. When simulating the pushing force direction of the bridge using finite element software, the angle between the pushing force direction and the Y-axis is shown in Table 5.

Tab. 4 - Angle between thrust direction and curve normal at various support locations

Pivot point	Platform#0	Pier #1	Pier #2	Pier #3	Pier #4	Pier #5	Pier #6
Angle (°)	0	0	0	0	0	0	0

Tab. 5 - Angle between thrust direction and Y-axis at various support locations

Pivot point	Platform#0	Pier #1	Pier #2	Pier #3	Pier #4	Pier #5	Pier #6
Angle (°)	9.96	7.16	3.58	0	-3.58	-7.16	-9.96

The maximum deformation in the transverse, longitudinal, and vertical directions of the main beam is shown in Figure 34. The stress deformation cloud diagram of the main beam during translation is shown in Figure 35. The maximum stress increments on the upper and lower edges, as well as the inner and outer sides of the main beam, are shown in Figure 36.

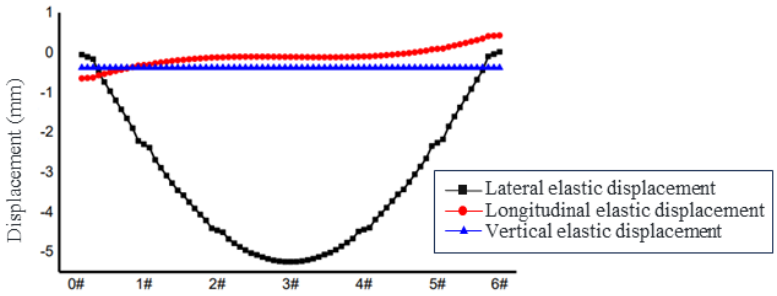

Fig. 34 – Three-dimensional elastic displacement of the main beam during translation process

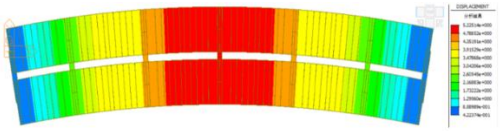

Fig. 35 – Deformation diagram of the translated main beam

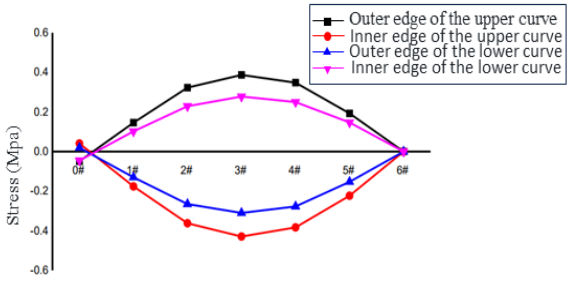

Fig. 36 – Stresses on the upper and lower flanges, inner and outer sides of the translated main beam

(3) Condition 3: The pushing force direction is along the line perpendicular to the beam end and pushing towards the inside of the curve. The maximum deformations in the transverse, longitudinal, and vertical directions of the main beam are shown in Figure 37. The stress deformation cloud diagram of the main beam during translation is shown in Figure 38. The maximum stress increments on the upper and lower edges, as well as the inner and outer sides of the main beam, are shown in Figure 39.

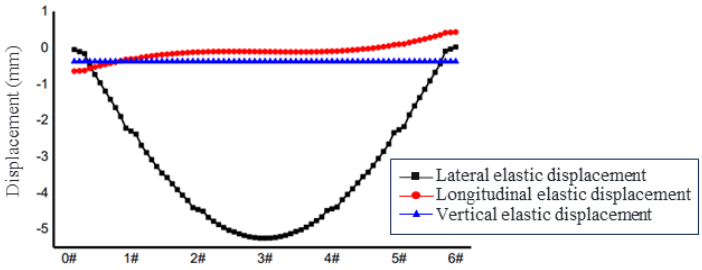

Fig. 37 – Three-dimensional elastic displacement of the main beam during translation process

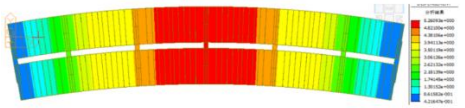

Fig. 38 – Deformation diagram of the translated main beam

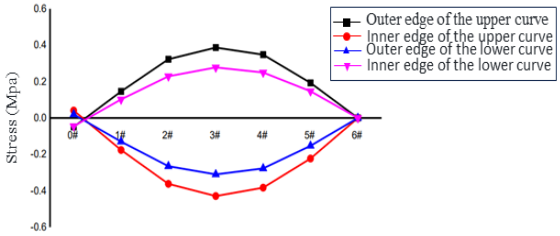

Fig. 39 – Stresses on the upper and lower flanges, inner and outer sides of the translated main beam

Condition 3, when compared to Conditions 1 and 2, exhibits smaller stresses and elastic deformations during construction, ensuring the safety of the beam structure. However, controlling the pushing force of the jacks during the pushing operation in Condition 3 can be challenging. If not finely controlled, there is a possibility that the pushing force may not overcome the frictional resistance, resulting in the inability of the beam to rotate.

Condition 2, in comparison to Condition 1, offers superior stress and deformation characteristics.

With the project located on a curved surface with a radius of curvature of 400 m, when pushing forces are applied perpendicular to the beam's end line, significant horizontal bending deformations of the main beam will occur during the pushing process, and the radius of curvature will decrease.

CONCLUSION

Discussion on the rigid body state of the bridge during the lifting, translation, and resetting construction process, deriving a reasonable method for bridge lifting and translation construction, as well as establishing a model. Proposing stress limitation criteria during the lifting and translation process. Then, based on the aforementioned model establishment method, a finite element model of the actual bridge is established, and a simulation analysis is conducted on the lifting and translation process of the project. The following conclusions are reached:

(1) Under various load conditions, temperature load (specifically system load) has a significant impact on the deflection of curved beam bridges. Its influence is even greater than the cumulative displacement caused by self-weight, construction phase load, gradient load, vehicle load, and bearing settlement, highlighting its importance. In China, there is a significant temperature difference between the north and south. In the southern regions, it is necessary to consider the overall temperature rise and its effects on the deflection of curved beam bridges, while in the colder northern regions, greater consideration should be given to the overall temperature decrease and its effects on the deflection of curved beam bridges.

(2) The closer the lifting height of the main beam at the pier and bridge abutment, the more similar the growth pattern of the section stress values. When synchronous lifting was employed, the stress values were all within 0.45 MPa and below the ultimate stress limit. Due to the large lifting height required for the project, it is necessary to control the stress differences. Therefore, the synchronous lifting construction method was adopted.

(3) During the translation construction phase of the beam, a concentrated force was applied to simulate the pushing force of a hydraulic jack. Combining with the model, the movement form and stress state of the beam under different pushing force directions and magnitudes during the translation process were discussed. Safety in construction and the difficulty of construction control were taken into consideration to derive a reasonable construction plan.

REFERENCE

[1] Zhai, Zhihao, Chengbiao Cai, and Shengyang Zhu. Implementation of Timoshenko curved beam into train-track-bridge dynamics modelling[J]. International Journal of Mechanical Sciences, 2023, 247: 108158.

[2] Linzell, D. G., and J. F. Shura. Erection behavior and grillage model accuracy for a large radius curved bridge[J]. Journal of Constructional Steel Research, 2010, 66(3): 342-350.

[3] Li, Ming, and Jingqiao Hu. Analysis of heterogeneous structures of non-separated scales using curved bridge nodes[J]. Computer Methods in Applied Mechanics and Engineering, 2022, 392: 114582.

[4] Tondini, Nicola, and Bozidar Stojadinovic. Probabilistic seismic demand model for curved reinforced concrete bridges[J]. Bulletin of earthquake engineering, 2012, 10: 1455-1479.

[5] Dimitrakopoulos, Elias G., and Qing Zeng. three-dimensional dynamic analysis scheme for the interaction between trains and curved railway bridges[J]. Computers & Structures, 2015, 149: 43-60.

[6] Wang, Jianwei, et al. Application of High-Viscosity Modified Asphalt Mixture in Curved Bridge Pavement[J]. Sustainability, 2023, 15(4): 3411.

[7] Seo, Junwon, and Daniel G. Linzell. Use of response surface metamodels to generate system level fragilities for existing curved steel bridges[J]. Engineering Structures, 2013, 52: 642-653.

[8] Kim, Woo Seok, Jeffrey A. Laman, and Daniel G. Linzell. Live load radial moment distribution for horizontally curved bridges[J]. Journal of Bridge Engineering, 2007, 12(6): 727-736.
[9] Zeng, Qing, Y. B. Yang, and Elias G. Dimitrakopoulos. Dynamic response of high speed vehicles and sustaining curved bridges under conditions of resonance[J]. Engineering Structures, 2016, 114: 61-74.
[10] Monzon, Eric V., Ian G. Buckle, and Ahmad M. Itani. Seismic performance and response of seismically isolated curved steel I-girder bridge[J]. Journal of Structural Engineering, 2016, 142 (12): 04016121.
[11] DeSantiago, Eduardo, Jamshid Mohammadi, and Hamadallah MO Albaijat. Analysis of horizontally curved bridges using simple finite-element models[J]. Practice Periodical on Structural Design and Construction, 2005, 10(1): 18-21.
[12] Ni, Yongjun, et al. Influence of earthquake input angle on seismic response of curved girder bridge[J]. Journal of traffic and transportation engineering (English edition), 2015, 2(4): 233-241.
[13] Wen, Q., et al. Control of human-induced vibrations of a curved cable-stayed bridge: Design, implementation, and field validation[J]. Journal of Bridge Engineering, 2016, 21(7): 04016028.
[14] Nevling, D., Daniel Linzell, and J. Laman. Examination of level of analysis accuracy for curved I-girder bridges through comparisons to field data[J]. Journal of Bridge Engineering, 2016, 11(2): 160-168.
[15] Zhang, Lixin, and Yin Gu. Seismic analysis of a curved bridge considering soil-structure interactions based on a separated foundation model[J]. Applied Sciences, 2020,10(12) :4260.

CIVIL ENGINEERING JOURNAL

Article no. 9

THE CIVIL ENGINEERING JOURNAL 1-2024

GEOTECHNICAL ANALYSIS AND REMEDIAL DESIGN OF A POTENTIALLY UNSTABLE CUTTING

Zdenek Siska

Czech Technical University in Prague, Faculty of Civil Engineering, Department of Geotechnics, Prague, Thakurova 7/2077, 166 29, Czech Republic; siskazde@fsv.cvut.cz

ABSTRACT

The article deals with the analysis of a potentially unstable cutting in weak rocks and a design of its remediation. It is described here the collection of information, its interpretation and stability analysis of the cutting, which focuses on deeper than just surface slip surfaces to assess the risk of slope movements with significant safety and economic impact. Based on the results of the evaluation, appropriate remediation measures are proposed.

KEYWORDS

Slope stability, Geological data collection, Structural analysis, Remedial measures

INTRODUCTION

Landslides can be a major geodynamic phenomenon with significant impacts on the environment and human activity. They usually arise when the stability of a slope is disturbed by its own weight, surface overload, inappropriate changes in slope, adverse changes in the water regime, as a result of earthquakes, etc.

Where terrain modification is required, slope movements should be prevented by appropriate design that identifies and evaluates potential risks. If there is already an existing unsatisfactory condition, this is followed by an assessment and design of remediation measures. Both cases should also be accompanied by appropriate monitoring. An example of the use of monitoring and the evaluation of data obtained in this way can be found, for example, here [1].

This article shows on a particular small-scale slope stability issue the usual procedure for evaluation and remedial design.

The area of interest can be seen in Figure 1. It is a cutting made approximately 80 years ago which in its northern part experiences a continuous sliding of material due to surface erosion. There is limited access to the cutting as it is adjacent to an existing structure. The constrained spatial conditions, together with the need for a cost-effective solution, limit to some extent the use of larger and more robust technologies for both exploration and subsequent remediation.

GEOLOGICAL CONDITIONS AND GEOTECHNICAL MODEL

The determination of the geological and geotechnical conditions, including material parameters, was based on in situ inspection, excavated probes, laboratory tests and archival and map materials of the Czech Geological Survey.

Geological conditions

The area of interest is located in the area through which passes a system of tectonic faults called the Blanice Graben, which was formed 305-300 million years ago. The cutting is made in the right bank slope of the valley in which the local brook is situated. The rocks exposed by the cutting

are alternating grey and red colored sandstones (see Figure 2). According to the 1:50 000 geological map [2], these are Upper Carboniferous and Permian in age. The Quaternary cover of the sandstones, according to in situ inspection, consists of sandy silts. According to the mapped slope deformations [3], there are no landslide areas in the area of interest.

The cutting consists of a stable part with healthy sandstone, which is covered with vegetation, and an unstable - exposed part (see Figure 1). The unstable part is the main focus of this paper, as it is identified as potentially the most critical part of the cutting.

Fig. 1 - The cutting with the stable part covered with vegetation and the exposed unstable part

Fig. 2 - A rock sample from the weathered face of the cutting with an interface of grey and red sandstone

Hydrogeological conditions

The water regime in the vicinity of the site of interest is described in an archival survey for the local irrigation reservoir [4]. Here it is noted that the local sandstones have a siliceous cement and very sparse fractures, often filled with surrounding material. Clay and clay shale, which are almost impermeable to water, also occur in the area. The borehole survey indicated only the presence of a shallow groundwater horizon in the alluvial sediments in the local brook inundation. In the boreholes located in the slopes outside the inundation, no water was detected at all. This survey was carried out during periods of heavy rainfall.

An in-situ inspection conducted on 3/2023 during the spring rainy season did not reveal any water discharge from the cutting. Also, a well was found in the very vicinity of the cutting in the brook's inundation area. A steady water level was found here approximately 3 meters below ground level. This is consistent with the above-mentioned archival survey.

Geotechnical cross-section

On the basis of the in-situ inspection and archival documents, a geotechnical profile was made (Figure. (4)3). The slope of the cutting is approximately 60° and the slope of the ground above the cutting is 27°.

The rock in the form of sandstone is overlaid by 2 m of sandy clay. The thickness of this Quaternary cover above the cutting was determined by in situ inspection considering the data in the archive borehole survey as well. Below the base of the cutting, the geotechnical profile took into account the brook inundation area according to the bedrock encountered during the nearby well excavation and also from the archival survey for the local irrigation reservoir [4]. A 0.5 m thick weathered zone was also defined in the face of the cutting representing weathered rock with poorer properties. The groundwater level was set at a depth of 3 m below the base of the cutting.

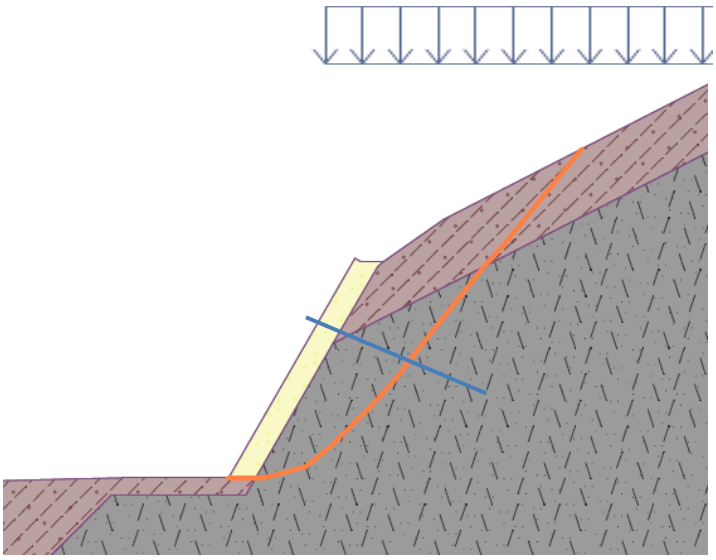

Fig. 3 - Optimized polygonal slip surface with marked snow load and position of extensometer in the upper third of the cutting

Laboratory tests and parameter determination

Sandstone samples were taken from the weathered zone during the in-situ inspection and were subjected to the point load test. Subsequently Mohr-Coulomb shear parameters were estimated using a conversion of the resulting point load index to obtain uniaxial compressive strength

and uniaxial tensile strength which is shown in Figure 4. The whole procedure is in detail explained in [5].

The resulting estimations of the effective angle of inner friction equals 32° and effective cohesion equals 21 kPa. As aforementioned, these parameters relate to the weathered zone. It wasn't possible to obtain rock samples from larger depths under the face of the cutting by hand because of rapid increase in strength of the sandstone. Therefore, these shear parameters represent very conservative lower limit of the solid sandstone capabilities, which can compensate for unknown positions of discontinuities or disintegration into blocks. Shear parameters for the weathered zone itself were chosen to have the same angle of inner friction as the ones estimated for the sandstone, but no cohesion which is supposed to characterize long term weathering. Shear parameters of the overlaying sandy clay were estimated with respect to parameters of the original rock and the parameters reported in the Czechoslovak national standard CSN 73 1001 [6]. The resulting Mohr-Coulomb material Parameters are summarized in Table 1.

Tab. 1 - Estimated effective material parameters for Mohr-Coulomb model of the cutting

Material	φ‘ [°]	c‘ [kPa]
Sandstone	32	21
Sandy clay	29	12
Weathered zone	32	0

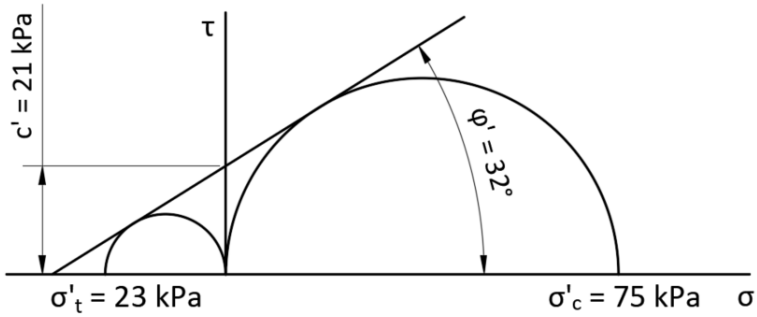

Fig. 4 - Determination of φ‘ = 32° and c‘ = 21 kPa based on uniaxial compressive and tensile strength [5]

STRUCTURAL ANALYSIS OF THE CUTTING

The actual slope stability evaluation was performed by the limit equilibrium methods using both the circular and polygonal slip surfaces and their optimalization. For this analysis a software GEO 5 was used. The slip surface was prevented from running parallel through the weathered face in order to trace potential slip surfaces within the slope. The shape of the most critical polygonal shear surface can be seen in Figure. 4. The snow load on the slope above the cutting was also considered and its magnitude was determined using a snow map to be q = 0.64 kN/m2 [7]. Another surface load above the cutting wasn't considered because the area here serves only as a fruit garden and the 27° slope doesn't allow for its another utilization. If these actual conditions changed, the analysis would have to be repeated reflecting a new situation.

The evaluation was carried out both by using the shear strength according to EN 1997-1 [8] using design approach 3 and by determining the factor of safety. Accordnig to EN 1997-1 [8], the result of the evaluation is presented in the form of a percentage of utilization of the total shear strength along the shear plane to withstand the resulting active forces acting on the body of the landslide. The factor of safety on the other hand is a ratio between the total shear strength along the shear plane and the resulting active forces acting on the body of the landslide.

The evaluation was made using the Bishop, Sarma, Spencer, Janbu and Morgenstern-Price methods. The minimum permissible degree of stability was determined according to the Czech technical standard CSN 73 6133 [9]. It requires a minimum factor of safety of the cutting in the rocks FS = 1.3 when considering the peak effective shear parameters. The results of all the methods are summarized in Table 2. According to these results, the cutting can be declared stable, only with problems caused by surface erosion. These are addressed by the remediation design in the next section.

Tab. 2 - Results of the static slope stability evaluation

Method	Utilization according to CSN EN 1997-1 DA3 (<100 %)	Factor of safety stability FS (>1,3)	Evaluation
Bishop	87,9 %	1,43	Comply
Sarma	85,2 %	1,46	Comply
Spencer	92,2 %	1,35	Comply
Janbu	95,3 %	1,31	Comply
Morgenstern-Price	95,3 %	1,31	Comply

SURFACE EROSION REMEDIATION DESIGN

Since the structural analysis did not identify problems with the stability of the slope, so the remediation design of the cutting may be limited to anti-erosion measures in the form of an anchored lining of its face. This measure is necessary for the part of the cutting visibly degraded by surface erosion, referred to in this text as the 'unstable part' (see Figure 1). It is possible that the part of the cut referred to in this text as 'stable' (see Figure 1), consisting of more solid rock, may not require this measure. However, since the stable part of the cutting is presently covered by climbing vegetation, it is not possible to assess it comprehensively in terms of rock quality, discontinuities, loose blocks of rock, etc. For this reason, and also for the sake of a uniform appearance of the face of the cutting, a single remediation design has been submitted for the entire cutting.

The proposed design consists of gabion lining covering the face of the cutting through the separating geotextile and surface water drainage situated at the crown and at the base of the cutting. The lining is secured by nailing up to the healthier rock (see Figure. 5). The nailed gabion lining system has been evaluated again by structural analysis. The design emphasizes construction using only hand tools with regard to the spatial constraints mentioned above and the need for a cost-effective solution. Other types of lining would be possible as well (e.g. sprayed concrete), but always in combination with nailing for securing its stability.

For verification of the design and the results of the structural analysis, an extensometer placed in the upper third of the cutting is proposed as monitoring. Its length is required to be 4 m to reach safely beyond the possible expected slip surface (see Figure 4). Various types of extensometers are possible to use here ranging from standard rod to FBG extensometers.

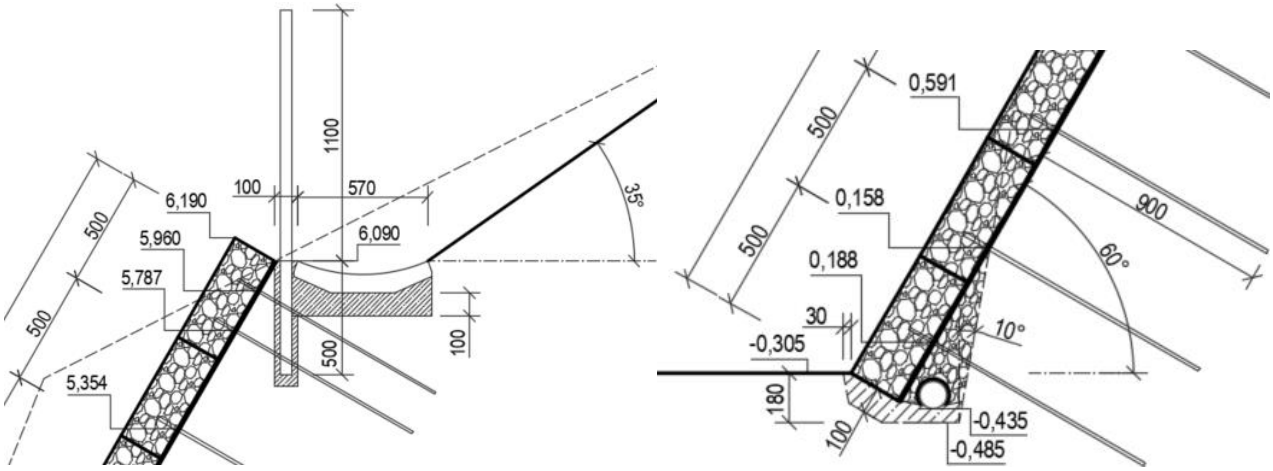

Fig. 5 - Preview of the anti-erosion measure of the face of the cutting - nailed gabion lining; on the left the drained back of the structure at the foot of the slope; on the right the surface drainage of rainwater above the cutting

Nailing of gabion lining

The gabion's back mesh is anchored through the base plates with a nail through the weathered face into the healthier rock. The primary purpose of the nails is horizontal and vertical stabilization of the erosion control lining.

The nails are 1 m long and consist of an M12 threaded stainless steel rod. They are inserted into 30 mm diameter boreholes 900 mm deep filled with cement grout. A 100 mm long nail will therefore protrude from the aligned and cleaned face. Stainless steel is essential when grouting with cement grout. This precludes the use of zinc-coated rods as the hardening cement loses its strength in the presence of zinc [10].

In place of stable rock, it is conditionally possible to use dowels, chemical anchors and other suitable anchoring material of shorter lengths instead of nails. It can be estimated that up to half of the wall area may be involved.

CONCLUSION

In its introduction, the article briefly summarizes typical geotechnical risks associated with slope stability and then shows the usual procedure for solving this problem. Using archival materials and in situ inspection, an introduction to the geology of the site of interest in which the cut is located is demonstrated. With this background and considering the possible risks mentioned in the introduction of the paper, a geotechnical model is developed, and the slope stability is analyzed. According to the results of the analysis, remediation measures are proposed together with recommendations for monitoring.

ACKNOWLEDGEMENTS

This article was supported by internal grant of Czech Technical University in Prague SGS24/081/OHK1/2T/11.

REFERENCES

[1] Zalesky, J., Capova, K., 2017. Monitoring and Assessment of Remedial Measures in Closed Open Cast Mine. Advancing Culture of Living with Landslides, no. 3: 597–605. DOI: 0.1007/978-3-319-53487-9.
[2] Geologicka mapa 1 : 50 000 - indexes, Geologicka mapa 1 : 50 000 - doplnky, Geologicka mapa 1 : 50 000, Klad listu ZM50. In: Geovedni mapy 1 : 50 000 [online]. Czech Geological Survey [cit. 2024-02-20]. Available from: https://mapy.geology.cz/geocr50/
[3] Mapovane svahove deformace, Registracni zaznamy, Listoklad ZM 10. In: Svahove deformace [online]. Prague: Czech Geological Survey [cit. 2024-02-20]. Available from: https://mapy.geology.cz/svahove_nestability/
[4] Muzik, P. et al., 1981. Ksely zavlahová nadrz – Predbezny inz. geologicky pruzkum staveniste (Agroprojekt projektovy a inzenyrsky podnik v Praze, Karlovy Vary)
[5] Siska, Z., 2023. Point Load Test and its Utilisation During the Assessment of a Cutting in Weak Rocks. In: 15. Slovenska Geotechnicka Konferencia. 151-160 ISBN 978-80-227-5313-5.
[6] CSN 73 1001. Zakladani staveb. Zakladova puda pod plosnymi zaklady Prague: Vydavatelstvi Uradu pro normalizaci a mereni, 1987. 76 p.
[7] Mapa zatizeni snehem na zemi. In: Mapa zatizeni snehem na zemi [online]. Prague: Czech Hydrometeorological Institute [cit. 2024-01-10]. Available from: https://clima-maps.info/snehovamapa/
[8] CSN EN 1997-1. Eurocode 7: Geotechnical design - Part 1: General rules. Prague: Czech Standards Institute, 2006. 138 p.
[9] CSN 73 6133. Road earthwork - design and execution. Prague: Czech Standards Institute, 2010. 68 p.
[10] Pokorny, P., 2012. The influence of galvanized steel on bond strength with concrete. Koroze a ochrana materialu, vol. 56, no. 4: 119–135. DOI: 10.2478/v10227-011-0020-9.

CIVIL ENGINEERING JOURNAL

Article no. 10

THE CIVIL ENGINEERING JOURNAL 1-2024

ANALYSIS ON THE MECHANICS AND DEFORMATION OF SIDE PILE STRUCTURE IN METRO STATION WITH THE PBA METHOD

Jianguo Gao1, Zhaofa Zeng1, Shuai Zhang2, Huijian Zhang2 and Xuemin Zhou2

1. *Guangzhou Metro Construction Management Co. Ltd, Guangzhou, 510330, China*
2. *School of Civil Engineering, Key Laboratory of Transportation Tunnel Engineering, Ministry of Education, Southwest Jiaotong University, No. 111, North Section, Second Ring Road, Jinniu District, Chengdu, Sichuan Province, 610031, China; 1165981488@qq.com; huijianz@163.com; xm.zhou@my.swjtu.edu.cn*

ABSTRACT

There is limited research on the interaction mechanism between the buckling load of the side pile top and the soil pressure behind pile (SPP) with the side pile. As the side pile serves as a crucial component of the lining structure in the metro, using the pile-beam-arch (PBA) method, it plays a vital role in maintaining the mechanical stability and deformation control of the station's lining system. Based on the Guangzhou Metro Line 11 project, this paper delves into the impact of mechanical characteristics and deformation of the side pile using the PBA method. It considers various factors such as different buckling loads, including horizontal load of arch (HLA), vertical load of arch (VLA) and SPP and offers corresponding construction suggestions. Our findings indicate that the lateral displacement and deformation of the side pile are primarily influenced by the HLA. The optimal HLA value stands at 1200kN. As the HLA increases, the side pile undergoes a transformation from a forward-inclined deformation mode to a belly distension deformation mode when moving towards the station’s interior. The influence of HLA on bending moments about the side pile surpasses that of axial force. The VLA exerts a more significant effect on vertical settlement of the side pile, yet its impact on lateral pile body deformation is minimal. An increase in HLA significantly impacts the axial force of the side pile, but has minimal effects on bending moments. The SPP holds significant influence on the stability of the side pile; hence, it is recommended to implement appropriate lining measures to guarantee stability when dealing with exceptionally high SPP values.

KEYWORD

PBA method, Side pile, Mechanical properties, Deformation law

INTRODUCTION

The stability of underground structures has always been a key area of research [1-4]. The PBA method, which was refined by Chinese engineers based on the shallow-buried excavation method by combining the technical achievements of cover excavation and frame structures, has

been successfully implemented in the construction of subway stations across numerous cities in China [5-7]. The core of PBA method is to form a lining structure system of underground with pile-beam-arch interaction through the organic combination of small pilot tunnel, arch, lining pile and other mature technologies, which can withstand the external load during the construction of underground station and form a strong and effective safe working space under its protection. This construction method has unique advantages such as remarkable control effect of surface settlement, flexible structure, high construction safety, and small influence on the nearby environment [8, 9]. So it is especially suitable for urban subway station construction projects with large surface traffic flow, complex and variable underground pipelines, limited construction sites, and high requirements of ground settlement [10-12].

During the construction of stations using the PBA method, the side pile emerges as a crucial element of the station's lining system [13]. Its functionality extends beyond merely transferring the upper load to deeper soil layers; it also serves to restrict lateral deformation triggered by station excavation. Presently, investigations into pile stress mechanisms are predominantly focused on projects involving foundation reinforcement [14-17], foundation pit lining [18-20], slope stabilization [21-24], and other related fields. Based on the foundation pit project of an underground passage, He [25] analyzed the impact about various CFG composite foundation parameters on the deformation of the envelope structure. It was found that CFG pile composite foundation can not only reduce the vertical displacement of soil, but also reduce the lateral deformation of soil. An *et al.* [26] studied the bearing characteristics of high-pressure rotating pile when strengthening soft soil foundation, analyzed the mechanism of pile group in reducing soil settlement and improving the bearing capacity of foundation. It was pointed out that high-pressure rotating pile can significantly control soil deformation from the depth of the surface to the bottom of the pile, and increase the pile diameters and material strength about pile can significantly increase the carrying capacities about composite foundation. Wang [27] studied the differences in the strengthening effects of high-pressure rotating pile, pit static pile and manual excavation pile on loess foundation, and found that manual excavation pile has the characteristics of high bearing capacity in single pile, good reinforcement effect, reliable construction quality, and obvious advantages in the reinforcement of collapsible loess. Liu *et al.* [28] investigated the effects of pile and cushion parameters on the deformation about composite foundation using deep mixed pile, and found that pile length has the most significant effect on controlling the deformation about composite foundation, while elastic modulus of cushion has little effect on it. Benmebarek *et al.* [29] demonstrated that free piles make little contribution to increasing the safety factor about the viscous-friction slope, and the pile arching effect would completely disappear due to soil flowing effect between piles when the pile spacing ratio is greater than four. Chen *et al.* [30] put forward a correction method for the ultimate lateral soil resistance of rigid piles in non-cohesive soil of slope, pointing out that in shallow soil layer, the lateral soil resistance gradually increased with the depths, and the lateral resistance of soil reduced with the increase of slope angle and reached the limit value more easily. To sum up, some scholars have conducted certain studies on the bearing capacity and mechanical performance of lining piles. And many important results have been obtained, mostly in the aspects of composite foundation, foundation pit, slope and so on. The unique mechanical nature of the side pile in the metro system utilizing the PBA

method differs significantly from the conventional vertically stressed pile and the lining pile that solely experiences lateral load. Therefore, it cannot be accurately analyzed using current calculation methods, and existing research results cannot be simply applied when dealing with the problem of the side pile in metro with PBA method.

Therefore, relying on the Tianhe East Station project of Guangzhou Metro Line 11 (constructed by PBA method), this paper studies the mechanical characteristics and deformation rules of the side piles of station under different key construction stages by using numerical calculation method, considering the influence factors such as different HLA, VLA and SPP, aiming to provide some important guidance for similar project.

PROJECT OVERVIEW

Guangzhou Metro Line 11 is a downtown metro line, and its total length is 43.2 kilometers. Tianhe East Station is the 7th station of Guangzhou Metro Line 11. It is laid under the surface of Tianhe North Road, as displayed in Figure 1 (a). The station belongs to a two-span station with one column and two underground layers, which is constructed by PBA method. The height, width and depth of the station is 21.4m, 25.5m and 9m, respectively. The side piles are in the form of manual excavation pile with the size (pile diameter × pile distance × pile length=1.2m × 1.5m × 15m). The cross-sectional arrangement of the station structure is displayed in Figure 1 (b). According to the site survey data of Guangzhou Metro Line 11, the side piles of the station are mainly located in the following three typical strata: strong weathering argillaceous siltstone, medium weathering argillaceous siltstone and breezy gravel coarse sandstone.

(a) Geographical location of the Guangzhou Metro Line 11

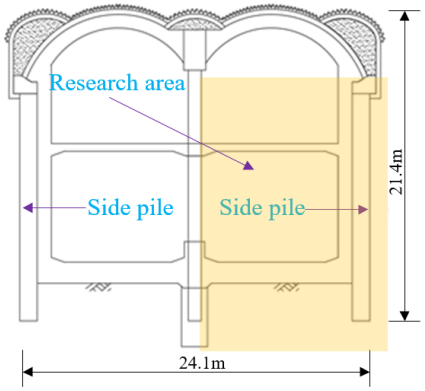

(b) Cross-sectional picture of the Tianhe East Metro Station

Fig. 1 - Basic overview of the Tianhe East Metro Station

CALCULATION INSTRUCTIONS

Calculation model

FLAC3D finite difference software is adopted for numerical simulation, and the relevant physical and geometric parameters about the calculation models are used through the actual

engineering data of Guangzhou Metro Line 11, and the established finite element model is displayed in Figure 2. For the boundary size about the model, in order to decrease the impact about “boundary effect” on the calculation results, the model size is width × height × longitudinal length = 72m×35m×21m. The normal displacement constraint is applied to the bottom and horizontal surrounding boundary of the model, and the load boundary is applied to the top to simulate the actual buried depth of the metro station. This paper uses the attach command method and the setting of common node recommended in the FLAC3D software [31] to define the contact of different components.

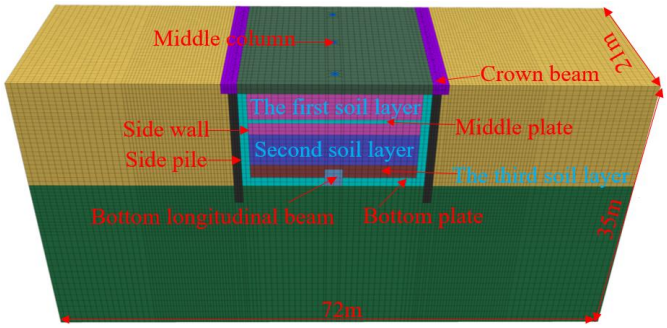

Fig. 2 - Numerical calculation model

Based on the principle of mechanical equivalence, the calculation model is simplified. The buckling force F_A of the arch of station is decomposed into VLA (F_y) and HLA (F_x) applied to the crown beam and mid-column structure, and a uniform load SSP (q) is imposed on the soil surface behind the pile to simulate the overlying soil pressure. The simplified calculation models are displayed in Figure 3. According to the calculation results from the bedded-beam model, it is obtained that the VLA and HLA of the crown beam structure are 1200kN/m and 800kN/m respectively. The VLA of the two arches on both sides of the mid-column structure is borne within 8m column spacing, and the HLA will cancel each other due to the symmetry of the left and right arches. It is calculated that the load (F) of the top of single column is 19200kN, and the SSP is 250kPa.

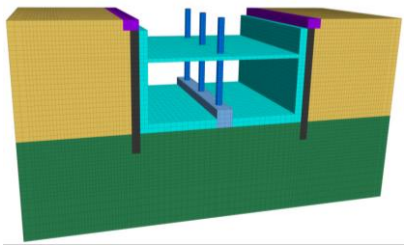

(a) Detail model of the station

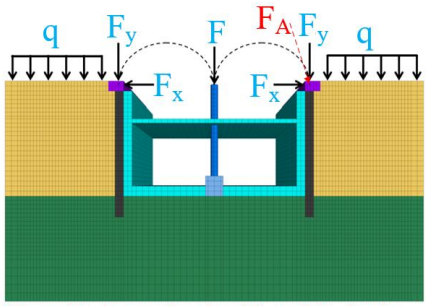

Note: F_A is resolved to F_x and F_y in the simulation model

(b) Simplification diagram of the load of arch

Fig. 3 - The simplified calculation models

Numerical simulation of the simplified PBA method

In this paper, the numerical simulation process of PBA method is carried out according to steps (a) ~ (i) : (a) Initial geostress equilibrium; (b) Application of the *q*; (c) Installation of side piles, crown beams, and middle columns; (d) Application of F_x and F_y to the crown beam and *F* to the middle column; (e) Excavation of the first soil layer of the main body of the station; (f) Installation of the center plate and side wall corresponding to the position of the first soil layer; (g) Excavation of the second soil layer of the main body of the station; (h) Excavation of the third soil layer of the main body of the station; (i) Installation of the bottom plate, bottom stringer and side wall. The main structure of the station has been completed.

Computation parameter

The surrounding rock as well as the lining structure of the station are simulated by solid elements, and the surrounding rock adopts the ideal elastic-plastic constitutive model and obeys the Mohr-Coulomb strength yield criterion [32, 33]. The lining structure is regarded as linear elastic material and adopts elastic constitutive model. The calculation parameters about surrounding rock as well as lining structure of the station are displayed in Table 1 and Table 2.

Tab. 1 - Calculation parameters about surrounding rock

Name	Density ρ /(kg/m^3)	Elastic modulus E /MPa	Cohesive force c /kPa	Friction angle φ /°	Poisson's ratio μ
Highly weathered argillaceous siltstone	2100	120	50	28	0.33
Medium weathered argillaceous siltstone	2500	500	150	30	0.25
Breezy gravelly coarse sandstone	2600	2000	260	32	0.25

Tab. 2 - Calculation parameters about station lining structure

Name	Lining material	Size	Density ρ /(kg/m^3)	Elastic modulus E /GPa	Poisson's ratio μ
Crown beam	C30 reinforced concrete	1.8×1.2m	2500	30.0	0.20
Middle column	C50 reinforced concrete	0.9m@8m	2700	63.5	0.20
Bottom longitudinal beam	C35 reinforced concrete	1.4×2.9m	2700	31.5	0.20
Sidewall	C35 reinforced concrete	Thickness =0.8m	2700	31.5	0.20

Middle plate	C35 reinforced concrete	Thickness =0.5m	2700	31.5	0.20
Bottom plate	C35 reinforced concrete	Thickness =1.2m	2700	31.5	0.20

Calculation conditions

The side pile is the key stress component in the lining structure with PBA method, which plays a vital role in the mechanical stability and displacement control about the lining system of station. Its stress state is not only related to the properties of the strata around the pile, but also closely related to the mechanical state about pile top (HLA and VLA), and the SPP (manifested by buried depth) and other factors. The load mode of the side pile is different from the bearing pile which mainly bears vertical load and the supporting pile which mainly bears lateral load. The pile top bears the load transmitted by the arch, and the pile body bears the lateral soil pressure caused by the soil behind the pile. However, at present, the theoretical research of station with PBA method still lags behind the practical experience of engineering, especially the interaction mechanism between the pile top buckling load (HLA and VLA) and the SPP and side pile is rarely involved, and the law of its influence on the mechanics as well as deformation about side pile is not completely clear. Based on this, this paper studies the mechanical characteristics as well as deformation laws about pile structure under different loads through changing these three main influencing factors (HLA, VLA and SPP). The specific calculation conditions are displayed in Table 3.

Tab. 3 - Calculation conditions

Influencing factor	Conditions				Instructions
HLA /(kN/m)	400	800	1200	1600	Fix VLA =1200 kN/m and SPP =250 kPa
VLA /(kN/m)	800	1200	1600	2000	Fix HLA =800 kN/m and SPP =250 kPa
SPP /kPa	125	250	375	500	Fix VLA=1200 kN/m and HLA =800 kN/m

ANALYSIS OF THE CALCULATION RESULTS

Influence of HLA on side pile

Deformation analysis of side piles

The evolution rule about lateral displacements of lower pile structure under different HLAs with the station construction process is displayed in Fig. 4. ***Note:*** for the description of convenience, the main construction stages are represented by stages A~D, namely, stage A (completion of the buckle arch), stage B (excavation of the 1st layer), stage C (excavation of the 2nd layer), stage D (completion of the bottom plate).

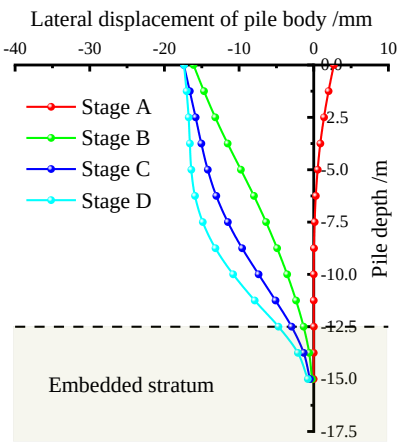

(a) HLA =400kN/m

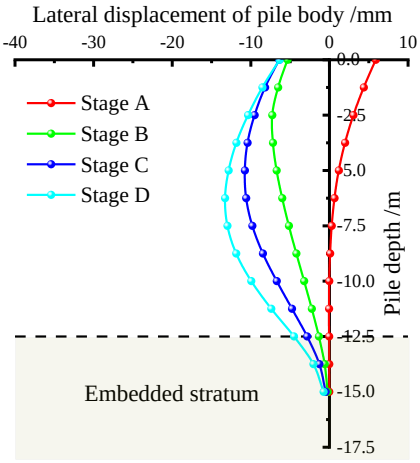

(b) HLA =800kN/m

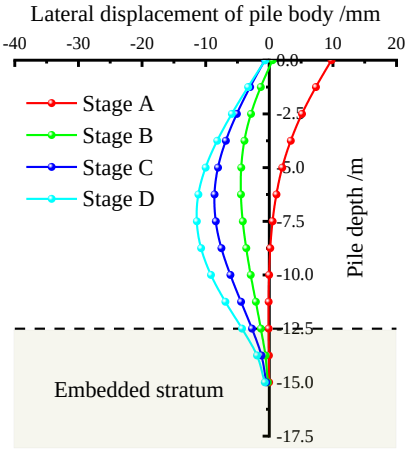

(c) HLA =1200kN/m

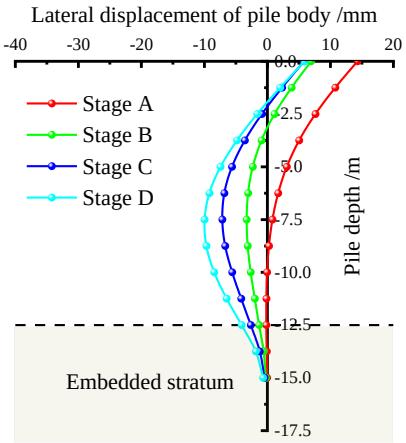

(d) HLA =1600kN/m

Fig. 4 - Evolution law of the lateral displacement about pile under various HLA

In Figure 4, since the side pile is similar to the cantilever beam structure after the completion of the buckle arch, under the action of HLA, the pile body generates a positive displacement to the outside of the station, and the value of the positive displacement increases with the HLA. Under each condition (HLA =400~1600 kN/m), the maximum lateral displacements about the pile body after the completion of the buckle arch appears at the top of the pile, and its displacement value is 2.71mm, 5.91mm, 9.80mm and 14.32mm in order. In other words, the greater the HLA, the greater the lateral displacements about the pile, and the more adverse it is to the side pile. Subsequently, with the excavation of soil inside the station, the side pile gradually migrates to the station, but the lateral deformation trend and amplitude of the pile body are different due to the different HLA on the pile top. For the HLA is small (only 400kN/m), when excavating the 1st soil layer, due to the excavation about the soil inside the station, the soil stresses on the pile side are released, and the lateral displacement about the pile body quickly changes from the “forward” deformation mode after the completion of the arch to “backward” deformation mode. The largest lateral displacements about the pile body still appears at the pile top, and the displacement changes greatly (up to 18.80mm). Once

the HLA increases to be more than 800kN/m, due to the large HLA on the pile top, the pile plays a better lateral lining role, resulting in the deformation characteristics about the side pile from “forward” mode to “bulging” mode when it migrates to the station interior. The results reveal that the lateral displacements about side piles are significantly affected by the HLA. When the HLA is small, the pile top cannot form good horizontal lining effect, and is prone to large deformation, which is not conducive to the stability of side pile.

The final lateral displacements of side pile under different HLA after the completion of station construction are shown in Figure 5, and the final peak lateral displacements of side piles are extracted, as shown in Table 4.

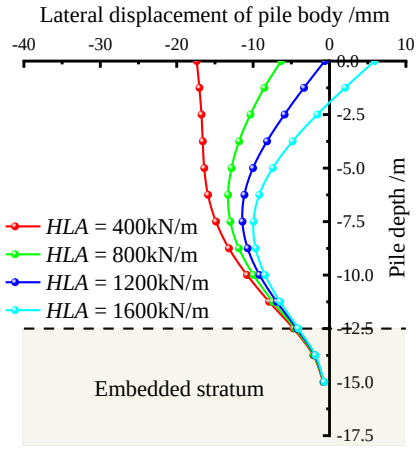

Fig. 5 - Comparison of the final lateral displacement of pile body

Tab. 4 - Peak value of the final displacement of pile body under different HLA /mm

Lateral displacement *X*	HLA = 400kN/m	HLA = 800kN/m	HLA = 1200kN/m	HLA = 1600kN/m
Maximum value X_{max}	-0.78	-0.74	-0.61	5.92
Minimum value X_{min}	-17.37	-13.27	-11.38	-9.94
Relative difference X_d	16.59	12.53	10.77	15.86

Note: the relative difference ($X_d = X_{max}-X_{min}$) about lateral displacements of pile body is adopted to describe the bending degree of pile body.

In Figure 5 and Table 4, with the adding of HLA, the constraint effect on side pile is enhanced, the lateral displacements about pile body gradually decreases, and the deformation characteristics also change, indicating that HLA imposes a crucial role in the lateral displacement about side pile. When the HLA ranges from 400kN/m to 1600kN/m, the peak lateral displacement of side piles are -17.37mm, -13.27mm, -11.38mm and -9.94mm, respectively. The difference between the two adjacent lateral displacement peaks is 4.10mm, 1.89mm and 1.44mm, which indicates that the lateral displacement about the pile gradually decreases with the increasement of the HLA, while the displacement reduction rate gradually decreases, and the controlling effect on the lateral

displacement is gradually weakened. With the increasement about HLA, the relative differences about pile lateral displacements decrease first and then increases. The greater the relative differences about lateral displacements of side pile, the more serious the bending degree of side pile. The minimum relative difference about lateral displacements of pile body occurs when the HLA is 1200kN/m, and the relative difference is only 10.77mm, which indicates that the HLA has a relatively optimal value on the bending deformation about pile. Whether the HLAs are too large or too small, the side piles are prone to produce large bending deformation of pile body, resulting in structural damage, so the influence of HLA on structure should be considered in the design of side pile.

The variation law about the deformation of pile top with HLA after the completion of station construction is shown in Figure 6.

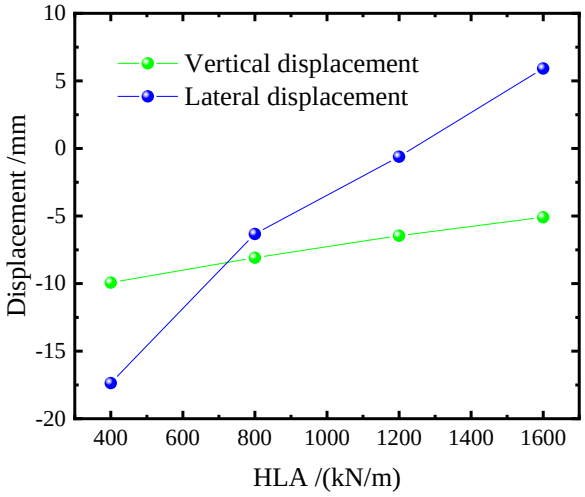

Fig. 6 - Variation law of the deformation about pile top with various HLA

In Figure 6, under constant VLA, the vertical settlement of pile top reduces with the increase of HLA. The reason is the lateral lining effect of HLA on pile top, which increases the contacting stresses between side pile and soil around the pile, resulting in a gradual increase in the side friction resistance about pile borne by side pile, thus reducing the vertical settlement of side pile. When the HLA increases to 1200kN/m, the lateral displacements about pile top changes from negative displacements inside the station to positive displacement outside the station, which indicates that HLAs play a vital role in deformation about pile top and should be paid more attention to it. It is worth mentioning that the vertical displacement and horizontal displacement are equal around HLA=700kN/m. This is because the main control factor in this section is HLA (i.e., horizontal force). With the increase of HLA, the horizontal displacement of pile top significantly decreases, while the vertical displacement of pile top is less affected by this.

Analysis of the variation law about internal force of pile

The variation law of internal forces of the lower pile structure under different HLA during the construction process is displayed in Figures 7~8. The final distribution about the comparison diagram of internal forces and peak value of side pile after the completion of station construction are shown in Figure 9.

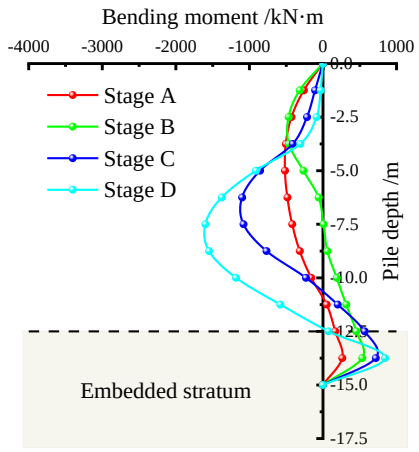

(a) HLA =400kN/m

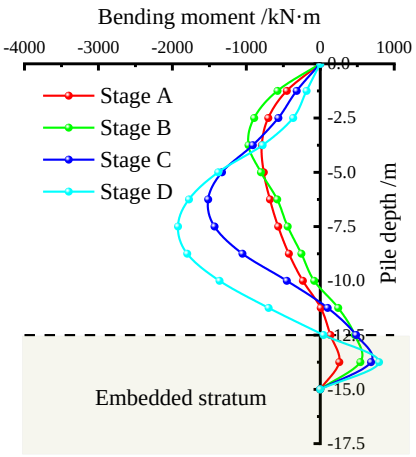

(b) HLA =800kN/m

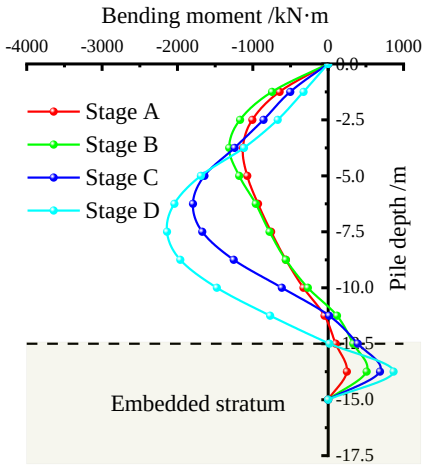

(c) HLA =1200kN/m

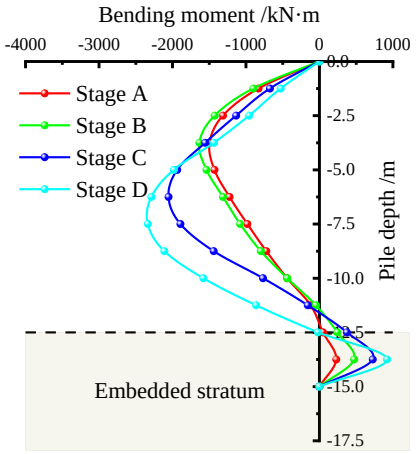

(d) HLA =1600kN/m

Fig. 7 - Evolution of the bending moments about side pile under different HLA

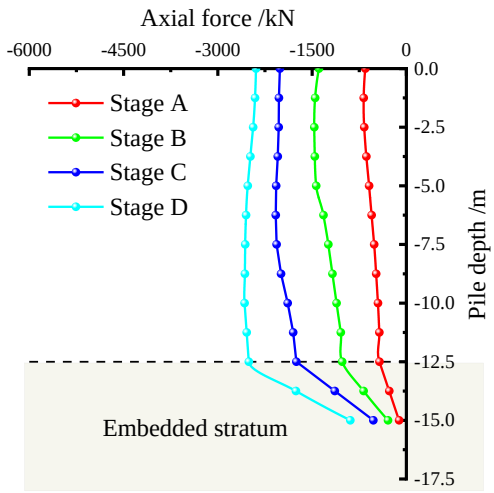

(a) HLA =400kN/m

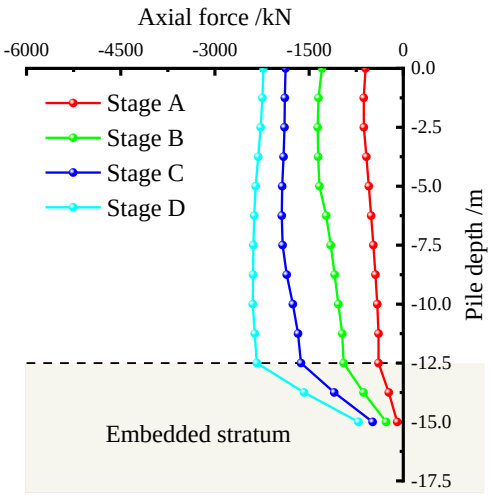

(b) HLA =800kN/m

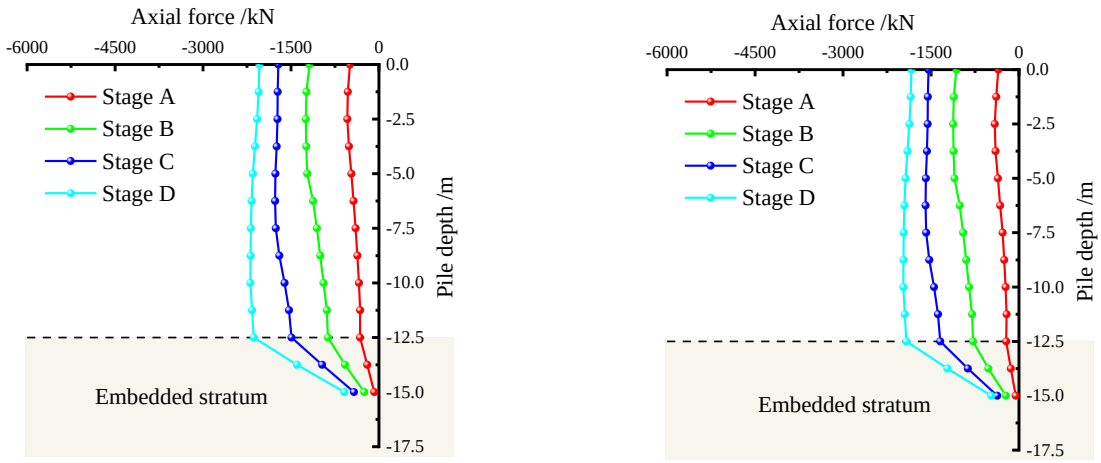

(c) HLA =1200kN/m *(d) HLA =1600kN/m*

Fig. 8 - Variation law of the axial forces about side piles under various HLA

In Figures. 7~8, during the construction of the station, the bending moments about the pile are basically presented as “bow” distribution with large in the middle and small at both ends. The pile part above the excavation faces about the soil is mainly strained on the excavation side of the station, while the pile body embedded in the lower soil layer is mainly strained on the side facing the soil behind the pile, and the position about the largest bending moments moves down with the continuous downward excavation of the soil. The axial forces about the side pile increase with the excavation of the station soil. This is because the soil at the excavation side of station is unloaded, the soil around the pile body being disturbed, then the side friction resistance provided to the side pile decreases, resulting in the axial forces about side pile increasing.

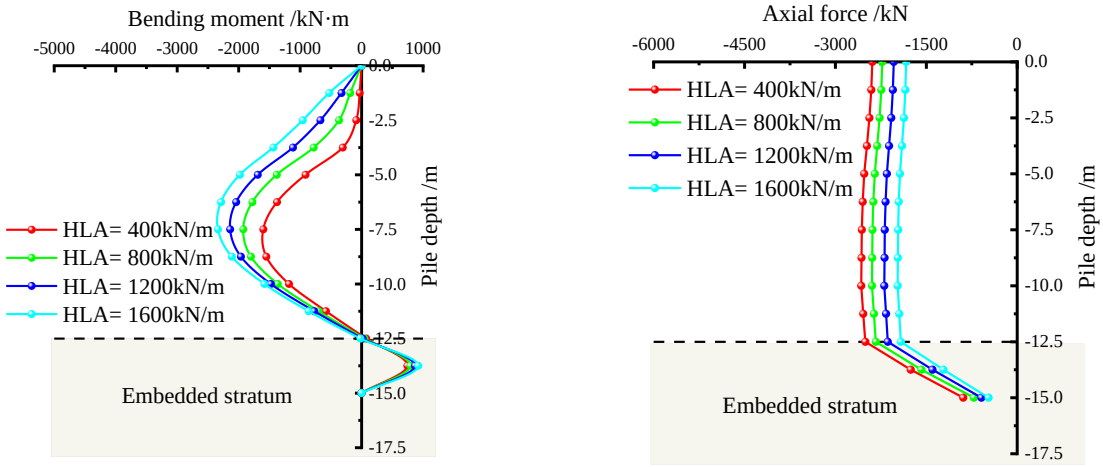

(a) Distribution diagram of bending moments *(b) Distribution diagram about axial force*

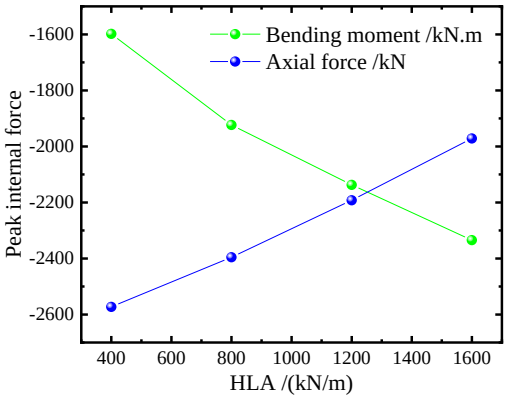

(c) The relationship between the peak internal force and HLA

Fig. 9 - Comparative diagram about the internal force in the final stage of side pile

In Figure 9, with the increase of the HLA, the bending moments of the side pile gradually increases, but the axial force about the pile gradually decreases. Taking the HLA of 400kN/m and 1600kN/m as an example, the bending moments as well as axial forces about the former are -1598.01kN·m and -2573.14kN respectively, and that of the latter are -2334.73kN·m and -1971.78kN respectively, which increase by 46.10% compared with the bending moments. The axial force value decreased by 23.37%, indicating that the impact about the HLA on the bending moments about side pile is greater than that of the axial force.

The influence of VLA on side pile

Deformation analysis of the pile

The evolution rule about lateral displacements of pile structure under different VLA along with the station construction process is displayed in Figure 10, and the final lateral displacements diagram about pile under different VLA after the station construction is shown in Figure 11.

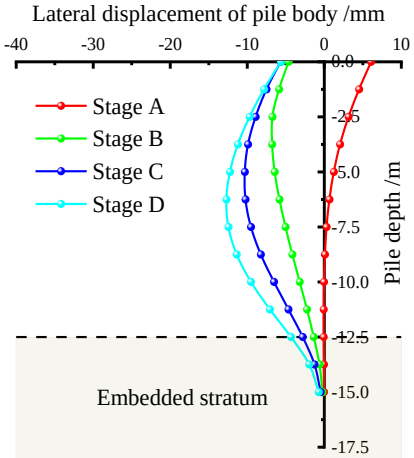

(a) VLA =800kN/m

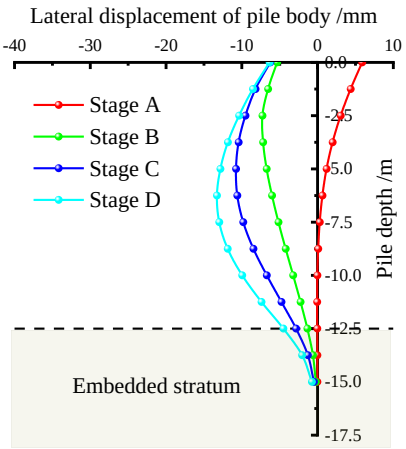

(b) VLA =1200kN/m

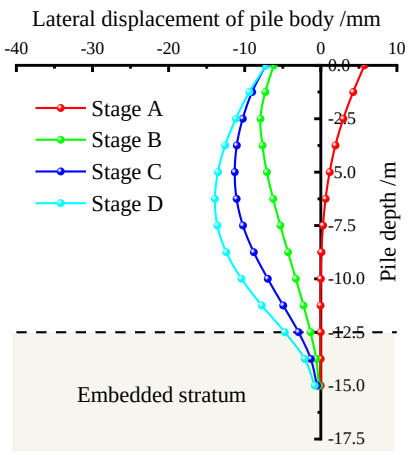

(c) VLA =1600kN/m

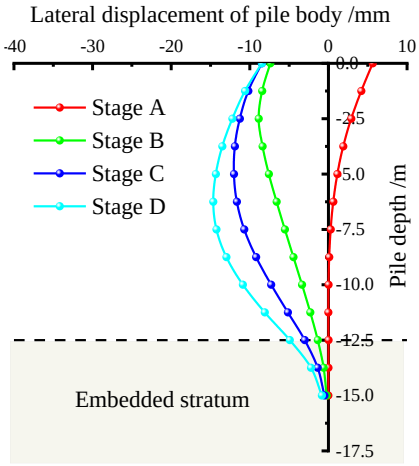

(d) VLA =2000kN/m

Fig. 10 - Evolution diagram of the lateral displacements about pile under various VLA

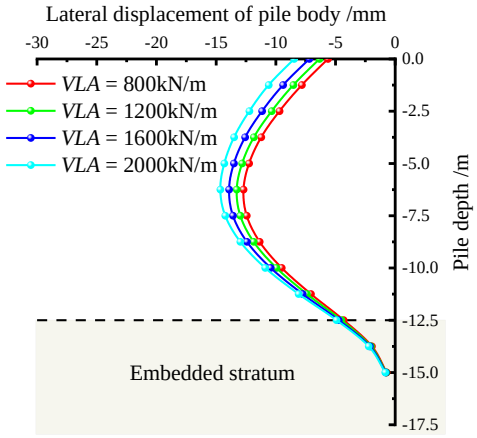

Fig. 11 - Comparison curve about final lateral displacements of pile under different VLA

In Figures. 10~11, the lateral displacements about side pile under different VLA are basically the same, which is mainly manifested as “forward” deformation mode when the buckling arch is completed, and transformed into “bulging” deformation mode after the soil excavation of station. When the VLA is 800kN/m, 1200kN/m, 1600kN/m and 2000kN/m, the final lateral displacement of side piles is 12.70mm, 13.27mm, 13.91mm and 14.64mm in sequence, and the VLA is 2000kN/m compared with 1600kN/m. The lateral displacement increases only by 0.73mm, that is, the final lateral displacements about the side pile gradually adds with the VLA, but the increasing extent is small. This is because the side pile in the station with PBA method is similar to the flexural component, and it is in a “slightly bent state” under the action of the inner soil excavation and the outer soil pressure. The increase of the VLA will increase the eccentric compression of the side pile, and the second-order effect of the VLA will be intensified, resulting in the trend about lateral displacements of pile increasing with the VLA, which is basically consistent with the conclusion of literature [34].

The peak value of lateral displacements about side pile in the final construction stage is

shown in Table 5.

Tab. 5 - Peak value of final displacement of pile body under different VLA /mm

Lateral displacement X /mm	VLA = 800kN/m	VLA = 1200kN/m	VLA = 1600kN/m	VLA = 2000kN/m
Maximum value X_{max}	-0.71	-0.74	-0.78	-0.82
Minimum value X_{min}	-12.70	-13.27	-13.91	-14.64
Relative difference X_d	11.99	12.53	13.13	13.82

In Table 5, the relative difference of lateral displacements about pile gradually adds with the VLA, but the change range is small. When the VLA is 800kN/m, 1200kN/m, 1600kN/m and 2000kN/m, the relative difference of lateral displacement of side pile body is 11.99mm, 12.53mm, 13.13mm and 13.82mm in sequence. It can be found that the difference between the two neighbours is 0.54mm, 0.60mm and 0.69mm, which indicates that the bending degree about pile grows slowly with the VLA.

The variation curves about the displacements of side pile top with the VLA after the completion of station construction is shown in Figure 12.

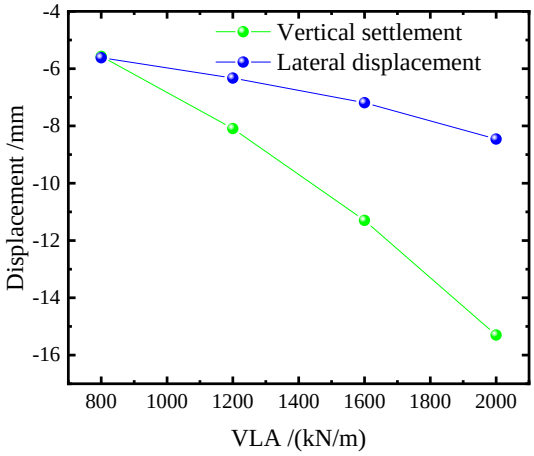

Fig. – 12 Variation curves about the displacements of pile top under different VLA

In Figure 12, under constant HLA, both vertical settlements as well as horizontal displacements about pile top grows with VLA. When the VLA is 800kN, the final vertical settlements as well as horizontal displacements about pile top are -5.57mm and -5.62mm, respectively. When the VLA increases to 2000kN/m, the vertical settlements as well as horizontal displacements about pile top are -15.30mm and -8.46mm, respectively. Compared with the VLA =800kN/m, the increment about vertical settlements as well as horizontal displacements is 9.73mm and 2.84mm, respectively, with an increase of 174.69% and 50.53%, respectively. It reveals that the vertical settlements about side piles is more significantly influenced by the increase of VLA, and the lateral displacements about pile only grows slightly due to the second-order effect of VLA.

Analysis of the variation law about internal forces of pile

The evolution law about internal force of the lower pile structure under different VLA during the construction process is displayed in Figures. 13~14. The distribution of final internal force and peak internal forces diagram about the pile after the completion of the station construction are shown in Figure 15.

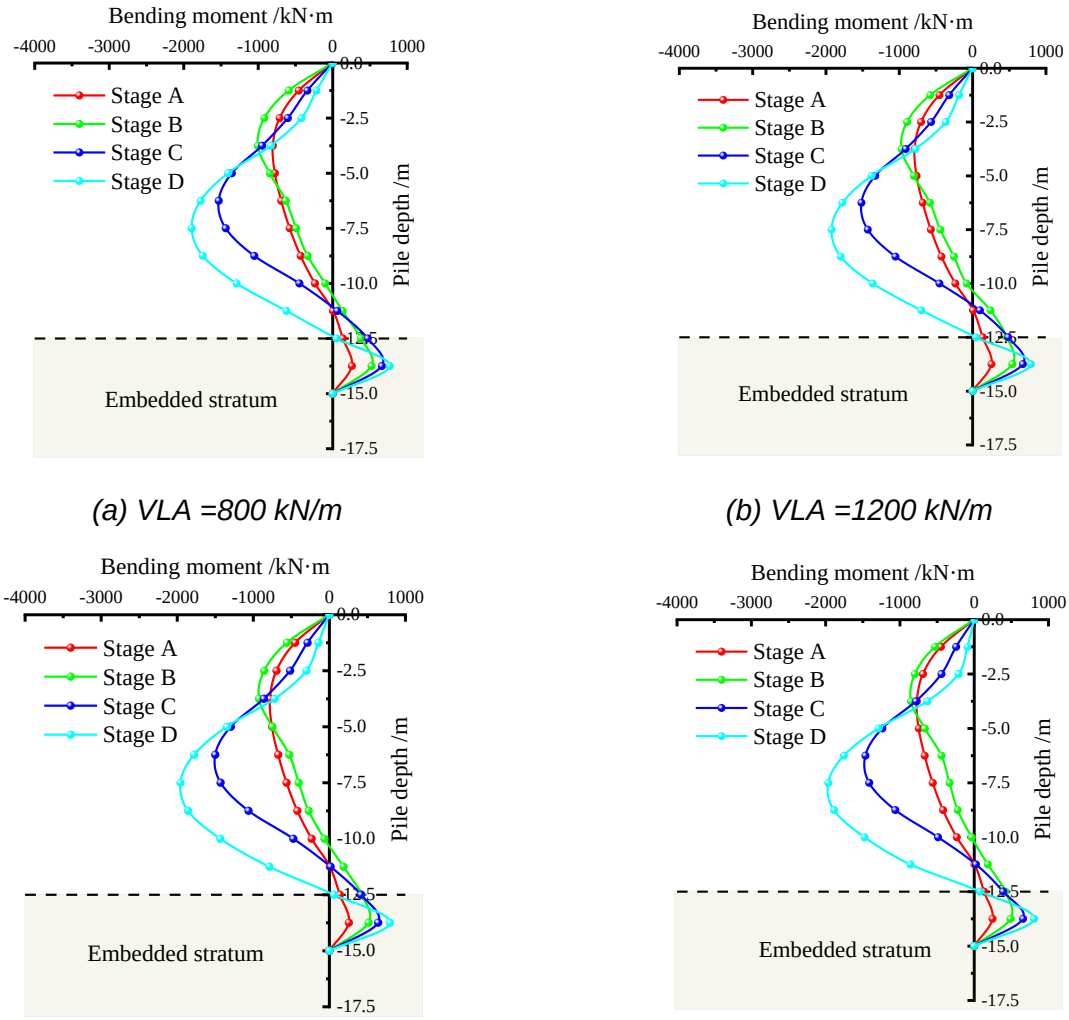

(a) VLA =800 kN/m

(b) VLA =1200 kN/m

(c) VLA =1600 kN/m

(d) VLA =2000 kN/m

Fig.13 - Evolution of the bending moment of pile under different VLA

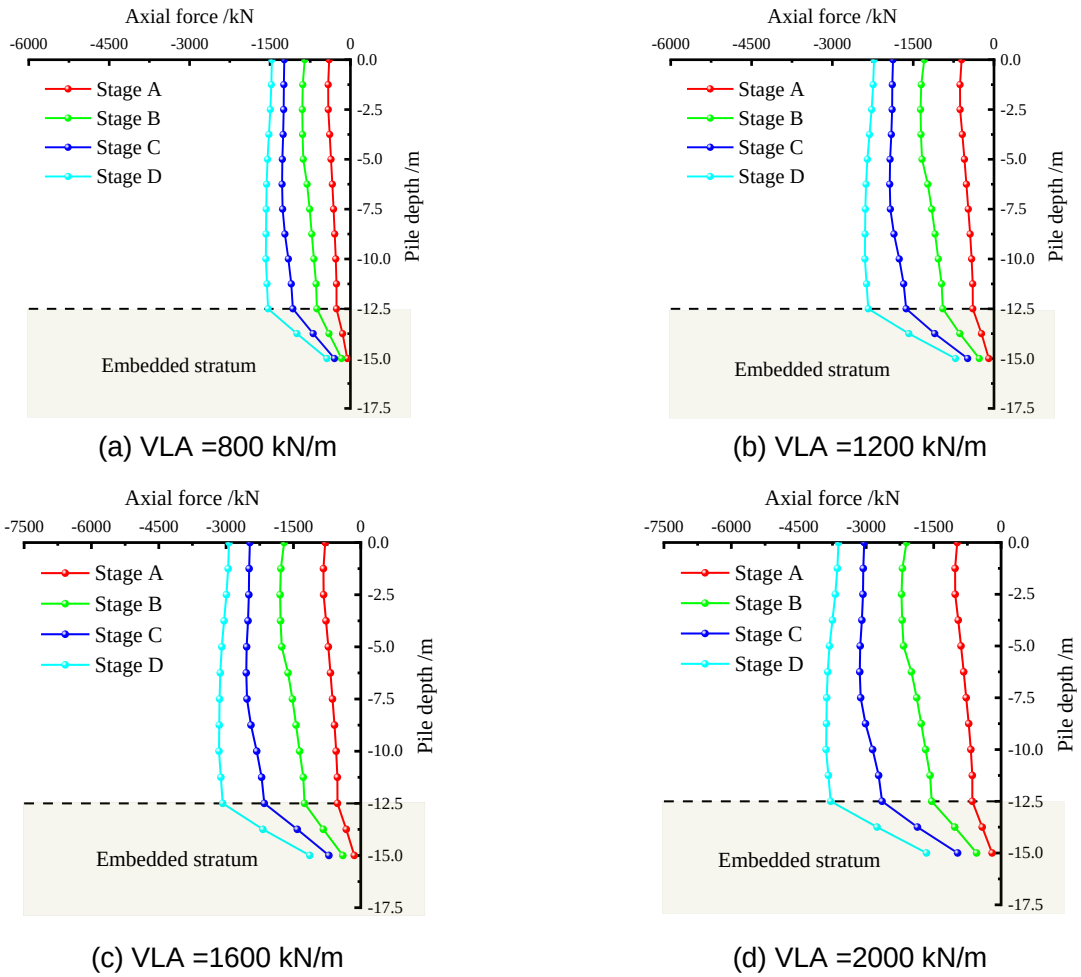

Figure – 14 Evolution diagram of the axial force of side pile under different VLA

In Figs. 13-14, during the construction process of station, the evolution law of internal force of side piles under different VLA is basically the same, and the bending moments about pile are basically presented as a “bow” distribution feature with large in the middle and small at both ends. In addition, the pile above the excavation face is mainly strained on the excavation side of the station, while the pile embedded in the lower soil layer is mainly strained on the side facing the soil behind the pile. The location of the largest bending moments decreases with the continuous downward excavation of the soil. The axial forces about the side pile grows with the excavation of the station soil, this is because the soil at the station excavation side is unloaded and the soil around the pile body is perturbance by the excavation. The side friction resistance provided to the side pile decreases, resulting in the increase of axial forces about the side pile.

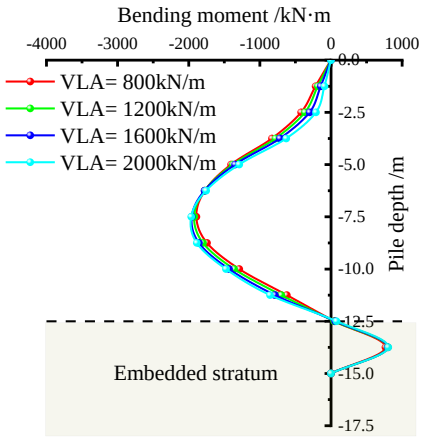

(a) Allocation diagram of the bending moment

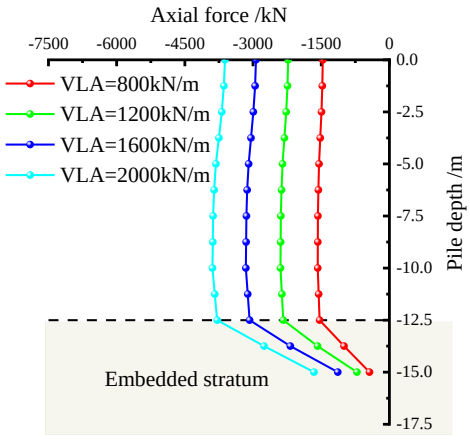

(b) Allocation diagram of the axial force

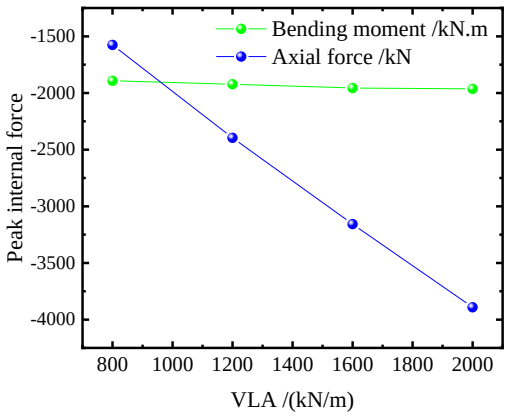

(c) The relationship between peak internal force and VLA

Fig. 15 - Comparison of the final internal force about side pile under various VLA

In Fig. 15, the bending moment and axial force of side pile both increase with VLA. When VLA is 800kN/m, the largest bending moments as well as axial forces about side pile are -1892.21kN·m and -1576.20kN respectively. When VLA increases to 2000kN/m, the largest bending moments as well as axial forces about side piles are -1964.09kN·m and -3891.70kN respectively. Compared with the VLA = 800kN/m, the largest bending moments as well as axial forces increase by 71.88kN·m and 2315.50kN respectively, which increases by 3.80% and 146.90% respectively. It reveals that the increase of VLA greatly affect the axial force of side pile, but little influence on bending moment.

Influence of the SPP on side pile

Deformation analysis about the pile

The evolution rule about lateral displacements of lower pile structure under the action of SPP along with the construction process of station is shown in Figure 16.

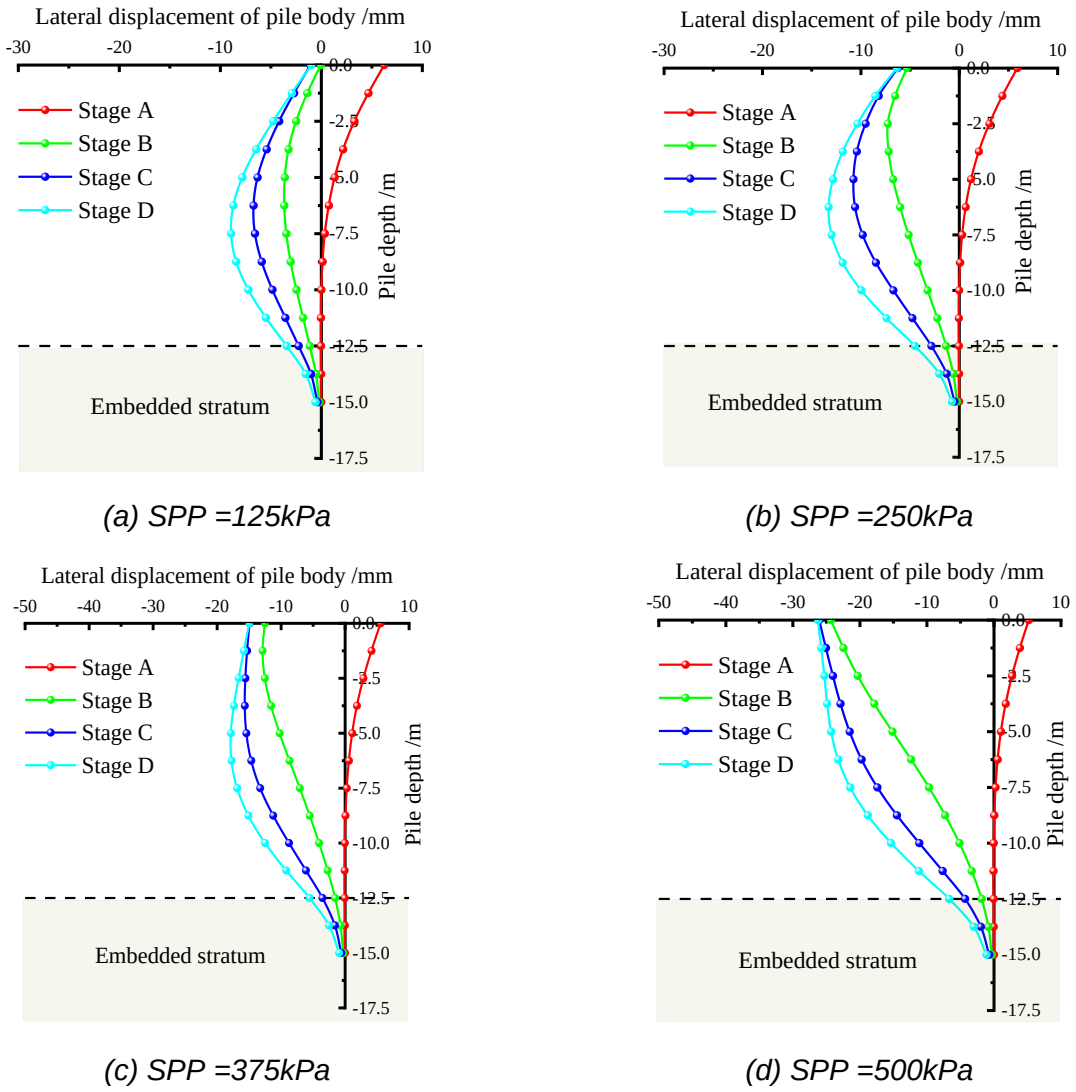

Fig. 16 - Evolution law of lateral displacements about the pile under various SPP

In Figure 16, after the completion of arch, the side pile produces a “forward” type positive displacement to the outside of the station due to the HLA, and with the increase of SPP, the positive displacement shows a gradually decreasing trend. When the SPP is 0.125 MPa, 0.250 MPa, 0.375 MPa, 0.500 MPa, the largest lateral displacements about the pile after the completion of arch all appears at the pile top, and the value is 6.24mm, 5.91mm, 5.57mm, 5.23mm, and the positive displacement gradually decreases. This is because under the action of SPP, the soil behind the pile compresses into the station, which plays a crucial role in restraining the positive displacements about the side pile caused by the HLA. Subsequently, due to the excavation of soil inside the station, the side pile gradually deviates to the station. There is no internal lining system in the side pile when the soil is excavated, and the pile top position is restricted and controlled only by the HLA, VLA and crown beam. With the increase of SPP, the lining effect about the pile top turns into unstable, and the deformation about pile body gradually change from the deformation mode of “bulging” to “backward”. When the SPP is large, the lateral soil pressures about the side pile increases, and the HLA and VLA on the side pile top is not enough to resist the SPP, and the instability failure occurs

first at the pile top, leading to large deformation.

The final lateral displacements diagram about pile structure under various SPP after the completion of station construction is shown in Figure 17, and the peak value of lateral displacements about pile under various SPP at the final stage is shown in Table 6.

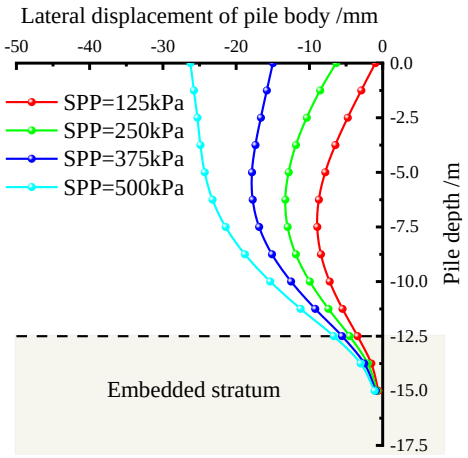

Fig. 17 - Comparison of the final lateral displacements about pile body

Tab. 6 - Peak value of the final displacements of pile under different SPP /mm

Lateral displacement X /mm	SPP =125kPa	SPP =250kPa	SPP =375kPa	SPP =500kPa
Maximum value X_{max}	-0.57	-0.74	-0.92	-1.10
Minimum value X_{min}	-8.92	-13.27	-17.83	-26.24
Relative difference X_d	8.35	12.53	16.91	25.14

In Figure 17, with the increase of SPP, the lateral displacements about the side pile increase, and the displacements about the pile body gradually change from “bulging” type to “backward” type. The position where the maximum lateral displacement occurs shifts from the middle of the pile to the pile top, and side pile begins to show a tendency of instability and failure. Therefore, the corresponding lining system should be set according to the SPP to guarantee the stabilities about side pile during construction.

In Table 6 and Figure 17, with the increase of SPP, the relative difference of lateral displacements about the pile gradually increases, and the change rate about growth gradually accelerates. When the SPP is 125kPa, 250kPa, 375kPa and 500kPa, the relative difference about lateral displacements of side pile is 8.35mm, 12.53mm, 16.91mm and 25.14mm, respectively. It can be found that the difference between the adjacent two is 4.18mm, 4.38mm and 8.23mm, which indicates that the greater the SPP, the greater the relative difference of lateral displacements about the pile, and the more serious the bending degree about the pile, which is more unfavourable to the stability of the side pile. When necessary, lining measures should be taken to strengthen the side pile.

The variation curve about the displacements of pile top with SPP after the completion of station construction is shown in Figure 18.

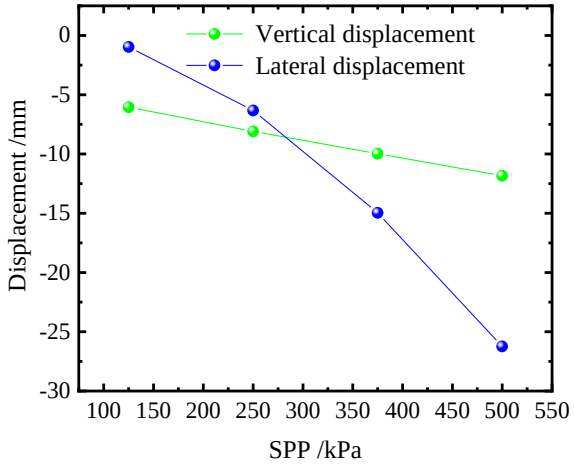

Fig. 18 - The variation curves about the displacement of pile top under different SPP

In Figure 18, with the increase of SPP, the side soil pressure borne by the side pile increases, and the vertical settlement of the pile top increases linearly. This is mainly due to the increasement about the SPP, the soil behind the pile is compressed and compacted, resulting in a certain vertical deformation, and at the same time, the side pile is also subjected to downward settlement deformation. The settlement amount is almost positively correlated with the SPP. Also, the lateral displacement about the pile top grows with the SPP, this is because the lateral lining strength about the pile top is becoming insufficient to resist the side soil pressure behind the pile, and the top of side pile gradually begins to show a trend of instability and failure. When the SPP is 125kPa, 250kPa, 375kPa and 500kPa, the lateral displacements about the side pile top are -0.97mm, -6.33mm, -14.96mm and -26.24mm, respectively, and the difference between the two adjacent piles is 5.36mm, 8.63mm and 11.28mm, respectively. This reveals that the SPP greatly influences the lateral displacements about pile top, and the lateral displacements about pile top grows significantly with the SPP.

Analysis of the variation rule about the internal forces of pile

The evolution curves about internal force of the pile under the action of SPP is shown in Figures 19~20. The final distribution law of internal force about the pile after the completion of the station construction and the comparison diagram of peak internal forces are shown in Figure 21.

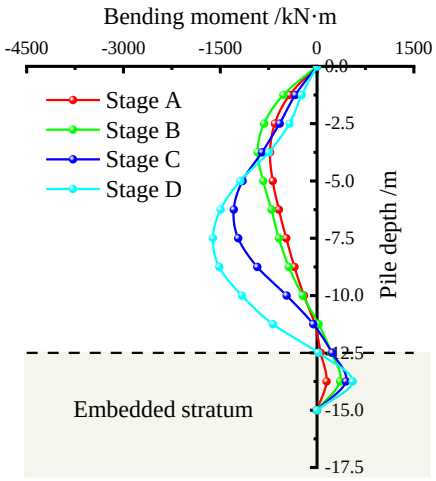

(a) SPP =125kPa

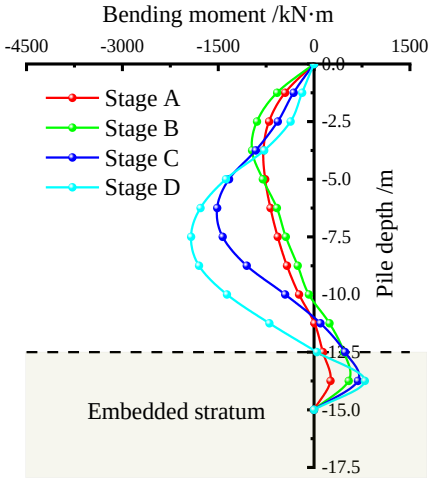

(b) SPP =250kPa

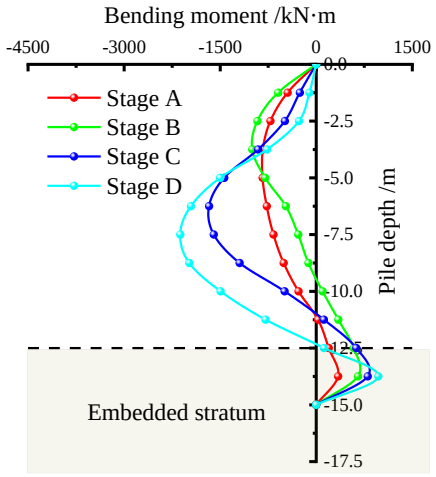

(c) SPP =375kPa

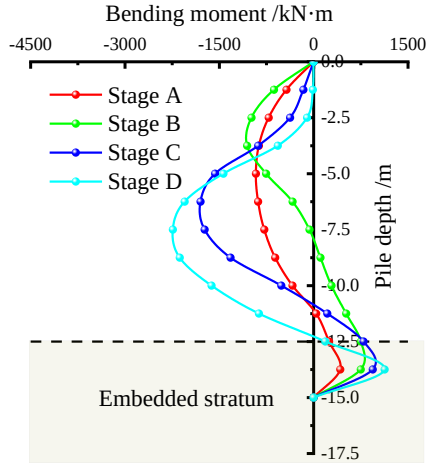

(d) SPP =500kPa

Fig. 19 - Evolution law of the bending moment of side pile under different SPP

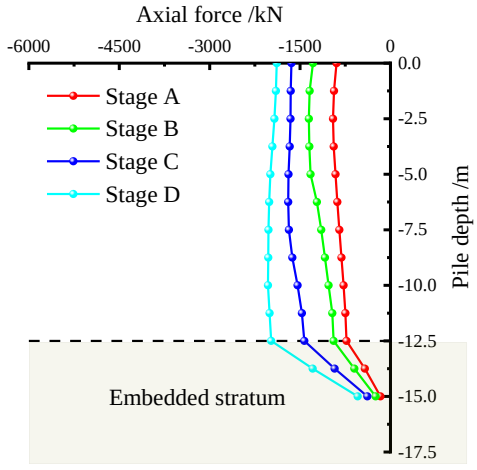

(a) SPP =125kPa

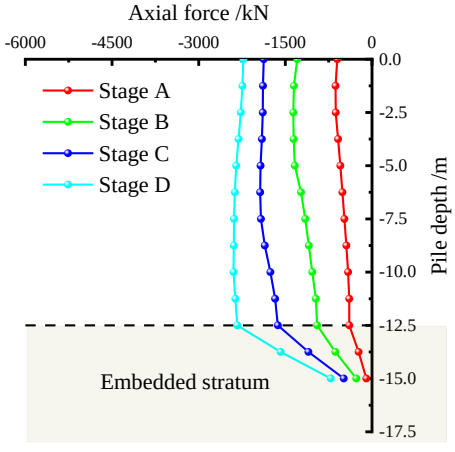

(b) SPP =250kPa

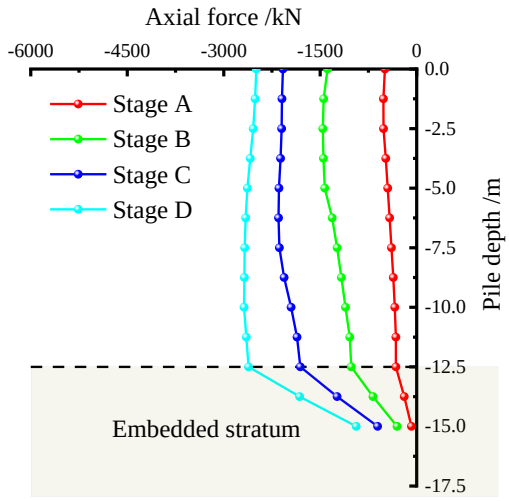

(c) SPP =375kPa

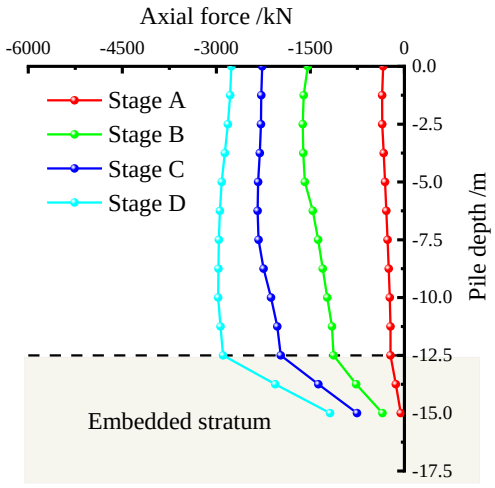

(d) SPP =500kPa

Fig. 20 - Evolution law of the axial forces of pile under different SPP

In Figures 19~20, under the action of SPP, the force morphology of side piles changes with the construction process in a basically consistent way, and the bending moments of piles are presented as “bow” distribution characteristics with large in the middle and small in both ends. The pile body above the excavation surface is mainly strained on the excavation side of the station, and the pile body imbedded in the lower soil layer is mainly strained on the side facing the soil behind the pile. The position about the largest bending moment moves down with the continuous downward excavation of the soil. The axial force of side piles increases gradually with the excavation of station soil. This is due to the soil unloading at the excavation side of the station, the soil around the pile body is perturbate by the excavation, and the side friction resistance provided to the side pile decreases, resulting in the increase of axial forces about the side pile.

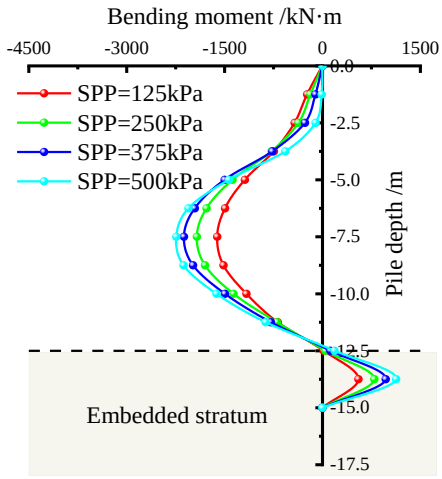

(a) Distribution diagram of bending moment

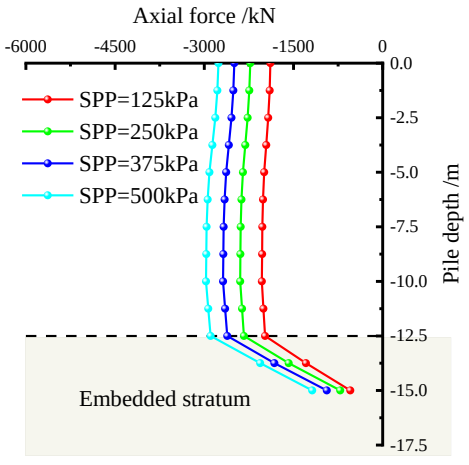

(b) Distribution diagram of the axial force

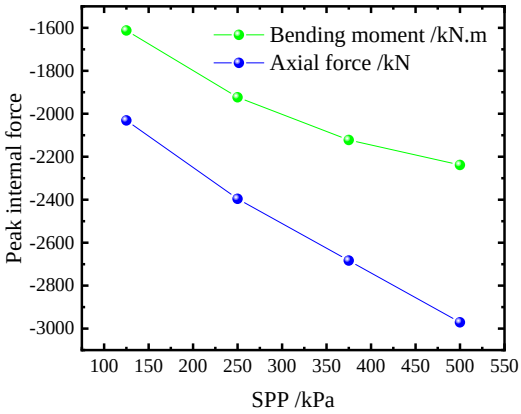

(c) The relationship between the peak internal force and the SPP

Fig. 21 - Final internal force diagram of side pile under different SPP

In Figure 21, the overall bending moments as well as axial forces of the side pile increase with SPP. Taking the SPP =125kPa and 500kPa as an example, the bending moments as well as axial forces about the former are -1612.33kN·m and -2030.96kN respectively. While that of the latter are -2238.49kN·m and -2970.85kN respectively, and the bending moments as well as axial forces increase by 626.16kN·m and 939.89kN respectively. Also, the increase rate of the largest bending moments about the pile decreases with the increase of the SPP. The peak bending moments of side piles under SPP= 125kPa, 250kPa, 375kPa and 500kPa are -1612.33kN·m, -1923.49kN·m, -2121.88kN·m and -2238.49kN·m, respectively. The increments between the two adjacent values are 311.16kN·m, 198.39kN·m and 116.61kN·m, respectively. The peak value gradually increases, but the change rate gradually decreases.

CONCLUSIONS

(1) HLA has a better control effect on the lateral deformation of the side pile, which effectively ensure the stabilities about the side pile. However, HLA has a relatively optimal value, and too large or too small HLA will lead to greater bending degree of the pile. The allowable value of HLA should be measured according to the actual post-pile load and flexural stiffness of the pile on the site. In this paper, the optimal HLA of the project is 1200kN, and the overall deformation of side piles tends to be more balanced, and the relative difference of lateral deformation is only 10.77mm.

(2) Compared with the lateral deformation of pile, the VLA significantly affects the vertical settlement of side pile. When the VLA increases from 800kN to 2000kN, the vertical settlement of side piles increases by 9.73mm, while the lateral displacement only increases by 2.84mm, with an increase of 174.69% and 50.53%, respectively. The VLA has a more significant influence on the vertical settlement about side piles, and the lateral displacements about pile body only increases slightly due to the second-order effect of VLA.

(3) The SPP greatly influences the stability of the side pile, the lateral pressures about soil behind the pile increase with the SPP, and the deformation of pile will change from the deformation

mode of “bulging” to “backward”. The top of the pile will easily produce large deformation, and the internal forces about the pile increases. For the case of large SPP, it is recommended to take appropriate lining measures to guarantee the stabilities about the side pile.

COMPETING INTERESTS

The authors have no relevant financial or non-financial interests to disclose.

DATA AVAILABILITY

All data, models, and code generated or used during the study appear in the submitted article.

REFERENCES

[1] Gao, Y.Q., Xiang, Q.M., Su, J.X., et al, 2022. Strata subsidence characteristics of shield tunneling in coastal soft soil area. Stavební Obzor - Civil Engineering Journal, Vol. 31, 625-635. https://doi.org/10.14311/CEJ.2022.04.0047

[2] Li, Y.F., Li, J.L., Zhao, J.H., et al, 2023. Research on a safety evaluation system for railway-tunnel structures by fuzzy comprehensive evaluation theory. Stavební Obzor - Civil Engineering Journal, Vol. 32, 122-136. https://doi.org/10.14311/CEJ.2023.01.0010

[3] Zhang, H.J., Liu, G.N., Liu, W.X., et al, 2023. Stability evaluation of rock pillar between twin tunnels using the YAI. Scientific Reports, Vol. 13, 13187. https://doi.org/10.1038/s41598-023-40167-9

[4] Zhao, J.P., Tan, Z.S., Yu, R.S., et al, 2022. Deformation responses of the foundation pit construction of the urban metro station: a case study in Xiamen. Tunnelling and Underground Space Technology, Vol. 128, 104662. https://doi.org/10.1016/j.tust.2022.104662

[5] Wang, T., Luo, F.R., Liu, W.N., et al, 2012. Study of surface settlement and flexible joint pipeline deformation induced by metro station construction with PBA method. China Civil Engineering Journal, Vol. 45, 155-161. (In Chinese). https://doi.org/10.15951/j.tmgcxb.2012.02.005

[6] Liu, Y.S., Huang, Y.Y., 2023. The surface settlement law of precipitation in pile-beam-arch station adjacent to pile foundation. KSCE Journal of Civil Engineering, Vol. 27, 1441-1457. https://doi.org/10.1007/s12205-023-2192-4

[7] Li, C.J., 2022. Research on adaptability of PBA improved construction method for underground station in loess area. Railway Standard Design, Vol. 66, 97-104. (In Chinese). https://doi.org/10.13238/j.issn.1004-2954.202102190006

[8] Zeng, Y., Bai, Y., Zou, Y., et al, 2022. Numerical study on stratigraphic and structural deformation patterns considering surface load with pile-beam-arch method construction. Symmetry, Vol. 14, 1892. https://doi.org/10.3390/sym14091892

[9] Guo, X.Y., Wang, Z.Z., Geng, P., et al, 2021. Ground surface settlement response to subway station construction activities using pile–beam–arch method. Tunnelling and Underground Space Technology, Vol. 108, 103729. https://doi.org/10.1016/j.tust.2020.103729

[10] Huang, B., Du, Y.H, Zeng, Y., et al, 2022. Study on stress field distribution during the construction of a group of tunnels using the pile–beam–arch method. Buildings, Vol. 12, 300. https://doi.org/10.3390/buildings12030300

[11] Yu, L., Zhang, D.L., Fang, Q., et al, 2019. Surface settlement of subway station construction using pile-beam-arch approach. Tunnelling and Underground Space Technology, Vol. 90, 340-356. https://doi.org/10.1016/j.tust.2019.05.016

[12] Li, T., Li, Y., Yang, T.Y., et al, 2023. Influence of the large-span pile-beam-arch construction method on the surface deformation of a metro station in the silty clay-pebble composite stratum. Materials, Vol. 16, 2934. https://doi.org/10.3390/ma16072934

[13] Wei, Y.L., Ma, H.L., 2023. Load-bearing deformation characteristics and application of reversed micro steel-pipe pile composite foundation. Journal of Anhui Jianzhu University, Vol. 31, 14-18. (In Chinese). https://doi.org/10.11921/j.issn.2095-8382.20230203

[14] Zhang, J.J., Sui, Q.Q., Guo, M., et al., 2023. Analysis and discussion of the load test of manually

digging piles of Qingdao Jiaodong International Airport. Mechanics in Engineering, Vol. 45, 765-776. (In Chinese). https://doi.org/10.6052/1000-0879-22-573

[15] Guo, Y.C., Lv, C.Y., Hou, S.Q., et al, 2021. Experimental study on the pile-soil synergistic mechanism of composite foundation with rigid long and short piles. Mathematical Problems in Engineering, Vol. 2021, 6657116. https://doi.org/10.1155/2021/6657116

[16] Fu, Q., Li, L., 2021. Vertical load transfer behavior of composite foundation and its responses to adjacent excavation: centrifuge model test. Geotechnical Testing Journal, Vol. 44, 191-204. https://doi.org/10.1520/GTJ20180237

[17] Zhang, D.S., Zhang, X.L., Tang H.T., et al., 2023. Effects of soil arching on behavior of composite pile supporting foundation pit. Computational Particle Mechanics, Vol. 10, 645-662. https://doi.org/10.1007/s40571-022-00518-1

[18] Liu, X.R., Liu, Y.Q., Yang, Z.P., et al, 2017. Numerical analysis on the mechanical performance of supporting structures and ground settlement characteristics in construction process of subway station built by pile-beam-arch method. KSCE Journal of Civil Engineering, Vol. 21, 1690-1705. https://doi.org/10.1007/s12205-016-0004-9

[19] Jin, G.L., Wang, Y., Gu, K.Y., 2012. Influence of constructing hand-dug piles closing to retaining wall. Journal of Shanghai Jiaotong University, Vol. 46, 84-88. (In Chinese). https://doi.org/10.16183/j.cnki.jsjtu.2012.01.018

[20] Liang, R.Z., Wei, S., Wang, X.X., et al., 2022. Comparative test and analysis of the deformation in enclosure structure of internally-braced and cantilevered locked steel-pipe pile foundation pits. Modern Tunnelling Technology, Vol. 59, 172-182. (In Chinese). https://doi.org/10.13807/j.cnki.mtt.2022.03.020

[21] Chen, Z.Q., Guo, G., Guo, W.X., et al, 2017. Stress characteristics and application of micro steel anti-slide piles. Journal of Lanzhou University, Vol. 53, 43-47. (In Chinese). https://doi.org/10.13885/j.issn.0455-2059.2017.01.006

[22] Hazarika, H., Watanabe, N., Sugahara, H., et al, 2017. Influence of placement and configuration of small diameter steel pipe pile on slope reinforcement. 19th International Conference on Soil Mechanics and Geotechnical Engineering, Seoul, Korea.

[23] Xiang, B., Zhang, L.M., Zhou, L.R., et al, 2015. Field lateral load tests on slope-stabilization grouted pipe pile groups. Journal of Geotechnical and Geoenvironmental Engineering, Vol. 141, 04014124. https://doi.org/10.1061/(ASCE)GT.1943-5606.0001220

[24] Kaczmarek, Ł., Dobak, P., Szczepański, T., et al, 2021. Triaxial creep tests of glacitectonically disturbed stiff clay–structural, strength, and slope stability aspects. Open Geosciences, Vol. 13, 1118-1138. https://doi.org/10.1515/geo-2020-0291

[25] He, T.F., 2021. Analysis on deformation of foundation pit retaining structure under the condition of CFG pile composite foundation. Subgrade Engineering, Vol. 218, 186-191. (In Chinese). https://doi.org/10.13379/j.issn.1003-8825.20210 3046

[26] An, G.F., Zhang, H.B., Liu, T.J., 2012. Numerical analysis of bearing characteristics of composite subgrade reinforced by chemical churning pile groups. Rock and Soil Mechanics, Vol. 33, 906-912. (In Chinese). https://doi.org/10.16285/j.rsm.2012.03.049

[27] Wang, Z., 2018. Research on reinforcement method of loess foundation under existing building. Xi'an University of Architecture and Technology, Master's thesis, Xi'an. (In Chinese).

[28] Liu, S., Guo, P.P., Li, X., et al, 2023. Settlement behavior of composite foundation with deep mixed piles supporting highway subgrades in water-rich flood plains. Water, Vol. 15, 2048. https://doi.org/10.3390/w15112048

[29] Benmebarek, M.A., Benmebarek, S., Rad, M.M., et al, 2022. Pile optimization in slope stabilization by 2D and 3D numerical analyses. International Journal of Geotechnical Engineering, Vol. 16, 211-224. https://doi.org/10.1080/19386362.2021.1972628

[30] Chen, L.J., Jiang, C., Pang, L., et al, 2021. Lateral soil resistance of rigid pile in cohesionless soil on slope. Computers and Geotechnics, Vol. 135, 104163. https://doi.org/10.1016/j.compgeo.2021.104163

[31] Chen, Y.M., Xu, D.P., 2013. FLAC/FLAC3D foundation and engineering application. China Water and Power Press, Beijing. (in Chinese).

[32] Huang, F., Li, Z.L., Zhu, L., et al, 2016. The study of ultimate support pressure of shield tunnel face subjected to user - defined constitutive model. Journal of Railway Science and Engineering, Vol. 13, 891-897. (in Chinese). https://doi.org/10.19713/j.cnki.43-1423/u.2016.05.015.

[33] Jia, F., Du, Y.Q., Yang, W.B., et al, 2023. Research on deformation laws of deeply buried tunnels with small clearance in soft rock by different tunnelling methods. Industrial Construction, Vol. 53, 21-28. (in Chinese).

https://doi.org/10.13204/j.gyjzG22091803.
[34] Li, T., Gao, Y., Shao, W., et al, 2019. Study on the influence of inclined load on the deformation law of side piles using PBA Method. Chinese Journal of Underground Space and Engineering, Vol. 15, 666-672. (in Chinese).